Un-mixing the Ocean
Double Diffusion and Turbulence in Polar Oceans

Leo Middleton

Supervisor: Dr. J.R. Taylor
Co-supervisors: Dr. P.R. Holland
Dr. K.W. Nicholls

Department of Applied Mathematics and Theoretical Physics
University of Cambridge
and
Polar Oceans Group
British Antarctic Survey

This dissertation is submitted for the degree of
Doctor of Philosophy

March 2022

To Wilf and Rox

Declaration

I hereby declare that except where specific reference is made to the work of others, the contents of this dissertation are original and have not been submitted in whole or in part for consideration for any other degree or qualification in this, or any other university. This dissertation is my own work and contains nothing which is the outcome of work done in collaboration with others, except as specified in the text and Acknowledgements. This dissertation is 150 pages long and contains around 35500 words, 110 equations and 26 figures.

Leo Middleton
March 2022

Un-mixing the Ocean
Double Diffusion and Turbulence in Polar Oceans
by Leo Middleton
Abstract

This thesis concerns theory, numerical simulations and observations of double-diffusion in polar settings. Double diffusion refers to processes occurring due to the difference in molecular diffusivities between two components that both contribute to the density. Specifically, these processes occur in the ocean due to the much slower diffusion of salinity compared to temperature. Within polar regions, thermohaline staircases have been frequently observed. These are layered structures in both temperature and salinity that can form due to double-diffusive processes, that give a characteristic ‘staircase’ shape to profiles of temperature and salinity. Thermohaline staircases provide observational evidence of the importance of double diffusion to small scale ocean mixing, and so motivate our discussion of double-diffusive convection in polar environments.

After an introduction to the topic, the first results chapter discusses the energetics of double diffusion, developing a new model for the flow of energy within double-diffusive fluids. The second results chapter is motivated by observations of thermohaline staircases beneath George VI Ice Shelf, Antarctica. We conducted Large-Eddy-Simulations to explore the interaction of double diffusive convection with turbulence forced at a prescribed rate. Utilising the theory developed in chapter 1, the transition between double diffusive convection and stratified turbulence is identified and a criterion is developed for that transition in terms of profiles in temperature, salinity, and turbulence rate.

The third results chapter considers observational turbulence data collected in the Chukchi Sea in the marginal seas of the Arctic Ocean. This data shows an oceanographic section of a warm core intrahalocline eddy, where thermohaline layering was observed. We develop a criterion to predict the observed turbulent dissipation rates using fine-scale temperature and salinity data, assuming double-diffusive convection is active. This criterion is based on the energetic model from the first results chapter and assumes a lateral stirring of ‘spice’ variance (compensated thermohaline variance) along isopycnals is the driver of turbulence. The final results chapter consists of an analysis of mooring data from beneath George VI Ice Shelf, at the same location as thermohaline staircases were observed. We find that shear-driven turbulence cannot explain the observed dissipation rates. Utilising the method from the third results chapter, we show that lateral variations in spice can explain the observed turbulent mixing, suggesting it exerts control over the ice shelf basal melt rate.

Acknowledgements

I would like to thank my supervisor John Taylor for his support and supervision throughout the PhD process. I always felt free to explore what I found most interesting, and he was always willing to engage constructively with wherever that research took us, for which I am incredibly grateful. My thanks are also to my co-supervisors Paul Holland and Keith Nicholls, who have consistently been kind in giving me their time and expertise. Although not official supervisors, Catherine Vreugdenhil and Peter Davis have always been on hand to provide advice, discuss ideas and give encouragement. Thank you Cat for always letting me draw all over your whiteboard. I couldn't have wished for a better supervisory team to lead me through the past four years.

I have been incredibly lucky to have two fantastic networks of researchers at both DAMTP and BAS that have been a source of inspiration and support. The Ice Shelf-Ocean Boundary Layer group meetings were consistently interesting, so in addition to the people above, thank you to Irena Vankova, Louis-Alexandre Couston, Ryan Patmore and Adrian Jenkins for sharing your research and ideas. Likewise, the Atmosphere-Ocean Dynamics group provided an opportunity to think and chat about a huge variety of topics in a casual setting, which kept my eyes open to the broader world of geophysical fluid dynamics. Thank you to the Polar Oceans team at BAS, who introduced me to the broad world of oceanography, and always endeavoured to involve PhD students, showing a level of respect that was refreshing. Thank you also to the George K. Batchelor laboratory group, who welcomed me, despite my total lack of laboratory work. Organising Friday lab lunch with Ben Young and Jeremy Parker was a real highlight and cutting up slabs of cheese for thirty people every Friday won't be quickly forgotten. A huge thanks to Alexander Brearley and Povl Abrahamsen for including me on the A68 cruise to Orkney Passage. Although the cruise work is not included within this thesis, it was a formative experience for me in developing my skills and my approach to research. Thank you also to the crew and scientists on the JCR for making the whole cruise happen and making it so enjoyable.

The PhD students at both BAS and DAMTP have consistently been there to celebrate, commiserate and support me throughout my PhD. Although I can't mention everyone here by name, I am humbled by the kindness and solidarity I have been shown. In particular, I would like to thank the ocean physics folks: Ryan Scott, Rachael Sanders, Lianne Harrison, David Bett, Jake Opher, Rachel Furner, Jo Zanker, Jon Rosser, Sam Lewin, Aaron Wienkers, and Chris Howland, for always being there to answer my questions, for keeping me company at conferences and for being exciting and dynamic researchers/people. I'd also like to thank my office mates: Sam Coffin, Arlie McCarthy and Kirstie Jones-Williams, for keeping my spirits up in the write up, and my DAMTP year-group: Ben Young, Jeremy Parker, Katherine Grayson and Karol Bacik, for being inspiring and encouraging throughout the PhD journey.

My friends, flatmates and family have been exceptionally important to me over the past four years. They have been my rock when I needed it, kept me hopeful and entertained throughout the pandemic, and kept me excited and inspired about the possibilities that life offers beyond my thesis. Thank you to Aoife O'Leary McNeice, Kate Schneider and Evan Wroe for keeping me sane in the first lockdown, and thanks to Kasia Warburton, Kalani Kariyawasam and Evan (again) for keeping me sane in the second. Throughout the pandemic, Aoife, Kate, Evan, Kasia and Kalani have been superb lockdown comrades, and I couldn't have wished for a stronger and kinder group of people to be stuck in a house with. I am grateful to my friends from QP for their great zoom chats and I long for when we can all be together again. Thank you to Danny Buss, Joe Ebo, Camila Marcias and Dieter Tetzner for the beautiful evenings spent eating and drinking. To Alice Fairnie, thank you for your presence in my life and for making me laugh, I look forward to seeing the world with you. To Reuben Ruxton, Matt Holmes and Luke Shaw, you have been there for me for the longest time, and I will always treasure your friendship. Thank you, Reuben, for the fantastic drawings, and the idea for my next paper included at the end of this thesis. Thank you to my parents, Holly and Giles, for their support, and for raising me with the outdoors so I always know what I'm missing when I sit at my computer. Finally, thank you to Wilfrid Middleton and Roxanne Middleton for being great friends as well as siblings. You have always inspired me to do more interesting things, and be more interested in things, for which I can't thank you enough. I dedicate this PhD to you both.

Table of contents

List of figures **xv**

List of tables **xxiii**

1 Introduction **1**

1.1 Double diffusion 2

1.2 Turbulence 7

1.2.1 Kolmogorov's Hypotheses 7

1.2.2 Stratification 10

1.2.3 Observational Methods 12

1.3 Polar Oceans 14

1.3.1 George VI Ice Shelf 16

1.3.2 Chukchi Sea 19

1.4 Chapter Summary 21

1.5 Double Diffusion Glossary 24

2 A general criterion for the release of background potential energy through double diffusion **27**

2.1 Introduction 27

2.2 Results 29

2.2.1 Governing Equations 29

2.2.2 Condition for an Up-gradient Buoyancy Flux 30

2.2.3 Potential Energy Budget 32

2.2.4 Evolution of Sorted Buoyancy 35

2.2.5 Application: Simulations of Salt Fingering 36

2.3 Discussion and Conclusion 38

2.4 Supplementary Material 39

2.4.1 Derivation of Energy Equations 39

2.4.2 MultiComponent n-Diffusion and Cross Diffusion 43
2.4.3 Thermal and Haline Potential Energies 45
2.4.4 Rate of Change of Buoyancy 47
2.5 Recent Developments 49

3 Numerical simulations of melt-driven double-diffusive fluxes in a turbulent boundary layer beneath an ice shelf 51
3.1 Introduction 51
3.2 Methods 55
3.2.1 Governing Equations 56
3.2.2 Simulations Details 58
3.2.3 Simulating Mechanical Turbulence 59
3.3 Results 61
3.3.1 Flow Regimes 61
3.3.2 Melt 65
3.4 Diapycnal Buoyancy Flux 67
3.4.1 Background Theory 67
3.4.2 Criterion for Convection 69
3.5 Discussion 73
3.6 Conclusions 76
3.7 Supplementary Material 77
3.7.1 Grid Stretching 77
3.7.2 Diffusive Solution 78
3.8 Recent Developments 80

4 Estimating dissipation rates associated with double diffusion (in an Arctic Eddy) 81
4.1 Introduction 82
4.2 Observations 85
4.3 Method 87
4.3.1 Diapycnal Buoyancy Flux 88
4.3.2 Down-scaled Spice Gradients 90
4.4 Results 93
4.4.1 Comparison with Microstructure 93
4.4.2 Method Sensitivity 95
4.4.3 Conclusion 96
4.5 Recent Developments 98

5 Double diffusion as a driver of melt in the stratified boundary layer under George VI Ice Shelf 101

5.1 Introduction 101

5.2 Observations 105

5.3 Double Diffusive Model 108

5.4 Heat Flux 111

5.5 Conclusions 113

5.6 Supplementary Material 114

5.6.1 Observation Processing 114

5.6.2 ε Estimate 114

5.6.3 χ_T Estimate 116

5.6.4 M21 Method 117

6 Implications and Future Directions 119

6.1 Double-Diffusive Energetics 119

6.2 Melt-Driven Convection 122

6.3 Predicting Double-Diffusive Dissipation 124

6.4 Double-Diffusive Ice Shelf-Ocean Boundary Layers 127

6.5 Outlook 129

References 133

List of figures

1.1 Global map of the ratio between molecular diffusivity for temperature κ_T and molecular diffusivity for salt κ_S. Data used to calculate κ_T and κ_S are decadally-averaged temperature and salinity at the sea surface (from the World Ocean Atlas Locarnini et al., 2018), using the equations from Sharqawy et al. (2010) for κ_T and from Vitagliano and Lyons (1956) for κ_S. We do not expect the varying ratio κ_T/κ_S across the ocean to significantly affect the dynamics, with a qualitative argument for this given in the conclusions chapter. 2

1.2 **A**. Shadowgraph of an ice block melting into a salinity gradient, where meltwater is highlighted with Fluorescein dye). Taken from Huppert and Turner (1980). **B**. Shadowgraph of 'lumpy' salt fingers with a picture width of 8.5 cm. Taken from Krishnamurti (2003). **C**. Shadowgraph of a staircase developing from the salt fingers in **B.**. Picture height is 101 cm. **D**. Shadowgraph of a salinity gradient heated from below. Numbers indicate successive times at which pictures were taken. Taken from Huppert and Linden (1979). 5

1.3 Figure taken from Rignot et al. (2013). 18

1.4 Figure taken from Fine et al. (2018). Map of the Chukchi shelf slope. Color represents temperature at 50 m depth, as determined by a global HYCOM model (Metzger et al. 2014). Barrow Canyon is just to the northwest of Alaska. The eddy survey region is enclosed in a black box. (right) Eddy survey pattern. Sections taken using the Shallow Water Integrated Mapping System (SWIMS), are shown as solid lines, and sections using the Mixed Microstructure Profiler as shown dashed lines. The average velocity relative to the eddy center in the 30–50 m depth range is shown for SWIMS sections. The red star indicates the inferred position of the eddy's center when the survey began. (bottom) Temperature measured in SWIMS survey along lines T1–T4. Note the T5 survey line is the only data we consider in Chapter 4. 20

1.5 Figure taken from Fine et al. (2018). (a) All temperature profiles taken on T5 of the eddy. The red box highlights a region with diffusive layers; the blue box highlights a region with thermohaline intrusions. (b) Salinity and temperature profiles at the top of the eddy. Distinctive steps are apparent, with well-mixed layers separated by sharp interfaces. The salinity profiles show some salinity spiking due to the abruptness of the interfaces. (c) Salinity and temperature profiles at the side of the eddy. Alternating layers of cold/fresh and warm/salty water indicate the presence of lateral intrusions. 22

2.1 (Left): A schematic to illustrate the angle made between surfaces of constant temperature and salinity. Generically the angle $\theta(\boldsymbol{x},t)$ varies in space and time. (Right): A schematic adapted from Winters et al. (1995), for a double-diffusive fluid. The arrows pointing up and down indicate energy exchanges with external and internal energy, respectively. 30

2.2 Buoyancy (top row) and diapycnal buoyancy flux (middle and bottom rows) from a 2D simulation of salt fingering. Dashed and solid contours in the top two rows show temperature and salinity, respectively. The bottom panels are scatter plots of the diapycnal buoyancy flux (colored as in the middle row) in (G_ρ,θ) space. Contours of f (Eq. 2.9) in (G_ρ,θ) space are shown in black, with the contour of $f = 0$ in bold. The panels to the right of the top rows show the sorted height (z^*) averages of the panels and the initial profiles are indicated with a dashed line. 37

3.1 Schematic of model domain with included snapshots of vertical velocity field and melt rate for warm, low mechanical forcing simulation 1B listed in Table 3.1. 57

3.2 Horizontally-averaged temperature (a), salinity (b) and density (c) averaged over an hour, at hours $1, 10, 50, 100$ and 200 for the cold, low mechanical forcing simulation 2B. Additionally we have shown the diffusive solution profiles (Martin and Kauffman, 1977) and the simulation profiles at $t = 10$ mins. The inset shows the upper 20 cm in each panel, showing the full variation in the scalars. 62

3.3 Time evolution of the horizontally-averaged turbulent buoyancy flux $\langle w'b' \rangle$ for simulation runs 2B (cold,low mechanical forcing), 2C (cold, high mechanical forcing) and 1B (warm, low mechanical forcing). Positive values signify stratification acting to transfer available potential energy to turbulent kinetic energy and negative values indicate stratification acting to transfer turbulent kinetic energy into available potential energy. First 30 hours of each simulation are shown concurrently, then later times are shown for simulations 1B and 2B. 63

3.4 Vertical velocity slices at $t = 1$ hr for simulation runs 2B (cold,low mechanical forcing), 2C (cold, high mechanical forcing) and 1B (warm, high mechanical forcing). All plots are on the same color scale to illustrate relative magnitudes of vertical velocities. Horizontal slices (lower panels) taken at 1m depth (location shown with dotted line in upper panels). . . 64

3.5 Turbulent flux of temperature, salinity and buoyancy, averaged between 1 m and 3 m depth, integrated in Fourier space up to wavenumber k. Values taken from 3D fields at $t = 1$ hr for simulation runs 2B (cold,low mechanical forcing), 2C (cold, high mechanical forcing) and 1B (warm, low mechanical forcing) as in Figure 3.4. The Fourier transform is denoted using $\hat{\cdot}$ and the complex conjugate is denoted by *. The wavenumber $k = \sqrt{k_x^2 + k_y^2}$ is the horizontal radial wavenumber. Values of the integral $\int_0^k \langle \hat{w}\hat{\Theta}^* \rangle dk$ converge for $\Theta = b', g\alpha T', g\beta S'$ with increasing wavenumber, suggesting the resolution is sufficient to capture the scalar fluxes. The cutoff frequency k_c used in the $\frac{2}{3}$ de-aliasing rule is included as a dashed vertical line. 65

3.6 Melt rate for cases 1A, 1B, 1C (the warm cases) and for cases 2A, 2B, 2C (the cold cases). The diffusive solution (Martin and Kauffman, 1977) is shown in a dotted line for both warm and cold cases. 66

3.7 Horizontal melt rate patterns for cases 1B and 2B. Snapshots taken at the same time as in Figure 3.4. Also included snapshot from the passive spin up simulation to compare patterning (melt rate values are inflated in this case due to lack of stable haline sublayer, so not included). 67

3.8 Diapycnal buoyancy flux (color) for warm cases 1B and 1C and cold cases 2B and 2C. 3D gradients are used to compute the diapycnal flux, $\nabla b_p \cdot \hat{\boldsymbol{n}}$, the gradient ratio $G_\rho = \frac{\alpha|\nabla T|}{\beta|\nabla S|}$ and the angle θ between $-\nabla T$ and ∇S. A random set of $\frac{1}{1000}^{th}$ of the points are then plotted as a scatter graph in (G_ρ, θ) space, coloured by the diapycnal flux. The line $f(G_\rho, \theta) = 0$ is plotted in black and divides the negative values of diapycnal flux (up-gradient) on the inside of the line from the positive (down-gradient) values outside of the line. To the right of each scatter plot is an average over the diapycnal flux across G_ρ i.e. $\langle \nabla b_p \cdot \hat{\boldsymbol{n}} \rangle_{G_\rho}$, on the same colour bar as the scatter plot. Note the gradient ratio G_ρ is on a log scale. 69

3.9 Vertical profiles of the gradient ratio G_ρ, the scalar angle $\cos\theta$, the diapycnal flux $\nabla b_p \cdot \hat{\boldsymbol{n}}$ and the density ρ in the upper 20 cm of a convecting simulation (warm, low mechanical forcing case 1B) and a non-convective simulation (cold, high mechanical forcing case 2C) at $t = 30$ hrs. The spatial mean is shown in solid with one spatial standard deviation denoted by the shaded region. The dashed lines denote the depths at which $\langle \cos\theta \rangle_{xy} = -1$ and $\langle \cos\theta \rangle_{xy} = \cos\theta_c$. The dotted line denotes the depth at which $\langle G_\rho \rangle_{xy} = \frac{\kappa_S}{\kappa_T}$. The insets are a close up version of the adjacent profiles on the same z axis. The far-field density is denoted with a vertical dashed line in the plot of ρ. Note the gradient ratio G_ρ in the left panel is on a log scale. 71

3.10 Diapycnal buoyancy flux (color) for cases 1-6 in Table 3.1 plotted in (G_ρ, θ) (left) and in (R_ρ, Re_b) space (right). The diapycnal buoyancy flux is normalised by the maximum (i.e. initial) difference $\Delta b_p = b_p^{\text{bottom}} - b_p^{\text{top}}$ across each simulation for comparison. The points were sampled from 2D x-z slices extracted from the 3D simulations at regular intervals. . . 72

3.11 Predicted time required for the system to transition from diffusive convection to stratified turbulence, calculated with the diffusive solution (Martin and Kauffman, 1977) with far field temperature T_∞ and prescribed turbulent dissipation rate, ε. 'Transition' occurs when $Re_b = 1$ at $R_\rho = \kappa_S/\kappa_T$. The far-field salinity $S_\infty = 34.572$ ppt in all cases and $T_{min} = \lambda_1 S_\infty + \lambda_2 + \lambda_3 P$ is the freezing temperature. Simulation values of $\varepsilon_{measured}$ are given by markers with bounds indicating maximum and minimum values. Circular markers indicate convecting simulations and cross markers indicate non-convecting simulations. The contour for diffusive solutions to take $t = 1$ s to transition is marked as a dividing point between the convecting and non-convecting simulations. Regions of parameter space occupied by the observations from Larsen C Ice Shelf (Davis and Nicholls, 2019), George VI Ice Shelf (Venables et al., 2014), and the LES for a shear driven boundary layer (Vreugdenhil and Taylor, 2019) shown with dashed boxes. 75

3.12 Grid spacing plotted with depth. Kolmogorov and Batchelor scales for both scalars are shown, with dissipation rates taken from passive simulation for $\varepsilon_0 = 8.7 \times 10^{-11} \mathrm{m^2 s^{-3}}$. 77

4.1 **A**. Temperature with 3 °C contour in black and angle f/N marked with white lines, with value calculated at line midpoint. **B**. Salinity with contours of ρ (kgm^{-3}) in grey. **C**. Density ratio $R_\rho = \alpha \frac{\partial T}{\partial z} / \beta \frac{\partial S}{\partial z}$. **D**. Shear $U_z = \sqrt{u_z^2 + v_z^2}$. 86

4.2 **A**. Horizontal average of the magnitude-squared coherence of vertical gradients in spice and buoyancy calculated for each CTD cast plotted against stretched wavenumber $\tilde{k}_z = k_z \frac{f}{N}$. One standard deviation in shading. **B**. PDF of spice gradients in stretched coordinates ($\tilde{z} = Nz/f$) on log scale. Lines correspond to isotropy in stretched coordinates ($y = x$) and unstretched coordinates ($y = Nx/f$). **C**. PSD for spice variance along isopycnals, averaged with depth. Interquartile range of isopycnal spectra shown in shaded region. 90

4.3 Comparison of predicted **A.**, **B.**, **C**. predicted dissipation rates ε ($\mathrm{m^2s^{-3}}$) (**A**) with microstructure-inferred values (**B**) (Fine et al., 2018). **D.**, Osborn (1980) estimate for the heat flux using $\Gamma = 1$ for predicted and microstructure ε. Horizontal mean (**C**,**D**), taken between 8 and 13km with shaded spatial standard deviations. **E.**, **F**. Log-histograms of ratio between the predicted ε_{pred} and observed ε_{obs} dissipation rate. **E**. Data calculated using $\tilde{k}^{-1}$ model, $\tilde{k}^{-2}$ model and $\tilde{k}^{-1}$ model excluding points where $Re_b = \frac{\varepsilon}{\nu N^2} > 20$. **F**. Subdivision of data by $R_\rho = \alpha\frac{\partial T}{\partial z}/\beta\frac{\partial S}{\partial z}$ value (see text). **G**. Buoyancy Reynolds number Re_b calculated using microstructure. 95

4.4 Top row shows inferred dissipation rate ε using T/S data sampled at the given resolution in the title. Middle row shows observed ε using full T/S data, subsampled at the given resolution. Bottom row shows ratio between top and middle figure values. Colorbar is on a log-scale and mean value corresponds to the peak of the distribution of $\varepsilon_{pred}/\varepsilon_{obs}$. . . 97

5.1 **A**. Schematic of mooring. **B**. Location of moorings. Maximum ocean temperature data taken from WOA decadal climatology (Locarnini et al., 2018). Water column depth taken from BedMachine (Morlighem et al., 2020). **C**. Temperature/Salinity plot of 34 CTD casts. upper 20 m highlighted as location of thermohaline staircase and $R_\rho = 1/2$ relationship given by dashed line. Buoyancy and spice contours included. **D**. CTD profiles including inset of upper 20 m for selected profiles. 104

5.2 **A**. Mean flow speed $\langle u \rangle$ timeseries for upper and lower MAVS. **B**. upper MAVS velocity against dissipation rate (burst estimates in grey) for GVIIS mooring data, LCIS mooring data included for comparison. **C**. Same as **B** but for lower MAVS. **D**. Friction velocity estimate $u^* = (\langle u'w' \rangle^2 + \langle v'w' \rangle^2)^{1/4}$ based on constant stress boundary layer for GVIIS upper and lower MAVS data (burst estimates in grey) 107

5.3 **A,C**. Power Spectral Density (PSD) of horizontal velocity fluctuations against wavenumber k, averaged by mean flow speed for upper and lower MAVS. Grey box represents a $f = 0.01$ frequency cutoff. **B,D** Same as **A,C** but averaged by burst-estimated dissipation rate. **E**. PSD of temperature fluctuations from lower MicroSquid thermistor, against wavenumber k, averaged by mean flow speed. **F**. PSD of temperature fluctuations from thermistor chain, against frequency f over the full timeseries. 109

5.4 **A**. PDFs of upper and lower MAVS observed dissipation rate and predicted dissipation rate. **B**. PDF of the log of the ratio between observed and predicted dissipation rate. **C**. Timeseries of observed and predicted dissipation rates for upper MAVS, along with filtered signal without high $Re_b > 20$ data. **D**. Same as **C** for lower MAVS data. 112

6.1 Preview of my next paper, courtesy of Reuben Ruxton. The problem of penguins: The influence of millions of tiny flippers on double diffusion. 147

List of tables

3.1 Table of simulation runs. Values for ΔT, ΔS, and R_ρ are averaged across the simulation. The turbulent vertical buoyancy flux $\langle w'b' \rangle$ is averaged across the simulation for depths 0.1 m $< z <$ 2.6 m for the first 35 hrs to enable comparison across simulations run for different lengths of time. Simulations above the dashed line are convecting throughout the simulated time, and those below are not. 60

Chapter 1

Introduction

In the IPCC's 2019 'Special Report on the Ocean and Cryosphere in a Changing Climate' (Meredith et al., 2019), they write

> The polar regions are losing ice, and their oceans are changing rapidly. The consequences of this polar transition extend to the whole planet, and are affecting people in multiple ways[1].

This fact is the broad motivator for all of the work within this PhD. My personal hope is that by improving our collective understanding of the implications of climate change, we can be better prepared for its effects and be better motivated to minimise its impacts in ways that will lead to a happier and healthier world. Polar regions are often referred to as the 'canary in the coal mine' for climate change. However, this phrase ignores the fact that the Arctic is a populated region and as the 2019 IPCC report points out, the current changes within the Arctic are already having a substantial impact on the way of life for those that live there.

To understand the implications of climate change, we must first understand the physical mechanisms connecting different aspects of the earth system. This thesis is concerned with ocean dynamics, and the role they play in transporting heat, salt and nutrients within the world's oceans; connecting the oceans with the cryosphere, atmosphere and biosphere. Ocean dynamics act across a wide range of scales in time and space and we will be primarily discussing high-frequency variability, considering processes on

---

[1] The current social-ecological impacts on indigenous and local arctic communities mentioned in the IPCC report include: food and water insecurity (Council—Alaska, 2015), increased safety risks from travel (Durkalec et al., 2015), water-born and food-born diseases (Parkinson and Berner, 2009), damage to infrastructure (Suter et al., 2019) and risks to individual and collective mental/emotional health (Gearheard et al., 2013)

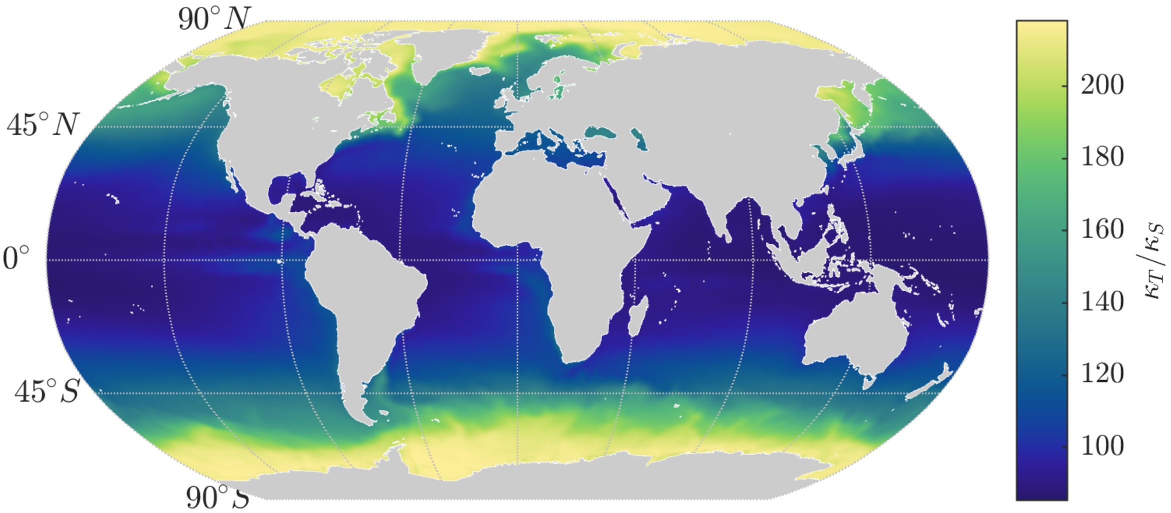

Fig. 1.1 Global map of the ratio between molecular diffusivity for temperature κ_T and molecular diffusivity for salt κ_S. Data used to calculate κ_T and κ_S are decadally-averaged temperature and salinity at the sea surface (from the World Ocean Atlas Locarnini et al., 2018), using the equations from Sharqawy et al. (2010) for κ_T and from Vitagliano and Lyons (1956) for κ_S. We do not expect the varying ratio κ_T/κ_S across the ocean to significantly affect the dynamics, with a qualitative argument for this given in the conclusions chapter.

small scales in time and space. Small scale processes are strongly linked to large scale dynamics, particularly via their control over vertical mixing.

On small scales, the transport of heat, salt and nutrients is heavily influenced by ocean turbulence, which can be driven by a variety of processes. One such process is known as 'double diffusion', which we will introduce first in this chapter then discuss at greater length throughout the thesis. We will introduce some basic notions to the study of ocean turbulence followed by some background on the polar oceans and the specific geographical regions considered within this thesis. Finally, we will give an outline of the following chapters.

1.1 Double diffusion

In the ocean, the density depends on both temperature and salinity. Temperature and salinity have differing rates of molecular diffusion, κ_T and κ_S, with $\kappa_S << \kappa_T$. In Figure 1.1 we have plotted the ratio between κ_T and κ_S as they vary across the world's oceans. In this thesis, 'double diffusion' refers to processes in which this difference in diffusivity between the two components influences the dynamics. Examples of double diffusion are present in many fluids, including stellar and planetary interiors (Garaud, 2018) and chemical reactions (Dewel et al., 1983). However, we will restrict our attention to the ocean, with an assumption that theory we discuss is applicable across all kinds of double-diffusive fluids, not limited to the ocean. Radko (2013) defines double diffusive convection as such

> Double-diffusive convection is a mixing process driven by the interaction of two fluid components that diffuse at different rates.

However, a suitable definition of 'mixing process' must be given before this definition can be fully understood. 'Mixing' is often understood as an irreversible process of homogenisation, so the title of this thesis 'Un-mixing the Ocean' is somewhat facetious. In the first chapter of this thesis, we will show that the common definition of 'mixing' of density in the ocean entails an 'un-mixing' process. Although the existence of 'un-mixing' suggests a poor definition of 'mixing', we find that this 'un-mixing' provides a useful conceptual framework, and definition, for double-diffusive convection.

A wide range of linear instabilities are possible due to double diffusion, and two common examples are known as 'salt fingering convection' and 'oscillatory diffusive convection'. In both of these linear instabilities, water at rest with a density increasing with depth (stable in a single-component fluid) is linearly unstable for certain parameter values. 'Salt fingering convection' (named for the 'finger-like' unstable modes as in Figure 1.2B) occurs when temperature is stably stratified and salinity is unstably stratified (warm and salty on top), and 'oscillatory diffusive convection' occurs when temperature is unstably stratified and salinity is stably stratified (cold and fresh on top). Much of the literature surrounding double diffusion is concerned with these linear instabilities and the subsequent nonlinear dynamics that result from them (Radko, 2013). However, the terms 'salt-fingering' and 'diffusive convection' are also often used for general non-linear turbulent motions that depend on double diffusion, where the background gradients are 'salt fingering favourable' (warm salty on top of cold fresh) or 'diffusive convection favourable' (cold fresh on top of warm salty), even when the mentioned linear instabilities may not actually occur[2]. Particularly within the ocean itself, distinguishing between regions with the potential to be linearly unstable and the actual occurrence of a linear instability is important for our understanding of the dynamics. The approach within this thesis will be to discuss general properties of double-diffusive flows and non-linear mechanisms in double diffusion, rather than focus on linear instabilities. To that end, when we discuss 'salt fingering' or 'diffusive convection', we are referring to the non-linear turbulent motions that occur when one of the background temperature and salinity gradients is stable and the other unstable.

---

[2] The 'Oscillatory Diffusive Convection' linear instability is only possible for a narrow range of density ratios in the ocean (see Glossary).

To identify regions in which the vertical gradients are conducive to linear instability, the 'density ratio' is often used, defined as

$$R_\rho \equiv \frac{\alpha \frac{\partial T}{\partial z}}{\beta \frac{\partial S}{\partial z}}, \tag{1.1}$$

for temperature T, salinity S and coefficients of thermal expansion and haline contraction (α, β) respectively i.e. the coefficients in the linear approximation for the equation of state for density $\rho = \rho_0 - \alpha T + \beta S$. Alternative definitions for the density ratio are sometimes used, where the temperature and salinity gradients are evaluated in different spatial directions (e.g. horizontally in Rudnick and Martin (2002)). The density ratio is also sometimes defined as the inverse of our definition i.e. R_ρ^{-1}, however we will use the definition in Eq. 1.1 throughout this thesis.

Given a monotonically increasing density profile with depth, diffusive convection occurs when the density ratio $0 < R_\rho < 1$. For salt-fingering convection $R_\rho > 1$, and when both components are stably distributed, then $R_\rho < 0$. Practically speaking, for small density ratios $R_\rho << 1$, diffusive convection will not occur, and for large density ratios $R_\rho >> 1$, salt fingering convection will not occur, however the exact bounds for R_ρ depend on the specific dynamics, so we will not give them here. If the density profile is unstable, then the ranges on the density ratio change, so in oceanography, the 'Turner angle' is often used, defined as

$$Tu \equiv \tan^{-1}\left(\alpha\frac{\partial T}{\partial z} - \beta\frac{\partial S}{\partial z}, \alpha\frac{\partial T}{\partial z} + \beta\frac{\partial S}{\partial z}\right), \tag{1.2}$$

where $\tan^{-1}$ is the four-quadrant arctangent function. The Turner angle distinguishes between statically stable and statically unstable density profiles, but we have included it for completeness and will not make significant use of Tu within this thesis.

Double-diffusive instabilities and mechanics are not limited to unstable vertical gradients in temperature or salinity. In the experiments of Ruddick and Turner (1979) and the theory of Holyer (1983), it is shown that horizontal gradients in temperature and salinity can trigger a linear instability in certain settings. The archetypal example of this instability is from the experiments discussed in Huppert and Turner (1980), shown in Figure 1.2A, in which a block of ice is placed into a tank of constant temperature water, stratified in salinity. The combined effect of freshening and cooling from the melting ice along the ice sidewall causes the formation of a series of intrusions. These intrusions

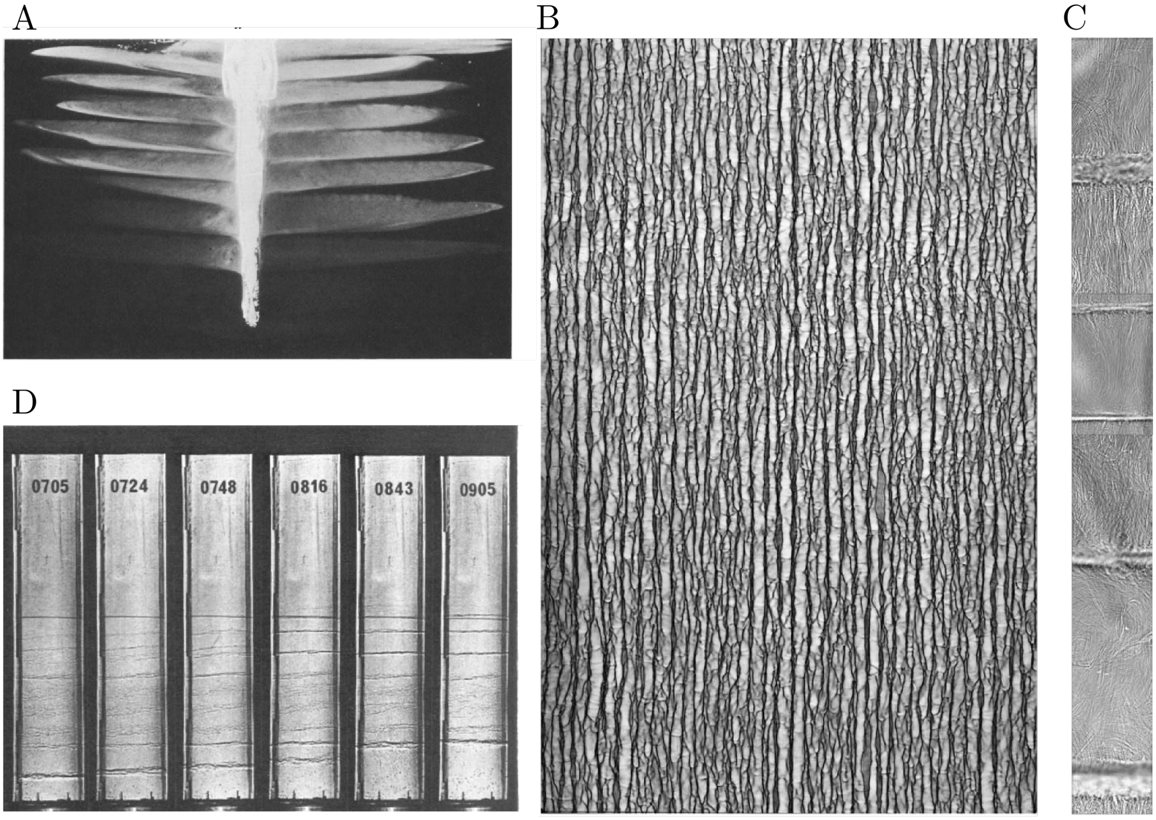

Fig. 1.2 **A**. Shadowgraph of an ice block melting into a salinity gradient, where meltwater is highlighted with Fluorescein dye). Taken from Huppert and Turner (1980). **B**. Shadowgraph of 'lumpy' salt fingers with a picture width of 8.5 cm. Taken from Krishnamurti (2003). **C**. Shadowgraph of a staircase developing from the salt fingers in **B.**. Picture height is 101 cm. **D**. Shadowgraph of a salinity gradient heated from below. Numbers indicate successive times at which pictures were taken. Taken from Huppert and Linden (1979).

have the form of convecting layers, and so give a 'staircase' structure within a profile of temperature and salinity. Similar structures adjacent to ice fronts (Jackson et al., 2020) and icebergs (Stephenson Jr et al., 2011) have been observed.

The formation of stacked 'layer' structures in double-diffusive convection is not limited to sidewall cooling and freshening. 'Thermohaline layers' (also referred to as a 'thermohaline staircase') can occur within the salt-fingering regime (see Figures 1.2B and 1.2C), the diffusive convection regime (see Figure 1.2D), and within horizontal interleaving (see Figure 1.2A). Although first discovered in a series of lab experiments (Turner, 1968), this layering phenomena has been identified within many ocean observations. In the Arctic Ocean, these layers are spatially and temporally coherent over large scales (Bebieva and Timmermans, 2019), however more dynamic layers have been observed in simulations and experiments. Layers within the Southern Ocean have been observed (e.g. Smith and Klinck, 2002), and in Bebieva and Speer (2019), the occurrence of layers within the thermocline beneath Antarctic sea-ice in the Ross Gyre was thought to mediate the growth-melt cycle of sea ice. Within polar oceans, the stratification is often 'diffusive convection favourable', which is one reason for the prevalence of staircases. Another reason, within the Arctic Ocean specifically, is the relatively low levels of internal wave activity (Levine et al., 1985). Polar regions therefore are prime locations to study the effects of double-diffusive convection.

The mechanisms behind ocean layer formation are still poorly understood. A variety of mechanisms have been proposed, including boundary forcing as in the experiments of Turner (1968) (shown in Figure 1.2D), linear instabilities due to the interaction with shear as in Radko (2019), and the inherent 'anti-diffusive' property of density that is common across double diffusion, discussed in Schmitt (1994) and elaborated on in Chapter 2. Thermohaline layers are relevant to this thesis due to their occurrence within the observational datasets of Chapters 3 and 4. Although staircases are often indicative of double-diffusive convection, double-diffusive convection does not always entail the formation of layers (as in Chapter 3), and so we will consider more general double-diffusive convection within this thesis, rather than focus on layering dynamics specifically.

Salt fingers are tall, thin, finger-like structures that may develop when warm salty water sits atop cold fresh water, shown in Figure 1.2B. Salt fingers tend to be more relevant to tropical regions (Radko, 2013), due to the warming and evaporation at the sea surface in the tropics. Under the influence of shear, these structure can tilt in the direction of shear (Linden, 1974, Kimura and Smyth, 2007) forming 'salt sheets' which can reduce the resulting heat and salt fluxes (Radko et al., 2015). Salt fingers are known to break down via the 'zig-zag' instability (Kimura and Smyth, 2011), and their formation into staircases has been studied in Radko (2003), Paparella and Von Hardenberg (2012) and Krishnamurti (2003) (see Figures 1.2B and 1.2C). Direct shadowgraph observations within the ocean have demonstrated finger-like structures, as well as inclined structures associated with salt sheets (Williams 3rd, 1975). We will use a simulation of salt fingers to demonstrate the application of our double-diffusive theory in Chapter 2, however the rest of the thesis is more concerned with the 'diffusive convection favourable' regime rather than the 'salt fingering favourable' regime.

The influence of shear on diffusive convection is relatively less understood than the effect of shear on salt fingering. For diffusive convection, observations in Bebieva and Timmermans (2016) suggest that a higher shearing leads to the breakdown of double-diffusive staircases in the diffusive convective regime. Recently, simulations by Brown and

Radko (2021) suggested that weak background shear may enhance the pre-existing double diffusive convection, leading to an enhanced heat flux through a diffusive convection staircase, which is a different response from the damping-effect of shear that is assumed in many studies of diffusive convection (e.g. Shibley and Timmermans, 2019). We will explore the influence of mechanically forced turbulence on boundary-forced diffusive convection in Chapter 3, and note the impact of high shear regions in the ocean interior in Chapter 4.

1.2 Turbulence

A precise definition of turbulence is difficult to give, and so features of turbulence are listed instead. Pope (2001) identified two key features of turbulence as: irregularity in the velocity field (chaotic motion where the individual paths of fluid parcels are hard to predict) and a range of length scales of turbulent motions from large to small eddies. Three dimensional fluctuations in vorticity, enabling 'vortex stretching', are also commonly identified as a key feature of turbulence, ruling out two-dimensional flows as being truly turbulent (Tennekes and Lumley, 2018).

1.2.1 Kolmogorov's Hypotheses

Turbulence is often identified using the Reynolds number $Re = UL/\nu$ where U is a characteristic velocity scale, L is a characteristic length scale and ν is the fluid's kinematic viscosity. Large Reynolds number flows, around $Re > 3000$ for channel flow (Schlichting and Gersten, 2016), are usually considered turbulent, and small Reynolds number flows (around $Re < 2000$ for channel flow) are usually considered laminar. The intermediate range of Reynolds numbers ($2000 < Re < 3000$ for channel flow) are often considered 'intermittently turbulent'. To describe the fundamentals in our understanding of developed turbulence, we will introduce Kolmogorov (1941)'s three similarity hypotheses. The first states

> in every turbulent flow at sufficiently high Reynolds number, the statistics of the small scale motions have a universal form that is uniquely determined by ε and ν.

where $\varepsilon \equiv \nu \left\langle \frac{\partial u_i}{\partial x_j} \frac{\partial u_i}{\partial x_j} \right\rangle$ is the dissipation rate of kinetic energy for velocity field $\mathbf{u} = (u_1, u_2, u_3)$ summed over indices i and j. Using ε and ν we can derive the 'Kolmogorov length scale'

$$\eta \equiv \left(\frac{\nu^3}{\varepsilon} \right)^{1/4}, \tag{1.3}$$

which represents the length scale of the smallest eddies present in the flow i.e. the length scale where energy is dissipated. When solving the Navier-Stokes equations in numerical simulations of turbulence (as in Chapter 3), it is generally accepted that a resolution of 2η is sufficient to fully resolve the turbulent velocity field (Bewley, 2012).

Kolmogorov's second hypothesis states that

> in every turbulent flow at sufficiently high Reynolds number, the statistics of the motions of scale l in the range $l_0 >> l >> \eta$ have a universal form that is uniquely determined by ε independent of ν.

Here l_0 is the eddy lengthscale $k^{3/2}/\varepsilon$ for the turbulent kinetic energy $k = u_1^2 + u_2^2 + u_3^2$. The second hypothesis suggests the existence of an 'inertial subrange', where the dissipation rate ε is the only controlling parameter, in contrast to the 'dissipation range' suggested by the first hypothesis.

The energy spectrum function $E(K)$ allows us to capture the scalings suggested by Kolmogorov's hypotheses by analysing the kinetic energy contained at each wavenumber $K = \sqrt{k_1^2 + k_2^2 + k_3^2}$ in (k_1, k_2, k_3) wavenumber space. To define $E(K)$ we first define the two-point correlation function for velocity field $\mathbf{u} = (u_1, u_2, u_3)$, as

$$R_{ij}(\mathbf{r}, t) \equiv \langle u_i(\mathbf{x}, t) u_j(\mathbf{x} + \mathbf{r}, t) \rangle, \tag{1.4}$$

for some averaging operator $\langle \cdot \rangle$. $R_{ij}(\mathbf{r}, t)$ is independent of position $\mathbf{x}$ within homogeneous turbulence. We will utilise a two-point correlation further in Chapter 4, as it is closely related to the power spectra for a given variable. Specifically, the energy spectrum can be defined as

$$E(K) \equiv \frac{1}{2} \oint |\hat{R}_{ii}(\mathbf{k}, t)|^2 dS(K), \tag{1.5}$$

where $\hat{R}_{ii}$ refers to a Fourier transform of the two point correlation R_{ii}, with summation over the index i. The surface $S(K)$ of integration is a sphere in wavenumber space $\mathbf{k} = (k_x, k_y, k_z)$, and so the integration process removes directional dependence. The energy spectrum function is related to the kinetic energy $k = u_1^2 + u_2^2 + u_3^2$ via

$$k = \int_0^\infty E(K) dK. \tag{1.6}$$

In the inertial subrange, $E(K)$ must depend only on the dissipation rate ε and the wavenumber K (assuming isotropy in wavenumber space). Therefore, using dimensional analysis, the form for the power spectrum in the inertial subrange is given by

$$E(K) = C\varepsilon^{2/3}K^{-5/3}, \tag{1.7}$$

for a constant C, experimentally derived to be $C = 1.5$. The inertial subrange is commonly observed in 'microstructure' measurements (measurements of the small, $O(\text{mm})$ scales) of shear in the ocean. The form in Eq. 1.7 may be used to fit a value of ε (e.g. Davis and Nicholls, 2019). However, more commonly, a model spectrum that includes a dissipative range is fit to the shear or temperature *gradient* spectra (Gregg, 1999)

Although the first two similarity hypotheses were stated in Kolmogorov (1941), 'Komogorov's third hypothesis', as it is sometimes known, was suggested in Gurvich and Yaglom (1967) based on Kolmogorov's theory. Kolmogorov's third hypothesis concerns the 'intermittency' of turbulence, i.e. the fact that neither k or ε are homogeneous in space and time. Kolmogorov's third hypothesis proposes that turbulence should be log-normally distributed. In certain circumstances, Kolmogorov's third hypothesis has been shown to be accurate, however ocean turbulence has been observed to be log-skew normally distributed (Cael and Mashayek, 2021) on average; potentially due to the existence of multiple sources of turbulence. Regardless of the exact distribution of turbulent dissipation rates, the 'intermittent' feature of turbulence is of importance when interpreting ocean turbulence measurements.

Within the ocean, Kolmogorov's hypotheses are useful for explaining measurements of ocean turbulence. However, the ocean has additional complicating factors; it is affected by a changing density with depth (or 'stratification'), controlled by active scalars (primarily temperature and salinity). There are also many passive scalars that are carried by the flow but have little or no influence on the turbulent dynamics, such as chemical species (Riley and Chester, 2016). The behaviour of scalars within developed turbulence was described in Batchelor (1959). For a diffusing scalar Θ, with diffusivity κ, further turbulent scaling regimes are possible, as discussed in Tennekes and Lumley (2018). In addition to the kinetic energy dissipation rate ε, the dissipation rate of scalar variance $\chi_\Theta \equiv \kappa|\nabla\Theta|^2$ plays a role. A common turbulence scaling regime found within ocean observations is the 'inertial subrange' for scalar variance. In this range, the important parameters are the dissipation rate of kinetic energy ε and the dissipation rate of thermal variance χ_T. Using dimensional analysis this gives the power spectrum for thermal variance as

$$E_T(K) = \tilde{C}\chi_T\varepsilon^{-1/3}K^{-5/3}, \tag{1.8}$$

where the constant $\tilde{C}$ is approximately 0.5 (see Tennekes and Lumley, 2018). The form of Eq. 1.8 may be used to fit to high-resolution sampling of temperature measurements to estimate the product $\chi_T \varepsilon^{-1/3}$ (Gregg, 1999).

Another scaling regime that we will utilise within this thesis is the 'viscous-convective range', also sometimes known as the 'Batchelor regime'. In this regime, χ_T and the wavenumber K are relevant, as in the inertial range, but rather than depending on ε, the relevant parameter is the magnitude of the strain-rate field $(\varepsilon/\nu)^{1/2}$. Using dimensional analysis, this gives the power spectrum for thermal variance as

$$E_T(K) = \tilde{C}\chi_T \nu^{1/2}\varepsilon^{-1/2}K^{-1}. \tag{1.9}$$

In Chapter 5, we find evidence of a Batchelor regime in our measurements of thermal variance. We use Eq. 1.9 to estimate the value of χ_T, combined with our estimates for ε.

1.2.2 Stratification

Stratification introduces a new length scale relevant for 'stratified turbulence': the Ozmidov length scale $L_{Oz} = \sqrt{\varepsilon/N^3}$, where $N = \sqrt{\partial b/\partial z}$ is the buoyancy frequency for buoyancy $b = g\alpha T - g\beta S$ (where density is $\rho = \rho_0 - \alpha T + \beta S$). The Ozmidov length scale represents the scale at which buoyancy effects become important (Dillon, 1982). For length scales smaller than the Ozmidov scale, an inertial subrange may exist, but for larger length scales, vertical motions are damped by stratification. The existence of an inertial subrange depends on the difference in scale between the Ozmidov length scale L_{Oz} and the Kolmogorov length scale η. The separation between these two scales is quantified using a ratio of the two,

$$\frac{L_{Oz}}{\eta} = \left(\frac{\varepsilon}{\nu N^2}\right)^{4/3} = Re_b^{4/3}, \tag{1.10}$$

where $Re_b = \varepsilon/\nu N^2$ is known as the 'buoyancy Reynolds number'. For a large Re_b, we may expect a well developed inertial subrange, and for small Re_b we may not (Caulfield, 2021). 'Stratified turbulence' is often identified based on a buoyancy Reynolds number $Re_b > O(10)$ (Bartello and Tobias, 2013), based on the occurrence of an 'inertial' scaling in the horizontal kinetic energy spectra, as suggested by Lindborg (2006). For large Re_b, the effects of stratification become negligible, as shown in the simulations of Portwood et al. (2019), where for $Re_b > 300$ the asymptotic regime of isotropic turbulence is observed. However, it is possible to be both stratified and turbulent (with large Reynolds numbers) in double-diffusive convection. We investigate this possibility in Chapter 5, where the horizontal kinetic energy spectrum shows evidence of an inertial scaling at larger length scales than the Ozmidov scale, suggestive of stratified turbulence, and the turbulence shows evidence of being double-diffusively driven.

Inoue et al. (2007) distinguished between double-diffusive convection and other forms of turbulence in ocean data using the buoyancy Reynolds number. Inoue et al. (2007) hypothesised that for $Re_b < 20$, double-diffusive convection would be active and for $Re_b > 20$, 'turbulence' (meaning turbulence from non-double-diffusive sources) would be active. Double-diffusive convection is often distinguished from 'turbulence' (St. Laurent and Schmitt, 1999), however correctly double diffusive convection may be seen as a form of turbulence: Reynolds numbers in double-diffusive convection can be high (e.g. Nayak and Bhattacharyya, 2012), and certainly the flow can be chaotic (Knobloch et al., 1986). Distinguishing between sources of turbulence is not simple; double-diffusive effects may influence turbulence driven by non-double-diffusive sources (e.g. gravity currents and plumes in Konopliv and Meiburg, 2016, Dadonau et al., 2020). The study of energetics in Chapter 2 will help us clarify the distinction between double-diffusive convection, turbulence influenced by double-diffusive effects and turbulence free from the effects of double diffusion, which we will discuss further within the conclusions chapter.

A particularly important form of turbulence within the ocean is boundary layer turbulence. This can occur due to the shearing of flow past either rigid boundaries (e.g. the ocean floor or ice shelves) or free surfaces (e.g. the ocean-atmosphere interface). 'Mixed Layers' adjacent to the surface often form due to vigorous turbulence driven by the shearing of a mean flow, or by convective instabilities forced at the surface. In an unstratified, shear-driven boundary layer, the standard model consists of three layers: adjacent to the surface, a viscosity controlled sublayer is hypothesised (millimetres or centrimetres thick), where surface roughness may play a dominant role in setting the length scales; below the viscous sublayer, a 'surface layer' is often observed in the upper few metres, where the impact of Earth's rotation is minimal due to the small length scale. In the surface layer, an argument of self-similarity can be made to derive the 'law-of-the-wall' scaling, which posits that the mean velocity at a point in the surface layer is proportional to the logarithm of the distance from the wall. The final layer is the outer planetary boundary layer, where Earth's rotation controls the mixing length (McPhee, 2008). In a stratified boundary layer, the law-of-the-wall breaks down, but corrections for stratification can be derived using Monin-Obukhov similarity theory (Monin and Obukhov, 1954). The outer layer can also then be controlled by the stratification as well as rotation. We discuss boundary layer dynamics within Chapters 3 and 5, specifically considering the impact of double-diffusive convection.

1.2.3 Observational Methods

The most commonly reported measurements of turbulence in the ocean are of the kinetic energy dissipation rate ε and the thermal variance dissipation rate χ_T. Direct measurements of these properties are made using so called 'microstructure' measurements. Shear probes are often used to measure ε and fast response thermistors are often used to measure χ_T (Lueck et al., 2002, Roget et al., 2006). Shear probes usually contain a small piezoelectric sensor, which reacts to the straining of the probe as water passes over it. Shear probes can only measure the velocity gradient in a single direction, so isotropic turbulence is often assumed, giving an approximation for the dissipation rate as $\varepsilon = \frac{15}{2}\left\langle \frac{\partial u'^2}{\partial z} \right\rangle$, for velocity component u and direction z dependent on the sensor orientation. Shear measurements can be considered in wavenumber space by applying the 'frozen-field hypothesis' (discussed further in Chapter 5). An empirical model wavenumber spectrum is fit to the measured power spectra to infer a dissipation rate (often the 'Nasmyth' spectrum is used, discussed in Oakey, 1982).

In fast-response thermistors, metal oxide sensors are commonly used due to their high temperature coefficient of resistance i.e. their resistance is particularly sensitive to small changes in temperature. Temperature measurements are usually converted into temperature gradient measurements, which can then be compared to an empirical model wavenumber spectrum to fit a value for χ_T, approximated using an assumption of isotropy i.e. $\chi_T = 6\kappa_T \left\langle \frac{\partial T'^2}{\partial z} \right\rangle$. Both thermal and velocity microstructure measurements are often made using free falling profilers, which can place tight constraints on the scales of velocity and thermal fluctuations that can be captured by a given profiler (Moum, 1990). This problem is exacerbated when trying to make simultaneous measurements of ε and χ_T that capture the inertial spectrum for both temperature and velocity.

Many microstructure surveys are designed to quantify the vertical turbulent fluxes of heat, salt or other ocean properties. Vertical turbulent fluxes take the form of a correlation between the vertical velocity w and the quantity of interest, for instance the average heat flux is written $F_H = \rho c_p \langle w'T' \rangle$ for the density ρ, specific heat capacity c_p and averaging operator $\langle \cdot \rangle$, where primes $'$ are understood as departures from the average. However, measuring direct correlations, such as $\langle w'T' \rangle$, is difficult as it requires co-locating sensors. To avoid this problem, measurements of χ_T are converted into heat flux estimates using the Osborn and Cox (1972) method. Alternatively, ε measurements are converted into heat flux estimates using the Osborn (1980) method.

The Osborn and Cox (1972) method relies on the budget for thermal variance

$$\frac{\partial\langle T'^2\rangle}{\partial t}+\langle\mathbf{u}\rangle\cdot\nabla\langle T'^2\rangle+\nabla\cdot\langle\mathbf{u}'T'^2\rangle-2K_h\langle|\nabla_h T|^2\rangle=2K_v\left\langle\frac{\partial T}{\partial z}\right\rangle^2-\chi_T, \tag{1.11}$$

where $\langle\cdot\rangle$ is some averaging operator with primes $'$ denoting a departure from the average, ∇_h denotes the gradient in the horizontal direction, K_h represents the horizontal turbulent diffusivity and K_v represents the vertical turbulent diffusivity. In the Osborn and Cox (1972) method, the terms on the left hand side of Eq. 1.11 are assumed to be small, giving the balance $\chi_T = 2K_v\left\langle\frac{\partial T}{\partial z}\right\rangle^2$. Coupled with the definition of the turbulent vertical diffusivity $K_v = -\langle w'T'\rangle/\frac{\partial\langle T\rangle}{\partial z}$, we can infer the vertical turbulent temperature flux $\langle w'T'\rangle$ from the dissipation of thermal variance χ_T. The Osborn and Cox (1972) method may be inaccurate in the presence of significant lateral fluxes as outlined in Davis (1994). However, within a variety of simulations of single-component stratified turbulence, Taylor et al. (2019) found that the Osborn and Cox (1972) method was effective at diagnosing the turbulent heat flux. Within layered simulations of double-diffusive convection, Flanagan et al. (2014) found that the Osborn and Cox (1972) method required significant temporal averaging to avoid the accumulation of thermal variance (i.e. the $\frac{\partial\langle T'^2\rangle}{\partial t}$ term was found to be important). In the observations of Fine et al. (2018), χ_T was calculated only over the well-mixed layers within a thermohaline staircase to avoid averaging over the potentially non-turbulent interface regions, where the isotropic assumption may not hold. Excluding the interface regions of thermohaline layers may help avoid any additional variance accumulation introduced by layering.

Another key method for estimating heat fluxes is the Osborn (1980) method. In this method, the heat flux is estimated using the dissipation rate ε and a model for the energetic balance within turbulence. In the Osborn (1980) method, shear production is the assumed driver of turbulent motions. Some of the energy provided by shear is dissipated via ε and some is lost to changes in potential energy via the turbulent vertical buoyancy flux $\langle w'b'\rangle$. A constant division of shear production between ε and $\langle w'b'\rangle$ is assumed. The relationship

$$\langle w'b'\rangle = \Gamma\varepsilon, \tag{1.12}$$

is postulated, for a constant 'mixing coefficient' Γ, usually taken as $\Gamma = 0.2$. Note that the mixing coefficient Γ is distinct from the 'mixing efficiency' which is defined as a value between 0 and 1 based on the definition of 'irreversible mixing' discussed in Chapter 2. The heat flux is inferred from $\langle w'b'\rangle$ by assuming that the turbulent vertical buoyancy diffusivity $K_b \equiv -\langle w'b'\rangle/N^2$ is equal to the turbulent vertical temperature diffusivity

$K_T \equiv -\langle w'T' \rangle / \frac{\partial \langle T \rangle}{\partial z}$ (which also implies that $K_T = K_S$). Using the Osborn and Cox (1972) method, approximations of $\langle w'T' \rangle$ can be made to estimate Γ within observations. Gregg et al. (2018) report on a variety of observational estimates of Γ and found values primarily between 0.1 and 0.3, with no observational basis for not using a value of 0.2. Similarly, Taylor et al. (2019) found that the Osborn (1980) method was effective at predicting heat fluxes in their single-component simulations.

Within double-diffusive convection, it is common to apply the Osborn (1980) method with a value of $\Gamma = 1$ (e.g. in St. Laurent and Schmitt, 1999, Inoue et al., 2007, Fine et al., 2018), assuming that $\langle w'b' \rangle = \varepsilon$. However, when applying the Osborn (1980) method to estimate heat flux, an assumption that $K_T = K_S$ must still be made, which should be treated with some caution. A better understanding of the flux ratio $\gamma \equiv \alpha \langle w'T' \rangle / \beta \langle w'S' \rangle$ could improve estimates of heat flux, but measuring salt flux in the ocean has large associated uncertainties. The difficulty of measuring salt flux $\langle w'S' \rangle$ is related to the problem of directly measuring correlations. Salinity is inferred from measurements conductivity, which is related to the salinity via measurements of temperature. Therefore, to achieve high-resolution measurements of salinity, we require co-located, high-resolution measurements of temperature and conductivity. High-resolution conductivity sensors do exist (Nash and Moum, 1999), however the associated uncertainties mean that determining a quantity such as the flux ratio $\gamma = \alpha \langle w'T' \rangle / \beta \langle w'S' \rangle$ is a challenge (Nash and Moum, 2002).

1.3 Polar Oceans

Both the Arctic Ocean and the Southern Ocean exist at a similar range of temperatures and salinities. Although there are distinct differences between the two regions, most notably the Antarctic Circumpolar Current (ACC), both oceans are shaped by their interactions with sea-ice and land-ice. In the Arctic Ocean there are many marine-terminating glaciers, however in the Antarctic, ‘ice shelves’ are a more common feature, where land-ice begins to float, leaving the land at ‘grounding zones’ to create vast, ice-covered regions of ocean. The Arctic Ocean surface is characterised by a seasonal pattern of sea-ice growth and retreat that has been changing radically over recent decades (Timmermans and Marshall, 2020). There is also a relatively small, and depleting, area of year-round sea-ice cover. In 2018, the year-round sea-ice covered a region of 4.59 million km^2, down 26% from the 1981-2010 average (Blunden and Arndt, 2019). The Southern Ocean is also heavily influenced by sea-ice, with multi-year ice and seasonal variations. However, there is not yet a significant decadal trend in Antarctic sea ice extent (Ludescher et al., 2019).

Land-ice is formed via extensive compression of frozen precipitation, and is significantly different in structure from sea-ice, which is formed by the freezing of salt water. Sea-ice is much more porous, and is often characterised as a 'mushy layer'. Sea-ice can trap salt water, giving sea ice a salinity of around 1 ppt (Cox and Weeks, 1974). Sea ice is typically around 1 to 2 metres thick in the Arctic, varying geographically and seasonally, occasionally reaching thicknesses of around 5 metres as measured by satellite in 2019 (Petty et al., 2020). Comparatively, ice shelves are much thicker, and can reach thicknesses of around 1000 m close to the grounding line (Griggs and Bamber, 2011). Although the structure of land-ice and sea-ice is vastly different, there are similarities in their impact on ocean stratification. During periods of freezing, 'brine rejection' occurs, where much of the freezing water's salt content is concentrated at the edge of the ice. Brine rejection causes dense water to form at the ice boundary, which can then cause deep convection (Talley et al., 2003). This thesis is not concerned with freezing dynamics, but we mention them for completeness. During periods of melt, cold and fresh melt water forms at the ice base, which can be mixed down, leading to a diffusive convection favourable stratification.

As mentioned in the introductory paragraphs, climate change is already having a significant impact on the polar regions. Within the Arctic Ocean, the most significant trend is the loss in Arctic sea ice. In Barton et al. (2018), they show that the location of the 'Polar Front', which divides the Atlantic source water (Barents Sea Water) from the colder and fresher Arctic Water, limits the extent of winter sea ice. As Atlantic Water warms, the Polar Front may further intensify, reducing sea ice extent, which helps contribute to the 'Atlantification' of the Arctic (Barton et al., 2018). Although much of the warming of the upper ocean in the Arctic is due to increased advection (Asbjørnsen et al., 2020), the subsequent weakening of the Arctic halocline in sea-ice free regions may permit a feedback between the intensity of mixing in the halocline and the reduction in ice cover. Polyakov et al. (2020) suggest that with reduced sea ice cover, the predominant mixing mechanism in the halocline moves from double-diffusive convection to shear-driven mixing, therefore increasing the vertical heat flux and further reducing sea ice cover. In this thesis however, our focus is on the Pacific sector of the Arctic, where a significant heat flux is contributed by poleward transport of heat from Pacific source waters. Although the role of double-diffusive convection in controlling the vertical heat flux from Atlantic-origin water is well-recognised (Timmermans and Marshall, 2020), the release of heat from Pacific-origin waters is relatively less understood (Fine et al., 2018).

In the Antarctic, although there is no significant trend in the changing sea ice cover, Antarctic Ice Shelves are losing mass at an alarming rate (see Figure 1.3 taken from Rignot et al. (2013)). The primary reason for the enhanced ice mass loss in the Antarctic is basal melt in the West Antarctic driven by intrusions of Circumpolar Deep Water (CDW) beneath the ice shelves. CDW is a relatively warm ($\sim 1-2°$C) and salty ($\sim 34.5-34.7$ ppt) water mass, found along the continental shelf break around Antarctica. In recent decades, intrusions of CDW across the shelf break and beneath ice shelves have become warmer (Nakayama et al., 2018) and more persistent (Moffat et al., 2009), which is primarily due to changing wind conditions in the West Antarctic driven by anthropogenic warming (Holland et al., 2019).

In this thesis we will consider observations taken within the Chukchi Sea (Chapter 4) in the Pacific-sector of the Arctic Ocean and underneath George VI Ice Shelf (Chapter 5) on the west Antarctic Peninsular. Although the two regions are distinct, one being beneath an ice shelf in the Antarctic and the other being in the open Arctic Ocean, there are some similarities between the two studied regions: both of these regions are above continental shelf, and so are relatively shallow compared to the central Arctic basin or the open Southern Ocean; and thermohaline layering has been observed in both regions (see Figure 1.5 for staircases in the Chukchi Sea and Kimura et al. (2015) and Venables et al. (2014) for staircases beneath George VI Ice Shelf).

1.3.1 George VI Ice Shelf

George VI Ice Shelf (GVIIS) is located on the west Antarctic Peninsular (wAP), pictured in Figure 1.3. It is situated between Palmer land on the wAP and Alexander Island, within a Cenozoic rift known as George VI Sound. The ice shelf itself covers an area of around 25000 km^2 (Potter and Paren, 1985)[3], similar in size and geometry to the Salish sea residing between Vancouver Island and mainland British Columbia. The majority of the ice in GVIIS comes flows in from Palmer Land, with the remaining 20% coming from surface accumulation (Potter et al., 1984).

The circulation beneath the ice shelf is relatively unknown, due to the ice cover and limited borehole access. However, using Conductivity, Temperature, Depth (CTD) transects along each of the two ice shelf edges, Jenkins and Jacobs (2008) derived geostrophic velocities that suggested around a 0.3-0.5 Sv inflow at the south end, of which half recirculates and outflows in the south and half passes all the way beneath GVIIS and outflows in the north. There is also a small 0.07 Sv inflow in the north that recirculates and outflows in the north.

---

[3] The size of Wales is around 20000 km^2 for comparison

In Jenkins and Jacobs (2008), evidence for thermohaline intrusions was presented in the CTD casts near the ice shelf mouth. It was suggested that the intrusions may form due to double-diffusive effects from nearby glaciers as mentioned in Section 1.1. Meltwater calculations from tracer measurements in Jenkins and Jacobs (2008) suggest that ~ 0.003 Sv are contributed from ice shelf melt, giving an estimated melt rate of 2.3-4.9 m yr^{-1}. This estimated melt rate is consistent with estimates of 2.1 m yr^{-1} from Potter and Paren (1985) and 2.78 ± 0.08m yr^{-1} from Corr et al. (2002), both derived from glaciological measurements. The discrepancy in melt rates potentially suggests a slight increase in melting over the three decades between the Potter and Paren (1985) measurement and the Corr et al. (2002) and Jenkins and Jacobs (2008) measurements. However, as Bishop and Walton (1981) showed, the spatial variability in melt across GVIIS is between 1 and 8 m yr^{-1} which may influence the ability to determine a melt rate trend from limited data.

The water entering beneath GVIIS is almost unmodified Circumpolar Deep Water (CDW), which is a water mass often found on the shelf break of the wAP. Intrusions of CDW onto the shelf and beneath ice shelves have been associated with an enhanced melting along the ice shelves of the Amundsen and Bellinghausen seas in recent decades (Dinniman et al., 2012). The enhanced basal melt along the wAP can be seen in Figure 1.3, derived from satellite data in Rignot et al. (2013). CDW is relatively warm, so has a high capacity to melt ice. CDW is also relatively salty and therefore remains dense so can underlay the cooler and fresher Winter Water (WW), and reach the critical 'grounding zone' of the ice shelf. The occurrence of warm and salty water at depth raises the question, how do heat and salt mix upwards towards the ice base to cause the enhanced melting that has been observed across the wAP in recent decades? Based on studies under sea-ice, there is an expected boundary layer close to the ice base that provides a mechanism for turbulent transport of heat and salt. Observations of turbulent boundary layers under ice shelves have been made (Stevens et al., 2020, Begeman et al., 2018), but they are few and far between, with even fewer examples of turbulence data being collected (Davis and Nicholls, 2019, Kimura et al., 2016).

In order to address the question of turbulent mixing in the boundary layer beneath ice shelves, a team from the British Antarctic Survey, led by Keith Nicholls, conducted a field campaign in 2012. Within this campaign they used hot-water drilling to make boreholes hundreds of metres deep on both Larsen C Ice Shelf (a relatively cold water shelf on the east side of the wAP) and George VI Ice Shelf. The data collected beneath Larsen C Ice Shelf was reported on in Davis and Nicholls (2019). They found that the

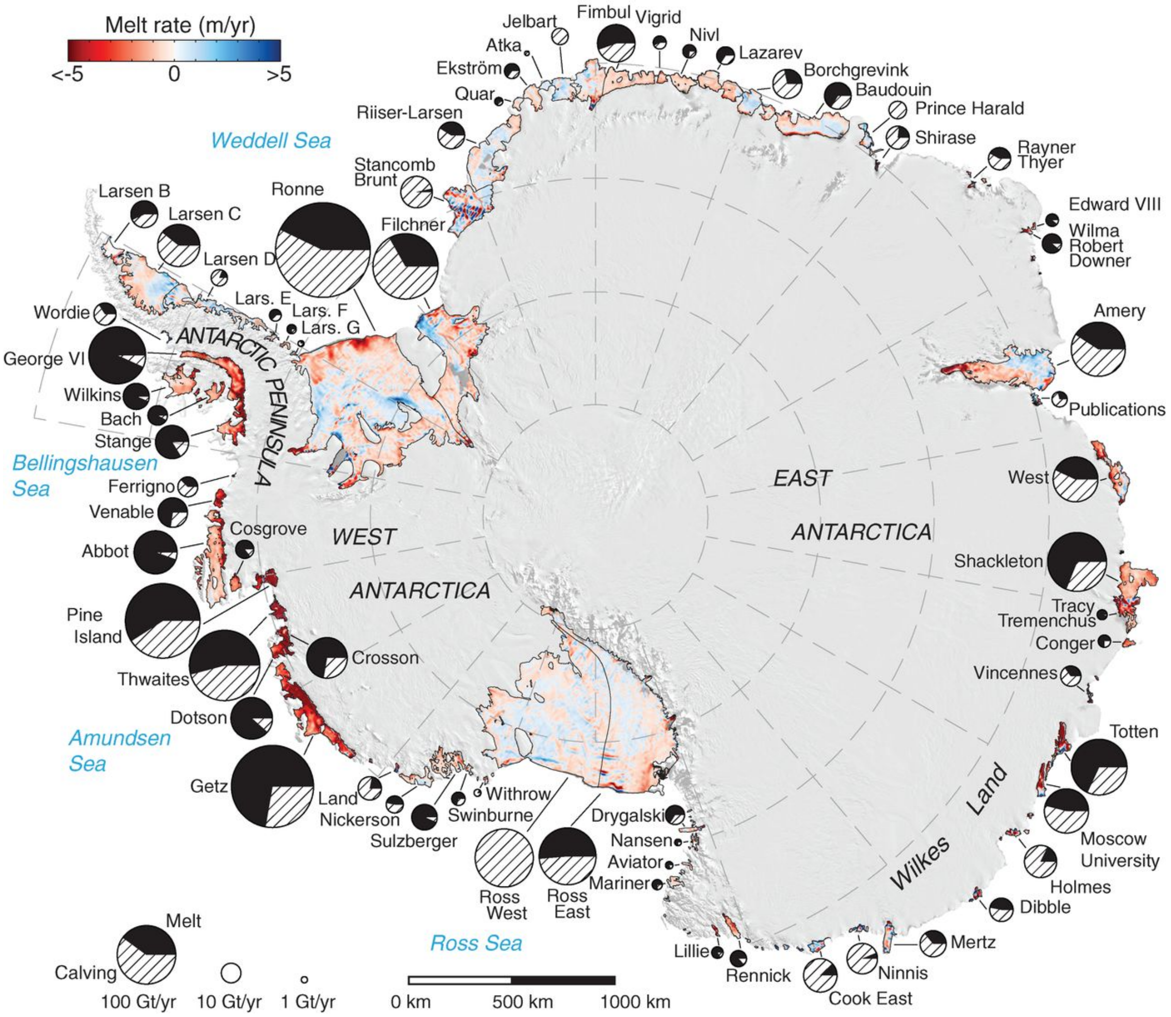
Melt rate (m/yr)
<-5
0
>5
Weddell Sea
Jelbart
Atka
Fimbul
Vigrid
Nivl
Lazarev
Ekström
Quar
Riiser-Larsen
Borchgrevink
Baudouin
Prince Harald
Shirase
Rayner
Thyer
Stancomb
Brunt
Larsen B
Ronne
Larsen C
Filchner
Larsen D
Edward VIII
Wilma
Robert
Downer
Lars. E
Lars. F
Lars. G
Wordie
ANTARCTIC PENINSULA
George VI
Amery
Wilkins
Bach
Publications
Stange
Bellingshausen
Sea
Ferrigno
EAST
ANTARCTICA
West
Venable
Cosgrove
WEST
ANTARCTICA
Abbot
Shackleton
Pine
Island
Tracy
Tremenchus
Conger
Thwaites
Crosson
Vincennes
Dotson
Amundsen
Sea
Totten
Getz
Land
Nickerson
Withrow
Swinburne
Sulzberger
Drygalski
Nansen
Aviator
Mariner
Moscow
University
Holmes
Wilkes Land
Dibble
Ross
West
Ross
East
Melt
Calving
100 Gt/yr
10 Gt/yr
1 Gt/yr
0 km
500 km
1000 km
Ross Sea
Lillie
Rennick
Mertz
Ninnis
Cook East

Fig. 1.3 Figure taken from Rignot et al. (2013).

data was consistent with a shear-driven turbulent boundary layer (McPhee, 2008), as in the ‘three equation model’ discussed in Holland and Jenkins (1999). However, within the George VI Ice Shelf data reported on in Kimura et al. (2015) and Venables et al. (2014), thermohaline staircases were observed in the upper 20 m, suggesting mixing processes beyond shear-driven turbulence.

Venables et al. (2014) presented sample casts from beneath GVIIS which clearly show a layered structure in both temperature and salinity. They also presented concurrent microstructure measurements of the dissipation rate ε. The casts containing staircases had relatively low dissipation rates, however a few casts showed elevated dissipation rates and no staircases. This is consistent with the notion that shearing can damp staircases and double-diffusive activity (Bebieva and Timmermans, 2016). The staircases appeared to be changing and merging between casts taken over a two day period. Kimura et al. (2015) found that the observed changes in staircase structure were consistent with staircase dynamics outlined in Radko et al. (2014). However, observed changes in the staircase structure could also be due to spatial variability advected past the borehole. The staircases decreased in width away from the ice, as in the experiments of Turner (1968). Turner (1968) heated a salinity gradient from below, and via a double-diffusive instability, this caused the progressive development of a staircase structure. In these experiments, the layer thickness reduced away from the wall, suggesting that the GVIIS staircase observations could be consistent with a surface cooling effect. This surface cooling staircase structure is also consistent with observations made in the Mixed Layer reported on in Walesby et al. (2015). We will discuss the data from beneath George VI Ice Shelf further in Chapters 3 and 5.

1.3.2 Chukchi Sea

The Chukchi Sea is a marginal sea of the Arctic Ocean, situated above the Bering Straight connecting Alaska with the Chukotka Peninsular. It sits with the East Siberian Sea to the west, and the Beaufort Sea to the east, and is named after the Chukchi people, who live on the shores of the Chukotka Peninsular. The observations discussed in Chapter 4 were taken on the Alaskan side of the Chukchi Sea on the Chukchi slope, off the coast of the North Slope Borough of Alaska, shown in Figure 1.4. Changes in sea ice conditions are having a substantial impact on the traditional practices and livelihoods of the Iñupiaq, Yup’ik, and Cup’ik people who live there (Huntington et al., 2017). Ocean heat fluxes are known to contribute to the growth-melt cycle of Arctic sea ice (Maykut and Untersteiner, 1971), however our understanding of the processes that transport heat towards Arctic sea ice are limited by a lack of observations (Carmack et al., 2015).

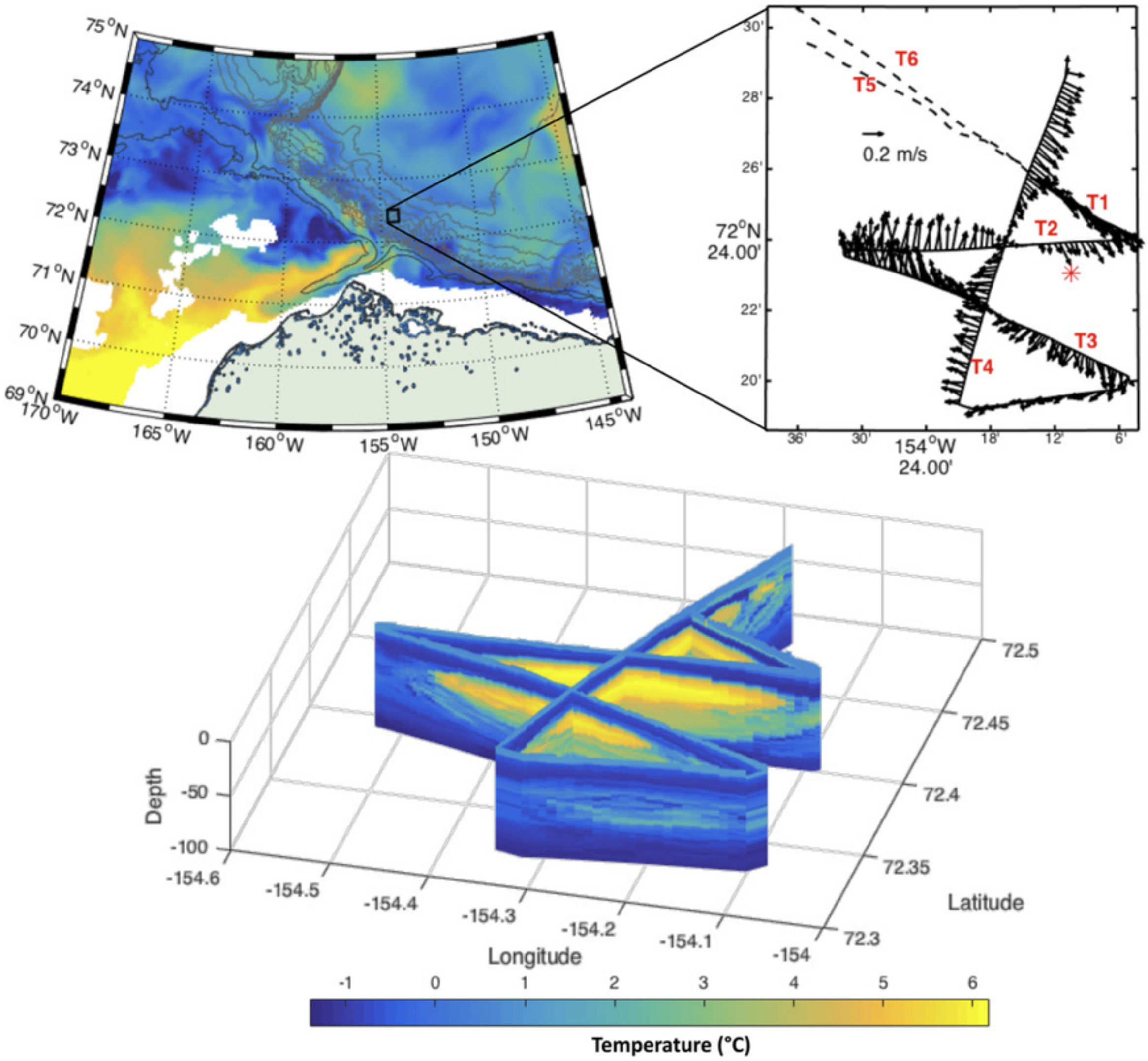
75°N
74°N
73°N
72°N
71°N
70°N
69°N
170°W
165°W
160°W
155°W
150°W
145°W
30'
28'
26'
72°N 24.00'
22'
20'
36'
30'
154°W 24.00'
18'
12'
6'
T6
T5
0.2 m/s
T1
T2
T3
T4
Depth
0
-50
-100
-154.6
-154.5
-154.4
-154.3
-154.2
-154.1
-154
Longitude
72.5
72.45
72.4
72.35
72.3
Latitude
-1
0
1
2
3
4
5
6
Temperature (°C)

Fig. 1.4 Figure taken from Fine et al. (2018). Map of the Chukchi shelf slope. Color represents temperature at 50 m depth, as determined by a global HYCOM model (Metzger et al. 2014). Barrow Canyon is just to the northwest of Alaska. The eddy survey region is enclosed in a black box. (right) Eddy survey pattern. Sections taken using the Shallow Water Integrated Mapping System (SWIMS), are shown as solid lines, and sections using the Mixed Microstructure Profiler as shown dashed lines. The average velocity relative to the eddy center in the 30–50 m depth range is shown for SWIMS sections. The red star indicates the inferred position of the eddy's center when the survey began. (bottom) Temperature measured in SWIMS survey along lines T1–T4. Note the T5 survey line is the only data we consider in Chapter 4.

Pacific Summer Water (PSW) enters the Arctic Ocean via the Bering Strait, and can be found at depths of between 50 m and 100 m (Steele et al., 2004). The lateral distribution of PSW is thought to influence sea ice extent (Shimada et al., 2006, Woodgate et al., 2010), however the mechanisms by which the heat content of PSW reaches the surface are unclear due to the persistent and strong haloclines that form (Toole et al., 2010). In Fine et al. (2018), they presented observations taken during the ArcticMix Cruise in 2015 that we will discuss further in Chapter 4. They report on finescale temperature and salinity data along with microstructure measurements of the dissipation rate ε and the rate of dissipation of thermal variance χ_T. Specifically, they surveyed an intrahalocline warm eddy (visible in Figure 1.4), and analysed its potential to transport heat north towards sea ice.

To analyse the heat transport within the eddy in Fine et al. (2018), they estimated the eddy lifetime. The circulation of the eddy was dominated by geostrophic velocities driven by the warm-core of the eddy, so by quantifying the rate of heat loss, they could estimate the longevity of the eddy structure. They identified lateral intrusions to be the dominant driver of heat loss, however a significant amount of heat was lost via thermohaline staircases observed at the top of the eddy. The staircases are pictured in Figure 1.5, and showed the importance of double-diffusive processes for the transport of PSW heat northwards. Double-diffusive processes are often invoked in the study of Atlantic Water, which lies deeper within the Arctic Ocean at around 200 m to 400 m depth, however their role in PSW transport is less well understood (Kawaguchi et al., 2012).

1.4 Chapter Summary

This thesis is split into four results chapters followed by a conclusions chapter. The first chapter concerns the energetics of double-diffusive fluids, and is adapted from an article published in the *Journal of Fluid Mechanics* in 2020. Throughout the thesis we take the energetic framework developed in the first chapter and apply it to double-diffusive convection in a variety of contrasting scenarios. In the first results chapter we apply the framework to simulations of salt fingering convection (common in the tropical ocean), in the second and fourth results chapters we apply the framework to double-diffusive convection within the ice shelf-ocean boundary layer (found at the fringes of the polar oceans), and within the fourth results chapter we apply the framework to interior ocean turbulence (found away from the ocean boundaries).

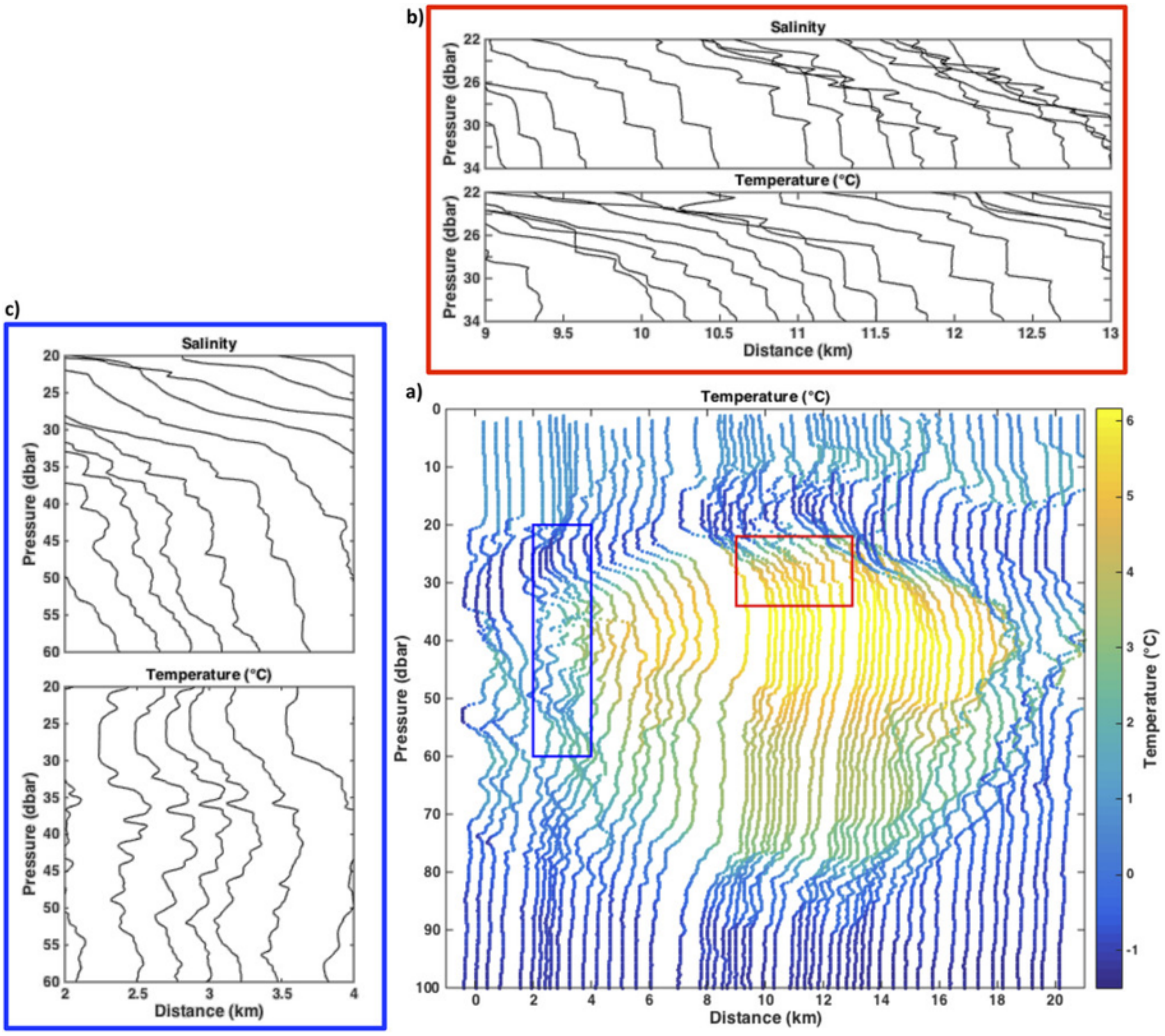

Fig. 1.5 Figure taken from Fine et al. (2018). (a) All temperature profiles taken on T5 of the eddy. The red box highlights a region with diffusive layers; the blue box highlights a region with thermohaline intrusions. (b) Salinity and temperature profiles at the top of the eddy. Distinctive steps are apparent, with well-mixed layers separated by sharp interfaces. The salinity profiles show some salinity spiking due to the abruptness of the interfaces. (c) Salinity and temperature profiles at the side of the eddy. Alternating layers of cold/fresh and warm/salty water indicate the presence of lateral intrusions.

In the first results chapter, we discuss the division of 'Available Potential Energy' (APE) and 'Background Potential Energy' (BPE) within double-diffusive fluids. APE and BPE were introduced by Lorenz (1955), and act to distinguish between parts of the potential energy that are 'available' for mixing and those that are not i.e. 'background'. There are multiple possible definitions of APE and BPE depending on the aspects of the flow you wish to highlight (Tailleux, 2013), however we use the standard definition for single-component flows (Lorenz, 1955, Winters et al., 1995, Peltier and Caulfield, 2003), where the BPE is the potential energy associated with the sorted density field. Using the formalism of Winters et al. (1995), we derive a criterion for the release of BPE into APE via diffusion, which isolates the purely double-diffusive effects, enabling a new characterisation for double diffusive convection. We run a 2D simulation of salt fingering to demonstrate the generality of our approach to different flavours of double-diffusive convection. We have also included some additional results and derivations not originally included within the 2020 paper due to space limitations.

The second results chapter concerns simulations of the ice shelf-ocean boundary layer, and is adapted from an article published in the *Journal of Physical Oceanography* in 2021. As mentioned previously in the introduction, the transport of heat and salt towards ice is a key point of connection between the oceans and the cryosphere. On the wAP in particular, mass loss is being driven by basal melting (Rignot et al., 2013), and so understanding the mechanisms of heat flux towards the ice is essential. Motivated by the observations of Kimura et al. (2015), we run some implicit Large-Eddy-Simulations (LES) of a melting ice boundary under the influence of mechanically forced turbulence. The simulation parameters are chosen to compare to the regimes observed beneath Larsen C Ice Shelf (Davis and Nicholls, 2019) and George VI Ice Shelf (Chapter 5). Kimura et al. (2015) suggested that the observed layers beneath GVIIS were driven by cooling and freshening at the surface, which we call 'melt-driven convection'. Melt-driven convection was investigated in the experiment of Martin and Kauffman (1977), however no external forcing was included, and subsequently Gade (1979) argued that ambient turbulence in the ocean would always be sufficient to damp the melt-driven convection. We investigate the hypothesis that mechanically forced turbulence will damp melt-driven convection, and find that for weak turbulence or strong thermal forcing, the damping effect of turbulence is weak. We use both our simulations and the theory developed in Chapter 2 to develop a criterion for when melt-driven convection can be expected to occur.

The third results chapter utilises the theory developed in Chapter 2 to estimate rates of dissipation within a high resolution dataset presented in Fine et al. (2018) and discussed above. Chapter 4 is adapted from an article published in *Geophysical Research Letters* in 2021. The theory developed in Chapter 2 shows that ‘Available Potential Energy’ is generated by an up-gradient diapycnal buoyancy flux in double-diffusive fluids. This suggests that when the rate of change of APE is small, the up-gradient diapycnal buoyancy flux will balance the turbulent buoyancy flux, which is known to be responsible for the generation of kinetic energy in double-diffusive convection. The criterion for an up-gradient diapycnal buoyancy flux depends solely on the gradients in temperature and salinity, so it allows us to estimate the rate of dissipation based only on the gradients in temperature and salinity. The main obstacle to this is that the gradients that force an up-gradient diapycnal buoyancy flux are on small scales. So, we estimate the size of small scale T/S gradients based on measurements of large scale T/S gradients. We develop a method for the process of amplifying the T/S gradients, and then apply the method to the data from Fine et al. (2018). There is a good match between our prediction and the observations, even when we use artificially coarse CTD data.

The final results chapter considers mooring data collected from beneath George VI Ice Shelf in the 2012 field campaign by the British Antarctic Survey, described above. This chapter is adapted from an article *in review* in September 2021. The mooring data was designed to be comparable to the mooring data analysed in Davis and Nicholls (2019). Davis and Nicholls (2019) found evidence of a shear-driven boundary layer, which fit previous theory developed beneath sea ice in McPhee et al. (1987). The George VI Ice Shelf mooring data consists of temperature measurements, two turbulence instruments and an Upward Looking Sonar. We first show that the measured dissipation rates do not correlate with mean flow speed, as would be expected of a shear-driven boundary layer. We then go on to apply the method we developed in Chapter 4 to estimate the dissipation rates from our measurements of temperature. There is a good correlation between our model for double-diffusive convection and the observed dissipation rates. This suggests that the measured lateral gradients in temperature are sufficient to explain the observed mixing beneath George VI Ice Shelf. We go on to discuss the observed heat flux, and the subsequent impact of double diffusion on melt rates.

1.5 Double Diffusion Glossary

There are a series of terms which are used within studies of double diffusion that we will define here for clarity. The definitions of these terms may vary within other studies of double diffusion, however we have chosen the definitions we found most useful in interpreting the literature:

Term	**Definition**
Double-Diffusive Fluid	A fluid in which two components, with differing rates of molecular diffusion, contribute to the density. Referred to as ‘Multi-component’ if there are more than two components.
Double Diffusion	A general catch-all term for processes in double-diffusive fluids that depend on the difference in diffusivities between the two components.
Double Diffusive Convection	A release of potential energy into kinetic energy (convection), enabled by the difference in diffusivity between the two components (i.e. it would not occur if the diffusivities were made equal).
Diffusive Convection	A form of double-diffusive convection in which cold fresh water overlies warm salty water i.e. $0 < R_\rho < 1$.
Semi-Convection	Another term for ‘Diffusive Convection’, used primarily in the astrophysical literature.
Oscillatory Diffusive Convection	An overstable linear instability, or convection triggered by this linear instability, in which the fluid is at rest and the density ratio $(\nu+\kappa_S)/(\nu+\kappa_T) < R_\rho < 1$. In the ocean the lower bound on R_ρ varies between 0.85 and 0.94.
Salt Fingering Convection	A form of double-diffusive convection in which warm, salty water overlies cold, fresh water i.e. $R_\rho > 1$. Alternatively this may refer to the ‘salt-fingering instability’ which is a linear instability of a double-diffusive fluid at rest when $1 < R_\rho < \kappa_T/\kappa_S$. The most unstable mode has the characteristic ‘salt finger’ pattern.
Salt Fingers	A finger-like pattern in the temperature, salinity and velocity of a fluid, forced by double-diffusive effects. These form due to the salt-fingering instability. When sheared they become tilted into ‘salt sheets’ aligned with the direction of shear.
Differential Diffusion	Processes where two components mix at different rates, but potential energy is not released. It is distinct from double-diffusive convection but still relies on differences in molecular diffusivity.
Thermohaline Convection	Another term for double-diffusive convection.
Thermohaline Layering	Alternating well-mixed regions and stratified ‘interfaces’ in both temperature and salinity. They may occur due to non-double-diffusive effects. Also known as a ‘staircase’.
Double-diffusive Layering	Layers that form in both temperature and salinity due to double-diffusive processes e.g. salt fingering or diffusive convection.
Thermohaline Intrusions	Lateral interleaving structures in both temperature and salinity. Can form due to double diffusive, or non-double-diffusive, mechanisms.

Chapter 2

A general criterion for the release of background potential energy through double diffusion

This chapter was published in *Journal of Fluid Mechanics: Rapids* in 2020 with coauthor John Taylor. Some minor edits have been made from the published version including an appendix containing derivations and ancillary results as well as a short note about updates in the field since our publication. I would like to thank Peter Haynes, Remi Tailleux and Catherine Vreugdenhil for very helpful discussions and comments.

2.1 Introduction

Double diffusion occurs when the density of a fluid is a function of two scalars which diffuse at different rates. Our primary motivation is double diffusion in the ocean, so we will refer to the faster diffusing scalar as temperature and the slower diffusing scalar as salt. Double diffusion can drive a variety of flows including diffusive convection, salt fingering, thermohaline intrusions, and thermohaline staircases (Turner, 1985, Schmitt, 1994, Radko, 2013), and may impact canonical flows including gravity currents, plumes and Kelvin-Helmholtz billows (Konopliv and Meiburg, 2016, Dadonau et al., 2020, Smyth et al., 2005). Here, we will analyze the energetics of double-diffusive fluids using the concepts of 'background' and 'available' potential energy.

The background potential energy (BPE) can be found by adiabatically sorting the density field into a monotonically decreasing function of height (Lorenz, 1955). The BPE is then defined as the potential energy associated with the sorted density field.

The available potential energy (APE) is defined as the difference between the potential energy of the un-sorted density and the BPE. The budgets for APE and BPE were first derived by Winters et al. (1995) for a single component, incompressible, Boussinesq fluid. Winters et al. (1995) showed that energy can be transferred from APE to BPE, but not vice versa (and hence termed *irreversible* mixing), via a diapycnal (across surfaces of constant density) diffusive buoyancy flux. This framework was used to formalize the definition of mixing efficiency, an often used concept in ocean mixing (e.g. Peltier and Caulfield, 2003, Gregg et al., 2018). Here, we extend the framework from Winters et al. (1995) to include double-diffusive effects.

A local budget for APE was introduced in both Scotti and White (2014), which was further generalized to include compressibility, a non-linear equation of state, and an arbitrary number of scalar components in Tailleux (2018b). Recently, Tailleux (2018a) derived a new expression for the local APE dissipation rate in a binary compressible fluid with a nonlinear equation of state and showed that in this case the APE dissipation is irreversible. Tailleux (2013, 2018a, 2018b) included terms to represent diabatic heat and salt fluxes, but did not explicitly consider diffusion or double-diffusive effects. Here we will follow the derivation in Winters et al. (1995) and extend their analysis of the global APE and BPE budgets to include double diffusion.

Smyth et al. (2005) considered the problem of double diffusion by applying the Winters et al. (1995) formulation to temperature and salinity separately, defining a background potential energy for each component by sorting temperature and salinity independently. While this approach is useful for quantifying irreversible mixing for each scalar, temperature and salinity do not have a gravitational potential energy separate from the fluid density. This approach also does not capture the single component limit of equal molecular diffusivities. For example, consider a situation where non-zero horizontal temperature and salinity gradients are compensating such that the density depends only on the vertical coordinate. If the molecular diffusivities of each component are equal and the equation of state is linear, then the analysis of Winters et al. (1995) can be applied to the fluid density; if the density profile is stable, the APE will be zero. However, the APE calculated from the temperature and salinity individually will be non-zero.

Here we offer three main results. First, we consider the general criterion for the diapycnal buoyancy flux in a double-diffusive fluid and show that its sign can be expressed in terms of what we call the 'gradient ratio', $G_\rho \equiv (\alpha|\nabla T|)/(\beta|\nabla S|)$, as well as the physical angle θ made between the scalar gradients (Fig. 2.1), and the ratio of the molecular diffusivities (κ_T, κ_S). Second, we extend the work of Winters et al. (1995) by deriving the volume-averaged APE and BPE budgets for an incompressible Boussinesq stratified fluid with a linear equation of state and two diffusing components. We show that the criterion for an up-gradient buoyancy flux obtained earlier can be related to a condition for a transfer of BPE to APE. Note that while this result changes the interpretation of the partition between APE and BPE, we will still use the terms APE and BPE to refer to the standard definitions based on the sorted buoyancy. The criterion that we derive is useful for identifying when double diffusion qualitatively changes the energy transfers in a multiple component fluid. Third, we generalize the evolution equation for the sorted buoyancy profile (Winters and D'Asaro, 1996, Nakamura, 1996) for a double-diffusive fluid and relate an up-gradient diapycnal buoyancy flux to a negative effective diffusivity in sorted buoyancy coordinates. We then test our criterion using a simulation of salt fingering (Fig. 2.2) and show that the previously observed negative diffusivity of salt fingering (e.g. St. Laurent and Schmitt, 1999) can be described in terms of G_ρ and θ, generalising previous results of Veronis (1965) and Garrett (1982).

2.2 Results

2.2.1 Governing Equations

We will consider the incompressible Boussinesq Navier Stokes equations,

$$\frac{D\boldsymbol{u}}{Dt} = -\frac{\nabla p}{\rho_0} + b\hat{\mathbf{k}} + \nabla\cdot\boldsymbol{\tau}, \qquad \nabla\cdot\boldsymbol{u} = 0, \tag{2.1)-(2.2}$$

where $D/DT = \partial/\partial t + \mathbf{u}\cdot\nabla$ denotes the material derivative and $\boldsymbol{u} = (u, v, w)$ is the velocity with respect to Cartesian coordinates (x, y, z). The fluid pressure is p, $\hat{\boldsymbol{k}}$ is the unit vector in the z direction, b is the buoyancy, and $\nabla\cdot\boldsymbol{\tau}$ is the divergence of the viscous stress tensor. Additionally we consider two advection/diffusion equations for the two stratifying elements, and a linear equation of state that relates these quantities to the fluid density, ρ, and hence buoyancy, $b \equiv -g(\rho-\rho_0)/\rho_0$ where g is the gravitational acceleration and ρ_0 is a constant reference density. The linear approximation to the nonlinear equation of state for seawater may be appropriate in regions with small variations in temperature and salinity, and in the shallow polar oceans the nonlinearities in the equation of state have been found to have a limited impact on the patterns of circulation (Roquet et al., 2015). Specifically, these equations are

$$b = g(\alpha T - \beta S), \qquad \frac{DT}{Dt} = \kappa_T\nabla^2 T, \qquad \frac{DS}{Dt} = \kappa_S\nabla^2 S, \tag{2.3)-(2.5}$$

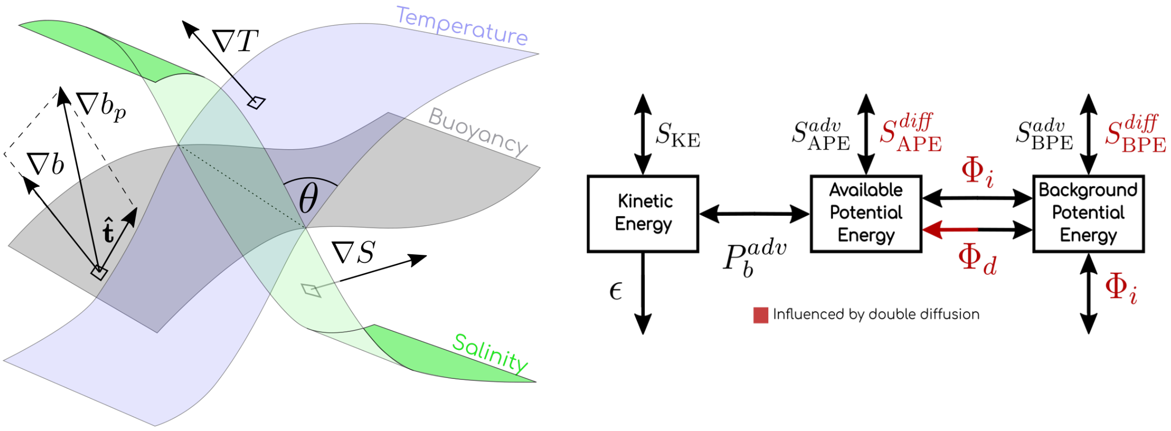
Temperature
∇T
∇b_p
∇b
Buoyancy
θ
$\hat{\mathbf{t}}$
∇S
Salinity
S_{KE}
S^{adv}_{APE}
S^{diff}_{APE}
S^{adv}_{BPE}
S^{diff}_{BPE}
Kinetic Energy
Available Potential Energy
Background Potential Energy
Φ_i
Φ_d
P^{adv}_b
ϵ
Φ_i
🟥 Influenced by double diffusion

Fig. 2.1 (Left): A schematic to illustrate the angle made between surfaces of constant temperature and salinity. Generically the angle $\theta(\boldsymbol{x}, t)$ varies in space and time. (Right): A schematic adapted from Winters et al. (1995), for a double-diffusive fluid. The arrows pointing up and down indicate energy exchanges with external and internal energy, respectively.

Note that T and S can be viewed as generic diffusing scalars, with molecular diffusivities (κ_T, κ_S).

2.2.2 Condition for an Up-gradient Buoyancy Flux

By introducing a new variable b_p, the buoyancy evolution equation can be written

$$\frac{Db}{Dt} = \nabla^2 b_p, \quad \text{where} \quad b_p \equiv g(\alpha\kappa_T T - \beta\kappa_S S). \tag{2.6}$$

We will refer to b_p as the 'buoyancy flux potential', since ∇b_p is the diffusive buoyancy flux. As illustrated in Fig. 2.1, ∇b_p is not necessarily in the same direction as ∇b (unlike in a single component fluid), which can result in a buoyancy flux along isopycnals (surfaces of constant density). We can divide the buoyancy flux into diapycnal and isopycnal components,

$$\nabla b_p = \underbrace{(\nabla b_p \cdot \hat{\boldsymbol{n}})\hat{\boldsymbol{n}}}_{\text{diapycnal buoyancy flux}} + \underbrace{(\nabla b_p \cdot \hat{\boldsymbol{t}})\hat{\boldsymbol{t}}}_{\text{isopycnal buoyancy flux}}, \tag{2.7}$$

where $\hat{\boldsymbol{n}} = \nabla b / |\nabla b|$ is the unit normal to the isopycnal surface, and $\hat{\boldsymbol{t}}$ is a unit vector tangent to the isopycnal surface, illustrated in Fig. 2.1.

Introducing the gradient ratio $G_\rho \equiv (\alpha|\nabla T|)/(\beta|\nabla S|)$, the diapycnal buoyancy flux can be written

$$\nabla b_p \cdot \hat{\boldsymbol{n}} = \frac{g^2 \kappa_S \beta^2 |\nabla S|^2}{|\nabla b|} \left(\frac{\kappa_T}{\kappa_S} G_\rho^2 + \left(\frac{\kappa_T}{\kappa_S} + 1 \right) G_\rho \cos\theta + 1 \right), \tag{2.8}$$

where $\cos\theta = -\nabla T \cdot \nabla S/(|\nabla T||\nabla S|)$ and $\theta(\boldsymbol{x}, t)$ is the angle between the vectors ∇T and $-\nabla S$. The scalar angle is defined such that when $\theta = 0, 2\pi$ the gradients in T and S point in opposing directions such that they contribute to the buoyancy gradient constructively. This definition implies θ is also the angle made between the T and S isoscalar surfaces (see Fig. 2.1).

We will refer to the term in brackets in Eq. 2.8 as $f(G_\rho, \theta, \frac{\kappa_T}{\kappa_S})$. Explicitly

$$f\left(G_\rho, \theta, \frac{\kappa_T}{\kappa_S}\right) \equiv \frac{\kappa_T}{\kappa_S} G_\rho^2 + \left(\frac{\kappa_T}{\kappa_S} + 1 \right) G_\rho \cos\theta + 1. \tag{2.9}$$

The function f sets the sign of the diapycnal buoyancy flux, $\nabla b_p \cdot \hat{\boldsymbol{n}}$, since the other terms in Eq. 2.8 are positive definite. Therefore, a condition for an up-gradient diapycnal buoyancy flux is $f < 0$. The dividing line between positive and negative diapycnal flux, $f = 0$, is a quadratic equation in G_ρ and $\cos\theta$, plotted in bold in Figure 2.2. The contours of f are also plotted in Figure 2.2. Since G_ρ, κ_T, and κ_S are positive, $\cos\theta$ is the only term in Eq. 2.9 that can be negative. Therefore the relative orientation of the surfaces of constant T and S is of central importance to the sign of the diapycnal buoyancy flux. A Reynolds-averaged version of f was derived as a term in the equation for the density variance by de Szoeke (1998) who showed that negative values of this quantity can lead to the production of density variance. The significance of the condition in Eq. 2.9 to the APE and BPE budgets will be discussed in the next section.

When $\theta = \pi$, the condition for a negative diapycnal buoyancy flux reduces to

$$\nabla b_p \cdot \hat{\boldsymbol{n}} < 0 \iff \frac{\kappa_S}{\kappa_T} < R_\rho < 1, \quad \text{where} \quad R_\rho \equiv \frac{\alpha \Delta T}{\beta \Delta S} \tag{2.10}$$

is the density ratio. This is a well-known result in the double-diffusive literature (e.g. Veronis, 1965, Garrett, 1982, St. Laurent and Schmitt, 1999, Radko, 2013). Therefore, Eq. 2.9 can be viewed as a generalization of Eq. 2.10 which includes horizontal T and S gradients. Note that salt fingering instability occurs when $R_\rho > 1$ in the case of vertically aligned gradients such that the diffusive buoyancy flux will be down-gradient (Radko, 2013). However, as we will demonstrate below, Eq. 2.9 can be used to analyze the energetics of active salt fingering convection by considering the T and S gradients associated with individual salt fingers.

The third row of Fig. 2.2 shows contours of $f(G_\rho,\theta)$, where the region of $f < 0$ is represented with dashed contours and the bounding line for this region is in bold. Superimposed is data from a simulation of salt fingers which will be discussed below. The $\nabla b_p \cdot \hat{\boldsymbol{n}} < 0$ region is bounded by a critical angle θ_c, where

$$\theta_c = \cos^{-1}\left(\frac{-2\sqrt{\frac{\kappa_T}{\kappa_S}}}{\frac{\kappa_T}{\kappa_S}+1}\right) \quad \Longrightarrow \quad \frac{\pi}{2} < \theta_c \leq \pi. \tag{2.11}$$

For $\kappa_T = 10^{-7}\mathrm{m}^2/\mathrm{s}$ and $\kappa_S = 10^{-9}\mathrm{m}^2/\mathrm{s}$, typical of the ocean, the critical angle is $\theta_c \simeq 100°$. In the limit as $\kappa_T/\kappa_S \to 1$, the critical angle $\theta_c \to 90°$.

2.2.3 Potential Energy Budget

In this section we extend the framework of Winters et al. (1995) to include double-diffusive effects. Within a static volume $\mathcal{V}$ with boundary $\mathcal{S}$, we can define the kinetic energy (2.12), potential energy (2.13), background potential energy (2.14) and available potential energy (2.15),

$$E_{\mathrm{KE}} = \frac{\rho_0}{2}\int_{\mathcal{V}} u^2+v^2+w^2 d\mathcal{V}, \qquad E_{\mathrm{PE}} = -\rho_0\int_{\mathcal{V}} bz d\mathcal{V}, \tag{2.12)-(2.13}$$

$$E_{\mathrm{BPE}} = -\rho_0\int_{\mathcal{V}} bz^* d\mathcal{V}, \qquad E_{\mathrm{APE}} = E_{\mathrm{PE}} - E_{\mathrm{BPE}} = \rho_0\int_{\mathcal{V}} b(z^*-z) d\mathcal{V}, \tag{2.14)-(2.15}$$

where z^* is the sorted buoyancy coordinate:

$$z^*(\boldsymbol{x},t) = \frac{1}{A}\int_{\mathcal{V}'} H(b(\boldsymbol{x},t) - b(\boldsymbol{x}',t))d\mathcal{V}', \tag{2.16}$$

H is the Heaviside function, and A is the cross sectional area of the volume $\mathcal{V}$. The sorted height $z^*(\boldsymbol{x},t)$ can be interpreted as the height of a fluid parcel after sorting the buoyancy field b into a stable configuration i.e. $b(z^*)$ is the sorted buoyancy profile. Alternatively, $z^*(b)$ is the normalized volume of fluid with buoyancy less than b. In practice z^* can be calculated by integrating the PDF of b (Tseng and Ferziger, 2001). Following the method outlined in Winters et al. (1995), the budgets of the energy components for a double-diffusive fluid are

$$\frac{dE_{\mathrm{KE}}}{dt} = \underbrace{-\oint_S \left(p\boldsymbol{u} - \frac{1}{2}\rho_0\boldsymbol{u}(u^2+v^2+w^2) - \boldsymbol{u}\cdot\boldsymbol{\tau}\right)\cdot\hat{\boldsymbol{n}}d\mathcal{S}}_{S_{\mathrm{KE}}} + \rho_0\underbrace{\int_{\mathcal{V}} bw d\mathcal{V}}_{P_b^{adv}} - \rho_0\underbrace{\int_{\mathcal{V}} \tau_{ij}\frac{\partial u_i}{\partial x_j}d\mathcal{V}}_{\varepsilon}, \tag{2.17}$$

$$\frac{dE_{\mathrm{PE}}}{dt} = \rho_0\oint_S (\underbrace{bz\mathbf{u}}_{S_{\mathrm{PE}}^{adv}} - \underbrace{z\nabla b_p}_{S_{\mathrm{PE}}^{dif}})\cdot\hat{\mathbf{n}}d\mathcal{S} - \rho_0\underbrace{\int_{\mathcal{V}} bwd\mathcal{V}}_{P_b^{adv}} + \rho_0\underbrace{(A\overline{b_p})_{\mathrm{top}} - (A\overline{b_p})_{\mathrm{bottom}}}_{\Phi_i}, \tag{2.18}$$

$$\frac{dE_{\mathrm{BPE}}}{dt} = \rho_0\oint_S (\underbrace{\psi\mathbf{u}}_{S_{\mathrm{BPE}}^{adv}} - \underbrace{z^*\nabla b_p}_{S_{\mathrm{BPE}}^{dif}})\cdot\hat{\mathbf{n}}d\mathcal{S} + \rho_0\underbrace{\int_{\mathcal{V}} \frac{dz^*}{db}(\nabla b_p\cdot\nabla b)d\mathcal{V}}_{\Phi_d}, \tag{2.19}$$

$$\begin{aligned}\frac{dE_{\mathrm{APE}}}{dt} = {} & \rho_0\underbrace{\oint_S (bz-\psi)\mathbf{u}\cdot\hat{\mathbf{n}}d\mathcal{S}}_{S_{\mathrm{APE}}^{adv}} + \rho_0\underbrace{\oint_S (z^*-z)\nabla b_p\cdot\hat{\mathbf{n}}d\mathcal{S}}_{S_{\mathrm{APE}}^{dif}} - \rho_0\underbrace{\int_{\mathcal{V}} bwd\mathcal{V}}_{P_b^{adv}} \\ & + \rho_0\underbrace{(A\overline{b_p})_{\mathrm{top}} - (A\overline{b_p})_{\mathrm{bottom}}}_{\Phi_i} - \rho_0\underbrace{\int_{\mathcal{V}} \frac{dz^*}{db}(\nabla b_p\cdot\nabla b)d\mathcal{V}}_{\Phi_d},\end{aligned} \tag{2.20}$$

These budgets can be derived by taking time derivatives of Eqns. 2.12-2.15 and applying integration by parts. Additionally, one must use the relations $\nabla z^* = (dz^*/db)\nabla b$ and $\langle dz^*/dt\rangle_{z^*} = 0$. By defining $\psi \equiv \int^b z^*(s)ds$ we also use the relation $\nabla\psi = z^*\nabla b$. These equations are presented schematically in Fig. 2.1. Although we follow the derivation in Winters et al. (1995), these equations may also be derived by volume integrating the local APE budgets derived in Tailleux (2018b). The letter S in Eqns. 2.17-2.20 denotes a surface flux, with a superscript adv denoting an advective flux, or dif denoting a diffusive flux. The term P_b^{adv} is the volume integral of the vertical advective buoyancy flux bw and ε is the volume integrated dissipation rate of kinetic energy. The term Φ_i is the exchange between internal energy and potential energy. This term is discussed extensively in Konopliv and Meiburg (2016) in the context of the potential energy associated with the horizontally-averaged buoyancy. In our volume-averaged formulation, Φ_i only involves boundary quantities and in a turbulent flow we might expect Φ_i to be small relative to Φ_d (Peltier and Caulfield, 2003).

Eqns. 2.17-2.20 differ from the single component case presented in Winters et al. (1995) in the expressions for the diffusive surface terms S_{PE}^{dif}, S_{BPE}^{dif}, S_{APE}^{dif}, Φ_i and the APE/BPE exchange term Φ_d where b_p now replaces κb. As a result, Φ_i can take negative values in a fluid where the density increases with depth, which is not possible in a single component fluid.

We define the quantity φ_d as the integrand of Φ_d, i.e.

$$\varphi_d \equiv \frac{dz^*}{db} \nabla b_p \cdot \nabla b, \tag{2.21}$$

and using Eq. 2.8, the sign of φ_d is set by the sign of $f(G_\rho, \theta, \kappa_T/\kappa_S)$ since $dz^*/db > 0$ by construction. There is a close connection between φ_d and the local diapycnal buoyancy flux $\nabla b_p \cdot \hat{\boldsymbol{n}}$.

Start by considering the average of an arbitrary continuous function, $g(\mathbf{x},t)$ over a surface of constant z^*,

$$\langle g(\mathbf{x},t)\rangle_{z^*} \equiv \frac{1}{A_s}\int_{\mathcal{S}^*} g(\mathbf{x},t)\, d\mathcal{S}^*, \tag{2.22}$$

where $\mathcal{S}^*$ is a surface with constant z^* and A_s is its area. Next, consider two isopycnals with buoyancy b and $b+\Delta b$ and let Δn and Δz^* denote the perpendicular and sorted distances between the isopycnals. Then, taking the limit as $\Delta b \to 0$, we can write

$$\begin{aligned}
\langle g(\mathbf{x},t)\rangle_{z^*} &= \lim_{\Delta b\to 0} \frac{1}{A_s}\frac{1}{\Delta z^*}\int_{\mathcal{S}^*} g(\mathbf{x},t)\frac{\Delta b}{\Delta n}\frac{\Delta z^*}{\Delta b}\Delta n\, d\mathcal{S}^*,\\
&= \lim_{\Delta b\to 0} \frac{A}{A_s}\frac{1}{A\Delta z^*}\int_{\Delta\mathcal{V}^*} g(\mathbf{x},t)|\nabla b|\frac{dz^*}{db}\, d\mathcal{V}^*,\\
&= \frac{A}{A_s}\frac{dz^*}{db}\langle g(\mathbf{x},t)|\nabla b|\rangle_{z^*},
\end{aligned} \tag{2.23}$$

where $\Delta\mathcal{V}^* = A\Delta z^*$ is the volume between the isopycnal surfaces. Winters and D'Asaro (1996) derived this relation for $g(\mathbf{x},t) = \kappa|\nabla b|$ (note that their result included a minus sign since they used density instead of buoyancy as the sorted variable).

Taking $g(\mathbf{x},t) = \nabla b_p \cdot \hat{\boldsymbol{n}}$ and using Eq. 2.23 gives

$$\langle \nabla b_p \cdot \hat{\boldsymbol{n}}\rangle_{z^*} = \frac{1}{A_S}\int_{\mathcal{S}^*} \nabla b_p \cdot \frac{\nabla b}{|\nabla b|} d\mathcal{S}^* = \frac{A}{A_S}\frac{dz^*}{db}\left\langle \nabla b_p \cdot \nabla b\right\rangle_{z^*} = \frac{A}{A_S}\langle\varphi_d\rangle_{z^*}, \tag{2.24}$$

and hence $\langle\varphi_d\rangle_{z^*}$ is related to the mean diapycnal buoyancy flux. Note that $\langle\varphi_d\rangle_{z^*}$ and $\langle\nabla b_p \cdot \boldsymbol{n}\rangle_{z^*}$ have the same sign since A and A_S are positive. Similarly, we can write the magnitude of the isopycnal buoyancy flux $\nabla b_p \cdot \hat{\boldsymbol{t}}$ averaged across surfaces of constant z^* as

$$\langle \nabla b_p \cdot \hat{\boldsymbol{t}}\rangle_{z^*} = g\alpha\beta|\kappa_T - \kappa_S|\frac{A}{A_S}\frac{dz^*}{db}\langle|\nabla T \times \nabla S|\rangle_{z^*}. \tag{2.25}$$

The isopycnal buoyancy flux does not appear in the volume-integrated energy budget (Eqns. 2.17-2.20) and clearly vanishes for $\kappa_S = \kappa_T$ or when ∇T and ∇S point in the same direction.

In a double-diffusive fluid, an up-gradient buoyancy flux can lead to $\langle \varphi_d \rangle_{z^*} < 0$. In practice it is easier to accurately measure gradients in temperature than salinity in the ocean (Klymak and Nash, 2009). It is therefore convenient to re-cast this condition in terms of the temperature gradient:

$$\langle \varphi_d \rangle_{z^*} < 0 \iff \left\langle \alpha |\nabla T| \frac{f(G_\rho, \theta, \frac{\kappa_T}{\kappa_S})}{G_\rho \sqrt{f(G_\rho, \theta, 1)}} \right\rangle_{z^*} < 0, \tag{2.26}$$

by noting $f(G_\rho, \theta, 1) = |\nabla b|^2/(g^2\beta^2|\nabla S|^2)$ and applying Eq. 2.24. Although G_ρ and θ depend on ∇S, if these variables were parameterized, then Eq. 2.26 could be used with measurements of the temperature gradient to infer the sign of the average diapycnal buoyancy flux and provides insight into the exchange between APE and BPE.

The criteria in Eqns. 2.9 and 2.26 can be applied to turbulent flows, including those in a doubly stable background stratification. We might expect vigorous turbulence to highly distort the scalar surfaces and influence the distribution of θ. If more points lie outside of the range of critical angles such that $\theta < \theta_c$ or $\theta > 2\pi - \theta_c$, where θ_c is defined in Eq. 2.11, then we might anticipate that the average diapycnal buoyancy flux will be positive (down-gradient). This hypothesis will be tested below using simulations of salt fingering.

2.2.4 Evolution of Sorted Buoyancy

Following the derivation in Winters and D'Asaro (1996) and Nakamura (1996) in the case of a single component fluid, we can derive an equation for the evolution of the sorted buoyancy profile, averaged in z^* coordinates for a double-diffusive fluid,

$$\frac{\partial}{\partial t}\langle b \rangle_{z^*} = \frac{\partial}{\partial z^*}\left(\left\langle \frac{dz^*}{db}\nabla b_p \cdot \nabla b \right\rangle_{z^*}\right) = \frac{\partial}{\partial z^*}\langle \varphi_d \rangle_{z^*}. \tag{2.27}$$

As in the single component case, the divergence of the diapycnal buoyancy flux sets the time rate of change of the sorted buoyancy. A similar equation was derived by Paparella and Von Hardenberg (2012) for the evolution of the horizontally-averaged buoyancy profile of a double-diffusive fluid, which evolved due to gradients in a combined advective and diffusive buoyancy flux. One advantage of Eq. 2.27 is that the diapycnal buoyancy flux does not directly involve the velocity field since the flux is purely diffusive.

The single component version of Eq. 2.27 was used by Salehipour et al. (2016) to propose a parameterization for the mixing efficiency in z^* coordinates and Taylor and Zhou (2017) used this framework to develop a criterion for layer formation within a single-component stratified flow. Similarly, Eq. 2.27 could provide a pathway to parameterise double-diffusive flows. For example, it might be possible to parameterize $\langle \varphi_d \rangle_{z^*}$ as a function of θ and G_ρ, although this is beyond the scope of this paper.

As discussed in Winters and D'Asaro (1996) and Nakamura (1996), Eq. 2.27 can be written in the form of a diffusion equation by defining an effective diffusivity for the sorted buoyancy, $\kappa_b(\boldsymbol{x},t) \equiv \langle \varphi_d \rangle_{z^*}/(db/dz^*)$. Therefore, a negative mean diapycnal buoyancy flux implies a negative effective diffusivity, since buoyancy increases monotonically with height in sorted coordinates and hence $db/dz^* \geq 0$. Previous work has shown that double-diffusive flows often develop a negative vertical turbulent diffusivity (e.g. Veronis, 1965, St. Laurent and Schmitt, 1999, Ruddick and Richards, 2003) and the expression for κ_b along with the definition of φ_b in Eq. 2.24 can be viewed as a generalization of this result when the averaging is applied in sorted buoyancy coordinates.

2.2.5 Application: Simulations of Salt Fingering

To demonstrate an application of the theory described above, we will consider a numerical simulation of a canonical double-diffusive flow: salt fingering. We time-stepped Eqns. 2.1-2.5 in a 2D (x-z) domain using a third order Runge-Kutta scheme and second order finite differences with an implicit Crank-Nicholson method for the viscous and diffusive terms. Details of the numerical method can be found in Bewley (2012). The initial condition consists of a horizontally uniform temperature and salinity field with linear dependence on height, z. Here the fields are non-dimensionalized such that for $z \in (0,1)$, the initial temperature field $T_0 \in (0,1)$. Periodic boundary conditions are applied in x with a non-dimensional domain width of 6 to allow multiple salt fingers to form and interact. At the top and bottom of the domain $\mathbf{u} = 0$, and temperature and salinity are set to their initial values. The profiles were set so that warm salty water overlies cold fresh water, a condition favorable for the formation of 'salt fingers'. We used a density ratio of $R_\rho = 1.01$, close in value to 1 to enable the most unstable mode to develop quickly (Kunze, 2003). We used a diffusivity ratio of $\kappa_T/\kappa_S = 20$, which implies $\theta_c \sim 115°$, and a Prandtl number $Pr = \nu/\kappa_T = 1$ to give a similar critical angle to the oceanic case ($\theta_c \sim 100$) without requiring a high resolution to resolve the Batchelor scales for the scalars. We used typical oceanic values in the linear equation of state $(\alpha, \beta) = (3.9\times10^{-5}\ (°C)^{-1}, 7.9\times10^{-4}\ \mathrm{ppt}^{-1})$. The simulation was initiated with a small amplitude random perturbation to the velocity. The results are qualitatively similar for a variety of parameter choices.

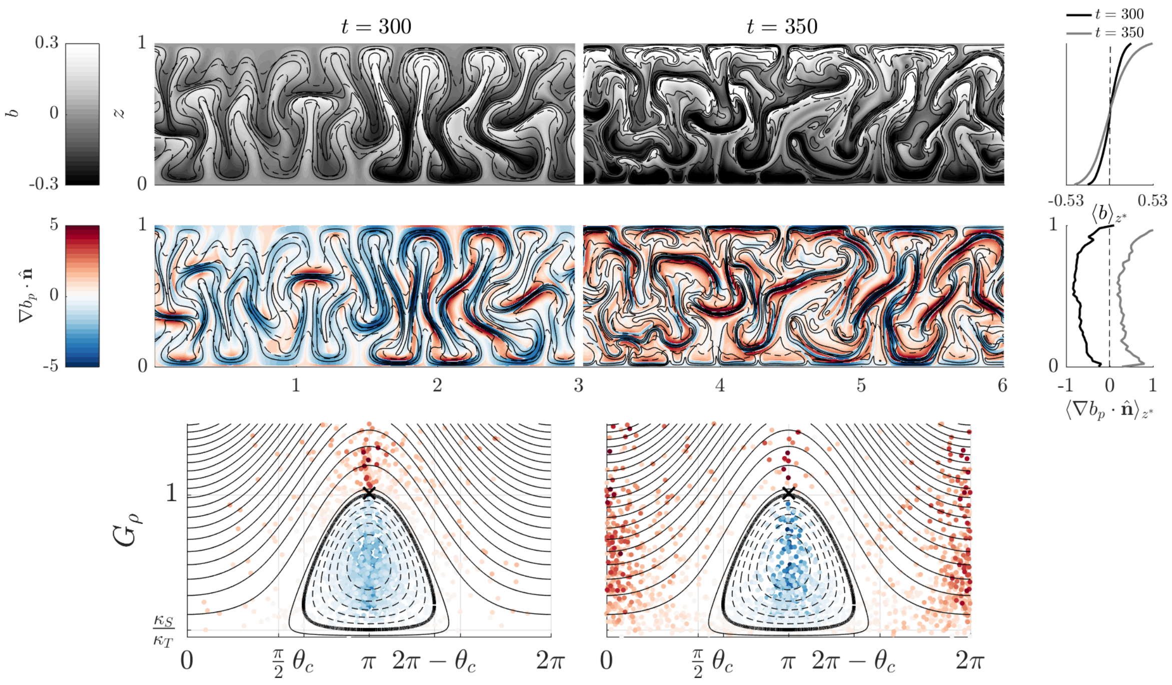

Fig. 2.2 Buoyancy (top row) and diapycnal buoyancy flux (middle and bottom rows) from a 2D simulation of salt fingering. Dashed and solid contours in the top two rows show temperature and salinity, respectively. The bottom panels are scatter plots of the diapycnal buoyancy flux (colored as in the middle row) in (G_ρ, θ) space. Contours of f (Eq. 2.9) in (G_ρ, θ) space are shown in black, with the contour of $f = 0$ in bold. The panels to the right of the top rows show the sorted height (z^*) averages of the panels and the initial profiles are indicated with a dashed line.

Figure 2.2 (upper row) shows the temperature, salinity, and buoyancy fields at two times. We only show half of the domain in x for each snapshot, however the patterns are qualitatively similar across the domain. At $t = 300$ (left panels) mature salt fingers are visible, and these fingers have broken down into a nonlinear chaotic flow at $t = 350$ (right panels). The panel in the upper right shows the sorted buoyancy profile, which exceeds the bounds of the initial profile - a situation possible in a double-diffusive fluid. The panels in the middle row show $\nabla b_p \cdot \hat{\boldsymbol{n}}$ at both times as well as the z^* averages. Between the two times shown, the z^*-average of the diapycnal buoyancy flux changes sign. This appears to be due to the breakdown in the salt fingers which preferentially increase salinity gradients.

A random subset of points are superimposed as a scatter plot of $\nabla b_p \cdot \hat{\boldsymbol{n}}(G_\rho, \theta)$ on top of f contours in the lower row of Fig. 2.2. The unperturbed initial conditions are denoted by a cross. As the salt fingers develop, local gradients in T and S increase. However, $|\nabla S|$ increases faster than $|\nabla T|$ and as a result G_ρ decreases. At $t = 300$, when salt fingers are present the scalar angle is primarily distributed around $\theta = \pi$, but enough points have $G_\rho < 1$ such that the diapycnal buoyancy flux is negative. At $t = 350$, after the salt fingers have broken down, the distribution of angles becomes bi-modal, with clustering of points near $\theta = \pi$ and $\theta = 0, 2\pi$. The magnitude of the diapycnal buoyancy flux is also maximum near these angles. At this time, the points with $\nabla b_p \cdot \hat{\boldsymbol{n}} > 0$ near $\theta = 0, 2\pi$ more than compensate for the points near $\theta = \pi$, resulting in a positive mean diapycnal buoyancy flux.

This simulation illustrates how salt fingers distort the temperature and salinity contours such that $|\nabla S|$ increases faster than $|\nabla T|$ leading to $G_\rho < 1$, and BPE is converted into APE on average. Once the flow becomes fully-developed, the T and S gradients align such that θ is close to 0,2π, and as a result the diapycnal buoyancy flux reverses sign and APE is converted into BPE on average. Although there is much left to explore, this example illustrates how the new criteria involving G_ρ and θ can be used to analyze the energetics of a double-diffusive flow.

2.3 Discussion and Conclusion

Here, we extended the energetic framework of Winters et al. (1995), Winters and D'Asaro (1996), and Nakamura (1996) to a double-diffusive fluid. In this framework, an up-gradient diapycnal buoyancy flux averaged in sorted height coordinates is equivalent to a negative buoyancy diffusivity for the sorted buoyancy profile and a transfer of energy from the background potential energy (BPE) to the available potential energy (APE).

We derived criteria for a transfer from BPE to APE in terms of the gradient ratio $G_\rho = \alpha|\nabla T|/(\beta|\nabla S|)$, the angle θ between ∇T and ∇S, and the ratio of molecular diffusivities, κ_T/κ_S (see Eqns. 2.9 and 2.26). We applied these critera to salt fingering, an important mixing mechanism within the ocean. The criteria could be applied to ocean observations or direct numerical simulations in other contexts. Finally, we derived an evolution equation for the sorted buoyancy profile.

A transfer of energy from BPE to APE is not possible in a single component fluid with a linear equation of state, where mixing is an 'irreversible' process. The finding that BPE can be converted into APE within double diffusion implies that some of the BPE can be made 'available' to drive fluid motion, and hence the interpretation of the APE from Winters et al. (1995) does not hold for a double-diffusive fluid. Nevertheless, the criteria in Eq. 2.26 provides a useful way to quantify the diffusive conversion of potential energy into a form that can be used to drive fluid motion in a double-diffusive fluid.

We formulated the results in this chapter assuming molecular diffusion for temperature and salinity. However, a similar analysis could be applied using turbulent diffusivities i.e. using the equations

$$\frac{DT}{Dt} = \nabla \cdot (K_T \nabla T), \quad \frac{DS}{Dt} = \nabla \cdot (K_S \nabla S), \tag{2.28}$$

where $K_T(\boldsymbol{x},t), K_S(\boldsymbol{x},t)$ are parameterized turbulent diffusivities. We can write the buoyancy flux as $\mathbf{P}_b == g\alpha K_T \nabla T - g\beta K_S \nabla S$, replacing the term ∇b_p with $\mathbf{P}_b$ throughout this chapter. Using this substitution, the energy budget equations remain the same, except that Φ_i can no longer be integrated and written as a surface term. The condition for an up-gradient buoyancy flux (i.e. $\nabla b_p \cdot \hat{\boldsymbol{n}} < 0$ in Eq. 2.9) remains the same, with a replacement of molecular diffusivities (κ_T, κ_S) with turbulent diffusivities (K_T, K_S). This allows our criterion in Eq. 2.9 to be applied to ocean models with parameterizations for K_T and K_S, provided that a linear equation of state remains a good approximation. Although we have focused on fluids where the density is a function of two components, the results hold for an arbitrary buoyancy flux potential, b_p. In particular this implies that our analysis could be extended to include more than two components.

2.4 Supplementary Material

This Supplementary Material is made to complement the above results. Note that the following material was not included in the 2020 publication. We will present the full forms of the energetic equations, and derive them in section 2.4.1. In section 2.4.2 we will illustrate the generality of our formulation to an arbitrary non-linear buoyancy flux, with specific application to multicomponent flows and cross diffusion equations. In section 2.4.3 we will present the formal definitions for the 'Component Potential Energy' of Smyth et al. (2005), and reformulate this idea using the framework presented in this chapter. This leads to some new expressions for the scalar diffusivities. In section 2.4.4 we will prove the result of Eq. 2.27.

2.4.1 Derivation of Energy Equations

In this section we will derive Eqns. 2.18-2.20. The derivation for Eq. 2.17 can be found in Bird and Stewart (1960). This work follows the derivation presented in Winters et al. (1995) but allows the buoyancy to be a function of two scalar fields (temperature and salinity). Taking the time derivative inside the integral within the definition of the potential energy

(Eq. 2.13), expanding $\partial b/\partial t$ and applying the chain rule gives

$$\frac{1}{\rho_{\text{ref}}}\frac{dE_{\text{PE}}}{dt} = -\int_{\mathcal{V}} z\frac{\partial b}{\partial t}d\mathcal{V} = \int_{\mathcal{V}} z\boldsymbol{u}\cdot\nabla b - z\nabla^2 b_p d\mathcal{V} \tag{2.29}$$

$$= -\int_{\mathcal{V}} b\nabla\cdot(z\boldsymbol{u})d\mathcal{V} + \int_{\mathcal{S}} bz\boldsymbol{u}\cdot\hat{\boldsymbol{n}}d\mathcal{S} + \int_{\mathcal{V}}\nabla b_p\cdot\nabla z d\mathcal{V} - \int_{\mathcal{S}} z\nabla b_p\cdot\hat{\boldsymbol{n}}d\mathcal{S}. \tag{2.30}$$

To simplify the volume integrals, we apply incompressibility to the first term, giving $\nabla\cdot(z\boldsymbol{u}) = w$. For the third term we note $\nabla b_p\cdot\nabla z = \partial b_p/\partial z$, and so we can integrate over the volume $\mathcal{V}$ giving,

$$\frac{1}{\rho_{\text{ref}}}\frac{dE_{\text{PE}}}{dt} = -\int_{\mathcal{S}}(bz\boldsymbol{u} - z\nabla b_p)\cdot\hat{\boldsymbol{n}}d\mathcal{S} - \int_{\mathcal{V}} bw d\mathcal{V} + (A\overline{b}_p)_{\text{top}} - (A\overline{b}_p)_{\text{bottom}}, \tag{2.31}$$

where the overbar indicates horizontal averaging and A is the cross sectional area of $\mathcal{V}$.

A similar process can be used to derive the budget for background potential energy. We first take the time derivative of E_{BPE} (Eq. 2.14),

$$\frac{1}{\rho_{\text{ref}}}\frac{dE_{\text{BPE}}}{dt} = -\int_{\mathcal{V}} z^*\frac{\partial b}{\partial t}d\mathcal{V} - \underbrace{\int_{\mathcal{V}} b\frac{\partial z^*}{\partial t}d\mathcal{V}}_{P_b^*} = \int_{\mathcal{V}}\left(z^*\boldsymbol{u}\cdot\nabla b - z^*\nabla^2 b_p\right)d\mathcal{V} - P_b^*. \tag{2.32}$$

The next step is to construct a potential for $z^*\nabla b$, which is possible since $\nabla\times(z^*\nabla b) = 0$. We can write this potential as $\psi = \int^b z^*(\hat{b})d\hat{b}$ since $\nabla\psi = z^*\nabla b$ using Leibniz's integral rule. Then applying Green's identity to the second term in Eq. 2.32, and noting that $\nabla z^* = \frac{dz^*}{db}\nabla b$, we obtain

$$\frac{1}{\rho_{\text{ref}}}\frac{dE_{\text{BPE}}}{dt} = \oint_{\mathcal{S}}(\psi\mathbf{u} - z^*\nabla b_p)\cdot\hat{\mathbf{n}}d\mathcal{S} + \int_{\mathcal{V}}\frac{dz^*}{db}(\nabla b_p\cdot\nabla b)d\mathcal{V} + P_b^*. \tag{2.33}$$

The equation for E_{APE} then follows by subtraction of the BPE from the PE.

We will now show that the term involving dz^*/dt in Eq. 2.32 (labeled P_b^*) vanishes. First we consider $\partial z^*/\partial t$ by taking the derivative of the definition of z^* given in Eq. 2.16. The definition of z^* is formulated as a volume integral over $\mathcal{V}'$, the total fixed volume in which the fluid sits, spanned by the Cartesian coordinates (x', y', z'). The prime superscript is applied to keep track of the correct variables in integration. We apply the chain rule to the derivative of the Heaviside function giving,

$$\begin{aligned}&\frac{\partial z^*}{\partial t}(x,y,z,t)\\&=\frac{1}{A}\int\int\int\delta(b(x,y,z,t)-b(x',y',z',t))\cdot\left(\frac{\partial b}{\partial t}(x,y,z,t)-\frac{\partial b}{\partial t}(x',y',z',t)\right)dx'dy'dz'.\end{aligned}\tag{2.34}$$

We now change variables within the integral,

$$\begin{aligned}\frac{\partial z^*}{\partial t}(b,p,q,t)&=\int\int\int\delta(b-b')\cdot\left(\frac{\partial b}{\partial t}(b,p,q,t)-\frac{\partial b}{\partial t}(b',p',q',t)\right)J(b',p',q')db'dp'dq'\\&=\frac{\partial b}{\partial t}(b,p,q,t)\int\int J(b,p',q')dp'dq'-\int\int\frac{\partial b}{\partial t}(b,p',q')J(b,p',q')dp'dq',\end{aligned}\tag{2.35}$$

where p' and q' are coordinates chosen such that $\nabla b'$, $\nabla p'$ and $\nabla q'$ are orthogonal. The coordinate b' is defined as $b(x',y',z',t)$ for b the buoyancy. To change integration variables, we multiply by the Jacobian $J(b,p,q)=|\partial(x,y,z)/\partial(b,p,q)|$. Note that the Jacobian will be singular if there is a three-dimensional subvolume within $\mathcal{V}$ where b is exactly constant. Here we will assume that this is not the case and will discuss this assumption further below.

If we now consider the full expression for P_b^*, we can again change variables,

$$\begin{aligned}P_b^*=\int_{\mathcal{V}}b\frac{\partial z^*}{\partial t}d\mathcal{V}&=\int\int\int b\frac{\partial z^*}{\partial t}(b,p,q,t)J(b,p,q)dbdpdq\\&=\int b\left(\int\int\frac{\partial z^*}{\partial t}(b,p,q,t)J(b,p,q)dpdq\right)db=\int b\mathcal{I}(b,t)db,\end{aligned}\tag{2.36}$$

for $\mathcal{I}$ referring to the term in brackets, here we have used the fact that b does not depend on p or q by construction. We will show that $\mathcal{I}=0$, and so $P_b^*=0$.

Considering $\mathcal{I}$ and applying the expression for $\partial z^*/\partial t$ from Eq. 2.35 gives,

$$
\begin{aligned}
\mathcal{I} &= \int\int \left(\frac{\partial b}{\partial t}(b,p,q,t) \int\int J(b,p',q')dp'dq' \right. \qquad (2.37)\\
&\left. - \int\int \frac{\partial b}{\partial t}(b,p',q',t) J(b,p',q')dp'dq' \right) dpdq \\
&= \int\int\int\int \frac{\partial b}{\partial t}(b,p,q,t) J(b,p,q) J(b,p',q')dp'dq'dpdq \\
&- \int\int\int\int \frac{\partial b}{\partial t}(b,p',q',t) J(b,p',q') J(b,p,q)dp'dq'dpdq \\
&= 0. \qquad (2.38)
\end{aligned}
$$

The final equality to zero can is due to the fact that the two terms in Eq. 2.37 are equivalent up to a relabelling of (p,q) to (p',q').

As mentioned above, we cannot fully describe the function $\frac{db}{dt}$ using coordinates (b,p,q) in the case where sub-volumes of our volume have constant buoyancy across them. In this case the function $z^*(\boldsymbol{x},t)$ is not uniquely defined for a given buoyancy field, so the framework as a whole breaks down to a certain extent. To illustrate this we will re-express the buoyancy time derivative,

$$
\frac{\partial b}{\partial t} = -\boldsymbol{u}\cdot\nabla b + g\alpha\kappa_T\nabla^2 T - g\beta\kappa_S\nabla^2 S. \qquad (2.39)
$$

The complication arises in the diffusive terms $\nabla^2 T$ and $\nabla^2 S$. Within a volume of constant buoyancy, the gradient $\nabla b = 0$, so the advective term $\boldsymbol{u}\cdot\nabla b$ is zero across the volume. However, $\nabla^2 T$ is not necessarily zero across this volume since it could exactly cancel $\nabla^2 S$ to result in $\nabla^2 b = 0$ (which must hold in a volume of constant buoyancy). Since we are scaling $\nabla^2 T$ and $\nabla^2 S$ by their diffusivities separately within the expression for $\frac{db}{dt}$, this situation would give rise to a non-zero rate of change of buoyancy within a volume of constant buoyancy. The assumption used here only breaks down if the buoyancy is *exactly* constant in a three-dimensional sub-volume. We will not consider this situation here since perfect compensation between T and S is highly unlikely. Considering the possible existence of a non-zero P_b^* term within the APE budget is left for future theoretical work.

We have shown that $P_b^* = 0$ for a fluid without any volumes of constant buoyancy. We note that the expression

$$
P_\Theta^* = \int_{\mathcal{V}} \Theta \frac{\partial z^*}{\partial t} d\mathcal{V}, \qquad (2.40)
$$

for scalar Θ is not zero by the above reasoning, so again, further work is needed to evaluate the term P_Θ^* within the component potential energy expression of section 2.4.3.

2.4.2 MultiComponent n-Diffusion and Cross Diffusion

Eqns. 2.18-2.20 describing the energy budget, derived in 2.4.1, are formulated for the incompressible Navier-Stokes equations with a linear equation of state coupled to two advection-diffusion equations with differing diffusivities. However both the equations defining the energetics and Eq. 2.27 that describes the evolution of density surfaces are derived only based on the relationship

$$\frac{Db}{Dt} = \nabla \cdot \boldsymbol{P}_b, \tag{2.41}$$

for some buoyancy flux $\boldsymbol{P}_b$. Therefore the same results hold for arbitrary $\boldsymbol{P}_b$. Note it is always possible to construct some $\boldsymbol{P}_b$ for an arbitrary non-linear equation of state, however the challenge is to write a locally meaningful expression. Eqns. 2.17-2.20 must be adapted by replacing ∇b_p with $\boldsymbol{P}_b$, and changing the expression for Φ_i to the more general

$$\Phi_i = \int_{\mathcal{V}} P_b^z \, d\mathcal{V}, \tag{2.42}$$

where $\boldsymbol{P}_b = (P_b^x, P_b^y, P_b^z)$. Now the condition for negative diffusivity of buoyancy becomes

$$\kappa_b < 0 \iff \boldsymbol{P}_b \cdot \nabla b < 0. \tag{2.43}$$

In particular this allows us to formulate our arguments in the exact same way for an arbitrary number of components. In the case where the buoyancy b depends on n diffusing components Θ_i with constant coefficients of expansion α_i, we may write

$$b = \sum_{i=1}^{n} \alpha_i g \Theta_i. \tag{2.44}$$

Coupled with an n-diffusive advection equation for constant scalar molecular diffusivity κ_i,

$$\frac{D\Theta_i}{Dt} = \kappa_i \nabla^2 \Theta_i, \tag{2.45}$$

the relevant form for b_p is then

$$b_p = \sum_{i=1}^{n} \kappa_i \alpha_i g \Theta_i. \tag{2.46}$$

To gain an intuition for the comparison to double diffusion, we can expand the diapycnal flux

$$\varphi_d^{\mathrm{nD}} = \frac{db}{dz^*}\left(\sum_{i=0}^{n}\alpha_i^2\kappa_i|\nabla\Theta_i|^2 + \sum_{i\neq j}\alpha_i\alpha_j(\kappa_i+\kappa_j)\nabla\Theta_i\cdot\nabla\Theta_j\right). \tag{2.47}$$

Note we now have to consider the cross gradients between each pair of scalars, but not the influence of three-way cross gradients. This form does not permit a simple reduction to a gradient ratio form.

We can also consider the case of cross diffusion terms (as in McDougall and Turner (1982)), which extends Eq. 2.45 to the form

$$\frac{D\Theta_i}{Dt} = \sum_{j=1}^{n}\kappa_{ij}\nabla^2\Theta_j, \tag{2.48}$$

where κ_{ij} refers to the cross-diffusivity of the scalar Θ_j effecting the scalar Θ_i ($\kappa_{ii} = \kappa_i$ within this notation).

Eq. 2.48 gives a buoyancy flux potential of

$$b_p = \sum_{i=1}^{n}\sum_{j=1}^{n}\alpha_i\kappa_{ij}\Theta_j. \tag{2.49}$$

In the case of double diffusion with cross-diffusion effects, the buoyancy flux potential becomes

$$b_p = (\alpha\kappa_T - \beta\kappa_{ST})T + (\alpha\kappa_{TS} - \beta\kappa_S)S, \tag{2.50}$$

which leads to the same form for φ_d

$$\varphi_d = \frac{dz^*}{db}\nabla b_p\cdot\nabla b = g^2\frac{dz^*}{db}|\nabla S|^2 f(G_\rho,\theta), \tag{2.51}$$

as in Eq. 2.21, with an altered characteristic polynomial $f(G_\rho,\theta)$. The form for f is now

$$f = \left(\kappa_T - \frac{\beta}{\alpha}\kappa_{ST}\right)G_\rho^2 + \left(\kappa_S + \kappa_T - \left(\frac{\alpha}{\beta}\kappa_{TS} + \frac{\beta}{\alpha}\kappa_{ST}\right)\right)G_\rho\cos\theta + \left(\kappa_S - \frac{\alpha}{\beta}\kappa_{TS}\right), \tag{2.52}$$

which when plotted for set values of κ_T, κ_S, κ_{TS} and κ_{ST} gives conditions on G_ρ and θ for negative diffusion to occur.

2.4.3 Thermal and Haline Potential Energies

A framework that has been used in the past by Smyth et al. (2005), is that of partitioning the potential energy into thermal and haline contributions as follows,

$$\begin{aligned} E_{\mathrm{PE}} &= -\int_{\mathcal{V}} bz\,d\mathcal{V} = -g\int_{\mathcal{V}} (\alpha T - \beta S) z\,d\mathcal{V} \\ &= -\alpha g \int_{\mathcal{V}} Tz\,d\mathcal{V} + \beta g \int_{\mathcal{V}} Sz\,d\mathcal{V} = E^{T}_{\mathrm{PE}} + E^{S}_{\mathrm{PE}}. \end{aligned} \tag{2.53}$$

Smyth et al. (2005) then formulated the background component potential energies as

$$\tilde{E}^{T}_{\mathrm{BPE}} = -\alpha \int_{\mathcal{V}} T z^{*}_{T}\,d\mathcal{V}, \tag{2.54}$$

$$\tilde{E}^{S}_{\mathrm{BPE}} = -\beta \int_{\mathcal{V}} S z^{*}_{S}\,d\mathcal{V}, \tag{2.55}$$

where

$$z^{*}_{\Theta} = \frac{1}{A}\int_{\mathcal{V}'} H(\Theta(\boldsymbol{x},t) - \Theta(\boldsymbol{x}',t))\,d\mathcal{V}', \tag{2.56}$$

is the sorted component coordinate for Θ referring to either T or S. The APE was formulated as $\tilde{E}^{\Theta}_{\mathrm{APE}} = E^{\Theta}_{\mathrm{PE}} - \tilde{E}^{\Theta}_{\mathrm{BPE}}$.

This formulation is useful in that it allows the thermal and haline terms to be clearly separated, and the rate of change equations remain the same as in the Winters '95 derivation, e.g. for the APE,

$$\begin{aligned} \frac{d\tilde{E}^{\Theta}_{\mathrm{APE}}}{dt} = \oint_{\mathcal{S}} (\Theta z - \psi_{\Theta})\boldsymbol{u}\cdot\hat{\boldsymbol{n}}\,d\mathcal{S} + \kappa_{\Theta}\oint_{\mathcal{S}} (z^{*}_{\Theta} - z)\nabla\Theta\cdot\hat{\boldsymbol{n}}\,d\mathcal{S} - \int_{\mathcal{V}} \Theta w\,d\mathcal{V} \\ + \kappa_{\Theta} A(\overline{\Theta}_{\mathrm{top}} - \overline{\Theta}_{\mathrm{bottom}}) - \kappa_{\Theta}\int_{\mathcal{V}} \frac{dz^{*}_{\Theta}}{d\Theta}|\nabla\Theta|^{2}\,d\mathcal{V}, \end{aligned} \tag{2.57}$$

The subscript Θ demarks an evaluation of the quantity using Θ instead of b i.e. ψ_{Θ} refers to the Casimir with respect to the scalar Θ.

This framework allows for quantification of irreversible mixing for each scalar, however the Background Potential Energies of the two scalars clearly interact, and without a relationship between the buoyancy coordinate z^{*} and the scalar coordinates z^{*}_{Θ}, it is not clear how the Smyth et al. (2005) formulation relates to the potential energy formulation discussed within this chapter.

Within the framework of this chapter (i.e. using buoyancy coordinates z^{*}), we can similarly split the APE and BPE into thermal and haline components by splitting the buoyancy term, as with the potential energy, e.g.

$$\begin{aligned} E_{\mathrm{BPE}} &= -\int_{\mathcal{V}} b z^* d\mathcal{V} = -g \int_{\mathcal{V}} (\alpha T - \beta S) z^* d\mathcal{V} \\ &= -\alpha g \int_{\mathcal{V}} T z^* d\mathcal{V} + \beta g \int_{\mathcal{V}} S z^* d\mathcal{V} = E^T_{\mathrm{BPE}} + E^S_{\mathrm{BPE}}. \end{aligned} \tag{2.58}$$

If we then define our component APE as $E^{\Theta}_{\mathrm{APE}} = E^{\Theta}_{\mathrm{PE}} - E^{\Theta}_{\mathrm{BPE}}$, it leads to the rate of change equation for the contribution of Θ to the APE,

$$\begin{aligned} \frac{dE^{\Theta}_{\mathrm{APE}}}{dt} = & \oint_{\mathcal{S}} \Theta(z - z^*)\boldsymbol{u} \cdot \hat{\boldsymbol{n}} d\mathcal{S} + \underbrace{\int_{\mathcal{V}} \Theta \frac{dz^*}{dt} d\mathcal{V}}_{P^*_{\Theta}} + \kappa_{\Theta} \oint_{\mathcal{S}} (z^* - z)\nabla\Theta \cdot \hat{\boldsymbol{n}} d\mathcal{S} - \int_{\mathcal{V}} \Theta w \\ & \underbrace{+ \Theta \boldsymbol{u} \cdot \nabla b \frac{dz^*}{db}}_{\varphi^{adv}_{\Theta}} d\mathcal{V} + \kappa_{\Theta} A(\overline{\Theta}_{\mathrm{top}} - \overline{\Theta}_{\mathrm{bottom}}) - \kappa_{\Theta} \int_{\mathcal{V}} \frac{dz^*}{db} \nabla\Theta \cdot \nabla b d\mathcal{V}. \end{aligned} \tag{2.59}$$

The key differences between this expression and that in Eq. 2.20 are in the new terms φ^{adv}_{Θ}, which is an advective diapycnal scalar flux between the available and background potential energies, and P^*_{Θ}, a buoyancy flux transfer between BPE and APE due to the changing coordinate velocity $w^* = dz^*/dt$. The term P^*_{Θ} may be non-zero if there is an isopycnal flux of Θ (i.e. Θ not constant along isopycnals). Both these new terms P^*_{Θ} and φ^{adv}_{Θ} cancel, such that $P^*_T - P^*_S = 0$ and $\varphi^{adv}_T + \varphi^{adv}_S = 0$. This is clear from comparing to Eqns. 2.18-2.20.

Often within the literature, effective scalar diffusivities are found to be negative. This is not possible when considering the diascalar formation, as the effective diascalar scalar diffusivity is always positive. However considering the effective diapycnal scalar diffusivity, the negative value is possible. Note that in this instance we also require an effective isopycnal scalar diffusivity to fully describe the scalar motion.

We can write our diapycnal scalar flux in a gradient ratio form,

$$\begin{aligned} \varphi^T_d &= \kappa_T \frac{dz^*}{db} \nabla T \cdot \nabla b = \frac{g\kappa_T}{\alpha} \beta^2 |\nabla S|^2 \frac{dz^*}{db} (G^2_{\rho} + G_{\rho} \cos\theta) \\ \varphi^S_d &= \kappa_S \frac{dz^*}{db} \nabla S \cdot \nabla b = g\kappa_S \beta |\nabla S|^2 \frac{dz^*}{db} (G_{\rho} \cos\theta + 1), \end{aligned}$$

and we find that for the thermal diapycnal flux, negative values may exist for any angles between $\pi/2$ and $3\pi/2$, provided that $\theta < \cos^{-1}(-G_{\rho})$. Equivalently for the haline diapycnal flux $\theta < \cos^{-1}(-G^{-1}_{\rho})$.

The effective diapycnal diffusivity for each scalar can be written

$$K_d^\Theta = \frac{\varphi_d^\Theta}{\frac{d\Theta}{dz^*}}.$$

So we can derive an expression for the ratio of effective diapycnal diffusivities

$$\frac{K_d^S}{K_d^T} = \frac{\kappa_S}{\kappa_T} R_\rho^* \frac{G_\rho^{-1} + \cos\theta}{G_\rho + \cos\theta}, \tag{2.60}$$

where

$$R_\rho^* = \frac{\alpha \frac{dT}{dz^*}}{\beta \frac{dS}{dz^*}}$$

is the density ratio in z^* coordinates. Note that generally this is not the same as the gradient ratio G_ρ, as the gradient ratio contains the effect of isopycnal gradients in T and S, and R_ρ^* does not.

If we consider $\cos\theta = \pm 1$, then we can further simplify Eq. 2.60 to

$$\frac{K_d^S}{K_d^T} = \frac{\pm\kappa_S R_\rho^*}{\kappa_T G_\rho}. \tag{2.61}$$

In the horizontally homogeneous limit this gives a constant flux ratio equal to the diffusivity ratio κ_S/κ_T. This constant flux ratio is similar to the Linden and Shirtcliffe (1978) result in which they find a constant flux ratio for a double-diffusive interface. Further work is needed to relate this result to previous parameterisations for the canonical forms of double-diffusive convection.

2.4.4 Rate of Change of Buoyancy

Within this section we will derive the equation for the rate of change of buoyancy within sorted coordinates, presented above. Applying the chain rule and averaging over surfaces of constant z^*, we get

$$\frac{\partial b}{\partial t}(z^*, t) = \left\langle \frac{\partial b}{\partial t}(\boldsymbol{x}, t) \right\rangle_{z^*} + \frac{db}{dz^*} \left\langle \frac{dz^*}{dt} \right\rangle_{z^*}. \tag{2.62}$$

Using the same reasoning as in section 2.4.1 we can see that

$$\left\langle \frac{dz^*}{dt} \right\rangle_{z^*} = 0, \tag{2.63}$$

so the second term disappears. We now follow Winters and D'Asaro (1996) and search for a function $\mathcal{F}$ such that

$$\frac{\partial b}{\partial t}(z^*,t) = \frac{\partial \mathcal{F}}{\partial z^*}. \tag{2.64}$$

Integrating this equation gives

$$\mathcal{F}(z^*,t) = \int_0^{z^*} \left\langle \frac{db}{dt} \right\rangle_{\tilde{z}^*} d\tilde{z}^*. \tag{2.65}$$

We now consider two surfaces of constant buoyancy, $z^* = (z_0, z_1)$ respectively, approaching one another. In the limit as they approach we may write

$$\mathcal{F}(z^*,t) = \lim_{z_0,z_1 \to z^*} \left(\frac{A}{\mathcal{S}} \int_{z_0}^{z_1} \mathcal{F}(z^*,t) dz^* \right), \tag{2.66}$$

where A is the surface area, and $\mathcal{S}$ is the volume bounded by the two surfaces. Defining $\overline{\mathcal{F}}$ as the term in brackets, we integrate by parts,

$$\begin{aligned}
\overline{\mathcal{F}} &= \underbrace{\frac{A}{\mathcal{S}}(z_1\mathcal{F}(z_1,t) - z_0\mathcal{F}(z_0,t))}_{I_1} - \frac{A}{\mathcal{S}} \int_{z_0}^{z_1} z^* \frac{\partial \mathcal{F}}{dz^*} dz^* \\
&= I_1 + \underbrace{\frac{A}{\mathcal{S}} \int_{z_0}^{z_1} z^* \langle \boldsymbol{u} \cdot \nabla b \rangle_{z^*} dz^*}_{I_2} - \frac{A}{\mathcal{S}} \int_{z_0}^{z_1} z^* \langle \nabla^2 b_p \rangle_{z^*} dz^* \\
&= I_1 + I_2 - \underbrace{\frac{A}{\mathcal{S}} \int_{z_0}^{z_1} \langle \nabla \cdot (z^* \nabla b_p) \rangle_{z^*} dz^*}_{I_3} + \underbrace{\frac{A}{\mathcal{S}} \int_{z_0}^{z_1} \langle \nabla z^* \cdot \nabla b_p \rangle_{z^*} dz^*}_{I_4}
\end{aligned}$$

In the limit as the two surfaces approach each other, the integrals tend to volume integrals

$$\begin{aligned}
&\lim_{z_0,z_1 \to z^*} \left(\frac{A}{\mathcal{S}} \int_{z_0}^{z_1} \langle f(\boldsymbol{x},t) \rangle_{z^*} dz^* \right) \\
&\qquad = \lim_{z_0,z_1 \to z^*} \left(\frac{A}{\mathcal{S}} \int_{z_0}^{z_1} \frac{1}{A} \int_{S(z^*)} f(\boldsymbol{x},t) dS dz^* \right) = \lim_{\mathcal{S} \to 0} \frac{1}{\mathcal{S}} \int_{\mathcal{S}} f(\boldsymbol{x},t) d\mathcal{V}.
\end{aligned}$$

For I_1, the function $f \to (z_1 - z_0)\frac{db}{dt}$, and as $(z_1 - z_0)/\mathcal{S} = A$, the integral tends to zero faster than the prefactor and so in the limit $I_1 = 0$.

Integrating I_2 by parts, and noting that $\nabla\times(z^*\nabla b)=0$, i.e. $z^*\nabla b$ is a conservative vector field and so $\nabla\psi=z^*\nabla b$ for some ψ, gives

$$I_2=\int_{\mathcal{S}}\boldsymbol{u}\cdot(\nabla\psi)d\mathcal{V}=-\int_{\mathcal{S}}\psi\nabla\cdot\boldsymbol{u}d\mathcal{V}+\int_{\delta\mathcal{S}}\psi\boldsymbol{u}\cdot\hat{\boldsymbol{n}}d\delta\mathcal{S}. \tag{2.67}$$

By incompressibility $\nabla\cdot\boldsymbol{u}=0$, so we are left with the integral over the surface of the volume bounded by the two isopycnals. As the normal vector $\hat{\boldsymbol{n}}$ is constructed to be pointing outwards, this term must cancel as the isopycnals approach one another. Similarly, I_3 can be written as a surface integral using the divergence theorem,

$$I_3=\int_{\mathcal{S}}\nabla\cdot(z^*\nabla b_p)d\mathcal{V}=\int_{\delta\mathcal{S}}z^*\nabla b_p\cdot\hat{\boldsymbol{n}}d\delta\mathcal{S}, \tag{2.68}$$

so I_3 will also tend to zero.

The integral I_4, however, does not tend to zero and so we may write,

$$\lim_{z_0,z_1\to z^*}\frac{A}{\mathcal{S}}\int_{z_0}^{z_1}\langle\nabla z^*\cdot\nabla b_p\rangle_{z^*}dz^*=\langle\nabla z^*\cdot\nabla b_p\rangle_{z^*}=\left\langle\frac{dz^*}{db}\nabla b_p\cdot\nabla b\right\rangle_{z^*}=\varphi_d \tag{2.69}$$

2.5 Recent Developments

Since this article was published, two relevant papers have been published which we will briefly discuss. Firstly the energetics of double diffusion were revisited in Ma and Peltier (2021). In Ma and Peltier (2021) they proposed an alternative definition of background potential energy and available potential energy, to avoid the flux from BPE to APE in our formulation. Specifically, they used equivalent definitions to Smyth et al. (2005) for the component potential energies by sorting the temperature and salinity fields separately. They then combined the two component potential energies into one ‘background potential energy’ and used that to define ‘available potential energy’. As mentioned above, we recognise the utility in defining component potential energies in this way, namely that irreversible mixing can be defined. This is in keeping with the philosophy of Tailleux (2013) who centres thermodynamics in his description of APE. However, when sorting temperature and salinity separately, the limit of equal diffusivities $\kappa_T=\kappa_S$ does not recapture the single-component definition of APE. Their APE does not necessarily represent perturbations to the potential energy, rather it represents perturbations to the temperature and salinity fields which may be compensated in their contribution to density. In the following chapters we will demonstrate the utility of our formulation, specifically by making the assumption that $dE_{\text{APE}}/dt=0$.

The second relevant publication is Penney et al. (2020), in which they develop an expression for the dynamics of a passive tracer Θ within the sorted coordinate system based on the buoyancy b. They use this expression to analyse the mixing of a passive tracer within simulations of Kelvin-Helmholtz instability. Their expression is similar to our equation 2.27, however distinct in that they are considering the evolution of a passive field within sorted coordinates rather than a double-diffusive field explicitly. Applying the work of Penney et al. (2020) to analyse the evolution of temperature and salinity within sorted coordinates could provide interesting insight into double-diffusive dynamics.

Chapter 3

Numerical simulations of melt-driven double-diffusive fluxes in a turbulent boundary layer beneath an ice shelf

This chapter was published in *Journal of Physical Oceanography* in 2021 with coauthors Catherine Vreugdenhil, Paul Holland and John Taylor. Some minor edits have been made from the published version including an additional section in the supplementary material giving a short derivation of the results from Martin and Kauffman (1977) as well as a short note about updates in the field since our publication. I gratefully acknowledge helpful comments from two anonymous reviewers and comments and feedback from the Ice Shelf-Ocean Boundary Layer (ISOBL) project team.

3.1 Introduction

Ice shelves are the floating extensions of ice sheets, found around Antarctica and Greenland. Regional ocean models of the cavities beneath them are often used to help predict the response of ice shelves to various oceanographic forcings (Holland et al., 2010). To calculate the response of the ice shelf to a given ocean state, the turbulent boundary layer in the upper tens of metres must be parameterised. The parameterisation commonly used in ice shelf cavity models was developed based on observations under sea ice (McPhee et al., 1987), and then adapted for the under ice-shelf environment (Holland and Jenkins, 1999). Observations necessary for parameterisation validation were previously minimal. However, ice shelf borehole measurements have recently increased in quantity and quality (Davis and Nicholls, 2019, Kimura et al., 2015, Jenkins et al., 2010, Begeman et al., 2018).

Davis and Nicholls (2019) analysed turbulence measurements made beneath the Larsen C Ice Shelf. Temperatures within the cold-water cavity were measured as $-2.01 \pm 0.05°C$ at about 2.6 m below the ice. Davis and Nicholls (2019) found their observations were consistent with the Holland and Jenkins (1999) parameterisation, which assumes a shear-driven boundary layer, where stratification due to basal melting has a minimal effect.

The effects of stratification on turbulence within the ocean boundary layer beneath an ice shelf were examined using a Large Eddy Simulations (LES) in Vreugdenhil and Taylor (2019). They considered a steady flow past a dynamically melting boundary and found that, under strongly stratified conditions, shear-driven turbulence was reduced and even damped out. The parameterisation of McPhee et al. (1987) is based on similar arguments, where stratification acts to damp turbulence. Holland and Jenkins (1999) argued that stratification effects in the McPhee et al. (1987) parameterisation have a minimal impact on cold cavity ice shelves, and so need not be included within regional ice cavity models. However, the work of Vreugdenhil and Taylor (2019) suggested that stratification effects may be important in cold cavity ice shelves, especially if the shear turbulence is weak within the boundary layer. Many ice shelf cavities, including those that are losing ice mass at the fastest rates (Rignot et al., 2013), are warm water cavities. Here the McPhee et al. (1987) parameterisation, and LES (Vreugdenhil and Taylor, 2019), suggest stratification plays a dominant role in the transport of heat and salt through the boundary layer.

Certain observations cannot be explained by the damping effect of stratification. Borehole observations made on the George VI Ice Shelf (Venables et al., 2014, Kimura et al., 2015), found layers (or ‘thermohaline staircases’) in the temperature and salinity profiles adjacent to the ice. Although layers can form in fluids with a single stratifying component (Phillips, 1972), Kimura et al. (2015) argued that the staircases observed beneath George VI Ice Shelf are associated with the difference between the molecular diffusivities of temperature and salinity. Thermohaline staircases can form when one scalar is unstably stratified whilst the other is stably stratified (Radko, 2013), and here the melting ice provides a stable salinity profile and an unstable temperature profile. This configuration is called the ‘diffusive convection favourable’ regime (when the unstable stratifying element is salinity, the regime is called ‘salt fingering favourable’). Staircases are a common signature of convection triggered by the difference in diffusivities, however double-diffusive convection may occur without staircase formation. In double-diffusive convection, on average turbulence is generated through the release of potential energy, despite the density increasing with depth. The parameterisation of McPhee et al. (1987) assumes that a diffusive buoyancy flux beneath a melting ice base creates a stratification that damps turbulence, so the parameterisation will not apply well if turbulent production is dominated by double-diffusive convection. The Kimura et al. (2015) hypothesis was that double-diffusive convection is forced at the ice base, leading to the signature staircases below, and we are primarily concerned with investigating this mechanism of 'melt-driven convection'.

Kimura et al. (2015) compared the under-ice shelf regime to the laboratory experiment of Martin and Kauffman (1977). In this experiment a block of ice was floated atop a box of salt-water (0 °C and 37.6 ppt salinity). Convection was observed throughout the box that persisted for the length of the experiment (two days). The diffusivity of heat is two orders of magnitude larger than the diffusivity of salt, so a diffusing thermal sublayer will thicken faster than a salt sublayer. In the Martin and Kauffman (1977) experiment, the density was dominated by the temperature profile beneath the salt boundary layer, causing a peak in density that triggered convection. The velocity field was not examined in this experiment, however a numerical study of a melting boundary was conducted by Keitzl et al. (2016), where similar convection was observed. The Keitzl et al. (2016) simulations showed convective plumes descending from a region immediately below the salt boundary layer. The far-field temperatures were larger in the simulations of Keitzl et al. (2016), varying between 10 °C and 24 °C. Martin and Kauffman (1977) did not observe staircase formation, however their experimental set-up had no ambient stratification. Turner (1968) observed the progressive formation of staircases when heating a stable salt stratification from below, suggesting staircases may form in a stable stratification when double-diffusive convection is forced by a destabilising flux at the boundary. Kimura et al. (2015) argued that diffusive boundary fluxes as in Martin and Kauffman (1977) and a stable stratification as in Turner (1968) led to the staircases observed beneath George VI Ice Shelf. Following Martin and Kauffman (1977) we will not consider staircase formation, and instead we will seek to understand the response of ice-triggered convection to turbulent mixing.

The experiments and observations described above suggest that double diffusion is potentially important beneath ice shelves. However, it is not clear how double-diffusive convection will interact with turbulence occurring within an ice shelf-ocean boundary layer. In steady state it can be shown (using the three equation model in Section 3.2.2) that double-diffusive convection implies a fresh salinity sublayer (below ~ 4 ppt), which was not observed by Kimura et al. (2015) or Martin and Kauffman (1977), implying the observed double-diffusive convection was transient. Nevertheless, the convection in the experiment of Martin and Kauffman (1977) was long lived, with a salinity sublayer growing on the diffusive time scale for salinity, thickening by 1 cm in around 20 hrs. Gade (1979) noted that by agitating crushed ice within salty water, one could inhibit double-diffusive convection, which otherwise caused the melt water to sink. Gade (1979) argued that convection was inhibited by the low-salinity boundary layer being mixed into the interior, where it had a dominant contribution to the density. The inhibition of double-diffusive convection by turbulence has also been observed in the ocean (Shibley and Timmermans, 2019, Guthrie et al., 2013) and in laboratory experiments (Crapper, 1976).

Although the observations from George IV Ice Shelf reported by Kimura et al. (2015) showed clear evidence for double-diffusive convection, Venables et al. (2014) noted that some turbulent shear profiles taken beneath George VI Ice Shelf showed low dissipation values concurrent with double-diffusive staircases, while others showed no staircases and high dissipation values. One hypothesis is that double-diffusive convection is suppressed when turbulence exceeds a critical threshold. Inspired by these observations, we will test this hypothesis and investigate double-diffusive convection forced by heat and salt fluxes at the ice boundary in the presence of ambient turbulence.

To investigate double-diffusion within an adjusting ice shelf-ocean boundary layer, we use idealised, high-resolution numerical simulations, inspired by field observations. We force ambient turbulence to reach a target dissipation rate similar to measurements beneath George VI Ice Shelf (Venables et al., 2014), then consider the evolution of a dynamically melting boundary under a homogeneous initial condition for temperature and salinity. We vary the far-field temperature and forced dissipation rate across simulations as controlling parameters. The initial condition of uniform scalars is not designed to capture staircase formation, and the focus instead is the interaction between turbulence and double diffusion near the ice base.

Double-diffusive convection will be distinguished from 'stratified turbulence' in this paper using the turbulent vertical buoyancy flux, defined as $\langle w'b' \rangle$, i.e. the correlation between the fluctuating vertical velocity w', where angle brackets denote a horizontal average and primes are departures from this average, and the fluctuating buoyancy $b' = g\alpha T' - g\beta S'$ for g the gravitational acceleration, T the temperature, S the salinity and (α, β) constant coefficients of thermal expansion and haline contraction, respectively. The buoyancy flux determines the energetic contribution of the buoyancy field (through potential energy) to the turbulent kinetic energy (TKE) as described in Section 3.2.3. Negative values imply that the buoyancy flux acts as a sink of TKE, and positive values imply the buoyancy flux increases the TKE. If double-diffusive convection is the dominant mechanism we expect a positive buoyancy flux ($\langle w'b' \rangle > 0$), otherwise stratification will dampen turbulence on average ($\langle w'b' \rangle < 0$). However, turbulent buoyancy flux is a noisy measure of energy exchange, that may locally change sign, as it depends on advection. This motivates dividing potential energy into two parts; an 'available' potential energy (APE), that exchanges energy back and forth with the TKE via $\langle w'b' \rangle$ (advection); and a 'background' potential energy (BPE) that exchanges energy with the APE based on the mixing of the buoyancy field (diffusion) (Winters et al., 1995).

For single component fluids the diffusive energy exchange between APE and BPE is one way, i.e. mixing always acts to increase BPE (Winters et al., 1995). The distinction between APE and BPE is complicated for double-diffusive fluids, as buoyancy gradients can sharpen due to diffusion (Merryfield, 2000). However, in Chapter 2, we applied the APE/BPE framework to double-diffusion, where now diffusion can cause 'un-mixing' i.e. a release of BPE into APE. In Chapter 2, we obtained a simplified criterion to identify transfers of energy from BPE to APE (Section 3.4.1), and here we will apply this criterion to quantify the importance of double diffusion in our simulations.

Section 3.2 outlines our simulation set up, focusing on the simulation geometry, forcing and numerical details of the grid and its relation to the turbulent length scales. In Section 3.3 we discuss the simulation evolution, considering differences between convective and stable regimes. Then in Section 3.4 we consider the diapycnal flux in our simulations. First we give a review of the criterion introduced in Chapter 2, then we show that convection in our simulations is caused by a region of negative diapycnal buoyancy flux near the ice base and it is well described using the framework in Chapter 2. The region is also well described by the density ratio and buoyancy Reynolds number, which we formulate into a criterion for the inhibition of double-diffusive convection by externally-forced turbulence. Finally, in Section 3.5 we apply our criterion to the diffusive solution, providing a point of comparison between our simulations, those of Vreugdenhil and Taylor (2019) and the observations. Concluding remarks are offered in Section 3.6.

3.2 Methods

The ocean boundary layer beneath a melting ice shelf is simulated in a rectangular box domain (Figure 3.1). We use periodic boundary conditions in the horizontal x, y directions and impenetrable conditions in the vertical z direction. Dynamic melting boundary conditions are imposed on the temperature and salinity fields locally across the top surface of the domain, along with a no-slip velocity condition. A no-flux, free slip condition is applied at the base. The simulations are initialised with a homogeneous temperature and salinity, which are restored to initial values below an ‘observation’ region of 2.6 m depth. Isotropic turbulence is forced at length scales larger than the observation region, using a methodology taken from Wang et al. (1996), applied as a forcing term discussed in Section 3.2.1. The mechanical forcing is designed to achieve a prescribed rate of turbulent kinetic energy dissipation, with values chosen similar to George VI Ice Shelf observations. The mechanically forced turbulence is intended to represent processes missing from the simulations, such as shear-driven turbulence, internal wave breaking, or interior double-diffusive convection.

3.2.1 Governing Equations

Our simulations solve the incompressible, non-hydrostatic, Boussinesq Navier-Stokes equations, with terms to apply mechanical velocity forcing and far-field scalar relaxation. These equations are

$$\frac{D\boldsymbol{u}}{Dt} = -\frac{1}{\rho_0}\nabla p + \nu\nabla^2\boldsymbol{u} - \frac{\Delta\rho}{\rho_0}g\boldsymbol{k} + \underbrace{\frac{\varepsilon_0\boldsymbol{u}}{\langle\boldsymbol{u}\cdot\boldsymbol{u}\rangle}}_{\text{Mechanical Forcing}}, \tag{3.1}$$

$$\nabla\cdot\boldsymbol{u} = 0, \tag{3.2}$$

$$\frac{DT}{Dt} = \kappa_T\nabla^2 T - \underbrace{\frac{1}{\tau_0}(\langle T\rangle - T_\infty)r(z)}_{\text{Far-Field Relaxation}}, \tag{3.3}$$

$$\frac{DS}{Dt} = \kappa_S\nabla^2 S - \overbrace{\frac{1}{\tau_0}(\langle S\rangle - S_\infty)r(z)}, \tag{3.4}$$

$$\frac{\Delta\rho}{\rho_0} = -\alpha(T - T_0) + \beta(S - S_0). \tag{3.5}$$

where $\frac{D}{Dt} = \frac{\partial}{\partial t} + \boldsymbol{u}\cdot\nabla$ is the material derivative for $\boldsymbol{u} = (u, v, w)$ the 3D velocity field with respect to position vector $\boldsymbol{x} = (x, y, z)$ and p pressure. The density is ρ, with $\rho_0 = 1000$ kgm^{-3} the reference density and $\Delta\rho = \rho - \rho_0$. We use $\nu = 1.8\times10^{-6}$ m^{2}s^{-1} as kinematic viscosity, and $g = 9.81$ ms^{-2} as gravitational acceleration. T is the temperature field in °C, with T_0 and T_∞ the reference and far-field temperatures respectively. Likewise S is the salinity field in parts per thousand, with S_0 and S_∞ the reference and far-field salinities. The molecular diffusivities are $\kappa_T = 1.3\times10^{-7}$ m^{2}s^{-1} for temperature and $\kappa_S = 7.4\times10^{-10}$ m^{2}s^{-1} for salt. Finally, the constants $(\alpha, \beta) = (3.87\times10^{-5}\ (^\circ\text{C})^{-1},\ 7.86\times10^{-4}\ (\text{ppt})^{-1})$

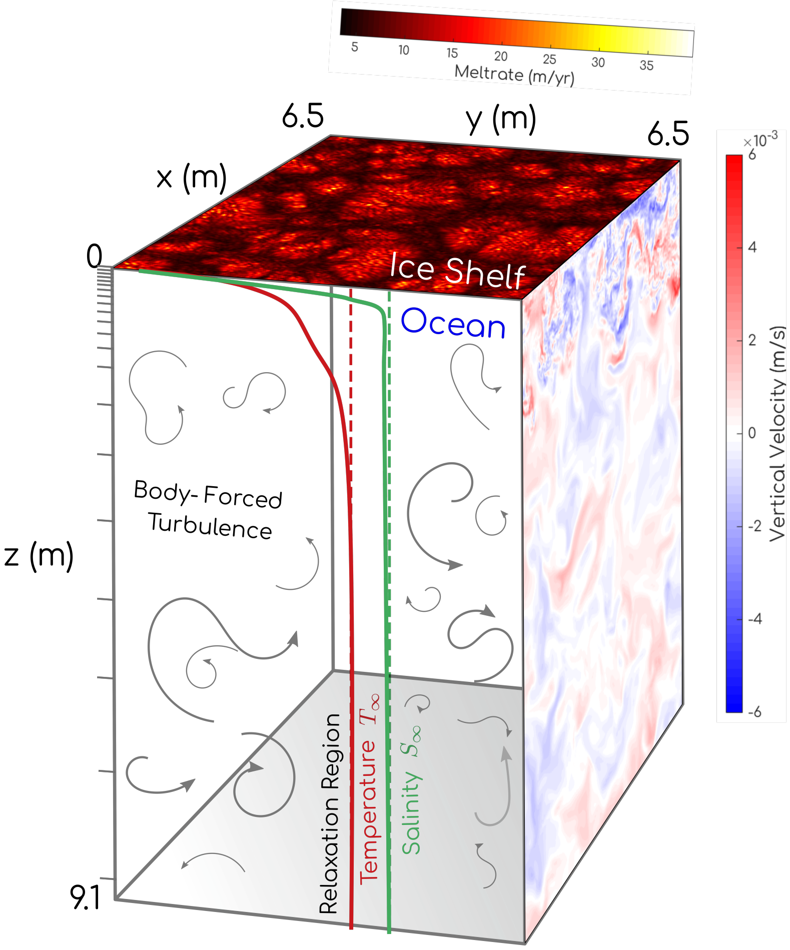
5
10
15
20
25
30
35
Meltrate (m/yr)
6.5
y (m)
6.5
x (m)
0
Ice Shelf
Ocean
Body- Forced Turbulence
z (m)
9.1
Relaxation Region
Temperature T_∞
Salinity S_∞
$\times10^{-3}$
6
4
2
0
-2
-4
-6
Vertical Velocity (m/s)

Fig. 3.1 Schematic of model domain with included snapshots of vertical velocity field and melt rate for warm, low mechanical forcing simulation 1B listed in Table 3.1.

(Jenkins et al., 2010) are the coefficients of thermal expansion and haline contraction. Within the relaxation term, the angled brackets $\langle\cdot\rangle$ represent a horizontal average and $\tau_0 = 200$ s is the relaxation timescale, chosen based on a far-field velocity scale of ~ 5 cms^{-1} and a domain height ~ 10 m. The term $r(z) = 0.5(\tanh(10-2z)+1)$ ensures that the relaxation term only acts in the far-field and $r \simeq 10^{-4}$ at $z = 2.6$ m. Therefore, the temperature and salinity are not forced at a depth similar to the mooring measurements made beneath the ice at Larsen C Ice Shelf and George VI Ice Shelf. Our simulations do not include the effect of Earth's rotation since the non-relaxed part of our domain is small (2.6 m) and there is no mean flow, so rotational effects will be weak. We explain the mechanical forcing term in Section 3.2.3.

3.2.2 Simulations Details

Eqns. 3.1-3.5 are discretised using a pseudo-spectral method in the horizontal, and a second order finite difference scheme in the vertical (see Taylor, 2008). The 2/3 de-aliasing technique (Orszag, 1971) is applied whereby the Fourier coefficients associated with the largest $\frac{1}{3}$ of wavenumbers are set to zero. This has the effect of dissipating scalar variance on scales smaller than 3Δ, where Δ is the horizontal grid spacing. In regions of the flow where the simulations do not resolve the Batchelor scale, the de-aliasing procedure and the numerical dissipation associated with the finite difference scheme acts like an implicit subgrid-scale model by removing small-scale variance. An implicit Crank-Nicholson method is used to time-step the viscous and diffusive terms, and a third order Runge-Kutta method for other terms.

Full details on the melt condition can be found in Vreugdenhil and Taylor (2019), however in summary, the method solves the diffusive three equation model (Frank, 1950) at the boundary, i.e. the equations

$$\rho_i L_i m = c_p \rho_w \kappa_T \left.\frac{\partial T}{\partial z}\right|_b, \tag{3.6}$$

$$\rho_i S_b m = \rho_w \kappa_S \left.\frac{\partial S}{\partial z}\right|_b, \tag{3.7}$$

$$T_b = \lambda_1 S_b + \lambda_2 + \lambda_3 P, \tag{3.8}$$

where m is the melt rate, T_b is the temperature at the ice base, and S_b is the salinity at the ice base. The constants are $c_p = 3974$ m^{2}s^{-2}kg^{-1}(°C)$^{-1}$ for specific heat capacity, $L_i = 3.35\times10^5$ m^{2}s^{-2}kg^{-1} for latent heat of fusion and $\rho_w = 1000$ kgm^{-3}, $\rho_i = 920$ kgm^{-3} for the densities of seawater and ice respectively. Here $\lambda_1 = -5.73\times10^{-2}$ °C, $\lambda_2 = 8.72\times$

10^{-2} °C and $\lambda_3 = -7.53 \times 10^{-4}$ °Cdbar^{-1} (Jenkins et al., 2010). The gradients $\frac{\partial S}{\partial z}$ and $\frac{\partial T}{\partial z}$ are calculated at the boundary, at each time step, in each grid cell, to give a dynamic melt condition. The heat and salt flux through the ice is set to zero, as suggested by Holland and Jenkins (1999). We neglect the volume input of melt water, as the interface moves slowly compared to the turbulent velocities.

Resolving the diffusive length scales for salinity everywhere in the domain is prohibitively expensive as the molecular diffusivity is small. Previous numerical simulations (Gayen et al., 2016) used artificially large diffusivities to resolve double-diffusive behaviour. However, this may lead to under-estimation of the double-diffusive effects. We use realistic molecular diffusivities for temperature and salinity and use a fine grid spacing to resolve the smallest diffusive scales within the scalar sublayers. In the turbulent region beneath these sublayers, turbulent fluxes will dominate heat and salt transport, and so it is sufficient that our simulations resolve the smallest velocity scales within the observation region, $z < 2.6$ m, using typical resolution criteria. In other words, the simulations can be classified as direct numerical simulations (DNS) near the ice where they resolve the scalar and velocity gradients and implicit large-eddy simulations farther from the ice where they resolve the turbulent eddies but not all scales of tracer variance. A similar approach has been used before to simulate turbulent scalar transport of active tracers (e.g. Hickel et al., 2007, Scalo et al., 2012). For further details relating to the grid spacing see Supplementary Material.

Table 3.1 lists the simulation runs. These are split into ‘warm’ simulations: 1A, 1B and 1C, with temperatures similar to George VI Ice Shelf (0.15 °C) (Venables et al., 2014), and ‘cold’ simulations: 2A, 2B and 2C, similar to cold-water ice shelves such as Larsen C Ice Shelf (−2.15 °C) (Davis and Nicholls, 2019). The warm temperatures are similar to the Martin and Kauffman (1977) experiment. We also consider small far-field temperatures (simulations 3 – 6) to investigate the simulation evolution when stratification is weak. The initial salinity $S_\infty = 34.572$ ppt, the same across simulations, is taken from an average of CTD profiles at 2.6 m depth from George VI Ice Shelf. The temperature and salinity fields are initialised with constant values T_∞ and S_∞ in each simulation. We consider two values of the target dissipation rate, ε_0, as described below in Section 3.2.3.

3.2.3 Simulating Mechanical Turbulence

The mechanical forcing term labeled in Eq. 3.1 is formulated so, in the absence of convection and buoyancy effects, the mean turbulent dissipation rate will be approximately ε_0.

Run	Mean Forced Dissipation ε_0 ($\mathrm{m^2s^{-3}}$)	T_∞ (°C)	ΔT (°C)	ΔS (ppt)	Turbulent Buoyancy Flux $\langle w'b'\rangle$	Density Ratio $R_\rho = \frac{\beta\Delta S}{\alpha\Delta T}$
1A	No Forcing	0.15	1.49	14.4	3.5×10^{-9}	197
1B	$(8.7\pm1.8)\times10^{-11}$	0.15	1.43	15.4	2.3×10^{-9}	220
1C	$(1.7\pm0.15)\times10^{-9}$	0.15	1.43	15.5	2.2×10^{-9}	220
2A	No Forcing	-2.15	5.8×10^{-3}	9.64×10^{-2}	6.0×10^{-12}	338
2B	$(8.7\pm1.8)\times10^{-11}$	-2.15	5.4×10^{-3}	10.3×10^{-2}	5.1×10^{-12}	383
2C	$(1.7\pm0.15)\times10^{-9}$	-2.15	5.9×10^{-3}	9.46×10^{-2}	-3.4×10^{-11}	325
3	$(8.7\pm1.7)\times10^{-11}$	-2.16	7.3×10^{-4}	1.04×10^{-2}	-5.2×10^{-14}	293
4	$(8.7\pm1.7)\times10^{-11}$	-2.161	1.8×10^{-4}	2.47×10^{-3}	-5.4×10^{-13}	274
5	$(8.7\pm1.7)\times10^{-11}$	-2.1613	1.5×10^{-5}	1.81×10^{-4}	-8.7×10^{-14}	242
6	$(8.7\pm1.7)\times10^{-11}$	-2.161325	4×10^{-7}	4.00×10^{-6}	-1.4×10^{-15}	220

Table 3.1 Table of simulation runs. Values for ΔT, ΔS, and R_ρ are averaged across the simulation. The turbulent vertical buoyancy flux $\langle w'b'\rangle$ is averaged across the simulation for depths $0.1\ \mathrm{m} < z < 2.6\ \mathrm{m}$ for the first 35 hrs to enable comparison across simulations run for different lengths of time. Simulations above the dashed line are convecting throughout the simulated time, and those below are not.

The volume-averaged turbulent kinetic energy (TKE) budget is

$$\frac{\partial k}{\partial t} = \underbrace{-\nu\left\langle \frac{\partial u_i'}{\partial x_k}\frac{\partial u_i'}{\partial x_k}\right\rangle}_{\substack{\text{Rate of}\\ \textit{Turbulent}\\ \text{Dissipation}\\ \varepsilon}} + \underbrace{\langle w'b'\rangle}_{\substack{\textit{Turbulent}\\ \text{Buoyancy Flux}}} + \underbrace{\varepsilon_0}_{\substack{\text{Mechanical}\\ \text{Forcing}}} \tag{3.9}$$

where $k = \frac{1}{2}(\langle(u')^2\rangle + \langle(v')^2\rangle + \langle(w')^2\rangle)$ is the TKE, $\langle\cdot\rangle$ denotes a volume average, and primes are departures from the volume average. There is an implicit sum over repeated subscripts.

For quasi-steady states, the rate of change of TKE is small. If the buoyancy flux is also small, the dominant energy balance is $\varepsilon \simeq \varepsilon_0$. We will refer to ε_0 as the target dissipation rate. In practice, target values of $1\times10^{-10}\ \mathrm{m^2s^{-3}}$ and $2\times10^{-9}\ \mathrm{m^2s^{-3}}$ resulted in dissipation rates of $(8.7\pm1.8)\times10^{-11}\ \mathrm{m^2s^{-3}}$ and $(1.7\pm0.15)\times10^{-9}\ \mathrm{m^2s^{-3}}$ within the passive spin-up simulation at steady state. The target value of $1\times10^{-10}\ \mathrm{m^2s^{-3}}$ is similar to the lower values measured beneath George VI Ice Shelf (Venables et al., 2014) and the forced value of $2\times10^{-9}\ \mathrm{m^2s^{-3}}$ is similar to the lower values measured beneath the Larsen C Ice Shelf (Davis and Nicholls, 2019).

The turbulent buoyancy flux $\langle w'b' \rangle$ represents energy transfer between kinetic and potential energy. In steady state, the melt condition and relaxation provide sources of potential energy. When the buoyancy flux is included, the dissipation rate will increase or decrease relative to the equilibrium rate ε_0 depending on the sign of $\langle w'b' \rangle$.

As in Wang et al. (1996), we only force the lowest wavenumbers and allow the turbulent cascade to form naturally at higher wavenumbers. This method of forcing stratified turbulence has been used extensively by previous authors (Rao and de Bruyn Kops, 2011, Taylor and Stocker, 2012) to simulate stratified turbulence, including by Taylor et al. (2019) to test the assumptions underlying studies of ocean mixing. Specifically, we force wavelengths greater than $L/2.5$ and less than L, where L is the domain size, following Wang et al. (1996). We want the smallest forced wavelength (i.e. $L/2.5$) to be no smaller than the height of the observation region (2.6 m), which sets the minimum vertical length scale as $L = 2.5 \times 2.6$ m $= 6.5$ m. In the relaxation region we set both the domain width and height equal to the minimum scale of (6.5 m) to achieve an isotropic forcing.

3.3 Results

3.3.1 Flow Regimes

In the case with no forced turbulence, once the scalars are initialised, the sublayers in temperature and salinity begin to grow. The thermal sublayer grows faster than the haline sublayer due to the larger molecular diffusivity of temperature. This leads to a double-diffusive boundary layer structure, comparable to the lower half of a double-diffusive interface (e.g. Carpenter et al., 2012), with a stable 'core' where the salinity dominates the density above a 'diffusive boundary layer' where the temperature dominates the density and leads to a peak in density. This behaviour is reproduced by the diffusive solution for T/S evolution beneath a melting interface from Martin and Kauffman (1977). The peak in density may then become unstable leading to diffusive convection. Figure 3.2 shows profiles of horizontally-averaged scalar fields for the cold, low mechanical forcing case 2B at various times. The early time behaviour of this simulation is similar to the unforced case and matches the diffusive solution. The plots are magnified to show the peak in mean density, however this variation is a small proportion of the total density difference which is largely contained in the T and S sublayers, as shown in the inset.

The addition of forced turbulence enhances vertical mixing of temperature and salinity, which acts to remove the mid-depth density maximum. As the flow evolves, the density peak increases in depth and decreases in magnitude. Changes in the magnitude

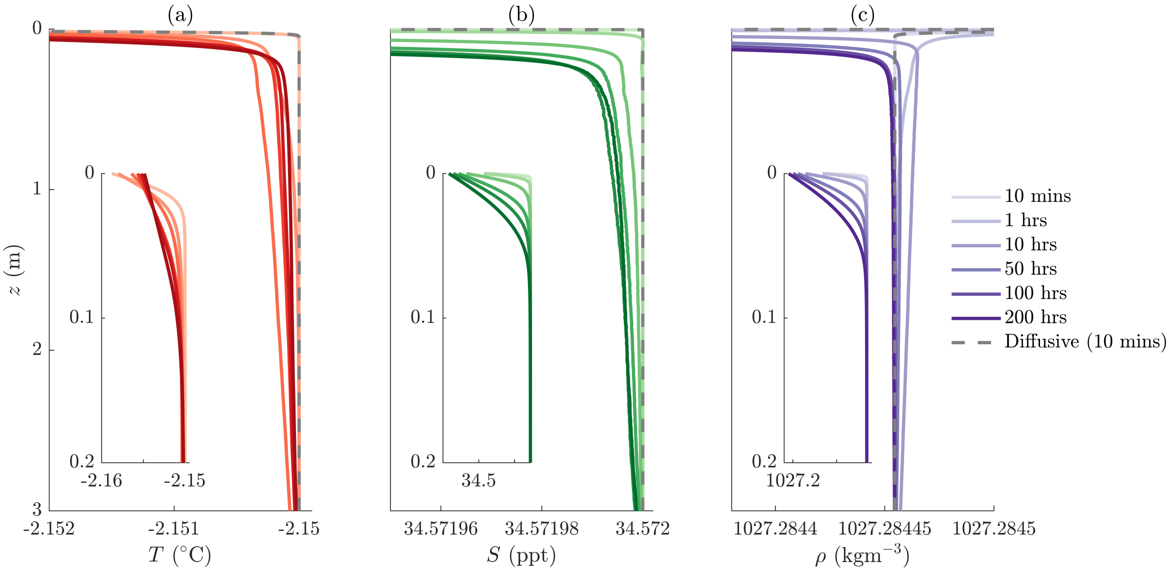

Fig. 3.2 Horizontally-averaged temperature (a), salinity (b) and density (c) averaged over an hour, at hours $1, 10, 50, 100$ and 200 for the cold, low mechanical forcing simulation 2B. Additionally we have shown the diffusive solution profiles (Martin and Kauffman, 1977) and the simulation profiles at $t = 10$ mins. The inset shows the upper 20 cm in each panel, showing the full variation in the scalars.

of the density peak are sometimes dominated by salinity and sometimes by temperature, and hence cannot be attributed to mixing of one scalar alone. In the warm simulations 1B, 1C and the unforced simulations 1A, 2A, the decrease in density peak magnitude is slow and the peak persists throughout the simulations (50+ hours in all cases). This suggests that if the conditions are sufficient to trigger convection, it may be long lasting. In the cold, mechanically forced cases (2B, 2C, 3, 4, 5, 6) the mean density profiles do become gravitationally stable during the simulation, with differing transition times dependant on the thermal and mechanical forcing. Case 2B, shown in Figure 3.2, took the longest of the cold cases to transition; the density profile has a peak in the mean profile until around 200 hrs, although at 100 hrs the peak is not visible without greater magnification. However, the lack of a peak in the mean density profile does not imply that no double-diffusive convection is present. It is possible that the stratification is still adding energy to the TKE via an up-gradient turbulent vertical buoyancy flux as discussed below in Section 3.4.1. Therefore, we use the sign of $\langle w'b' \rangle$ to identify double-diffusive convection.

Figure 3.3 shows the horizontally-averaged turbulent vertical buoyancy flux $\langle w'b' \rangle$ for three simulations: the warm, low mechanical forcing case 1B; the cold, low mechanical forcing case 2B and the cold, high mechanical forcing case 2C. Positive values of $\langle w'b' \rangle$ indicate that the potential energy is acting as a source of TKE, and negative values

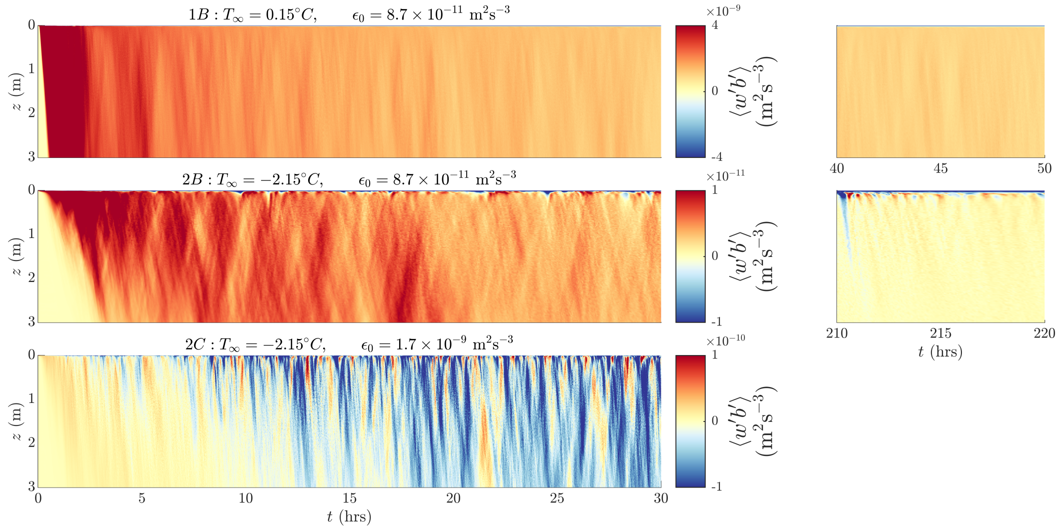

Fig. 3.3 Time evolution of the horizontally-averaged turbulent buoyancy flux $\langle w'b' \rangle$ for simulation runs 2B (cold,low mechanical forcing), 2C (cold, high mechanical forcing) and 1B (warm, low mechanical forcing). Positive values signify stratification acting to transfer available potential energy to turbulent kinetic energy and negative values indicate stratification acting to transfer turbulent kinetic energy into available potential energy. First 30 hours of each simulation are shown concurrently, then later times are shown for simulations 1B and 2B.

indicate that TKE is converted into potential energy. Initially, a region with $\langle w'b' \rangle > 0$ descends through the domain in all cases, due to the density peak discussed above. In the cold, low mechanical forcing cases, there are areas of $\langle w'b' \rangle < 0$ visible after some time. In case 2B these patches are initially confined near the ice base, however at later times they descend throughout the domain. In case 2C the regions quickly develop throughout the domain, however regions of $\langle w'b' \rangle$ are still present, despite not being the dominant contribution to the horizontal average. In the warm case 1B, $\langle w'b' \rangle > 0$ throughout the simulation length (50 hrs), and there are no regions of $\langle w'b' \rangle < 0$ descending through the domain. The mean density profile is relatively effective at determining the sign of $\langle w'b' \rangle$. In case 2C the density profile transitions after ~ 4 hrs, close to the time when $\langle w'b' \rangle$ changes sign (~ 2 hrs). However, there are still regions of $\langle w'b' \rangle > 0$ in case 2C, and in case 2B the changing sign of $\langle w'b' \rangle$ is sufficiently noisy that the direction of energy transfer between APE and TKE is not clear. Some variation in the sign of $\langle w'b' \rangle$ may be attributed to reversible exchanges between potential energy and TKE i.e. 'stirring' (Winters et al., 1995), however double-diffusive effects may also be responsible.

The magnitude of $\langle w'b' \rangle$ is also relevant. When $\langle w'b' \rangle$ is large and positive, it can dominate the TKE budget, but for small values it may not be energetically important.

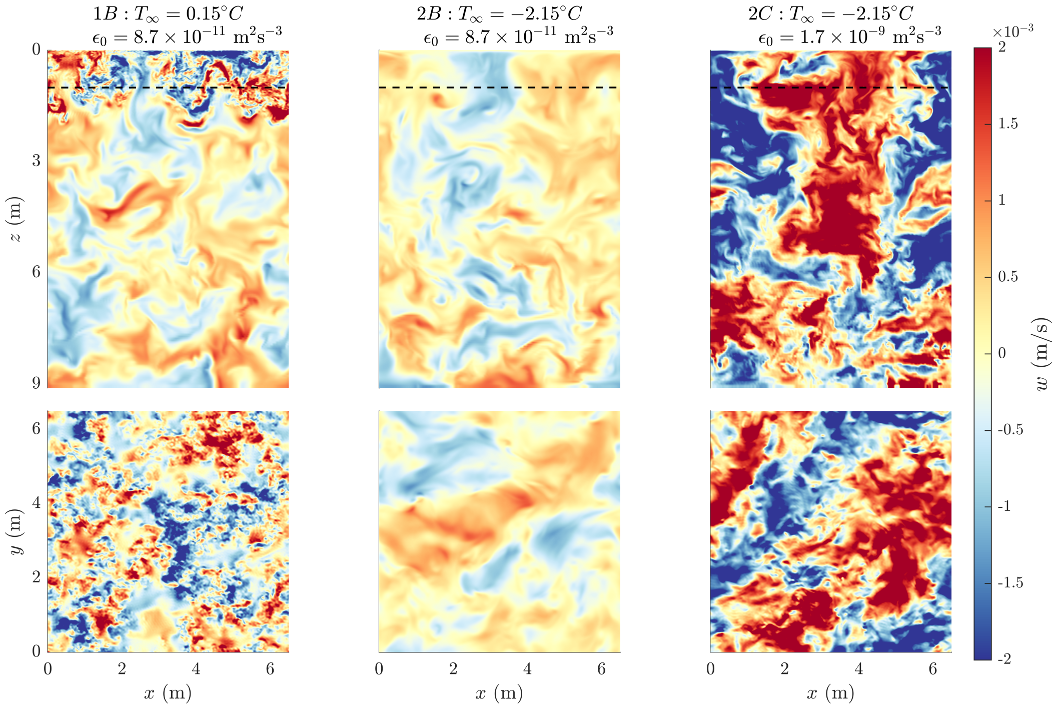

Fig. 3.4 Vertical velocity slices at $t = 1$ hr for simulation runs 2B (cold,low mechanical forcing), 2C (cold, high mechanical forcing) and 1B (warm, high mechanical forcing). All plots are on the same color scale to illustrate relative magnitudes of vertical velocities. Horizontal slices (lower panels) taken at 1m depth (location shown with dotted line in upper panels).

Figure 3.4 shows a snapshot of the vertical velocity field w for the three simulations 1B, 2B and 2C at $t \sim 2$ hrs. The influence of the descending region of elevated buoyancy flux (see Figure 3.3) is visible in Figure 3.4 in case 1B as an elevated value of w close to the ice base that moves down through the domain. However, in the cold cases 2B and 2C there is no visible contrast in the vertical velocity field. Even when buoyancy flux does not affect the velocity field, preferential diffusion may still affect the evolution of the scalar profiles which determine the melt rate.

In our convecting simulations, the magnitude of $\langle w'b' \rangle$ can be approximated by $g\alpha\langle w'T' \rangle$ away from the ice, which in turn can be approximated using the melt rate (not shown). The dominant mode of scalar transport is the large scale forced eddies, amplified by the convective motions as shown in the warm case in Figure 3.4. We show that the largest scales are responsible for the majority of the scalar fluxes in Figure 3.5 by considering the fluxes in wavenumber space. The co-spectrum of the scalar flux is calculated as $\langle \hat{w}\hat{\Theta}^* \rangle$ for scalars Θ, $\hat{}$ denoting the Fourier transform and * denoting the complex conjugate. We show the turbulent scalar fluxes for $\Theta = b', g\alpha T', g\beta S'$ i.e.

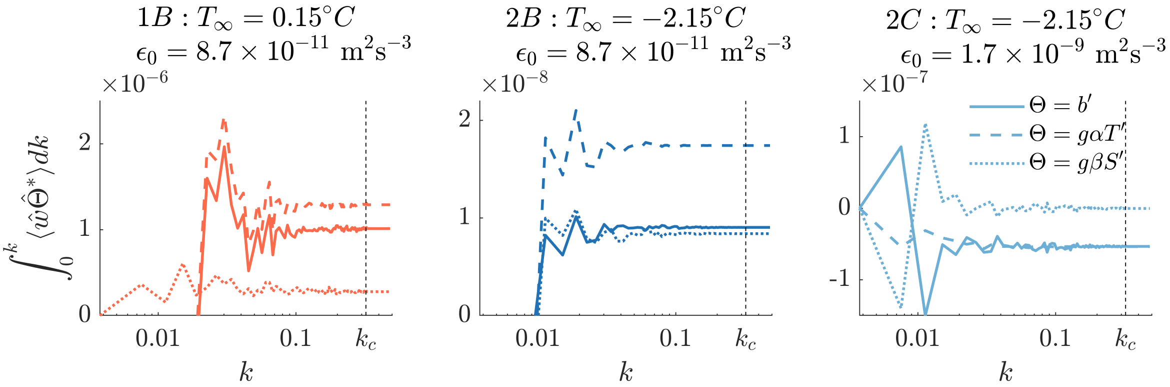

Fig. 3.5 Turbulent flux of temperature, salinity and buoyancy, averaged between 1 m and 3 m depth, integrated in Fourier space up to wavenumber k. Values taken from 3D fields at $t = 1$ hr for simulation runs 2B (cold,low mechanical forcing), 2C (cold, high mechanical forcing) and 1B (warm, low mechanical forcing) as in Figure 3.4. The Fourier transform is denoted using $\hat{}$ and the complex conjugate is denoted by *. The wavenumber $k = \sqrt{k_x^2 + k_y^2}$ is the horizontal radial wavenumber. Values of the integral $\int_0^k \langle \hat{w}\hat{\Theta}^* \rangle dk$ converge for $\Theta = b', g\alpha T', g\beta S'$ with increasing wavenumber, suggesting the resolution is sufficient to capture the scalar fluxes. The cutoff frequency k_c used in the $\frac{2}{3}$ de-aliasing rule is included as a dashed vertical line.

the turbulent buoyancy flux, and the thermal and haline components of the turbulent buoyancy flux. The scalar fluxes are averaged between 1 m and 3 m away from the ice, and then integrated between 0 and k, the radial wavenumber. The convergence of the integral in Figure 3.5 shows that the largest scales are responsible for the majority of the integrated turbulent scalar fluxes, which suggests the details of the smallest scales (which we do not resolve) will have a small effect on the scalar fluxes. We have marked the cutoff frequency k_c in the application of the $2/3$ de-aliasing rule (see Section 3.2.2). The thermal component of the buoyancy flux dominates the buoyancy flux in Figure 3.5, which holds throughout the convective regime.

3.3.2 Melt

Figure 3.6 shows the horizontally-averaged melt rate as a function of time. The diffusive theory is accurate for early times in all cases. After the diffusive phase, all simulations show an increase in the melt rate due to turbulent mixing. For the cases with persistent convection (i.e. all apart from the cold, high mechanical forcing case 2C), the melt rate continues to decrease as $t^{-1/2}$ after the onset of convection. This can be explained by the fact that the salinity sublayer continues to grow on the diffusive timescale as the diffusive salt flux from the melting boundary is much larger than the turbulent vertical salt flux

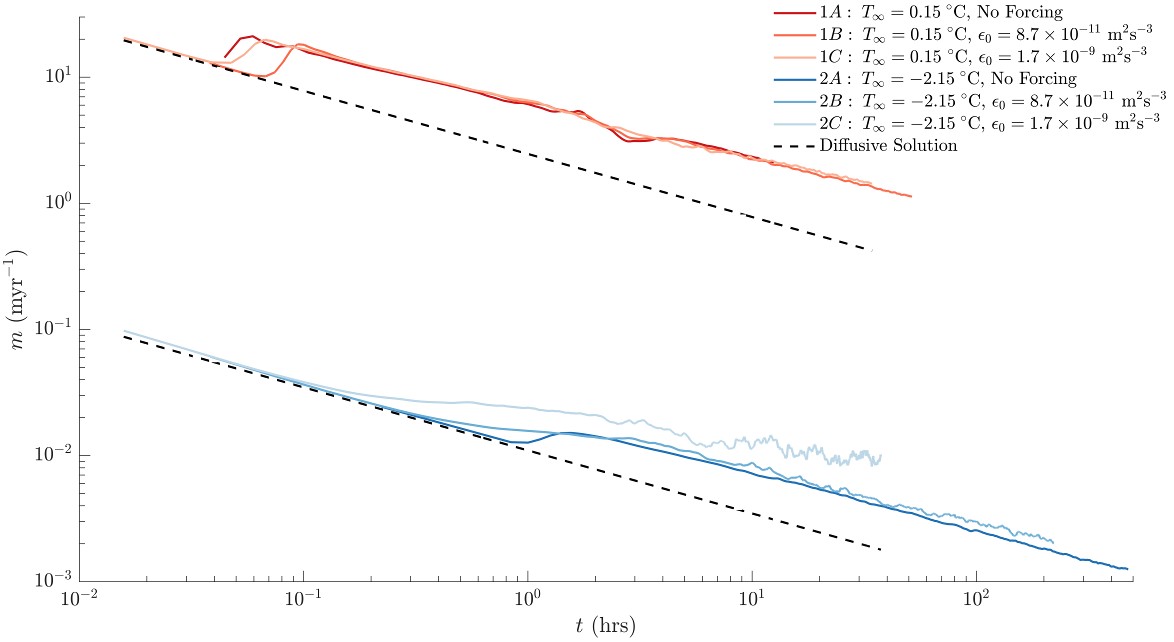

Fig. 3.6 Melt rate for cases 1A, 1B, 1C (the warm cases) and for cases 2A, 2B, 2C (the cold cases). The diffusive solution (Martin and Kauffman, 1977) is shown in a dotted line for both warm and cold cases.

in the convecting region. On the other hand, the boundary heat flux rapidly comes into balance with the turbulent vertical heat flux (not shown). As the gravitationally stable haline sublayer grows, turbulence is damped out over a larger area close to the ice base, reducing the turbulent vertical heat flux. This leads to a reduction in the boundary heat flux, which coupled with the reduction in the boundary salt flux, reduces the melt rate on the time scale of the growing salinity sublayer. Eventually the boundary diffusive salt flux will come into balance with the turbulent vertical salt flux and the system can reach a steady state. In the cold, high mechanical forcing case 2C, the system has almost reached this steady point near the end of the simulated period.

There is an imprint of convection on the spatial patterns of the instantaneous melt rate, although this effect is limited to cases in which $\langle w'b' \rangle$ is large compared to ε_0 (i.e. warm cases). Figure 3.7 shows snapshots of the melt rate for three simulations. In the cold case 2C the melt rate follows the patterns of the forced turbulence, illustrated by the passive case. In the warm, low mechanical forcing case 1B, where convection is strong, plume-like structures are visible in the melt rate. We may expect qualitatively different roughness patterns to develop on the underside of ice in the presence of strong double-diffusive convection. However, including feedbacks from a moving boundary would be necessary to test this hypothesis.

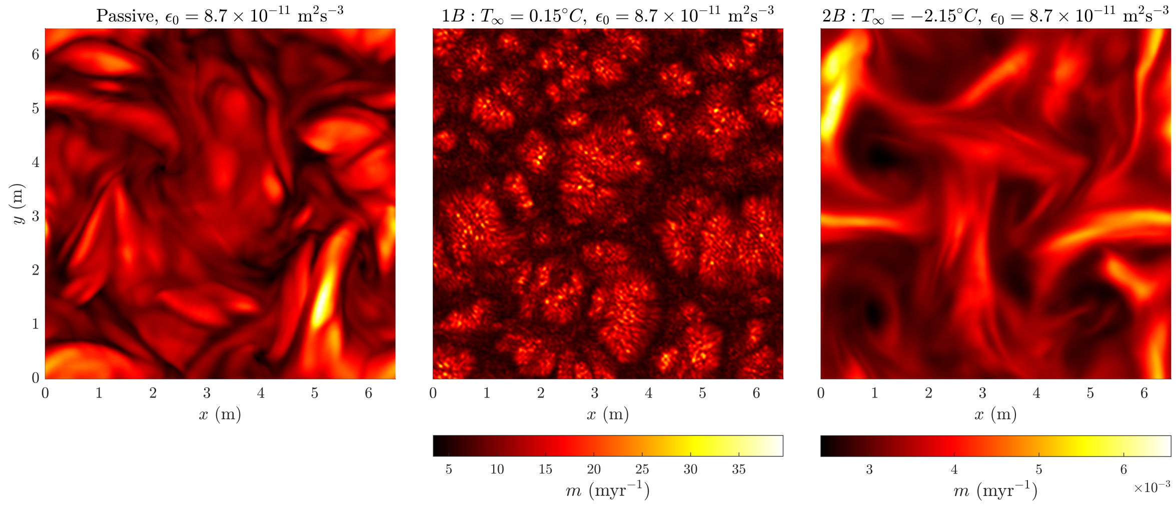

Fig. 3.7 Horizontal melt rate patterns for cases 1B and 2B. Snapshots taken at the same time as in Figure 3.4. Also included snapshot from the passive spin up simulation to compare patterning (melt rate values are inflated in this case due to lack of stable haline sublayer, so not included).

3.4 Diapycnal Buoyancy Flux

In this section we identify a mechanism for the double-diffusive convection discussed within Section 3.3. We propose that the dominant forcing for double-diffusive convection is a region of negative diapycnal buoyancy flux near the ice base and we locate it based on a criterion given in Chapter 2. We first review the criterion and its motivation in terms of double-diffusive energetics.

3.4.1 Background Theory

Here, we define the diapycnal buoyancy flux as the diffusive flux of buoyancy across surfaces of constant buoyancy, or isopycnals. For double-diffusive fluids, the diapycnal buoyancy flux can be up-gradient, which corresponds to a negative buoyancy diffusivity (Radko, 2013). The energetics of this was described in Chapter 2 as a diffusive release of 'background' potential energy (BPE). Background potential energy is defined as the potential energy associated with an adiabatic rearrangement (i.e. sorting) of the density field, and 'available' potential energy is the remaining potential energy after the background portion is subtracted. Winters et al. (1995) formalised the budget for the BPE for a single scalar, and showed the diapycnal buoyancy flux acts to transfer energy from APE to BPE, and so is associated with 'irreversible mixing' (Winters et al., 1995). Extending the same framework, we showed in Chapter 2 that, in a double-diffusive fluid, the up-gradient buoyancy flux corresponds to a conversion of BPE into APE which can then be modified into TKE via the turbulent vertical buoyancy flux $\langle w'b' \rangle$.

In Chapter 2, we provided a criterion for a negative diapycnal buoyancy flux in terms of the 3D scalar gradients. Specifically, the sign of the buoyancy flux is set by the following function,

$$\mathrm{sign}(\nabla b_p \cdot \hat{\boldsymbol{n}}) = \mathrm{sign}\left(f\left(G_\rho, \theta, \frac{\kappa_T}{\kappa_S} \right) \right), \tag{3.10}$$

where $\nabla b_p = g\alpha\kappa_T \nabla T - g\beta\kappa_S \nabla S$ is the diffusive buoyancy flux, $\hat{\boldsymbol{n}} = \nabla b / |\nabla b|$, and hence $\nabla b_p \cdot \hat{\boldsymbol{n}}$ is the diapycnal component of the diffusive buoyancy flux. The polynomial f is

$$f\left(G_\rho, \theta, \frac{\kappa_T}{\kappa_S} \right) = \frac{\kappa_T}{\kappa_S} G_\rho^2 + \left(\frac{\kappa_T}{\kappa_S} + 1 \right) G_\rho \cos\theta + 1, \tag{3.11}$$

where the 'gradient ratio', $G_\rho = \alpha|\nabla T| / \beta|\nabla S|$ is the 3D analogue to the density ratio $R_\rho = \alpha\frac{dT}{dz} / \beta\frac{dS}{dz}$, and θ is the angle formed between the gradient vectors ∇S and $-\nabla T$. When $\theta = 0$ the gradient vectors contribute to the buoyancy gradient constructively, and when $\theta = \pi$ they have opposing contributions to the buoyancy gradient. Negative values of f (and an up-gradient diapycnal buoyancy flux) require $\theta_c < \theta < 2\pi - \theta_c$, where

$$\theta_c = \arccos\left(\frac{-2\sqrt{\frac{\kappa_T}{\kappa_S}}}{\frac{\kappa_T}{\kappa_S} + 1} \right) \sim 98.6^\circ, \tag{3.12}$$

where the $f < 0$ region is bounded by θ_c and $2\pi - \theta_c$. Generally, an up-gradient diapycnal buoyancy flux is possible when the gradient vectors ∇T and ∇S make opposing contributions to the buoyancy gradient $\nabla b = g\alpha\nabla T - g\beta\nabla S$. The $f < 0$ region is also bounded by $G_\rho = 1$ and $G_\rho = \frac{\kappa_T}{\kappa_S}$ i.e. the salinity gradient must dominate the buoyancy gradient magnitude, but the temperature gradient must dominate the buoyancy flux gradient $\nabla b_p = g\alpha\kappa_T\nabla T - g\beta\kappa_S\nabla S$ magnitude. For 1D fields the angle $\theta = 0$ or π, and restricting variation to the z direction, this reduces to

$$f < 0 \iff \frac{\kappa_S}{\kappa_T} < R_\rho < 1, \tag{3.13}$$

which is a well known criterion for up-gradient buoyancy flux in double diffusive fluids (Veronis, 1965, St. Laurent and Schmitt, 1999).

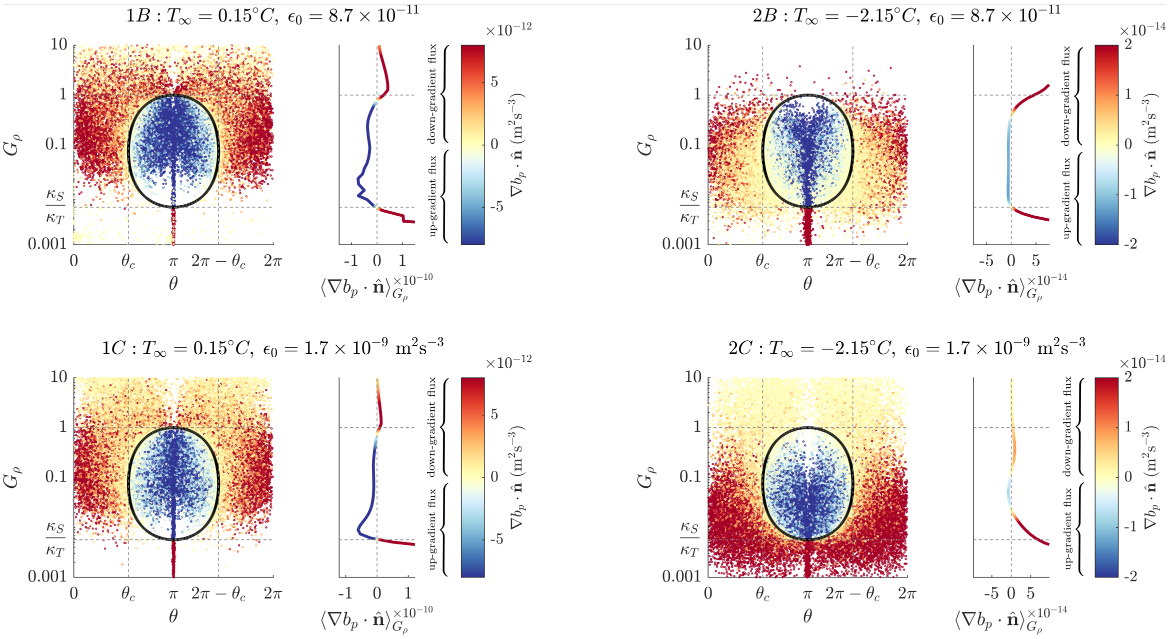

Fig. 3.8 Diapycnal buoyancy flux (color) for warm cases 1B and 1C and cold cases 2B and 2C. 3D gradients are used to compute the diapycnal flux, $\nabla b_p \cdot \hat{\boldsymbol{n}}$, the gradient ratio $G_\rho = \frac{\alpha|\nabla T|}{\beta|\nabla S|}$ and the angle θ between $-\nabla T$ and ∇S. A random set of $\frac{1}{1000}^{th}$ of the points are then plotted as a scatter graph in (G_ρ, θ) space, coloured by the diapycnal flux. The line $f(G_\rho, \theta) = 0$ is plotted in black and divides the negative values of diapycnal flux (up-gradient) on the inside of the line from the positive (down-gradient) values outside of the line. To the right of each scatter plot is an average over the diapycnal flux across G_ρ i.e. $\langle \nabla b_p \cdot \hat{\boldsymbol{n}} \rangle_{G_\rho}$, on the same colour bar as the scatter plot. Note the gradient ratio G_ρ is on a log scale.

3.4.2 Criterion for Convection

The cold, low mechanical forcing simulation 2B shows a positive turbulent buoyancy flux (Figure 3.3) despite a horizontally-averaged density profile increasing with depth (Figure 3.2) at late times, i.e. the turbulent buoyancy flux is up-gradient. In this setting, convection is forced by preferential diffusion of temperature out of fluid parcels near the ice/ocean boundary, causing an increased density and forcing parcels to descend into the turbulent region below. In some cases this leads to a gravitationally unstable mean density profile. However, as case 2B shows, convection can also occur when the mean density profile is stably stratified. The positive buoyancy flux in case 2B is an example of an energy transfer from BPE to APE. Below, we examine this in detail by calculating the local diapycnal buoyancy flux.

To understand the influence of turbulence on the criterion for a negative diapycnal buoyancy flux, it is useful to consider the full 3D temperature and salinity fields. Figure

3.8 shows a scatter plot of the diapycnal buoyancy flux calculated from a 3D snapshot of the scalar fields for cases 1B, 1C, 2B and 2C, in (G_ρ, θ) space. Here the criterion in Eq. 3.11 is exact and plotted as a black line. Also plotted is the diapycnal flux averaged for constant G_ρ. For $G_\rho < \kappa_S/\kappa_T$, the averaged diapycnal buoyancy flux $\langle \nabla b_p \cdot \hat{\boldsymbol{n}} \rangle_{G_\rho}$ is dominated by large positive values and $\theta \simeq \pi$. These points are located in the salinity sublayer, where ∇T and ∇S are nearly vertical. For other values of G_ρ, the points are spread across all angles θ. This shows the role of turbulence in distorting temperature and salinity contours. In the non-convecting case 2C, there is scatter in θ even for $G_\rho < \kappa_S/\kappa_T$. In case 2B convection is weak but active and $\langle w'b' \rangle$ is up-gradient as the density profile is a monotonic function of height at the time shown. Here, the turbulent scatter is primarily restricted to the range $\kappa_S/\kappa_T < G_\rho < 1$.

The points within the sublayer with $\theta \sim \pi$ are split into points with positive and negative diapycnal buoyancy flux. Close to the boundary $G_\rho \sim R_\rho < \kappa_S/\kappa_T$ and salinity forms the largest contribution to the buoyancy flux and buoyancy gradient. Farther from the boundary $G_\rho \sim R_\rho > \kappa_S/\kappa_T$ and temperature makes a larger contribution to the buoyancy flux whilst salinity still contributes most to the buoyancy gradient, leading to an up-gradient buoyancy flux. In the convecting cases 1B and 1C, the 1D criterion $\kappa_S/\kappa_T < R_\rho < 1$ for an up-gradient buoyancy flux is sufficient to explain the averaged profile $\langle \nabla b_p \cdot \hat{\boldsymbol{n}} \rangle_{G_\rho}$ if we take $G_\rho \sim R_\rho$. However, in the marginally convecting case 2B, the 3D criterion is necessary to explain the positive average diapycnal buoyancy flux for $0.2 < G_\rho < 1$ and in the non-convecting case 2C, the 1D approximation of $G_\rho \sim R_\rho$ performs poorly.

Figure 3.9 shows profiles of horizontally-averaged gradient ratio, scalar angle and diapycnal buoyancy flux from a convective simulation (case 1B) and a non-convective simulation (case 2C) as a function of depth in the upper 20 cm at $t = 30$ hrs. Shading indicates one standard deviation about the horizontal average. The depth where $\langle G_\rho \rangle = \kappa_S/\kappa_T$ is indicated with a blue dotted line, and the depths where $\langle \cos\theta \rangle = -1$ and $\langle \cos\theta \rangle = \cos\theta_c$ are indicated with red dashed lines. At the ice base, the gradient ratio will always be less than κ_S/κ_T as argued in Section 3.2.2. Farther from the ice, the temperature gradient exceeds the salinity gradient giving $\langle G_\rho \rangle > \kappa_S/\kappa_T$. The convective simulation shows significant negative diapycnal buoyancy flux in the region of $\langle G_\rho \rangle > \kappa_S/\kappa_T$ and $\langle \cos\theta \rangle < \cos\theta_c$ below the salinity sublayer and above the turbulent region. The critical angle θ_c is an exact bound on the local up-gradient diapycnal buoyancy flux. However it is not necessary that the horizontally-averaged value gives the bound we see in the convecting case since the 3D criterion (Eq. 3.11) is nonlinear. The negative diapcynal buoyancy flux peaks at the depth where $\langle \cos\theta \rangle = -1$ in all convecting simulations. Non-

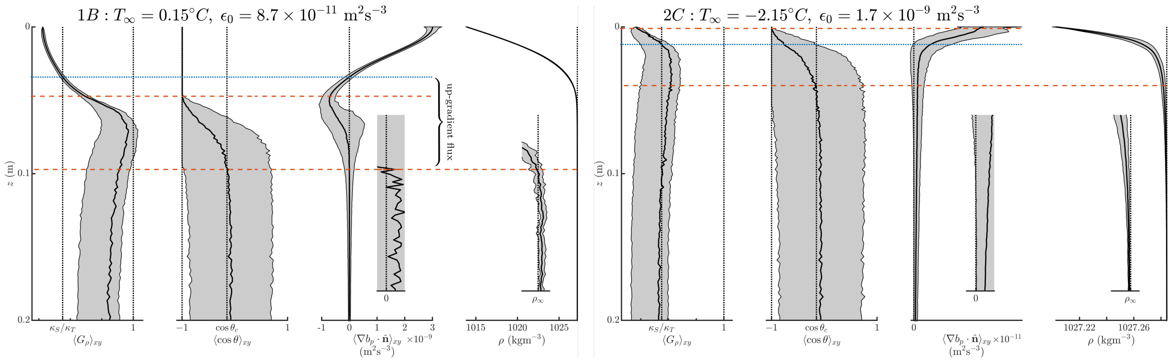

Fig. 3.9 Vertical profiles of the gradient ratio G_ρ, the scalar angle $\cos\theta$, the diapycnal flux $\nabla b_p \cdot \hat{\boldsymbol{n}}$ and the density ρ in the upper 20 cm of a convecting simulation (warm, low mechanical forcing case 1B) and a non-convective simulation (cold, high mechanical forcing case 2C) at $t = 30$ hrs. The spatial mean is shown in solid with one spatial standard deviation denoted by the shaded region. The dashed lines denote the depths at which $\langle \cos\theta \rangle_{xy} = -1$ and $\langle \cos\theta \rangle_{xy} = \cos\theta_c$. The dotted line denotes the depth at which $\langle G_\rho \rangle_{xy} = \frac{\kappa_S}{\kappa_T}$. The insets are a close up version of the adjacent profiles on the same z axis. The far-field density is denoted with a vertical dashed line in the plot of ρ. Note the gradient ratio G_ρ in the left panel is on a log scale.

convecting simulations have a positive mean diapycnal buoyancy flux at all depths, and the depth at which $\langle \cos\theta \rangle = -1$ is above the depth at which $\langle G_\rho \rangle = \kappa_S/\kappa_T$. This implies that turbulence influences the distribution of angles θ in the region of $\langle G_\rho \rangle > \kappa_S/\kappa_T$ where otherwise it is possible to form an up-gradient diapycnal buoyancy flux.

Figure 3.9 suggests that convection can be described using the relative thickness of two regions. The first is the region of $\langle G_\rho \rangle < \kappa_S/\kappa_T$, where the diapycnal buoyancy flux will always be down-gradient. This region is determined to first order by the relative thickness of the temperature and salinity sublayers. The second is the region of $\langle \cos\theta \rangle = -1$, where turbulent velocities do not alter the temperature or salinity fields. When the second region is thicker than the first, there is a region where the scalar gradients ∇T and ∇S are vertical, and $\kappa_S/\kappa_T < R_\rho < 1$, leading to an up-gradient diapycnal buoyancy flux, which causes the release of BPE and subsequently double-diffusive convection. We can also identify the region of $\langle \cos\theta \rangle < \cos\theta_c$, where on average the angle between ∇T and ∇S is conducive to an up-gradient diapycnal buoyancy flux. Below this region, $\cos\theta > \cos\theta_c$, and we expect the horizontally-averaged diapycnal flux to be positive due to turbulent motions.

G_ρ and θ are combinations of three-dimensional scalar gradients, and measuring these quantities in the field would be very challenging. It would be useful to have an approximate criterion that involves measurable quantities. In our simulations, the

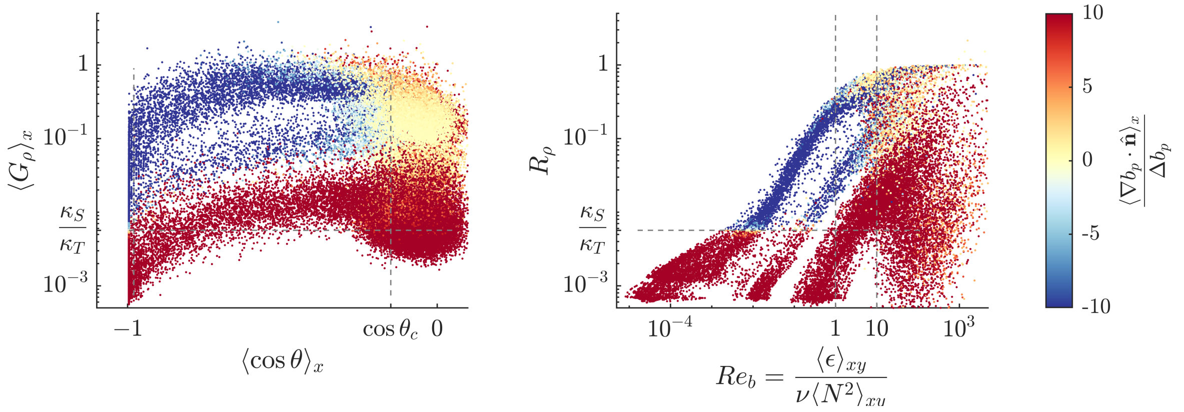

Fig. 3.10 Diapycnal buoyancy flux (color) for cases 1-6 in Table 3.1 plotted in (G_ρ,θ) (left) and in (R_ρ,Re_b) space (right). The diapycnal buoyancy flux is normalised by the maximum (i.e. initial) difference $\Delta b_p = b_p^{\text{bottom}} - b_p^{\text{top}}$ across each simulation for comparison. The points were sampled from 2D x-z slices extracted from the 3D simulations at regular intervals.

$G_\rho < \kappa_S/\kappa_T$ region is well described by the 1D approximation $R_\rho < \kappa_S/\kappa_T$. Our simulations also show a strong monotonic relationship, in a statistically averaged sense, between the angle θ and a common metric for turbulence, the buoyancy Reynolds number,

$$Re_b = \frac{\varepsilon}{\nu N^2}, \tag{3.14}$$

where $N^2 = \partial b/\partial z$ is the buoyancy frequency. We calculate Re_b using horizontally averaged values for both ε and N^2. The buoyancy Reynolds number quantifies the extent of the inertial subrange of the energy spectrum i.e. the separation between the Kolmogorov scale (the scale below which viscous effects dominate) and the Ozmidov scale (the scale above which buoyancy effects dominate). The buoyancy Reynolds number has also been used to identify double diffusion in the open ocean (Inoue et al., 2007).

For $Re_b < 1$ the flow will be laminar (Smyth and Moum, 2000), and hence we might expect $\cos\theta \simeq -1$. The region of $\cos\theta < \cos\theta_c$ is well described by $Re_b < 10$, so for simulations with a region of negative mean diapycnal buoyancy flux, this region is bounded by $Re_b = 10$. For $1 < Re_b < 10$ we can consider the flow very weakly turbulent, and for larger buoyancy Reynolds numbers $Re_b > 10$, we find the turbulence is sufficiently developed to give $\langle\cos\theta\rangle > \cos\theta_c$, causing a positive mean diapycnal buoyancy flux.

Figure 3.10 shows how the horizontal mean diapycnal buoyancy flux varies with G_ρ, θ, and Re_b. Each point was calculated from 2D slices of the scalar fields at regular intervals throughout the simulations. The 2D slices are taken throughout the simulated period for all of the simulations conducted (listed in Table 3.1), and the mean profiles from all the sampled times are plotted in Figure 3.10. For simulations with a density peak, the buoyancy frequency can be negative i.e. $N^2 < 0$, which causes $Re_b < 0$. However, the region of interest is adjacent to the ice base so only points above the density peak are included. The points are plotted in (G_ρ, θ) space, where the colouration denotes the magnitude of the diapycnal buoyancy flux. The left panel shows that the region with an up-gradient buoyancy flux (blue points) is mostly bounded by $\langle G_\rho \rangle > \kappa_S/\kappa_T$ and $\cos\theta < \cos\theta_c$, indicated using dashed lines. For the non-convecting simulations, there are points with positive diapycnal flux for $\langle \cos\theta \rangle < \cos\theta_c$ and $G_\rho > \kappa_S/\kappa_T$, which does not occur for the convecting simulations.

The right panel in Figure 3.10 plots the same data as the left panel, but now as a function of R_ρ and Re_b. The gradient ratio, G_ρ is a good approximation to the density ratio, R_ρ in the diffusive sublayer, but they differ in the turbulent region. In all simulations, $Re_b < 1$ adjacent to the ice, suggesting that the near-ice region is laminar. If turbulent eddies existed close to the ice they would feel the effect of the wall, however no such eddies occur due to the strength of the stratification. The points that lie within the region $R_\rho > \kappa_S/\kappa_T$ and $Re_b < 1$ have a negative diapycnal buoyancy flux and these points occur at the top of the boundary layer in the convecting simulations. This leads to the following hypothesis: Convection will occur at the melting ice-base if the depth at which $Re_b = 1$ is deeper than the depth at which $R_\rho = \kappa_S/\kappa_T$. In the next section we will use this criterion to extend our results to a wider range of parameters.

3.5 Discussion

The criterion for diffusive convection described in Section 3.4.2 allows us to extrapolate our results to a wider range of parameters. For example, given a temperature and salinity profile, we can find the dissipation rate ε required to give $Re_b = 1$ at the depth where $R_\rho = \kappa_S/\kappa_T$. In practice, field measurements of T/S profiles within the ice-shelf ocean boundary layer cannot yet resolve the diffusive sublayers, with reliable measurements limited to depths of $O(10\text{ cm})$. However observations may be combined with assumptions and models to estimate the relative depths of $Re_b = 1$ and $R_\rho = \kappa_S/\kappa_T$. This provides an estimate for the dissipation rate above which turbulence suppresses diffusive convection.

In the absence of T/S profiles, we can estimate the conditions that will be favorable for diffusive convection by considering the development of diffusive boundary layers into a fluid with initially uniform temperature and salinity. The solution of the unsteady diffusion equations forced by the melt boundary condition was derived by Martin and Kauffman (1977). Since heat diffuses down faster than salt, the density profile will be initially unstable with the potential to trigger diffusive convection. Over time, the addition of fresh water from melting will deepen the haline sublayer, decreasing the salinity gradient, and so decreasing N^2 in the halocline at the depth where $R_\rho = \kappa_S/\kappa_T$. The reduction in N^2 increases Re_b. Once $Re_b > 1$ at the depth where $R_\rho = \kappa_S/\kappa_T$, turbulence begins to suppress the up-gradient buoyancy flux which maintains diffusive convection.

Given an initial temperature, salinity and dissipation rate, we can calculate the time taken for the diffusive solution to meet our criterion for the shutdown of convection. This time is shown in Figure 3.11 for a fixed salinity $S_\infty = 34.572$, matching our simulations, while varying the initial temperature, T_∞ (normalised by the freezing temperature $T_m = \lambda_1 S_\infty + \lambda_2 + \lambda_3 P$), and the rate of dissipation, ε. Note that the diffusive solution does not account for turbulent mixing of the temperature and salinity profiles, so the transition times will not be quantitatively accurate. However, the diffusive solution provides a point of comparison between different levels of thermal forcing and rates of dissipation.

The simulations listed in Table 3.1 are included in Figure 3.11 for comparison. Convecting simulations are marked with circles and non-convecting simulations are marked with crosses and can be separated using a transition time of $t = 1$ s. This indicates that the predicted transition time might be a useful way to distinguish between convecting and non-convecting states in terms of their bulk parameters. The parameter space suggested by the observations of Larsen C Ice Shelf (Davis and Nicholls, 2019) and George VI Ice Shelf (Venables et al., 2014) as well as the parameter space explored in the shear-driven Large-Eddy Simulations of Vreugdenhil and Taylor (2019) (inferred from a law-of-the-wall scaling) are marked using dashed boxes. The parameter space for the Larsen C Ice Shelf observations and the LES cover relatively short transition times, indicating double-diffusive convection may not occur. However, the George VI Ice Shelf parameter space has a long transition time and hence the flow is amenable to transient double-diffusive convection as suggested by Kimura et al. (2015).

In the simulations and analysis here, we used idealised initial conditions with uniform temperature and salinity. However, diffusive convection can occur in other configurations. For example, consider a turbulent ice-ocean boundary layer in a non-convecting steady state. If turbulence levels decrease (e.g. due to weakening currents), the buoyancy Reynolds number will decrease, so the depth at which $Re_b = 1$ will increase. If this depth at which $Re_b = 1$ becomes deeper that the depth at which $R_\rho = \frac{\kappa_S}{\kappa_T}$ then the criterion from Section 3.4.2 is satisfied and convection will ensue. The double-diffusive convection preferentially transports heat over salt, so we would expect the salt boundary layer to grow slowly. Therefore a boundary layer in warm or weakly turbulent conditions may take a long time to adjust to modest changes in turbulence levels.

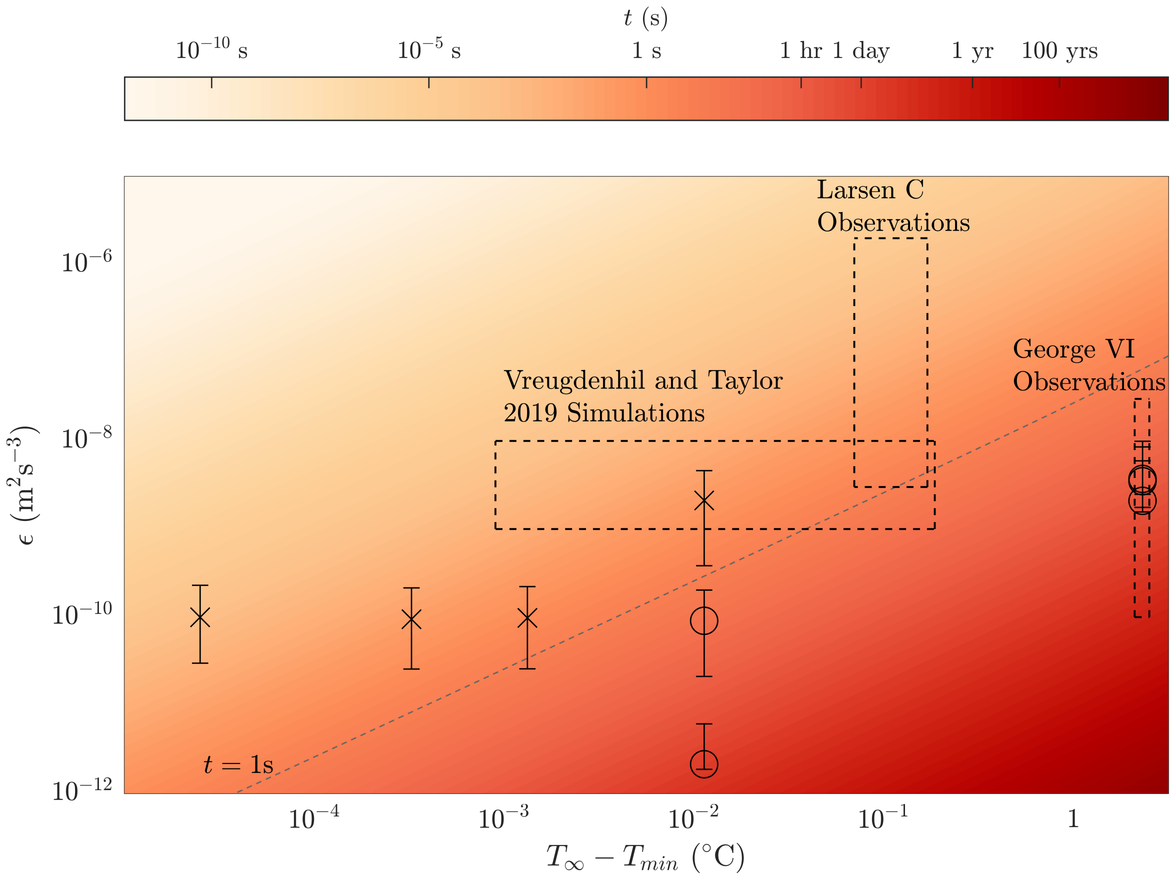

Fig. 3.11 Predicted time required for the system to transition from diffusive convection to stratified turbulence, calculated with the diffusive solution (Martin and Kauffman, 1977) with far field temperature T_∞ and prescribed turbulent dissipation rate, ε. 'Transition' occurs when $Re_b = 1$ at $R_\rho = \kappa_S/\kappa_T$. The far-field salinity $S_\infty = 34.572$ ppt in all cases and $T_{min} = \lambda_1 S_\infty + \lambda_2 + \lambda_3 P$ is the freezing temperature. Simulation values of $\varepsilon_{measured}$ are given by markers with bounds indicating maximum and minimum values. Circular markers indicate convecting simulations and cross markers indicate non-convecting simulations. The contour for diffusive solutions to take $t = 1$ s to transition is marked as a dividing point between the convecting and non-convecting simulations. Regions of parameter space occupied by the observations from Larsen C Ice Shelf (Davis and Nicholls, 2019), George VI Ice Shelf (Venables et al., 2014), and the LES for a shear driven boundary layer (Vreugdenhil and Taylor, 2019) shown with dashed boxes.

3.6 Conclusions

Motivated by observations made beneath George VI ice shelf in Antarctica, we conducted a series of numerical simulations of an idealised ocean boundary layer beneath a melting ice shelf. The simulations were initialised with constant salinity and temperature and the evolution of the system under a thickening salt sublayer was studied.

Two distinct flow regimes were observed. In one regime, the mean density profile increased with depth and the density field acted to damp the forced turbulence. This is the standard assumption in stratified melting ice-ocean boundary parameterisations. In the other regime, double-diffusive convection occurred and potential energy was converted into kinetic energy, forced by an up-gradient buoyancy flux in a region near the ice base. All simulations started in the convective regime, but some quickly transitioned to a turbulence-damping state. Simulations in different regimes exhibit qualitatively different patterns in the velocity field, melt rate and melt pattern.

We examined the influence of temperature and ambient turbulence levels on the flow regime by systematically varying the initial and far-field temperature and the strength of the mechanical forcing. A criterion for an up-gradient buoyancy flux using the $3D$ scalar gradients was applied to the simulation data. This criterion identified the region of up-gradient diapycnal buoyancy flux near the ice base, responsible for convection.

We developed a simple prediction for an up-gradient buoyancy flux at the ice base based on local values of the density ratio and the buoyancy Reynolds number Re_b. We found double-diffusive convection if the depth of the region beneath the ice of $Re_b \lesssim 1$ is deeper than the region of $R_\rho \lesssim \kappa_S/\kappa_T$. We then used solutions from the unsteady diffusion equations from Martin and Kauffman (1977) to estimate when the boundary layer will be favourable to double-diffusive convection based on the turbulent dissipation rate and the far field temperature.

The interaction of melt-driven convection with thermohaline layering and anisotropic turbulence (including shear) could modify some of our conclusions, and in particular the specific value of the buoyancy Reynolds number used in the criterion for the shutdown of double-diffusive convection could be sensitive to the source of turbulence. This could be investigated in future studies. We anticipate that the principles used here to distinguish between externally-forced turbulence and double-diffusive convection could be applied to other settings and will be a useful starting point in future work.

Our results indicate that melt-driven double-diffusive convection can dominate the dynamics within the ice shelf-ocean boundary layer if the turbulence is sufficiently weak and/or the thermal driving is sufficiently large. This study suggests future ice-ocean

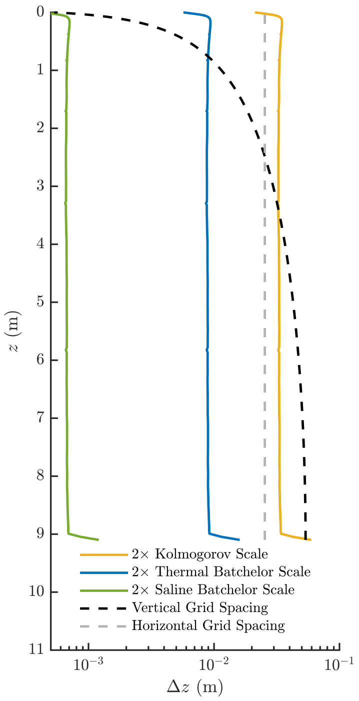

Fig. 3.12 Grid spacing plotted with depth. Kolmogorov and Batchelor scales for both scalars are shown, with dissipation rates taken from passive simulation for $\varepsilon_0 = 8.7 \times 10^{-11} \mathrm{m}^2 \mathrm{s}^{-3}$.

boundary layer parameterisations may need to distinguish between convective and non-convective conditions in the melting regime. However, more observations in warm, weakly turbulent conditions are needed to assess the prevalence of double-diffusive convection beneath ice shelves.

3.7 Supplementary Material

3.7.1 Grid Stretching

The Kolmogorov length scale gives a measure of the smallest turbulent eddies and is defined as

$$\eta = \left(\frac{\nu^3}{\varepsilon}\right)^{\frac{1}{4}} \tag{3.15}$$

We resolve the Kolmogorov scale within the ‘observation region’ of our domain ($z < 2.6$ m). The diffusivities for heat and salt are smaller than the diffusivity for momentum (i.e. kinematic viscosity ν), so variability on scales smaller than the Kolmogorov scale is possible. These scales are quantified using the thermal and haline Batchelor scales, defined as

$$l_B^T = \frac{\eta}{Pr^{\frac{1}{2}}} = \left(\frac{\nu\kappa_T^2}{\varepsilon}\right)^{\frac{1}{4}}, \qquad l_B^S = \frac{\eta}{Sc^{\frac{1}{2}}} = \left(\frac{\nu\kappa_S^2}{\varepsilon}\right)^{\frac{1}{4}}. \tag{3.16}$$

Figure 3.12 shows the grid spacing graphically, comparing the distance between grid points Δz to the Kolmogorov and Batchelor scales, calculated based on the dissipation rate profile of the passive spin up. We have compared our grid spacing to the turbulent length scales multiplied by a factor of 2 as a commonly argued factor.

Vreugdenhil and Taylor (2018) found that including 7 grid points within the conducting sublayer was sufficient to resolve the diffusive fluxes at the wall in their simulations of stratified plane Couette flow, a criterion which was then applied to resolve salt fluxes in the ice-ocean boundary layer simulations of Vreugdenhil and Taylor (2019)). We use the same criterion here, and we have further verified that our simulations follow the analytical diffusive solution (see Figure 3.2) at early times, before turbulent mixing increases the haline sublayer thickness. Using the definition of the salinity sublayer as when the salinity reaches 99% of its far field value, we find that, for the diffusive solution, we have 7 grid points within the haline sublayer after $t = 25$ minutes. Before this time, the simulated scalar fields match the diffusive solution which suggests the scalar fluxes are resolved at the boundary throughout our simulations.

3.7.2 Diffusive Solution

Martin and Kauffman (1977) (referred to as MK77) derived a solution for the diffusive evolution of temperature and salinity profiles beneath a melting boundary, represented by a diffusive three equation model. Their initial condition is of constant temperature and salinity, as in our simulations, although their solution allows for a moving boundary. We will present the derivation in a condensed form.

First assume the ice motion is slow compared to the temperature and salinity sublayer growth so that the ice boundary condition can be applied at a fixed location, $z = 0$. Below we will discuss the solution with a moving boundary. Secondly assume the scalar profiles are functions of the similarity variable $z/\sqrt{t}$ for time t. Substituting into the diffusion equations,

$$\frac{\partial T}{\partial t} = \kappa_T \nabla^2 T, \quad \frac{\partial S}{\partial t} = \kappa_S \nabla^2 S, \tag{3.17}$$

yields a set of ordinary differential equations. Applying $T = T_b$ and $S = S_b$ at the ice base, with initial conditions $T = T_\infty$ and $S = S_\infty$, gives solutions as error functions,

$$T = T_\infty + A\left(\frac{z}{2\sqrt{\kappa_T t}}\right), \tag{3.18}$$

$$S = S_\infty + B\left(\frac{z}{2\sqrt{\kappa_S t}}\right), \tag{3.19}$$

where $A = A(T_\infty, S_\infty, T_b, S_b)$ and $B = B(T_\infty, S_\infty, T_b, S_b)$ are functions of the far-field values T_∞ and S_∞ and the boundary values T_b and S_b. Incorporating a moving boundary with a diffusive three equation model (Eqns. 3.6-3.8), allows the boundary values T_b, S_b to be related to the initial values T_∞ and S_∞.

In the diffusive three equation model the melt rate is proportional to the boundary temperature gradient $\frac{\partial T}{\partial z}\big|_b$. Taking the derivative of Eq. 3.18 shows that the melt rate is proportional to $t^{-1/2}$ of the form,

$$m(t) = \xi t^{-1/2}, \tag{3.20}$$

where ξ is a function of T_∞ and S_∞ to be found. The boundary location z_b is found by integrating the melt rate in time, giving $z_b = 2\xi\sqrt{t}$. T_b and S_b can be found by substituting $z = z_b$ into Eqns. 3.18-3.19.

The boundary temperature gradient $\frac{\partial T}{\partial z}\big|_b$ can be found from the derivative of Eq. 3.18. Substituting this into the boundary heat flux condition (Eq. 3.6), gives an expression for A,

$$A = -\frac{2L\rho_i}{c_p\rho_w}\sqrt{\frac{\pi}{\kappa_T}}\,\xi e^{\frac{\xi^2}{\kappa_T}}. \tag{3.21}$$

Substituting expressions for T_b and S_b into the Liquidus condition (Eq. 3.8) then gives the prefactor B,

$$B = \frac{H - A\left(\frac{\xi}{\sqrt{\kappa_T}}\right)}{\left(\frac{\xi}{\sqrt{\kappa_S}}\right)}, \tag{3.22}$$

where $H = T_\infty - \lambda_1 S_\infty - \lambda_2 - \lambda_3 P$ is the difference between the far-field temperature T_∞ and the freezing temperature $T_{min} = \lambda_1 S_\infty + \lambda_2 + \lambda_3 P$.

The solution for ξ can be found by substituting S_b and $\frac{\partial S}{\partial z}\big|_b$ from Eq. 3.19 into the boundary salt flux condition (Eq. 3.7). This gives

$$\frac{2L\rho_i}{c_p\rho_w}\sqrt{\frac{\kappa_S}{\kappa_T}}\xi e^{\frac{\xi^2}{\kappa_T}}\left(\frac{\xi}{\sqrt{\kappa_T}}\right) = \frac{\xi(H-T_\infty)\left(\frac{\xi}{\sqrt{\kappa_S}}\right)}{e^{-\frac{\xi^2}{\kappa_S}}+\sqrt{\pi}\left(\frac{\xi}{\sqrt{\kappa_S}}\right)} - H\sqrt{\frac{\kappa_S}{\pi}}. \tag{3.23}$$

Given initial values T_∞ and S_∞, we numerically solve for ξ using Eq. 3.23, giving a melt rate from Eq. 3.20. We then solve for the temperature and salinity profiles using A and B from Eqns. 3.21-3.22. This provides the diffusive evolution of the scalar profiles in the absence of turbulent motion given a far-field temperature and salinity.

3.8 Recent Developments

Since the publication of our article in *Journal of Physical Oceanography*, another paper conducting Large-Eddy-Simulations of double-diffusive convection in the ice shelf-ocean boundary layer has been published. In Rosevear et al. (2021) they run LES similar to our simulations in that they have a dynamically melting ice base, enhanced resolution near the ice-base and study an initial value problem. The differences between Rosevear et al. (2021) simulations and ours is that within their simulations they force turbulence using shear, and include an initial ambient stratification.

Rosevear et al. (2021) observe two regimes, one of double-diffusive convection, for low shearing rates, and one of stratified turbulence, damped by stratification, as in our work. They additionally find the development of layered structures in their heavily convective simulations, suggestive that the hypothesis from Kimura et al. (2015) may be valid as a mechanism for forming layers beneath an ice shelf. Rosevear et al. (2021) identified the source of their convection as a density overturn near the ice base, suggestive of melt-driven convection as in our simulations. The agreement between our simulations and those of Rosevear et al. (2021) suggests the results of both may be more robust. Particularly given that the simulations use different forcings, and different simulation packages (which use different sub-grid scale schemes for mixing). Rosevear et al. (2021) mapped out the transition region in parameter space between convection and stratified turbulence, but using empirical data from their simulations only. It is left as future work to apply the criteria we developed in this work to the simulations of Rosevear et al. (2021), although a preliminary analysis suggests that the criteria applies well to the sheared and stratified case of Rosevear et al. (2021).

Chapter 4

Estimating dissipation rates associated with double diffusion (in an Arctic Eddy)

> Nau loved the sight of the bright, shimmering gusts as they sprang up suddenly over the sea; sparkling jets of water leaping high in the air, with the sun riffling through them, weaving in glittering rainbows.
>
> *Yuri Rytkheu*
> translated by
> *Ilona Yazhbin Chavasse*

This chapter was published in *Geophysical Research Letters* in 2021 with coauthors Elizabeth Fine, Jennifer MacKinnon, Matthew Alford and John Taylor. Some minor edits have been made from the published version including a short note about updates in the field since our publication. I thank Barry Ruddick and an anonymous reviewer for their valuable input on the development of this manuscript. Shipboard and microstructure data are available for download (http://www.rvdata.us/catalog/SKQ201511S and https://microstructure.ucsd.edu, respectively). Code for applying our method to CTD data can be found at DOI: 10.5281/zenodo.4665777.

4.1 Introduction

Recent decades have seen a decline in Arctic sea-ice thickness and extent (Carmack et al., 2015). Sea-ice melting is influenced by vertical ocean heat transport (Timmermans and Marshall, 2020). For example, a doubling of the Beaufort Gyre halocline heat content has influenced sea-ice extent (Timmermans et al., 2018, Shimada et al., 2006). Heat exchange between the surface layer and sub-surface water masses depends on small-scale turbulent processes and identifying turbulent regions helps to quantify this heat flux (Fine et al., 2018). The most direct measurements of turbulent mixing require high-resolution measurements (microstructure) which are costly and difficult to obtain across large spatial scales. A natural solution is to parameterise turbulence based on properties measured on the finescale (e.g. Polzin et al., 2014, Whalen et al., 2015). However, common shear and strain based parameterisations for internal wave breaking do not apply well to areas of double-diffusive convection (Gregg, 1989).

Buoyancy gradients in the upper Arctic ocean are dominated by salinity, which enables heat to be trapped sub-surface. Opposing vertical gradients in temperature (T) and salinity (S) and a relatively weak internal wave field make the Arctic favorable for double-diffusive convection (e.g. Bebieva and Timmermans, 2016), where it can play a dominant role in upwards transport of the trapped heat (Carmack et al., 2012). Double-diffusive convection refers to convective processes that rely on the difference between the molecular diffusivities of heat ($\kappa_T \sim \mathcal{O}(10^{-7})$ m^{2}s^{-1}) and salt ($\kappa_S \sim \mathcal{O}(10^{-10})$ m^{2}s^{-1}) (Schmitt, 1994). A variety of flow structures may develop due to double diffusion. For example, vertical gradients in temperature and salinity can force convective motions, leading to step-like temperature and salinity profiles in a thermohaline ‘staircase’ (e.g Timmermans et al., 2008). Other results of double diffusion include thermohaline intrusions (Ruddick and Richards, 2003, Ruddick and Kerr, 2003) and salt fingers (Kunze, 2003). Traditionally these processes are analysed and parameterised separately, however, in Chapter 2 we presented an energetic framework that describes the dynamics of all cases where potential energy is released into kinetic energy via double diffusion (our definition of double-diffusive convection).

Several studies have shown a close connection between large-scale circulation and double-diffusive fluxes. Shibley et al. (2017) showed that the prevalence of thermohaline staircases, and by inference the double-diffusive fluxes, are modified by the large-scale circulation patterns within the Arctic basins. Individual layers associated with thermohaline staircases can extend for several hundred kilometers with significant variations in T/S properties along this length (Bebieva and Timmermans, 2019). This suggests a possible connection between lateral fluxes of heat and salt and vertical fluxes associated with double-diffusive convection.

Estimating double-diffusive heat fluxes generally requires either microstructure measurements or parameterizations of specific double-diffusive processes. For example, Shibley et al. (2017) use a 4/3 flux law to estimate heat fluxes across diffusive interfaces in thermohaline staircases, and Inoue et al. (2007) combine two parameterisations for different double-diffusive regimes, distinguished using the density ratio $R_\rho = \alpha\frac{\partial T}{\partial z}/\beta\frac{\partial S}{\partial z}$. Fine et al. (2018) showed that the turbulent dissipation rate can be used to infer the vertical heat flux in double-diffusive conditions. Here, we propose a new statistical technique to estimate turbulent dissipation rates associated with general double-diffusive processes from a CTD section. We rely on the notion that lateral stirring of T/S along isopycnals (surfaces of constant density) gives rise to large T/S gradients that are 'compensated' in terms of their contribution to density (Rudnick and Ferrari, 1999). This compensated T/S (or 'spice') variance is preferentially fluxed to small scales.

The central concept behind our method is that large spice gradients generated by along-isopycnal stirring drive double-diffusive motions through an up-gradient buoyancy flux and that the resulting small-scale turbulence fluxes energy further down scale until it is ultimately dissipated. We use a synthetic model spectrum to extrapolate along-isopycnal spice variance measured from a CTD section down to the scale of the largest turbulent overturns and use this result along with other assumptions to estimate the up-gradient buoyancy flux and the turbulent dissipation rate through the framework described in Chapter 2.

The standard model for shear-driven ocean mixing is that energy is input to small scales via shear forced by a larger structure (e.g. internal waves and mean flows). Some portion of this energy gets transferred to micro-scales and ultimately dissipated at a rate ε, and some portion is lost to potential energy via the turbulent buoyancy flux $w'b'$; used to irreversibly mix the density field. This division is quantified using a parameter Γ, the flux coefficient (Gregg et al., 2018), that has been evaluated from observations, experiments and simulations (e.g. Holleman et al., 2016, Jackson and Rehmann, 2003, Howland et al., 2020). The complication is that the exchange of potential energy and kinetic energy via $w'b'$ is reversible and in fact dominated by adiabatic internal waves. This was resolved by Winters et al. (1995) who divided the potential energy into a 'Background Potential Energy' (BPE) and an 'Available Potential Energy' (APE) and considered their budgets. They found that APE is transformed into BPE via a diapycnal (across surfaces of constant density) buoyancy flux φ_d, which they associated with 'irreversible mixing' of density as φ_d is always positive in a single-component fluid. However, in double-diffusive convection, variations in density (i.e. APE) are created by the action of diffusion, so the standard model of shear-driven irreversible mixing of density does not apply.

Extending the Winters et al. (1995) framework to include double diffusion, in Chapter 2 we showed that the 'mixing' of density may be reversed; in a double-diffusive fluid, BPE (as defined in Winters et al. (1995)) can be converted into APE via an up-gradient diapycnal buoyancy flux, i.e. $\varphi_d < 0$. In a statistically steady state, we might then expect the generation of APE to be converted into kinetic energy through the vertical turbulent buoyancy flux, i.e. $\langle w'b' \rangle \simeq -\langle \varphi_d \rangle$, averaging across an appropriate volume. Further, if double-diffusive convection is the only source of turbulence, then the input of kinetic energy comes entirely from potential energy, so the average rate of dissipation of kinetic energy, $\langle \varepsilon \rangle$, should balance the vertical turbulent buoyancy flux $\langle w'b' \rangle$, which gives the balance $\langle \varepsilon \rangle \simeq \langle w'b' \rangle \simeq -\langle \varphi_d \rangle$. The form for φ_d can be expressed in terms of the local gradients in temperature and salinity and their respective molecular diffusivities, which provides a pathway for predicting the dissipation rate associated with double diffusion from T and S alone.

The diapycnal buoyancy flux, φ_d, as formulated in Chapter 2, involves the *molecular* diffusive fluxes of heat and salt. Therefore, diagnosing φ_d requires three-dimensional gradients of T and S at small scales. While this is possible in direct numerical simulations, it is not practical using observational data. Here, we follow the theory of Haynes and Anglade (1997) and Smith and Ferrari (2009) and assume that spice is stirred along isopycnals by quasi-geostrophic motions. The possibility of double-diffusive instabilities developing in response to along-isopycnal stirring of spice was raised in Garrett (1982) and Smith and Ferrari (2009). However, we believe our work is the first attempt to use this principle to estimate the dissipation rate associated with double-diffusive processes.

To demonstrate our method and test the underlying assumptions, we use a CTD section through a sub-surface warm-core eddy reported in Fine et al. (2018) and compare our estimated dissipation rates with those inferred from microstructure measurements. Fine et al. (2018) surveyed an intrahalocline warm-core eddy on the Chuchki Slope in September 2015, collecting shear and thermal microstructure data as well as finescale T and S across multiple eddy transects. Eddies such as this are thought to be an important source of heat into Canada Basin (Watanabe, 2011), where the implications for sea-ice are not well understood. This was confirmed by Fine et al. (2018), who showed that the regions of enhanced heat flux at the top of the eddy, inferred from thermal microstructure data, could lead to a significant upwards heat flux if extrapolated over the eddy's lifetime. Fine et al. (2018) found that the top of the eddy was also associated with enhanced dissipation rates, which were used to estimate the heat flux.

The method we introduce here uses physical reasoning to link along-isopycnal stirring of spice with double-diffusive convection and ultimately energy dissipation. The primary assumption that we make is that double-diffusive convection is the sole driver of turbulence i.e. shear production is negligible. When compared with the data from Fine et al. (2018), the dissipation rate inferred using our method closely matches the dissipation rate inferred from a microstructure probe except in regions with relatively low Richardson number where Fine et al. (2018) hypothesized that shear-driven turbulence was active. This shows that our method can be used in conjunction with direct microstructure measurements to identify the relative importance of double diffusion. When microstructure measurements are not available, our method provides a means to estimate the turbulent dissipation rate in regions that are dominated by double diffusion from a high resolution CTD section.

This chapter is organised as follows. In the first section we introduce the observations from Fine et al. (2018). In the second section we describe the method for estimating turbulent dissipation rates associated with double-diffusive convection. In the third section we compare our results to the observations. We find a good match across most of the section, including the top of the eddy, where dissipation rates can be linked to the vertical heat flux. We also find a good match across ‘doubly-stable’ regions without opposing background T/S gradients. The estimated double-diffusive dissipation rate is significantly smaller than the microstructure dissipation rate only in regions where the gradient Richardson number is low and the buoyancy Reynolds number $Re_b > 20$, indicating active shear-driven turbulence. Finally, we test how the method performs on a coarse sub-sampling of the data, suggesting applicability to data with lower spatial resolution.

4.2 Observations

In this section we briefly discuss the observations from the Arctic Ocean that we use to test the new method for estimating the double-diffusive dissipation rate. These data will also be used to test some assumptions made in the next section. Fine et al. (2018) described data collected from an anomalously warm anti-cyclonic eddy on the Chukchi slope in September 2015. The temperature and salinity from one of the sections are shown in Figure 4.1. Isopycnals are shown in grey in panel B and the 3 °C isotherm which outlines the eddy is shown in black. In most places density variations are controlled by salinity, although temperature plays a role within the eddy. Concurrent microstructure measurements of the kinetic energy dissipation rate, ε, and thermal variance dissipation,

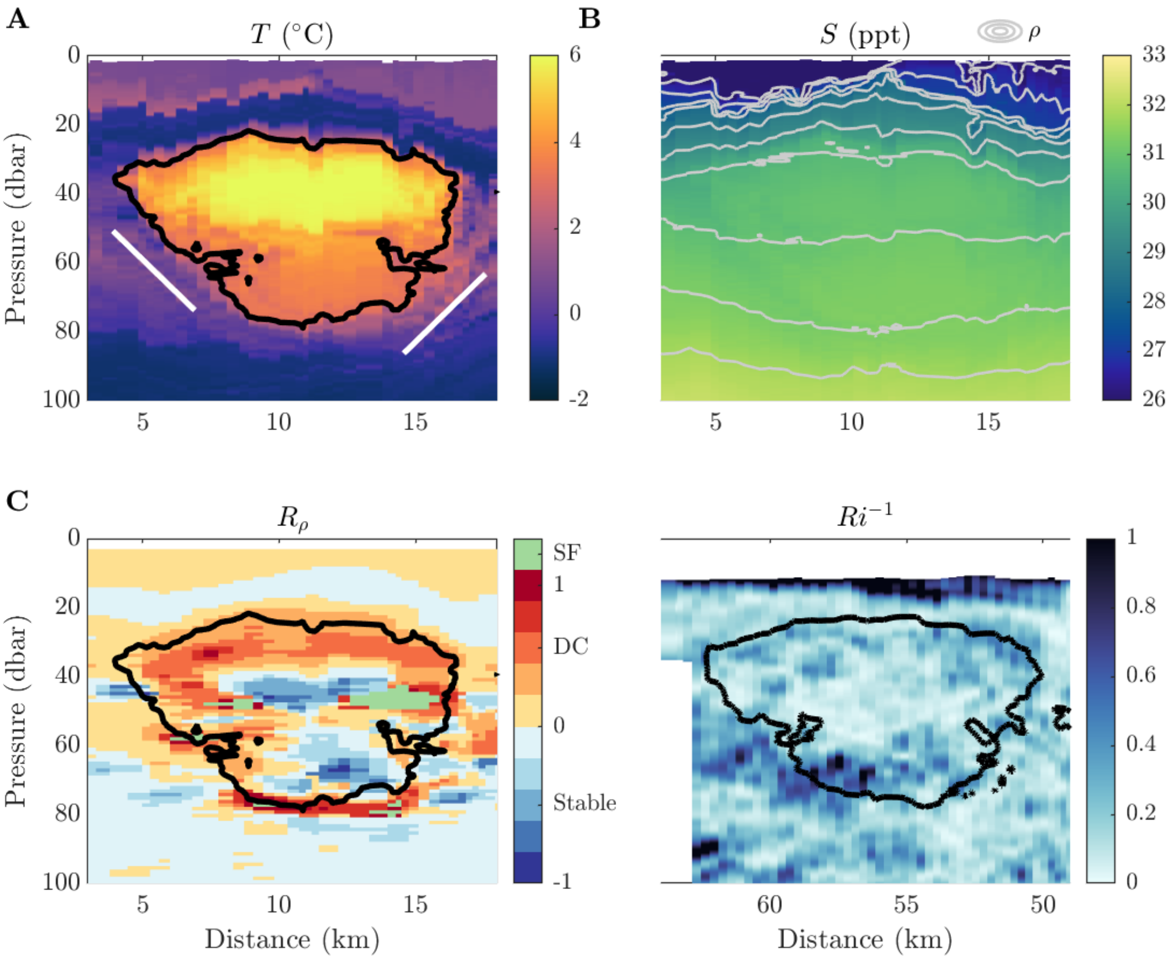

Fig. 4.1 **A**. Temperature with 3 °C contour in black and angle f/N marked with white lines, with value calculated at line midpoint. **B**. Salinity with contours of ρ ($\mathrm{kgm^{-3}}$) in grey. **C**. Density ratio $R_\rho = \alpha\frac{\partial T}{\partial z}/\beta\frac{\partial S}{\partial z}$. **D**. Shear $U_z = \sqrt{u_z^2 + v_z^2}$.

χ_T, were used to identify regions of high dissipation along the top, sides and bottom of the eddy. Practical issues regarding the processing of microstructure data in the presence of thermohaline layering and instrument noise floors are discussed in Fine et al. (2018) and not included here. The heat flux was also inferred from the microstructure profiles and used to estimate the lifetime of the eddy. The lateral heat flux along the eddy flanks (~ 2000 Wm^{-2}) was found to have the largest impact on the eddy evolution, giving an estimated eddy lifetime of ~1 year, although the heat flux along the top of the eddy (5 Wm^{-2}) was also significant. The dissipation rate, ε, was used to estimate the heat flux using the Osborn (1980) model, where a good agreement was found with the estimates from χ_T using the Osborn and Cox (1972) model with .

The data from Fine et al. (2018) provides a useful testing grounds for our method since it contains a variety of regimes. Different processes were identified by Fine et al. (2018) based on visual identification of coherent features (layers and intrusions), Richardson number $Ri^{-1} = U_z^2/N^2$ (see Figure 4.1) and the relative alignment of temperature and salinity gradients. The density ratio R_ρ (plotted in Figure 4.1, smoothed with a median filter) indicates a 'Diffusive Convection'-favourable (DC) region along the top of the eddy where staircases were observed ($0 < R_\rho < 1$), a 'Salt-Fingering'-favourable (SF) region in the middle and at the base of the eddy ($R_\rho > 1$) and a 'Doubly-Stable' region within and below the eddy ($R_\rho < 0$) where shear-driven mixing was thought to occur based on the enhanced Richardson number below the eddy (panel D). Traditionally, different types of double-diffusive convection are parameterised separately (e.g. Inoue et al., 2007). However, our method does not depend on the type of double diffusion based on measured T/S gradients, instead assuming that the opposing gradients necessary for double diffusion are created by sub-measurement scale spice variance. The T/S gradients can take any alignment relative to one another, subject to the condition for an up-gradient diapycnal buoyancy flux (Φ_d) derived in Chapter 2.

4.3 Method

In this section we start by presenting a new form for the diapycnal buoyancy flux, φ_d, in terms of spice gradients before describing our method for down-scaling the observed spice gradients (i.e. inferring their size at sub-measurement scales) in order to estimate φ_d and the dissipation rate, ε.

Our method can be summarized as follows. First, assuming double-diffusive convection is the driver of turbulence, we take $\langle\varepsilon\rangle = -\langle\varphi_d\rangle$, where $\langle\cdot\rangle$ is an implicit average over the volume between observations. The diapycnal flux φ_d is then re-expressed in terms of spice gradients and buoyancy gradients. We assume that the buoyancy and spice gradients are anti-correlated, justified with reference to the observations, which gives an approximate upper bound for -$\langle\varphi_d\rangle$. Hypothesising that the sub-measurement scales are dominated by quasi-geostrophic (QG) stirring along isopycnals, we assume the buoyancy gradients are constant and the spice variance is modelled with the QG wavenumber scaling for passive tracers i.e. $\tilde{k}^{-1}$ in stretched coordinates. This scaling is taken to hold down to the critical scale at which φ_d drives convective overturns. The amplitude of the synthetic spice power spectrum is estimated using a two-point correlation calculated locally from the observations. The power spectrum is then used to estimate the mean spice gradient magnitude down to the overturning scale, which is then used to estimate φ_d and ε.

4.3.1 Diapycnal Buoyancy Flux

In Chapter 2, we wrote the diapycnal buoyancy flux

$$\varphi_d = \frac{(g\kappa_T\alpha\nabla T - g\kappa_S\beta\nabla S)\cdot\nabla b}{b_z^*}, \tag{4.1}$$

where (κ_T, κ_S) are the molecular diffusivities for T and S, g is the gravitational acceleration, $b = g\alpha T - g\beta S$ is the buoyancy using a linear equation of state for (α, β) the coefficients of thermal expansion and haline contraction respectively, and b_z^* is the gradient of the sorted buoyancy profile.

The definition of spice is complicated by the non-linear equation of state (Jackett and McDougall, 1985). However, we will use a linear approximation and define spice as $s_p \equiv \alpha T + \beta S$. Our method is applied across small changes in temperature (T) and salinity (S) between CTD casts, and so it is reasonable to assume linearity on the sub-measurement scale. We can re-express T and S in terms of buoyancy (b) and spice, i.e. $g\alpha T = (gs_p + b)/2$ and $g\beta S = (gs_p - b)/2$, where g is the gravitational acceleration. This leads to the new expression

$$\varphi_d = \frac{\kappa_T + \kappa_S}{2b_z^*}|\nabla b|^2 + g\frac{\kappa_T - \kappa_S}{2b_z^*}\nabla b\cdot\nabla s_p. \tag{4.2}$$

In the single-component limit where the two diffusivities are equal, the second term disappears, so we can consider it as a double-diffusive contribution. Using molecular values for the diffusivities, $\kappa_T >> \kappa_S$ so $\kappa_T + \kappa_S \approx \kappa_T \approx \kappa_T - \kappa_S$ and hence the two prefactors are of similar size, aside from the factor of g.

In order to estimate the dissipation rate due to double diffusion, we will assume that the dissipation is entirely forced by an up-gradient buoyancy flux as discussed in the introduction. In Chapter 2, we showed that background potential energy is converted into available potential energy when the average of φ_d over a given volume (Φ_d) is negative. Here, we attempt to estimate $\Phi_d \equiv \langle \varphi_d \rangle$ where angle brackets denote an average over a volume bounded by neighboring T/S measurement points. We then assume that all of the potential energy released by the up-gradient buoyancy flux is converted into kinetic energy and ultimately dissipated and set $\langle \varepsilon \rangle = -\langle \varphi_d \rangle$.

The average of Eq. 4.2 involves the correlation between buoyancy and spice gradients on sub-measurement scales. Here, we assume that the buoyancy and spice gradients are anti-correlated at the scales that contribute to $\langle \varphi_d \rangle$. In other words, we assume that $\left\langle \nabla b \cdot \nabla s_p \right\rangle = \left\langle |\nabla b||\nabla s_p| \cos(\psi) \right\rangle \approx -\left\langle |\nabla b||\nabla s_p| \right\rangle$, where $\cos(\psi)$ is the correlation coefficient. Since we assume that $\cos(\psi) = -1$, our method provides an approximate upper bound to the dissipation rate associated with double diffusion. There is evidence to support this assumptions in the data from Fine et al. (2018). Figure 4.2(A) shows the coherence between the vertical spice and buoyancy gradients

$$C_{s_p,b} = \frac{\overline{\left| \widehat{\partial_z s_p} \widehat{\partial_z b}^* \right|^2}}{\overline{\left| \widehat{\partial_z s_p} \right|^2} \; \overline{\left| \widehat{\partial_z b} \right|^2}}, \tag{4.3}$$

where $\widehat{\cdot}$ denotes a Fourier transform applied to de-trended vertical profiles and $\overline{\cdot}$ refers to an average of different realisations of the spectrum. We calculate the coherence for each CTD cast, obtaining multiple realisations of the spectra using the method of Welch (1967). The line in Figure 4.2(A) shows the average of $C_{s_p,b}$ across all profiles with one standard deviation indicated by shading. The coherence increases at small scales, implying that buoyancy and spice gradients are correlated, so $\left\langle \left| \nabla b \cdot \nabla s_p \right| \right\rangle \approx -\left\langle |\nabla b| \left| \nabla s_p \right| \right\rangle$ is a reasonable assumption. While the coherence is positive by definition, the vertical buoyancy and spice gradients are anti-correlated when $|R_\rho| < 1$ which is true for most of the section (Fig. 4.1C). Note that the averaging procedure does not heavily affect the sorted buoyancy gradient b_z^* by its definition.

When Eq. 4.2 is evaluated directly with buoyancy and spice gradients calculated using the available observations, the corresponding dissipation rate is very small $\sim O(10^{-12})$W/kg. This shows, unsurprisingly, that molecular diffusion is weak at the resolution of the observations (~300m in the horizontal and ~ 0.5m in the vertical). The central hypothesis of our method is that spice variance is transferred downscale by along-

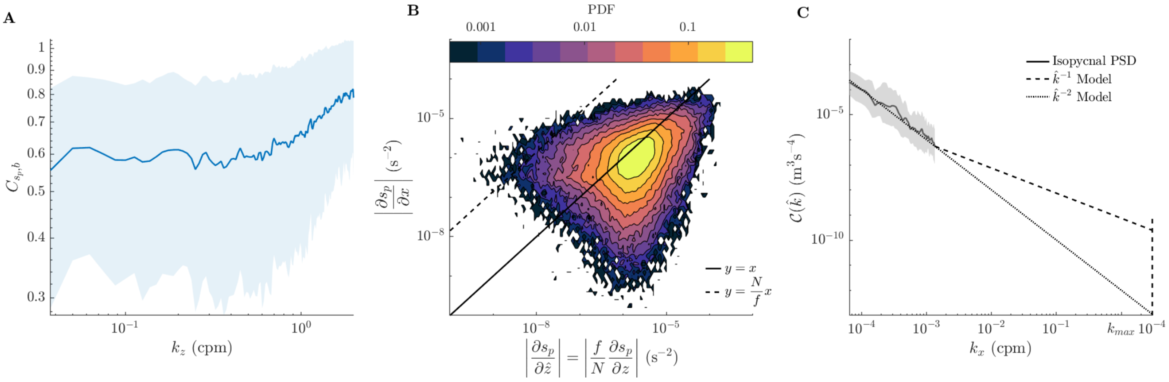

Fig. 4.2 **A**. Horizontal average of the magnitude-squared coherence of vertical gradients in spice and buoyancy calculated for each CTD cast plotted against stretched wavenumber $\tilde{k}_z = k_z \frac{f}{N}$. One standard deviation in shading. **B**. PDF of spice gradients in stretched coordinates ($\tilde{z} = Nz/f$) on log scale. Lines correspond to isotropy in stretched coordinates ($y = x$) and unstretched coordinates ($y = Nx/f$). **C**. PSD for spice variance along isopycnals, averaged with depth. Interquartile range of isopycnal spectra shown in shaded region.

isopycnal stirring until it reaches a scale where the up-gradient buoyancy flux drives double-diffusive motions. Since the hypothesised stirring is along-isopycnal, we take the buoyancy gradient on sub-measurement scales to be constant. Specifically, this allows us to assume first that $\langle|\nabla b||\nabla s_p|\rangle \approx \langle|\nabla b|\rangle\langle|\nabla s_p|\rangle$, and second that $\langle|\nabla b|\rangle = |\langle\nabla b\rangle|$, so the buoyancy gradient magnitude can be estimated by the value on the measurement scale. However, we have not assumed that the spice gradient is constant on sub-measurement scales, so $\langle|\nabla s_p|\rangle \neq |\langle\nabla s_p\rangle|$ in general and we must estimate $\langle|\nabla s_p|\rangle$ by other means. In the next section we describe a method for estimating the magnitude of the spice gradient on sub-measurement scales.

4.3.2 Down-scaled Spice Gradients

To estimate the sub-measurement-scale spice gradients, we use a statistical method based on the assumption that spice is stirred along isopycnals by quasi-geostrophic (QG) motions. The Rossby number associated with the eddy shown in Figure 4.1 is about 0.2 which is not inconsistent with the QG limit (Fine et al., 2018). Based on theory from Charney (1971), Haynes and Anglade (1997) and Smith and Ferrari (2009) showed that QG flow generates filaments of passive tracers (such as spice) with a horizontal to vertical aspect ratio of N/f where N is the buoyancy frequency $N = \sqrt{-\partial b/\partial z}$ and f is the Coriolis parameter. The data appear to be generally consistent with an N/f aspect ratio. Lines with a slope matching the local f/N slope are indicated in panel A of Figure

4.1. Figure 4.2(B) shows a joint PDF of spice gradients in stretched coordinates. The peak in the distribution lies close to the $y = x$ line, corresponding to isotropy in the stretched coordinate system.

Based on QG theory, for scales that are small compared to the eddies responsible for stirring, spice variance is expected to follow $\tilde{k}^{-1}$ (inertial-convective scaling) where $\tilde{k} = \sqrt{k_x^2 + k_y^2 + \tilde{k}_z^2}$ is the wavenumber magnitude in the stretched coordinate system $(k_x, k_y, \tilde{k}_z) = (k_x, k_y, f k_z / N)$ (Smith and Ferrari, 2009). In contrast, the QG buoyancy variance spectrum is much steeper ($\sim \tilde{k}^{-5}$), consistent with our assumption that the buoyancy gradients are constant on sub-measurement scales. Based on this theory, we use the following model for the sub-measurement-scale spice power spectrum,

$$\mathcal{P}_{s_p}(\tilde{k}) = A\tilde{k}^{-1}, \tag{4.4}$$

where A is a pre-factor that depends on the rate of generation of spice variance. The dependence of Eq. 4.4 on $\tilde{k}$ alone, reflects the isotropy of the spice variance in stretched coordinates. As will be discussed later, other forms of the spice variance spectrum can be used with this method.

The along-isopycnal spice variance spectrum from the Fine et al. (2018) data (Figure 4.2C) shows a $\tilde{k}^{-2}$ scaling, consistent with other observations of passive tracers at these scales (Klymak et al., 2015, Callies and Ferrari, 2013). Our modeled $\tilde{k}^{-1}$ spectrum at sub-measurement scales is indicated with a dashed line. MacKinnon et al. (2016) shows observational evidence for a k^{-1} scaling of temperature in salinity-controlled mixed layers for two separate observational datasets, however the transition to this scaling occurs at horizontal wavelengths $\sim$ 300m which is smaller than the available observations. In Section 4.4.1 we discuss the sensitivity of our results to the model spice power spectrum.

To estimate the spice gradients that contribute to φ_d we extrapolate the spice variance spectrum down to a scale corresponding to the convective overturns driven by double diffusion. Our underlying assumption is that the available potential energy generated by the up-gradient buoyancy flux at this scale drives convective motions and that the resulting turbulence fluxes kinetic energy further downscale until it is dissipated at the same rate. Hence, although spice gradients will persist down to the haline Batchelor scale, we estimate the spice gradients at the scale of the largest 3d turbulent motions which we take to be the Ozmidov scale $L_{Oz} = \sqrt{\frac{\varepsilon}{N^3}}$. This choice is consistent with the scaling for the layer thickness in diffusive convection proposed by Fernando (1989). Other choices are discussed in Zhou et al. (2016) who suggest that $L_Z = (\varepsilon^3 / \kappa_T N^8)^{1/4}$ provides a better match with observations and lab experiments. However, since $L_{Oz} = (Re_b Pr)^{1/4} L_Z$

and Re_b is small for the Fine et al. (2018) dataset (see Figure 4.3G) the two lengthscales yield similar dissipation rate estimates and we use L_{Oz} for simplicity.

We estimate the amplitude of the spice power spectrum, A, by calculating the along-isopycnal two-point correlation,

$$R(\tilde{r}) = \langle |s_p(\mathbf{x},t) - s_p(\mathbf{x}+\tilde{r}\mathbf{a},t)|^2 \rangle, \tag{4.5}$$

where $\tilde{r}$ is a distance in the stretched coordinate system and $\mathbf{a}$ is the along-isopycnal unit vector. Here, we calculate the two-point correlation between neighboring measurement points, interpolated vertically onto an isopycnal surface, centering our calculation of R between adjacent CTD casts. We can relate the two-point correlation to the spice power spectrum extrapolated down to the Ozmidov scale by taking the Fourier transform of Eq. 4.5 and applying the translation by $\tilde{r}\mathbf{a}$ as a wavenumber modulation in Fourier space, yielding

$$R(\tilde{r}) = 2\int_0^{\tilde{k}_{Oz}} \mathcal{P}_{s_p}(\tilde{k})(1-\cos(\tilde{k}\tilde{r}))d\tilde{k}, \tag{4.6}$$

where $\tilde{k}_{Oz} = 2\pi f/(NL_{Oz})$ is the Ozmidov wavenumber in stretched coordinates. Using the model spice spectrum (Eq. 4.4) then gives the amplitude

$$A = \frac{R(\tilde{r})}{2\int_0^{\tilde{k}_{Oz}} \tilde{k}^{-1}(1-\cos(\tilde{r}\tilde{k}))d\tilde{k}}, \tag{4.7}$$

where the integral in the denominator is related to the exponential integral.

We can then estimate the spice gradient magnitude (in stretched coordinates) using the 2-norm $\langle |\tilde{\nabla} s_p| \rangle \approx \sqrt{\langle |\tilde{\nabla} s_p|^2 \rangle}$ and applying Parseval's theorem (in stretched coordinates), using the model spectrum from Eq. 4.4,

$$\langle |\tilde{\nabla} s_p|^2 \rangle = \int_0^{\infty} \tilde{k}^2 \mathcal{P}_{s_p}(\tilde{k})d\tilde{k} = A\int_0^{\tilde{k}_{Oz}} \tilde{k}d\tilde{k} = \frac{1}{2}A\tilde{k}_{Oz}^2. \tag{4.8}$$

Applying isotropy in stretched coordinates, we can re-scale the vertical coordinate to write the average spice gradient in unstretched coordinates, $\langle |\nabla s_p| \rangle$, in terms of the spice gradient in stretched coordinates, $\langle |\tilde{\nabla} s_p| \rangle$, giving

$$\langle |\nabla s_p| \rangle = \sqrt{\frac{2}{3} + \frac{N^2}{3f^2}} \langle |\tilde{\nabla} s_p| \rangle. \tag{4.9}$$

Evaluating the spice gradient magnitude $|\nabla s_p|$ in Eq. 4.2, we get the form for the average dissipation rate $\langle\varepsilon\rangle$. In summary, the method can be written as a series of steps

Algorithm 1: Method summary

```
Step 1: Calculate the two-point correlation, $R(\tilde{r})$, for the spice field (Eq. 4.5).
Step 2: Make an initial guess for $\langle\varepsilon\rangle$ to estimate $k_{Oz}$.
Step 3: Calculate $A$ using Eq. (4.7).
Step 4: Update the estimate for $\langle\varepsilon\rangle$ using
    $\langle\varepsilon\rangle = -\langle\varphi_d\rangle = -\frac{\kappa_T+\kappa_S}{2b_z^*}\langle|\nabla b|^2\rangle + g\frac{\kappa_T-\kappa_S}{2b_z^*}\langle|\nabla b|\rangle\sqrt{\frac{2}{3}+\frac{N^2}{3f^2}}\sqrt{\frac{A}{2}}k_{Oz},$    (4.10)
    applied at each point.
Step 5: Return to Step 3 and continue until $\langle\varepsilon\rangle$ converges.
```

4.4 Results

4.4.1 Comparison with Microstructure

The results of our method as applied to the data from Fine et al. (2018) are shown in Figure 4.3A. The match between the estimated and measured dissipation rates is generally very good. Both the pattern and magnitude of the dissipation are captured by the method, even in areas of doubly stable stratification, not traditionally thought of as active areas of double-diffusive convection. In the centre of the eddy, where the stratification is very weak, the method predicts very low levels of dissipation ($< 10^{-10}$ m^{2}s^{-3}), however the noise floor for the shear probe observations of ε is about 10^{-10} m^{2}s^{-3} so we cannot compare these small values. Comparing the horizontal averages of dissipation rate on the right we can also see the close match between observations and our method. Figure 4.3D shows the horizontal average of the heat flux inferred from the dissipation rate using the Osborn (1980) method using a mixing coefficient $\Gamma = 1$, following Fine et al. (2018) and St. Laurent and Schmitt (1999). Following the method described in Fine et al. (2018) we exclude values where 'interfaces' were identified using a threshold $\frac{\partial T}{\partial z} > 0.2$ °Cm^{-1}). The agreement between the Osborn (1980) method for microstructure and our prediction implies that we can also estimate heat fluxes along the top and sides of the eddy. There is a discrepancy beneath the eddy that is discussed below, which suggests that double diffusion is not the dominate source of turbulence in this region. We have applied an assumption that $\Gamma = 1$ everywhere to obtain our estimate for the heat flux, however this may overestimate the heat flux in regions where turbulence is driven by non-double-diffusive processes, such as below the eddy, where $\Gamma = 0.2$ is a more appropriate assumption (Gregg et al., 2018). The fluxes at the eddy base are small partly due to weak temperature gradients at this location.

Microstructure measurements of ε have an uncertainty of a factor of around 2 (Fine et al., 2018). Histograms of the ratio of the estimated and observed dissipation rates are shown in Figure 4.3E,F (points with ε_{pred} below the instrument noise floor of 10^{-10} m^{2}s^{-3} are excluded). The comparison in panel E shows a log-normal distribution around an average bias of 0.89 with a tail to the distribution for small values. The mean bias corresponds to an average observed dissipation of 9.7×10^{-10} m^{2}s^{-3} and average predicted dissipation of 8.5×10^{-10} m^{2}s^{-3}. Excluding points with buoyancy Reynolds numbers $Re_b = \frac{\varepsilon}{\nu N^2} > 20$ (a threshold value for double-diffusion used by Inoue et al. (2007) amongst others) removes the tail such that 72% of the estimated dissipation rates are within a factor of 3 of the observed values, although note that very little data here have $Re_b > 20$ (as shown in Figure 4.3G). Differences between our prediction and observations (at low Re_b) are similar to those occurring due to natural variability (Moum et al., 1995). The enhanced Re_b may be the result of shear as the Richardson number is smaller above and below the eddy (Figure 4.1), however it is still unclear when shear will damp or enhance double-diffusive convection (Padman, 1994, Shibley and Timmermans, 2019). The enhanced Re_b beneath the eddy explains the discrepancy between the horizontally averaged prediction and observation in Figure 4.3C.

Panel F divides the data between areas usually identified as 'double-diffusive convection favourable' ($0 < R_\rho < 1$), 'salt fingering favourable' ($R_\rho > 1$) and 'doubly-stable' ($R_\rho < 0$). This panel shows that the method works well for 'DC' and 'DS' regimes but potentially overestimates the dissipation rate in 'SF' regimes. It is possible that salt-fingers are present, which may change the appropriate overturning length scale. Another explanation is that our assumption of anti-correlating buoyancy and spice gradients breaks down for $|R_\rho| > 1$. However, there is too little 'SF'-data here to fully analyze these possibilities and the method still works relatively well in 'SF' regions. Alternatively, if we were to assume a persistent $\tilde{k}^{-2}$ scaling down to the Ozmidov scale, the patterns of the estimated dissipation rate would be qualitatively similar, but the magnitude of the dissipation rate would decrease by about a factor of 3 (see panel E). The model spice spectrum represents the largest sensitivity in the method and further observations of the $\mathcal{O}(1) - \mathcal{O}(100)$ m scales could help test and improve the method.

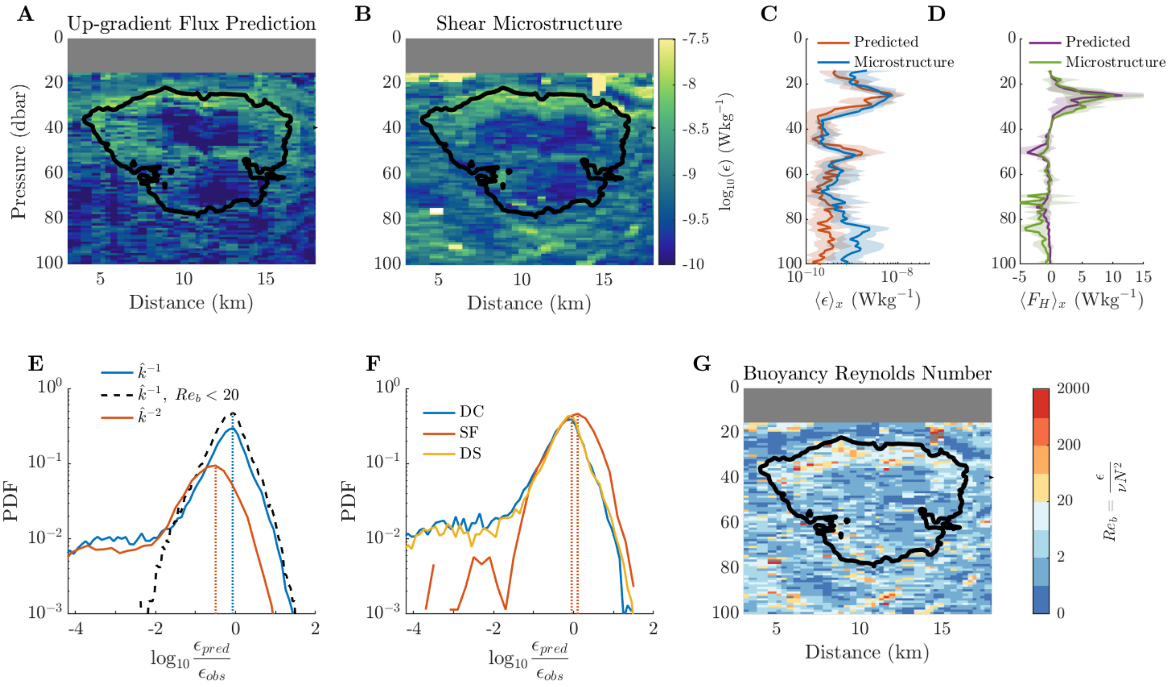

Fig. 4.3 Comparison of predicted **A**., **B**., **C**. predicted dissipation rates ε (m^{2}s^{-3}) (**A**) with microstructure-inferred values (**B**) (Fine et al., 2018). **D**., Osborn (1980) estimate for the heat flux using $\Gamma = 1$ for predicted and microstructure ε. Horizontal mean (**C**,**D**), taken between 8 and 13km with shaded spatial standard deviations. **E**., **F**. Log-histograms of ratio between the predicted ε_{pred} and observed ε_{obs} dissipation rate. **E**. Data calculated using $\tilde{k}^{-1}$ model, $\tilde{k}^{-2}$ model and $\tilde{k}^{-1}$ model excluding points where $Re_b = \frac{\varepsilon}{\nu N^2} > 20$. **F**. Subdivision of data by $R_\rho = \alpha\frac{\partial T}{\partial z}/\beta\frac{\partial S}{\partial z}$ value (see text). **G**. Buoyancy Reynolds number Re_b calculated using microstructure.

4.4.2 Method Sensitivity

The T/S section from Fine et al. (2018) has a high resolution ($\Delta x \sim 200-1000$ m in the horizontal and $\Delta z = 0.25$ m in the vertical). A natural question is whether the method would work when applied to a lower resolution section of T/S. To test this, we subsample the original data at lower horizontal resolution. Figure 4.4 shows three different resolution comparisons in the three columns. In each comparison we calculate the dissipation rate using subsampled temperature and salinity sections, and we compare the result with the observed double-diffusive dissipation rate subsampled at the same resolution. Note that the data in Figure 4.4 are calculated based on horizontally gridded T/S data, whereas the method in Figure 4.3A is applied to ungridded data (which gives a better agreement with observations). Using lower resolution T/S data somewhat increases the estimated dissipation rate, although the method performs well even at significantly reduced resolution. This suggests that our method could be applied to lower resolution CTD sections which are much more widely available.

For the observations of Fine et al. (2018), the first term in Eq. 4.10 is small, and $N \gg f$, so we can write

$$\langle \varepsilon \rangle = \left(\frac{1}{\sqrt{6}} \pi g (\kappa_T - \kappa_S) \frac{\langle |\nabla b| \rangle}{b_z^*} N^{\frac{3}{2}} \sqrt{A} \right)^{\frac{2}{3}} . \tag{4.11}$$

Eq. 4.11 more clearly shows the dependence of $\langle \varepsilon \rangle$ on the rate of generation of spice variance via A, the buoyancy frequency N and the term $\langle |\nabla b| \rangle / b_z^*$ which gives a measure of the curvature of isopycnals. If we set the term $\langle |\nabla b| \rangle / b_z^*$ constant, we underestimate the dissipation rate along the top of the eddy, where the isopycnals heave, suggesting that the large-scale variations in density may have a direct effect on the small scale turbulence.

If we vary the spice spectrum amplitude A (Eq. 4.7), by a scale factor a, although the pattern of the dissipation rate remains similar to Figure 4.3A, the magnitude changes by a factor of about $a^{1/3}$ (by considering Eq. 4.11). Therefore, an error in A by a factor of 10 would result in an estimate of ε that is incorrect by a factor of ~ 2.15. This relatively low sensitivity to A is the reason for the lack of sensitivity to the scale at which the $\tilde{k}^{-2}$ spectrum transitions to $\tilde{k}^{-1}$ in our model. This also explains why the method maintains skill at low resolution (Figure 4.4) despite the disagreement between the assumed $\tilde{k}^{-1}$ spectrum and the observed $\tilde{k}^{-2}$ spectrum (Figure 4.2). This effect may be corrected for by using a more complex model spectrum, however that is left as future work. The size of the eddy is also important here. The $\tilde{k}^{-1}$ slope is hypothesised to be the result of the eddy stirring, so for larger eddies we may expect the $\tilde{k}^{-1}$ model spectrum to hold at larger scales.

Although we calculate α and β at each grid point using the fully non-linear equation of state, we assume a linear equation of state on sub-measurement scales in our method. If we use a single constant value for α and β across the whole section, the estimated dissipation rate would change by up to a factor of 1.8, so the effects of a non-linear equation of state also represent an uncertainty in our method that may explain some of the discrepancies in Figure 4.4.

4.4.3 Conclusion

We have introduced a new method for estimating the dissipation rates associated with double diffusive turbulence from a temperature and salinity section. We used an energetic argument and a statistical approach which applies to general double-diffusive processes.

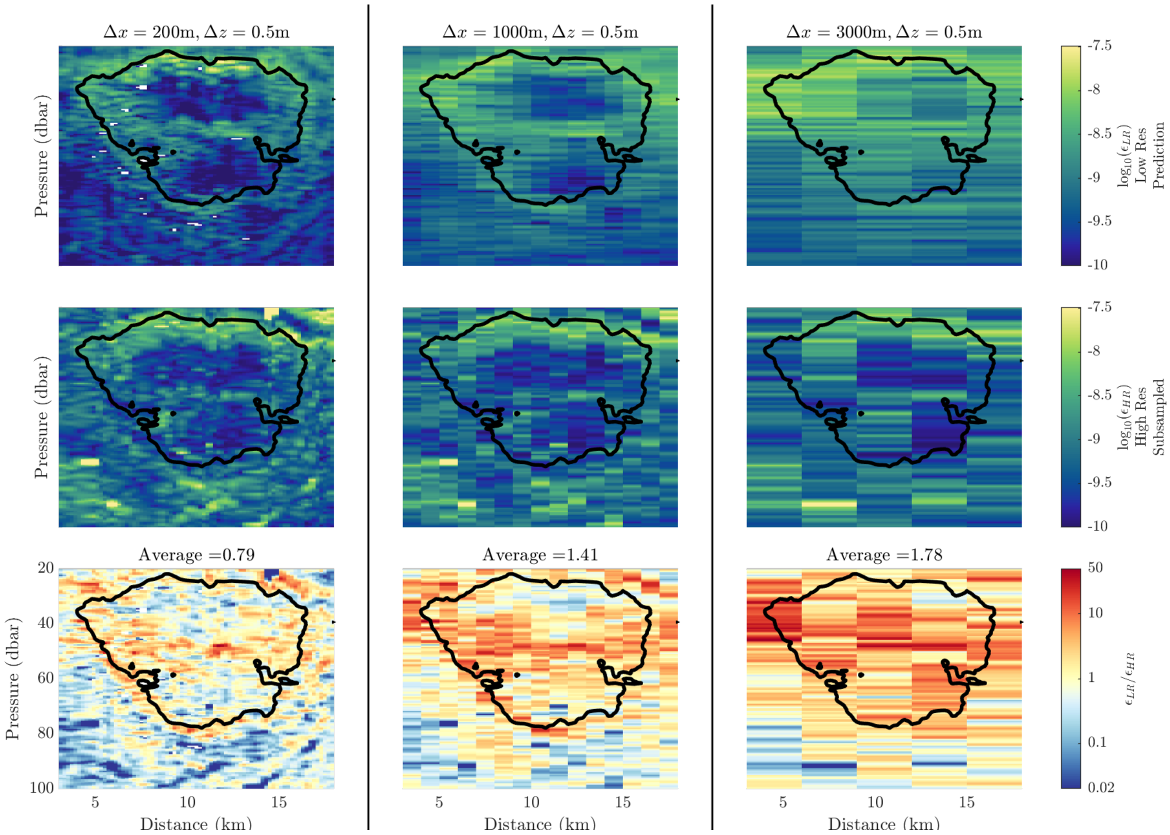

Fig. 4.4 Top row shows inferred dissipation rate ε using T/S data sampled at the given resolution in the title. Middle row shows observed ε using full T/S data, subsampled at the given resolution. Bottom row shows ratio between top and middle figure values. Colorbar is on a log-scale and mean value corresponds to the peak of the distribution of $\varepsilon_{pred}/\varepsilon_{obs}$.

For points with low buoyancy Reynolds number ($Re_b < 20$) in the data from Fine et al. (2018), our method closely matches observations (72% of estimated dissipation rates are within the observational uncertainty). Fine et al. (2018) used observations of dissipation rate to infer heat fluxes that matched those calculated using thermal microstructure observations. The close match in dissipation rates between our method and observations suggests our method may be used to infer heat fluxes in other locations where double diffusion is active. Finally, we showed that our method can be applied (with additional uncertainties) to T/S data with coarse spatial resolution, opening the door to applying the method to more widely-available lower resolution CTD sections.

4.5 Recent Developments

Since the publication of this article, an article written by Elizabeth Fine has been submitted to the *Journal of Physical Oceanography* and is currently in review. In this article, on which I am a coauthor, they analyse data from a microstructure survey of thermohaline intrusions found during the same Chukchi slope expedition in 2015 as the data from Fine et al. (2018). They collected the same form of data as a similar resolution to the data from Fine et al. (2018). As part of the analysis of this intrusion data, they apply our methodology for predicting dissipation rates. They initially apply a $\hat{k}^{-1}$ model for spice variance, but find that it overestimates the dissipation rate across much of the intrusion. However, using a $\hat{k}^{-2}$ scaling down to the Ozmidov scale, they found that our method predicted well the variation and magnitude of dissipation rate across the intrusion feature. They argue that the observations show a k^{-2} along-isopycnal spice variance and that this can be assumed to continue down to smaller scales. Future observations of $O(1\text{ m})$ to $O(100\text{ m})$ scales are required to ascertain when we can expect a $\hat{k}^{-1}$ scaling and when we can expect a $\hat{k}^{-2}$ scaling. In Chapter 5 we will show evidence of a $\hat{k}^{-1}$ scaling at these intermediate scales beneath George VI Ice Shelf.

Fine et al. (*in review*, 2021) also apply the Gregg (1989) finescale parameterisation of dissipation from internal wave-breaking based on shear measurements. They find that some features in the observations are captured well by the shear parameterisation and some are captured well by our method. However, the most accurate match to observed dissipation rates is achieved by adding the predicted dissipation rates from our method and the predicted dissipation rates from the Gregg (1989) parameterisation. The turbulence on sub-measurement scales likely varies spatially, with some regions driven by breaking internal waves, some regions with double-diffusive convection and some regions where both processes are important. Further work needs to be done to analyse the crossover between these two parameterisations, and the reason why a simple addition is so effective at reproducing observations.

Chapter 5

Double diffusion as a driver of melt in the stratified boundary layer under George VI Ice Shelf

> As we drew nearer we could see it more and more clearly. At first sight the Barrier appeared as a sweeping crescent of ice about 150 *shaku* high; it was like a series of pure white folding screens, or perhaps a great white snake at rest.
>
> *Nobu Shirase*
> from
> *Nankyokuki (1913)*

This chapter has been submitted as a paper with coauthors Peter Davis, Keith Nicholls and John Taylor. Some minor edits have been made from the submitted version.

5.1 Introduction

Over recent decades ice mass loss from Antarctica has been the most dramatic on the West Antarctic Peninsula (Rignot et al., 2019). This is primarily due to warmer and more persistent intrusions of Circumpolar Deep Water (CDW) onto the continental shelf. CDW is particularly warm ($\sim 1 - 2°C$), with a high capacity to melt ice. CDW is also relatively dense, due to its high salinity ($\sim 34.5-34.7$ ppt), leading CDW to intrude at depth beneath ice shelves. Turbulent processes flux heat upwards towards the ice, causing enhanced melting. In many locations, turbulence is driven by shearing flow past the ice (Davis and Nicholls, 2019, Jenkins et al., 2010). Within regional ice shelf cavity models, a parameterization is used that relates the melt rate to the velocity some distance away from the ice (Holland and Jenkins, 1999, Dinniman et al., 2016).

The most common parameterization is the 'three equation model' (Holland and Jenkins, 1999, Hellmer and Olbers, 1989). This couples budgets for heat and salt with a phase change condition that relates the freezing temperature of water to the salinity and pressure at the ice boundary,

$$F_m^T = F_i^T + F_O^T, \tag{5.1}$$

$$F_m^S = F_i^S + F_O^S, \tag{5.2}$$

$$T_b = \lambda_1 S_b + \lambda_2 + \lambda_3 P. \tag{5.3}$$

Here S_b and T_b are the boundary salinity and temperature, P the pressure and $\lambda_{1,2,3}$ are constants. F_m represents fluxes from melting (i.e. latent heat and freshwater flux), F_i represents fluxes from the ice (usually neglected for ice shelves (Holland and Jenkins, 1999)) and F_O represents fluxes from the ocean. Ocean fluxes F_O^T and F_O^S are the focus of the parameterization. Models and observations often assume these fluxes are linearly related to the difference between far field and boundary values (i.e. $F_O^T \propto \Delta T = T_\infty - T_b$ and $F_O^S \propto \Delta S = S_\infty - S_b$), and depend on the far-field mean flow speed $\langle U \rangle$ (usually linearly i.e. $F_O^T, F_O^S \propto \langle U \rangle$). More complex parameterizations account for the turbulence-damping effects of stratification (McPhee et al., 1987, Vreugdenhil and Taylor, 2019), but a linear relationship to ΔT, ΔS and $\langle U \rangle$ is often assumed (Dinniman et al., 2016), with proportionality constants constrained by observations (Malyarenko et al., 2020). We will refer to the combination of Eqns. 1-3 with linear parameterizations for the ocean fluxes F_O^T and F_O^S as the 'three-equation formalism'.

Davis and Nicholls (2019) presented turbulence mooring data collected beneath Larsen C Ice Shelf (LCIS) in 2012. Their data were consistent with a shear-driven boundary layer, varying with the tidal cycle (McPhee, 2008). Davis and Nicholls (2019) found that the three-equation formalism gave accurate melt rates using similar proportionality constants to Jenkins et al. (2010). In this chapter we will consider data collected beneath George VI Ice Shelf (GVIIS) in the same 2012 field campaign as the LCIS data using the same sampling techniques. The effects of stratification on turbulence underneath LCIS were thought to be weak (Davis and Nicholls, 2019). However, the stratification observed underneath GVIIS is much stronger, extending up into the boundary layer (Kimura et al., 2015, Venables et al., 2014), shown in Figure 5.1D.

The effect of stratification on the ice shelf-ocean boundary layer has been investigated in simulations (Vreugdenhil and Taylor, 2019) and in data collected beneath sea-ice (McPhee et al., 1987, Holland and Jenkins, 1999). In these studies, stratification acts to damp shear-driven turbulence, and this effect can be modelled using the self-similarity theory of Monin and Obukhov (1954). However, beneath GVIIS, Conductivity, Temperature, Depth (CTD) profiles taken via the boreholes in the 2012 field campaign suggest a more complex role for stratification (Venables et al., 2014, Kimura et al., 2015). Persistent layers in temperature (T) and salinity (S) in the 20 m directly beneath the ice were found (shown in Figure 5.1D inset). This was the first time layering had been observed directly adjacent to the base of an ice shelf, however the number of observations beneath ice shelves is limited. Kimura et al. (2015) suggested the observed T/S layering was due to double-diffusive convection, where the differences in molecular diffusivity for heat and salt enable the release of potential energy. Active double-diffusive convection suggests that stratification may act to enhance boundary layer turbulence, rather than damping it. Within quiescent under-ice shelf regimes, Begeman et al. (2018) and Stevens et al. (2020) both suggested the presence of double-diffusive convection away from the boundary layer, but so far limited evidence of this has been presented.

Kimura et al. (2015) suggest layers adjacent to the ice are formed by 'melt-driven convection', where destabilising temperature gradients near the ice base drive convection, overcoming salinity gradients due to the faster diffusion of heat compared with salt. This theory is supported by Large-Eddy-Simulations from Rosevear et al. (2021), who found layers developing due to melt-driven convection in their simulations of a sheared, stratified ice-ocean boundary layer. Similar simulations were conducted in Chapter 3 with no ambient stratification or shearing, where turbulence was forced isotropically to match observed dissipation rates. In Chapter 3, we found persistent double-diffusive convection in a 'George VI-like' parameter regime, without layers forming, suggesting layers are not necessary for the presence of double-diffusive convection beneath an ice shelf. In this chapter we apply a framework, developed in Chapters 2 and 4, to estimate the dissipation rate associated with double-diffusive processes without relying on the presence of thermohaline layers.

In our analysis of the GVIIS mooring data, we find that kinetic energy dissipation rates do not vary with mean flow speed, unlike in the data from beneath LCIS (Davis and Nicholls, 2019). The data from GVIIS are not consistent with a shear-driven boundary layer, or the assumption that heat and salt fluxes are related to far-field velocity in the

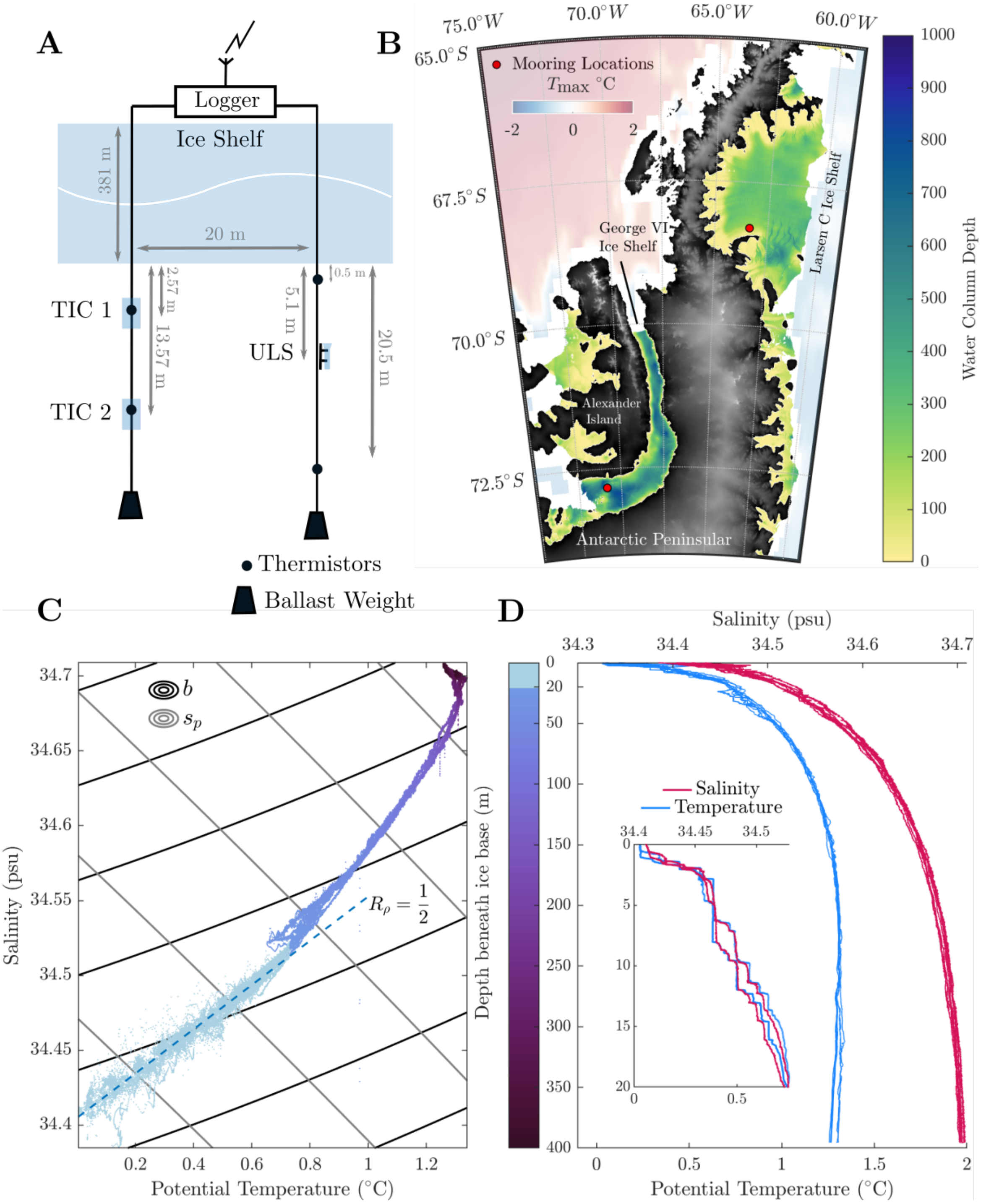

Fig. 5.1 **A**. Schematic of mooring. **B**. Location of moorings. Maximum ocean temperature data taken from WOA decadal climatology (Locarnini et al., 2018). Water column depth taken from BedMachine (Morlighem et al., 2020). **C**. Temperature/Salinity plot of 34 CTD casts. upper 20 m highlighted as location of thermohaline staircase and $R_\rho = 1/2$ relationship given by dashed line. Buoyancy and spice contours included. **D**. CTD profiles including inset of upper 20 m for selected profiles.

three-equation formalism. However, turbulence is still present and drives a melt rate of 1.4 m yr^{-1}.

To explain the observed turbulence, we use the method from Chapter 4 (referred to as the M21 method) which hypothesises that double-diffusive convection is linked to along-isopycnal stirring of temperature and salinity. At small-scales, diffusion of the resulting temperature and salinity gradients from along-isopycnal stirring causes an up-gradient diapycnal buoyancy flux that drives turbulence. We apply the M21 method using temperature measurements taken every $\sim$ 20 minutes, and the predicted dissipation rates compare favourably to the observed dissipation rates throughout the year-long mooring timeseries. This suggests that heat and salt fluxes associated with double diffusion could be driving the observed melting.

In this chapter, we first present the details of the mooring measurements beneath GVIIS. We show that dissipation rates beneath GVIIS do not depend on mean flow speed, in contrast to the assumption of shear-driven heat flux in the three-equation formalism and the data from beneath LCIS (Davis and Nicholls, 2019). In the third section we introduce the M21 method and show that observed dissipation rates beneath GVIIS can be explained by the stirring of temperature and salinity variance along isopycnals. Finally, in the fourth section we show that our hypothesis of a double-diffusive boundary layer is consistent with the observed heat flux through the boundary layer and the observed melt rates.

5.2 Observations

Two access holes, 20 m apart, were drilled using hot water, through GVIIS (S 72° 49.9', W 070° 50.6', see Figure 5.1) in January 2012. Multiple Conductivity, Temperature, Depth (CTD) profiles were taken through both holes over a 5 day period, as well as microstructure profiles, reported on by Venables et al. (2014) and Kimura et al. (2015). Using the first hole, Turbulence Instrument Clusters (TICs), consisting of Modular Acoustic Velocity Sensors (MAVS), thermistors and MicroSquid temperature sensors, were installed at 2.57 m and 13.57 m beneath the ice base (identified at 333.4 dbar). In the second access hole, (ice base identified at 334.84 dbar), a thermistor chain was installed, with 11 thermistors (we use two in the boundary region, at depths in Figure 5.1), and an Upward-Looking Sonar (ULS) was installed 5.1 m beneath the ice base. The ice thickness was 381.2 m, with a water column depth of 636.3 m.

The water column was strongly stratified, with a maximum temperature of 1.29 °C and maximum salinity 34.71 ppt (see Figure 1), suggestive of lower Circumpolar Deep

Water (Moffat et al., 2009). The melt rate averaged 1.4 m yr^{-1} over the year-long mooring, varying between around 0.5 and 3 m yr^{-1} on weekly timescales, consistent with previous estimates for GVIIS (Jenkins and Jacobs, 2008, Bishop and Walton, 1981, Corr et al., 2002).

The TICs sampled in 15 minute bursts every 2 hours, providing dissipation estimates and mean flow speeds averaged over a 15 minute period. Mean flow speeds vary between 0.5 and 13 cm s^{-1} (see Figure 5.2A), compared with the wider range of speeds of between 1 and 25 cm s^{-1} beneath LCIS (Davis and Nicholls, 2019). There was no strong spring-neap tidal cycle visible, unlike beneath LCIS; however, significant diurnal (K1, O1) and semidiurnal (S2, M2) tides are present, consistent with data from Potter and Paren (1985).

We found an inertial subrange ($k^{-5/3}$ wavenumber slope) in the horizontal kinetic energy spectra (shown in Figure 5.3) derived from the MAVS. Since the water column was strongly stratified, this is suggestive of a 'stratified turbulence' regime (Lindborg, 2006), as opposed to unstratified three-dimensional turbulence assumed in Davis and Nicholls (2019). We used the Lindborg (2006) scaling to estimate dissipation rates (further details of our instrumentation and methodology are given in Supplementary Material). The dissipation rate $\varepsilon = \nu \left\langle \frac{\partial u_i'}{\partial x_j}^2 \right\rangle$ against mean flow speed $\langle u \rangle$ is shown in Figure 5.2, panels B and C, as a function of the mean flow speed $\langle u \rangle$. The averaging operator $\langle \cdot \rangle$ denotes an average over the 15 minute sampling burst. We find no significant correlation between mean flow speed and dissipation rate at either the upper or lower MAVS, particularly compared with the data from Davis and Nicholls (2019). The magnitude and trend in the GVIIS data is significantly reduced compared with the LCIS data.

There is also a lack of correlation between the Reynolds stress-based estimate of the friction velocity $u^* = (\langle u'w' \rangle^2 + \langle v'w' \rangle^2)^{1/4}$ (McPhee, 2008, Davis and Nicholls, 2019) and the mean flow speed (see Figure 5.2D). The prime $'$ denotes a departure from the 15 minute burst mean, such that $u = \langle u \rangle + u'$. This suggests that a constant drag coefficient $C_d = \langle u \rangle^2 / u^{*2}$ model for the friction velocity is inappropriate at this location. Assuming a constant-stress boundary layer to apply the u^* estimate in Figure 5.2D, gives a planetary length scale $u^*/f = 7.5 \pm 5.3$ m, for f the Coriolis parameter and ± indicating a standard deviation. The 'surface layer' in a shear-driven boundary layer denotes the region unaffected by rotation, with a depth estimated as $0.05u^*/f = 0.38 \pm 0.27$ m (Davis and Nicholls, 2019), which is above the upper TIC. The 'outer layer' denotes the region affected by rotation and shear, estimated as $0.23u^*/f = 1.73 \pm 1.23$ m (Fer and Sundfjord, 2007), which reaches the upper TIC during periods of large u^* ($u^* > 0.15$ cm s^{-1}). We find no evidence of correlation between dissipation rate and mean flow speed even when only considering large u^* values (not shown). The possibility of shear-driven turbulence

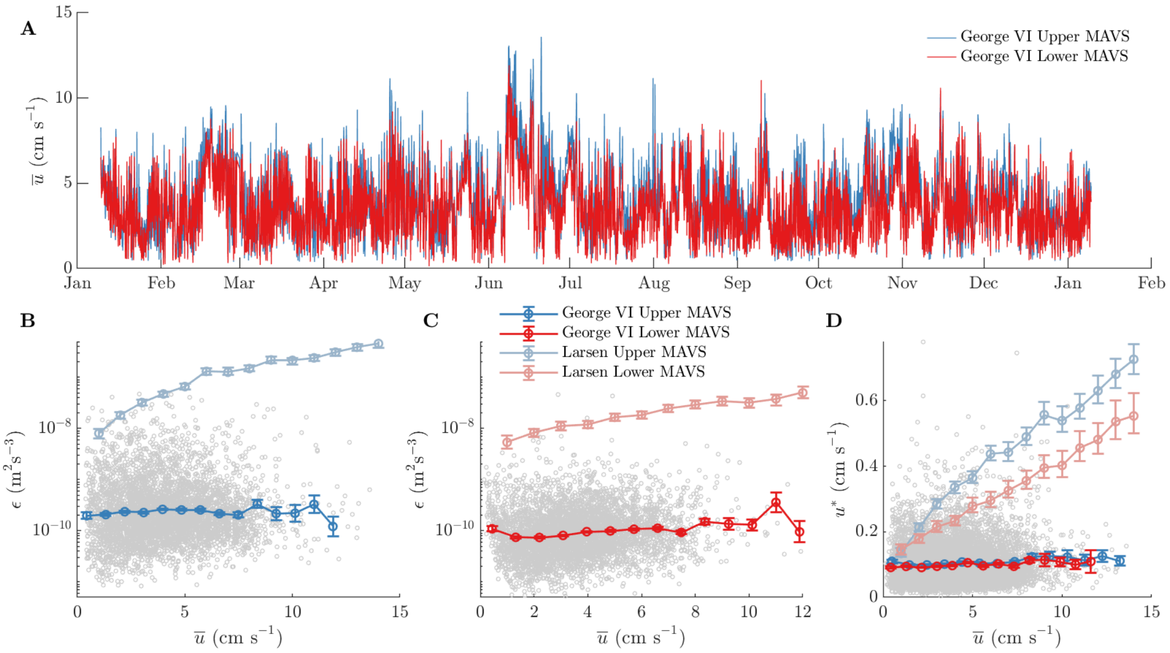

Fig. 5.2 **A**. Mean flow speed $\langle u \rangle$ timeseries for upper and lower MAVS. **B**. upper MAVS velocity against dissipation rate (burst estimates in grey) for GVIIS mooring data, LCIS mooring data included for comparison. **C**. Same as **B** but for lower MAVS. **D**. Friction velocity estimate $u^* = (\langle u'w' \rangle^2 + \langle v'w' \rangle^2)^{1/4}$ based on constant stress boundary layer for GVIIS upper and lower MAVS data (burst estimates in grey)

above our upper TIC cannot be ruled out. However, in the absence of double diffusion we would expect shear-driven turbulence at the upper TIC, which is not observed.

In Figure 5.3, panels A and C, we show the power spectral density (PSD) for horizontal kinetic energy (as defined in Lindborg, 2006), averaged over mean flow speed, plotted against wavenumber inferred from Taylor's 'frozen field hypothesis' (see Supplementary Material for details). The frozen field hypothesis is only considered valid when $u'_{\rm rms} << \langle u \rangle$ (Bluteau et al., 2011), which holds throughout our data. There is evidence of a $k^{-5/3}$ slope at low wavenumbers as mentioned above. In stratified turbulence, the PSD for horizontal kinetic energy is given by $E_{k_h} = 0.49\varepsilon^{2/3}k^{-5/3}$ (Lindborg, 2006). The kinetic energy spectra at low wavenumbers collapse onto the same $k^{-5/3}$ line when bin-averaged by $\langle u \rangle$ (Figure 5.2A,C), indicating a lack of correlation between dissipation rate and mean flow speed. The regions in which there is instrumental noise (see Supplementary Material) are shaded and the data in these regions are not included in our analysis. When the PSD for horizontal kinetic energy is averaged based on inferred dissipation rate within each burst (Figure 5.2B,D), the spectra no longer collapse, demonstrating the variation in turbulence levels across the data collection period.

5.3 Double Diffusive Model

To explain the variation in dissipation rate ε, we will investigate an alternative driver for turbulence in the ice shelf-ocean boundary layer: double-diffusive convection. Double-diffusive convection is a term for a form of convection (a release of potential energy), facilitated by the difference in molecular diffusivities of heat and salt. Double-diffusive convection is a turbulent mixing process driven by gradients in temperature and salinity. However, this mixing process must be resupplied with heat and salt in order to maintain itself. In Chapter 4, we suggested that the stirring of spice, $s_p = \alpha T + \beta S$ (α and β are the coefficients of thermal expansion and haline contraction), along isopycnals could be a generic mechanism for the supply of compensated gradients in temperature and salinity that drive double diffusion at small scales. We used this principle to develop a method to estimate small-scale double-diffusive buoyancy fluxes that force turbulence, using CTD data. We apply the M21 method to predict rates of double-diffusive convection in our mooring data using only coarsely-sampled thermistor data and the T/S relation from the initial CTD casts.

Details of our application of the M21 method are given in the Supplementary Material, however the key assumptions are as follows

- Double-diffusive convection is the only source of turbulence.
- Spatial variations in temperature and salinity that are not resolved by measurements are dominated by stirring along isopycnals, so gradients in spice s_p are much larger than gradients in density $\rho = \rho_0 - \alpha T + \beta S$ at small scales.

To complete the method, a model power spectrum for spice variance associated with along-isopycnal stirring is required. In Chapter 4, we use the form $\mathcal{P}_{s_p} = A\tilde{k}^{-1}$, where $\tilde{k}$ is the wavenumber magnitude in coordinates stretched by a factor of N/f in the vertical ($N = \sqrt{\partial \langle b \rangle / \partial z}$ is the buoyancy frequency, and f is the Coriolis parameter). In Chapter 4, we verified that the vertical to horizontal aspect ratio for spice gradients in the Arctic Ocean was close to N/f; however, resolution constraints prevented us from directly assessing the wavenumber scaling $\tilde{k}^{-1}$. In our mooring data, we have a range of scales of temperature variation, and as spice s_p is dominated by temperature, we can gain some clues about the scaling of spice. Based on CTD data we estimate N/f varies between 100 and 200 in the upper 2 m, which is comparable to a median value of 124 for the ratio between $\frac{\partial \langle T \rangle}{\partial z}$ and $\frac{\partial \langle T \rangle}{\partial x}$ measured by the upper thermistor (initially at 0.5 m depth). Vertical temperature gradients are calculated using a vertically-spaced pair of thermistors, and horizontal gradients are calculated by advecting temperature measurements laterally

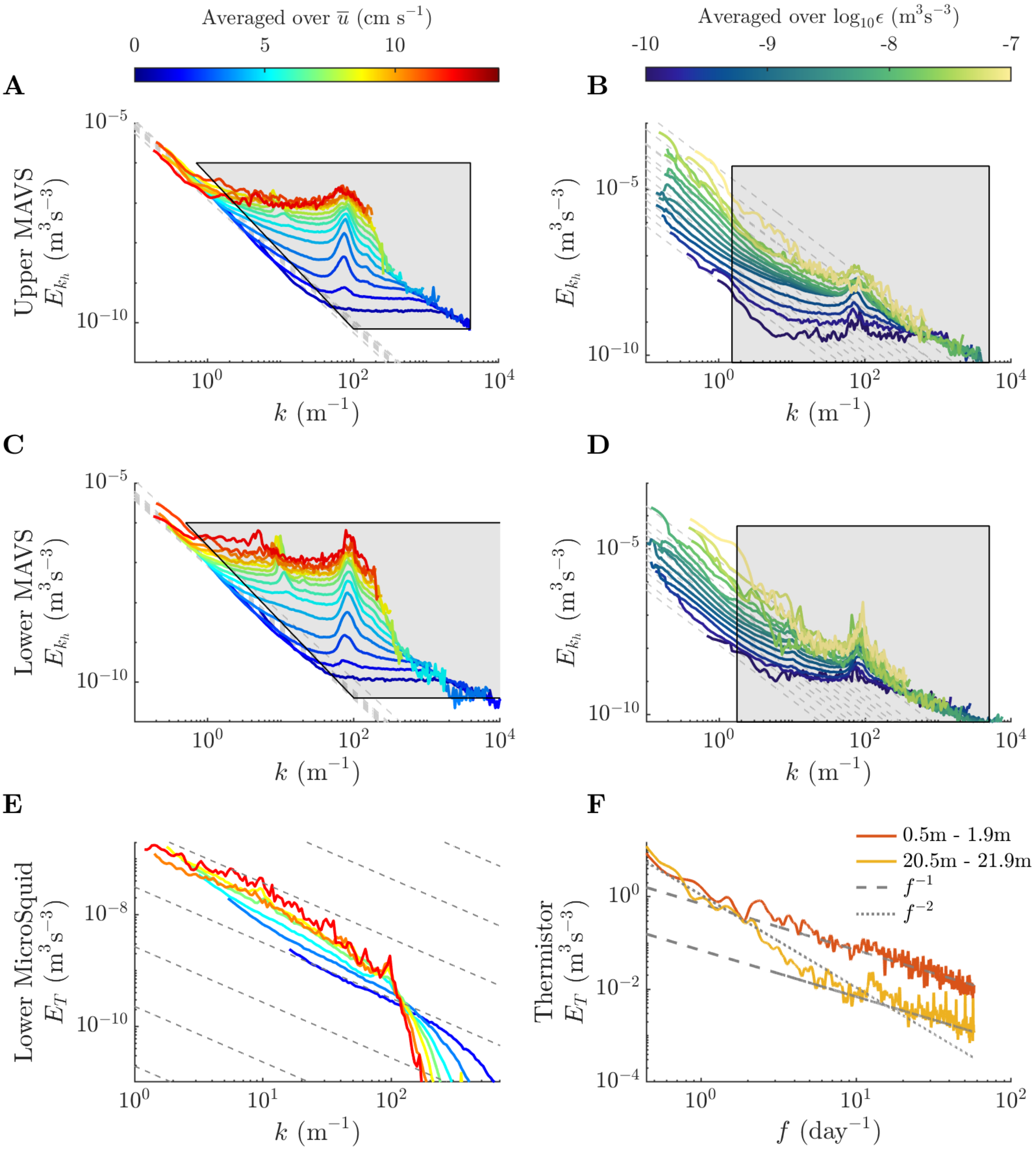

Fig. 5.3 **A,C**. Power Spectral Density (PSD) of horizontal velocity fluctuations against wavenumber k, averaged by mean flow speed for upper and lower MAVS. Grey box represents a $f = 0.01$ frequency cutoff. **B,D** Same as **A,C** but averaged by burst-estimated dissipation rate. **E**. PSD of temperature fluctuations from lower MicroSquid thermistor, against wavenumber k, averaged by mean flow speed. **F**. PSD of temperature fluctuations from thermistor chain, against frequency f over the full timeseries.

using the mean flow speed $\langle u \rangle$ (applying the frozen field hypothesis). The deeper thermistor (initially at 20.5 m) averages $\frac{\partial \langle T \rangle}{\partial z} \sim 10 \frac{\partial \langle T \rangle}{\partial x}$ which is a little lower than the values of N/f between 20 and 30 at ~ 20 m depth. These values indicate that the N/f aspect ratio is a reasonable assumption.

In Figure 5.3E we show data from the lower TIC, which included a high resolution MicroSquid FP07 temperature sensor. Plotting the power spectra averaged by mean flow speed against wavenumber (applying the frozen field hypothesis), we find a k^{-1} slope at low wavenumbers, consistent with a $\tilde{k}^{-1}$ slope in the spice variance spectrum. In Figure 5.3F we show the frequency spectrum for the thermistor data. The thermistors sample every 5 minutes, giving a large coverage in frequency space over the year-long mooring. The frozen field hypothesis can only be applied over relatively short time periods, so we do not plot the wavenumber power spectra for the thermistors. However, at high frequencies, where the frozen field hypothesis is valid, the wavenumber variation should be similar to the frequency variation. The spectral slope transitions from a f^{-2} scaling to a f^{-1} scaling in both thermistors, potentially due to temporal changes in temperature rather than spatial ones. However, a f^{-1} slope at high frequencies is consistent with our model $\tilde{k}^{-1}$ spice variance spectrum for sub-thermistor scales.

The simplified expression for the dissipation rate in the M21 method is

$$\langle \varepsilon \rangle = \left(\frac{1}{\sqrt{6}} \pi g (\kappa_T - \kappa_S) \frac{\langle |\nabla b| \rangle}{b_z^*} \sqrt{A} \right)^{\frac{2}{3}} N, \tag{5.4}$$

where A represents the magnitude of spice variance estimated using the two point correlation $R(\tilde{r}) = \langle |s_p(\mathbf{x}, t) - s_p(\mathbf{x} + \tilde{r}\mathbf{a}, t)|^2 \rangle$ with stretched coordinate $\tilde{r}$ taken along isopycnals. The method inputs are the buoyancy gradient $|\nabla b|$ (estimated as the buoyancy frequency squared $N^2 = \partial \langle b \rangle / \partial z$), the sorted buoyancy gradient b_z^*, and the two-point correlation for spice variance $R(\tilde{r})$. The mooring contained no salinity sensors, so we rely on temperature sensors and initial CTD T/S relationship to determine salinity for calculations of buoyancy and spice.

We compare the M21 method predictions with the observed dissipation rates in Figure 5.4. The M21 method is inherently statistical, so we expect some spread around the predicted dissipation. The mean dissipation rate estimated from the M21 method is within a factor of 1.15 and 1.20 of measured values at the lower and upper MAVS, respectively. The variation in dissipation rate at both upper and lower MAVS is also captured, with the predicted standard deviation within a factor of 1.08 of the observed standard deviation for both MAVS. We also capture the difference in dissipation rate between the upper and lower MAVS, suggesting that our method has predictive skill.

Our method underestimates the dissipation rate when the buoyancy Reynolds number $Re_b = \varepsilon/\nu N^2 > 20$, consistent with the application of the method to data from the Arctic from Chapter 4. The periods of high Re_b are associated with an order of magnitude larger dissipation rate (on average 1.3×10^{-9} m^{2}s^{-3} compared with 1.5×10^{-10} m^{2}s^{-3} at the upper MAVS). This could indicate that when $Re_b > 20$, double diffusion is not the only driver of turbulence. However, the majority of points in our dataset have $Re_b < 20$; at the upper MAVS, $Re_b > 20 \sim 21\%$ of the time and at the lower MAVS, $Re_b > 20$ only $\sim 9\%$ of the time. Similar intermittent behaviour is also observed in the microstructure profiles presented in Venables et al. (2014). Some CTD profiles show a strong staircase structure concurrent with low dissipation rates ($2-4 \times 10^{-10}$ m^{2}s^{-3}), whereas others show no staircase structure and elevated dissipation rates ($2-3 \times 10^{-8}$ m^{2}s^{-3}). In the LCIS data, values of Re_b are at least $O(1000)$ (Davis and Nicholls, 2019), providing a clear distinction between the two regimes. However, in the GVIIS data, the Re_b values do not correlate with mean flow speed (not shown), suggesting that the points with $Re_b > 20$ might be associated with internal wave breaking rather than shear-driven boundary layer turbulence. Further investigation is required to isolate the driver of the $Re_b > 20$ events.

5.4 Heat Flux

To estimate the turbulent heat flux, $\langle w'T' \rangle$, we use a direct measurement of the dissipation of thermal variance, $\chi_T = \kappa_T \langle |\nabla T|^2 \rangle$ from the lower TIC MicroSquid sensor, and apply the method of Osborn and Cox (1972) that assumes $\chi_T = 2\langle w'T' \rangle \frac{\partial \langle T \rangle}{\partial z}$. We estimate χ_T by fitting a k^{-1} slope to the temperature power spectra in Figure 5.3E using a viscous-convective range scaling (Batchelor, 1953) (see Supplementary Material for details). The heat flux estimate at the lower TIC is 3.2 ± 0.8 Wm^{-2}, which corresponds to a melt rate of 0.33 ± 0.08 m yr^{-1} (± denotes a standard deviation in χ_T), lower than the observed 1.4 m yr^{-1} (13.7 Wm^{-2}).

At the upper TIC, the MicroSquid sensor failed. However, if we assume that double-diffusive convection drives turbulence, then we can equate the turbulent buoyancy flux to the dissipation rate i.e. $\langle w'b' \rangle = \varepsilon$. We relate the turbulent heat flux to the turbulent buoyancy flux using the flux ratio $\gamma = \alpha \langle w'T' \rangle / \beta \langle w'S' \rangle$ via $\langle w'b' \rangle = \alpha \langle w'T' \rangle (1 - \gamma^{-1})$. We calculate γ at the lower TIC by equating our two estimates for $\langle w'T' \rangle$ from χ_T and ε. This gives a value between $\gamma = 0.26$ and $\gamma = 0.43$. Using the mean γ from the lower TIC gives a heat flux at the upper TIC of 9.6 ± 2.4 Wm^{-2} (± denotes a standard deviation in γ) which corresponds to a melt rate of 0.98 ± 0.28 m yr^{-1}, still lower than the observed 1.4 m yr^{-1}.

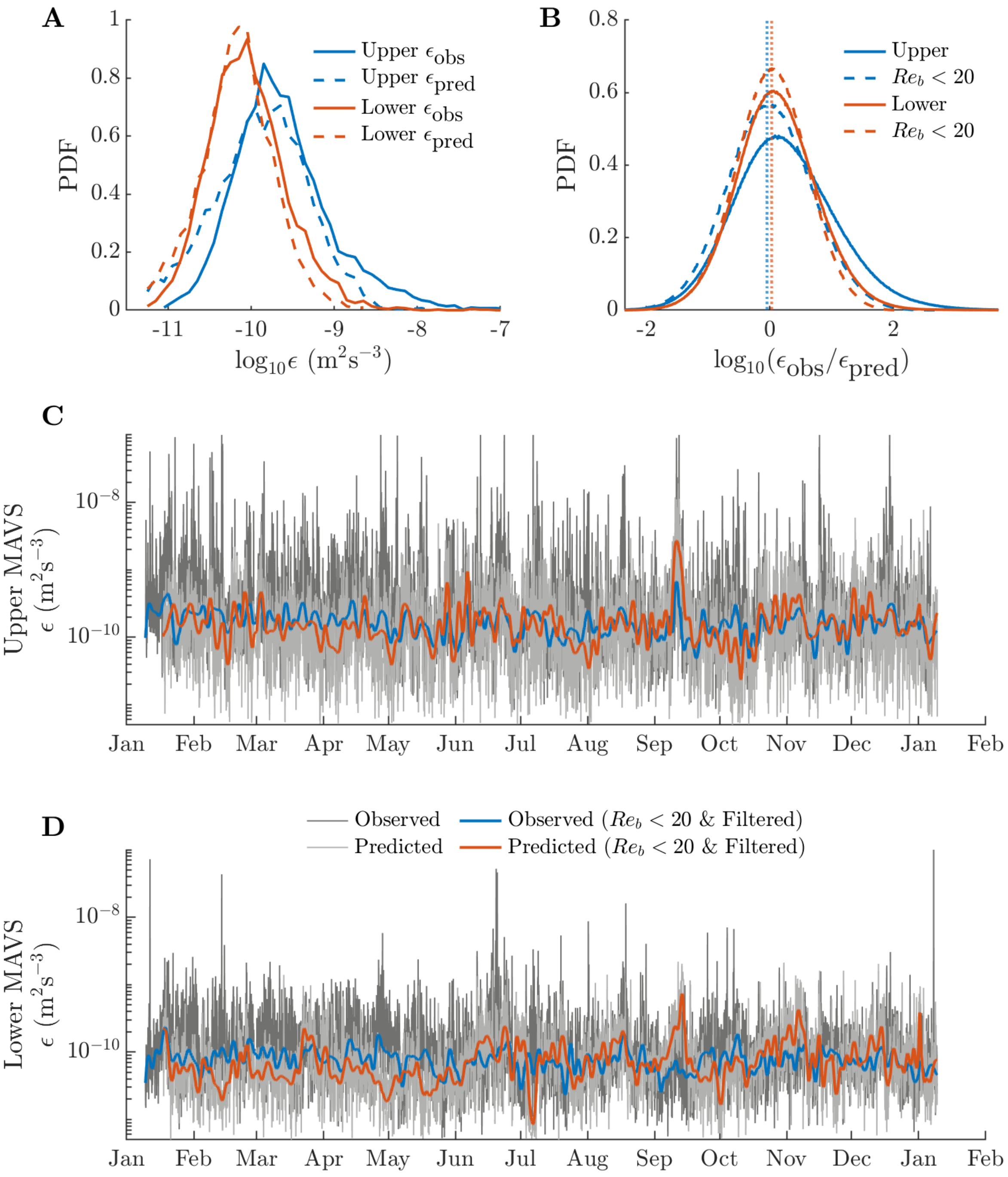

Fig. 5.4 **A**. PDFs of upper and lower MAVS observed dissipation rate and predicted dissipation rate. **B**. PDF of the log of the ratio between observed and predicted dissipation rate. **C**. Timeseries of observed and predicted dissipation rates for upper MAVS, along with filtered signal without high $Re_b > 20$ data. **D**. Same as **C** for lower MAVS data.

The increase in predicted heat flux from the lower TIC to the upper TIC is due to both an increase in the lateral gradients in temperature, giving a larger value of A in Eq. 5.4, and to an increase in stratification. The term $|\nabla b|/b_z^*$ in Eq. 5.4, which we approximate as N^2/b_z^*, gives a measure of spatial variations in isopycnals; flat isopycnals would give a value of $N^2/b_z^* = 1$. Both factors in Eq. 5.4 that depend on buoyancy, $(|\nabla b|/b_z^*)^{2/3}$ and N, are larger at the upper TIC, contributing to the larger dissipation rate. Although the heat flux at the upper TIC is insufficient to cause the observed melting, we know from the initial CTD profiles that the stratification increases closer to the ice, giving a larger value of N. The variance in temperature also increases, which is visible in the difference between the temperature spectra at 0.5 m and 20.5 m in Figure 5.3F. An increase in temperature variance implies an increase in the spice variance magnitude A which potentially implies an increase in buoyancy variations and so an increase in the value of N^2/b_z^*. Therefore, we may expect larger rates of turbulence closer to the ice and a larger heat flux, perhaps sufficient to match the observed melt rate. In order to maintain a statistically steady state, a larger vertical heat flux closer to the ice must be balanced by a divergence in the lateral heat flux

5.5 Conclusions

We showed in Section 5.2 that the dissipation rate does not depend on the mean flow speed, in contrast to the notion of a shear-driven boundary layer that has been observed at other under-ice shelf locations (Jenkins et al., 2010, Davis and Nicholls, 2019). The lack of dependence on mean flow speed is consistent with the simulations from Chapter 3 and those of Rosevear et al. (2021). Instead, we found that double-diffusive convection can explain the observed dissipation rates. Using the method from Chapter 4, we related the observed dissipation rates to large scale variations in along-isopycnal temperature, which are hypothesized to generate small scale gradients in spice that drive double-diffusive convection. The intensity of double-diffusive convection predicted by the M21 method increases with stratification and temperature variance, and we found an increase in heat flux towards the ice consistent with the stronger stratification and temperature variance. The predominant variation in heat flux appears to be associated with changes in turbulence driven by horizontal spice variance, rather than the mean flow speed.

Our observations suggest that in certain locations, the along-isopycnal spice variance might be a better indicator of basal melting than the flow speed. This has implications for modelling studies that rely on the three equation formalism to predict melt rates. A parameterization of the double-diffusive boundary layer could be developed based on far-field stratification and isopycnal spice variance. It is not yet clear how prevalent double-diffusive ice-ocean boundary layers are, as a result of the limited number of borehole observations. However, our observations suggest that for values of the buoyancy Reynolds number $Re_b = \varepsilon/\nu N^2 < 20$, double-diffusive convection may be the dominant source of turbulent dissipation in ice-ocean boundary layers.

5.6 Supplementary Material

5.6.1 Observation Processing

The TICs each consisted of a Nobska Modular Acoustic Velocity Sensor (MAVS), that collects 3-D velocity data based on differential acoustic travel time (Thwaites and Williams, 1996), and a Rockland Scientific International 'MicroSquid' fast response temperature sensor (FP07), as well as a slow response thermistor. The TICs sampled in 15 minute bursts every 2 hours at a rate of 5 Hz, and data were collected over a 366 day period, however the upper FP07 sensor failed after 4 weeks. Also installed in a second hole (20 m from the TICs), was a thermistor chain that sampled every 5 minutes (not logged during the MAVS sampling period) for a 358 day period and an Upward Looking Sonar (ULS) that collected data every hour for a 360 day period. The MAVS data were processed using the methodology outlined in Davis and Nicholls (2019), removing samples that did not complete a full 15 minute burst. The MAVS thermistors were calibrated to agree with the CTD profiles taken at the beginning of the mooring period. The thermistors on the thermistor chain did not begin sampling correctly until five days after the MAVS begun sampling, so we accounted for the changing temperature in the water column observed by the MAVS thermistors.

5.6.2 ε Estimate

To calculate a turbulent dissipation rate ε, we computed the power spectrum for the fluctuating horizontal velocity components u', v' and w', where u is in the direction of mean flow, v as the across flow component and w as the vertical component (i.e. $\langle v\rangle = 0$ and $\langle w\rangle = 0$). We then constructed the horizontal kinetic energy spectrum in terms of frequency, defined as the average of the power spectra for u', v' and w' (Lindborg, 2006) over horizontal wavenumbers i.e.

$$E_{k_h} \equiv \frac{t_0}{2\pi} \sum_{|k_x|=k_h} \frac{1}{2}\hat{u}_i\hat{u}_i^{\star}, \tag{5.5}$$

where t_0 is the averaging period (15 minutes), $\hat{u}_i$ is the Fourier transform of the i_{th} velocity component and summation over i is implied, * denotes a complex conjugate, and k_x is the along-stream wavenumber. As we apply the frozen-field hypothesis, we cannot average over the across-stream wavenumber variations as in the full definition from Lindborg (2006). We used a Welch method to calculate the power spectral density (PSD), averaging over four spectral windows, chosen to maximise the averaging whilst leaving enough of the PSD uncontaminated by noise to fit a slope to. We found a broad spectral peak at a frequency of $f = 0.1\ \mathrm{s}^{-1}$, which corresponds to the frequency of vibration of the mooring cable (Davis and Nicholls, 2019, McPhee, 2008), so we removed all data with frequencies larger than $0.01\ \mathrm{s}^{-1}$ to avoid including the aliased signal. We have included a shaded region that represents the frequencies above the cutoff range (these frequencies change with mean flow speed in Figure 3A,C and not with Figure 3B,D as changes in mean flow speed are averaged over).

We applied Taylor's frozen field hypothesis to convert frequency to wavenumber $k = 2\pi f / \langle U \rangle$ and frequency spectrum to wavenumber spectrum $E_{k_h} = E_{f_h} \langle U \rangle / 2\pi$. In the wavenumber spectra, we observed another spectral peak at a constant wavenumber, caused by eddies shedding from the central pole of the MAVS (Davis and Nicholls, 2019), however this peak has a higher frequency than our filter and hence is not included in our analysis. The resulting spectra, averaged by mean flow speed, and by dissipation rate estimate, are plotted in Figure 3.

The horizontal kinetic energy spectra follow a $k^{-5/3}$ scaling at the wavenumbers unaffected by instrumental noise. Calculating the Ozmidov scale, $L_{Oz} = \sqrt{\varepsilon / N^3}$, using a value of N from the CTD profiles, we find that the $k^{-5/3}$ slope occurs at wavelengths larger than the Ozmidov wavenumber. Previous observations (Riley and Lindborg, 2008) and theory (Lindborg, 2006), regarding 'stratified turbulence', have demonstrated that a $k^{-5/3}$ subrange may exist in the horizontal wavenumber direction, via a turbulent energy cascade, whilst the vertical motions are damped by stratification. Lindborg (2006) suggests the scaling for stratified turbulence as,

$$E_{k_h} = c\varepsilon^{2/3} k^{-5/3}, \tag{5.6}$$

where c is a constant equal to the Kolmogorov constant $\kappa_k \sim 0.49$, and E_{k_h} denotes the horizontal kinetic energy spectrum. We estimate the dissipation rate by calculating the power spectrum for horizontal kinetic energy, given as the average of the along and across stream power spectra (Lindborg, 2006), before fitting Eq. 5.6 to the portion uncontaminated by instrumental effects. We choose this method rather than estimating dissipation rate from each velocity component's power spectrum as in Davis and Nicholls (2019), due to the small Ozmidov scale.

We find that the spectra for each burst are smooth enough to fit a $k^{-5/3}$ spectrum to. Bursts where the spectra depart from the fit slope by more than a factor of 10 are discarded from our analysis. The dissipation estimates obtained by averaging individual burst estimates of ε with respect to mean flow speed are very close to those obtained by first averaging the spectra, binned by mean flow speed (shown in blue and grey respectively in Figure 2). Likewise, when binning spectra by ε for Figure 3B,D, the averaged spectra ε estimates are within a factor of 2 of the burst-by-burst ε estimates, despite the nonlinear relationship between spectral slope and ε (Eq. 5.6). This holds above $\varepsilon = 5 \times 10^{-12}$ m^{2}s^{-3}, which we take as the instrument noise floor.

5.6.3 χ_T Estimate

We calculated our estimate of $\chi_T = \kappa_T \langle |\nabla T|^2 \rangle$ using the power spectra of temperature fluctuations $T' = T - \langle T \rangle$ from the lower MicroSquid FP07 thermistor. When averaged by mean flow speed (see Figure 3E), the temperature spectra (calculated using a Welch method and frozen field hypothesis in the same way as the horizontal kinetic energy spectra) show a k^{-1} slope at low wavenumbers. We then fit a Batchelor spectrum (Batchelor, 1953) to the spectra, of the form

$$E_T = \tilde{c} \chi_T \varepsilon^{-1/2} \nu^{1/2} k^{-1}, \tag{5.7}$$

where ν is the kinematic viscosity and $\tilde{c} \sim 0.5$ is a constant. Coupled with the measurement of ε in each burst, we can then calculate a value for χ_T for each burst at the lower TIC.

To calculate the wavenumber spectra from the thermistors in Figure 5.3 we used a Lomb-Scargle periodogram smoothed with a Hanning window. The thermistor data was not sampled during the MAVS bursts, so the effective resolution is decreased by the 2 hourly missing data samples which are missing for a period of around 20 minutes. Using a Welch method, as we did for the MAVS spectra, would only allow for a maximum resolved frequency of around 1/40 min^{-1} however using the Lomb-Scargle periodogram we can resolve frequencies up to around 1/20 min^{-1} before sampling artefacts are present.

To calculate the flux ratio $\gamma = \alpha \langle w'T' \rangle / \beta \langle w'S' \rangle$ as discussed above, we equate two approximations of the turbulent heat flux $\langle w'T' \rangle$. Firstly we apply the Osborn and Cox

(1972) method and write

$$\langle w'T' \rangle = \frac{\chi_T}{\frac{\partial T}{\partial z}}, \tag{5.8}$$

where $\frac{\partial T}{\partial z}$ is obtained from the thermistor data in the same manner as N discussed below. Secondly we estimate $\langle w'T' \rangle$ by equating the turbulent buoyancy flux $\langle w'b' \rangle$ with the dissipation rate ε based on the assumption of double-diffusive convection,

$$\varepsilon = \langle w'b' \rangle = \alpha \langle w'T' \rangle (1 - \gamma^{-1}). \tag{5.9}$$

Equating the two methods for calculating $\langle w'T' \rangle$ we get the expression for γ as

$$\gamma = \left(1 + \frac{2\varepsilon \frac{\partial T}{\partial z}}{\alpha g \chi_T} \right)^{-1}. \tag{5.10}$$

5.6.4 M21 Method

The M21 method is based on the energetic balance between the turbulent buoyancy flux $\langle w'b' \rangle$ and the diapycnal buoyancy flux φ_d. The diapycnal buoyancy flux can be estimated based on temperature and salinity gradients alone, and so provides an avenue to predict the dissipation rate when the dissipation is entirely forced by a double-diffusive buoyancy flux i.e. $\varepsilon = \langle w'b' \rangle = -\langle \varphi_d \rangle$. To estimate φ_d, we need the temperature and salinity gradients on small scales, in particular at the overturning scale (taken as the Ozmidov scale $L_{Oz} = \sqrt{\varepsilon / N^3}$). To estimate small scale temperature and salinity gradients using large scale T/S information, we assume that gradients in spice $s_p = \alpha T + \beta S$ dominate on small scales compared to gradients in buoyancy $b = g\alpha T - g\beta S$. The buoyancy and spice gradients must also be assumed to be anti-correlated (an assumption we cannot assess with our mooring instrumentation). The M21 method can be applied using the steps outlined in Chapter 4.

The thermistors at 0.5 m and 20.5 m sample every 5 minutes and are located in a borehole 20 m away from the TIC thermistors, which sample only at the start of each 15 minute burst every 2 hours. We linearly interpolate the thermistor chain measurements onto the same time as the TIC thermistor measurements during each TIC burst to create a vertical profile of temperature. From this vertical profile of temperature, we can calculate a buoyancy profile using salinity from the CTD relation. Horizontal sections are then obtained using the frozen field hypothesis by advecting the time-varying temperature and salinity profiles with the mean velocity, $\langle u \rangle$. We then calculate N, the sorted buoyancy gradient b_z^*, and the two point correlation $R(\tilde{r})$ along isopycnals, all interpolated vertically onto the locations of the MAVS. Note that b_z^* is calculated by sorting the buoyancy section in the vertical and horizontal directions using the method from Tseng and Ferziger (2001). The TEOS10 package (McDougall and Barker, 2011) is used to calculate the buoyancy frequency N, which is also used to approximate the buoyancy gradient magnitude i.e. $|\nabla b| \sim N^2$. At the measured temperatures under George VI Ice Shelf, the thermal diffusivity is $\kappa_T \sim 1.39 \times 10^{-7}\ \mathrm{m^2s^{-1}}$ (Sharqawy et al., 2010) and the haline diffusivity is $\kappa_S \sim 7.36 \times 10^{-10}\ \mathrm{m^2s^{-1}}$ (Vitagliano and Lyons, 1956).

We interpolate the MAVS thermistor measurements onto the same time as the thermistor cable measurements before and after each MAVS burst to create a vertical line of temperature measurements with which we can calculate N. To calculate the two point correlation $R(\tilde{r}) = \langle |s_p(\mathbf{x},t) - s_p(\mathbf{x}+\tilde{r}\mathbf{a},t)|^2\rangle$ along isopycnals, we first estimate salinity based on the temperature profiles and the CTD relationship, before calculating spice and buoyancy. We then interpolate the spice data into buoyancy space to calculate the along-isopycnal two point correlation for spice.

Chapter 6

Implications and Future Directions

6.1 Double-Diffusive Energetics

Summary

In Chapter 2 we presented a model for the energetics of double-diffusive fluids. Specifically, we extended the work of Winters et al. (1995), by deriving budgets for 'available potential energy' (APE) and 'background potential energy' (BPE) in double-diffusive fluids. In the Supplementary Material of Chapter 2, we also extended the Winters et al. (1995) budgets to fluids with more than two components contributing to the density, and to fluids where cross-diffusion effects are important. We used the definitions of APE and BPE for single component fluids proposed by Lorenz (1955), where BPE is defined as the potential energy of the sorted buoyancy field and APE is the difference between potential energy and BPE. Using this definition of BPE splits the adiabatic and diabatic fluid motions, and retains the link between APE and density perturbations.

We found that the diapycnal buoyancy flux Φ_d, which is positive for single component fluids, can become negative under double-diffusion, thereby releasing BPE into APE. The transfer of APE to BPE is usually associated with 'irreversible mixing', and Φ_d represents the diffusive flux of buoyancy across isopycnals. In double-diffusive fluids, the diffusive diapycnal buoyancy flux can act up-gradient ($\Phi_d < 0$), releasing BPE into APE via 'un-mixing' of density. We derived a criterion for $\Phi_d < 0$ based on the ratio between the magnitude of gradients in temperature and salinity, G_ρ, and the angle made between ∇T and ∇S, notated as θ. We also derived an equation for the evolution of the sorted buoyancy field b^*, which related the diapycnal buoyancy flux to the effective diffusivity for buoyancy K_b. This demonstrated that our criterion for $\Phi_d < 0$ distinguished between diffusive $K_b > 0$ and anti-diffusive $K_b < 0$ behaviour in the buoyancy field. We demonstrated how our criterion could be applied using 2D simulations of salt fingers.

Implications

The diapycnal buoyancy flux for a double-diffusive fluid in Chapter 2 was written in terms of spice and buoyancy in Chapter 4,

$$\varphi_d = \frac{\kappa_T + \kappa_S}{2b_z^*}|\nabla b|^2 + \frac{\kappa_T - \kappa_S}{2b_z^*}\nabla s_p \cdot \nabla b. \tag{6.1}$$

The energetic model for double-diffusive convection given in Chapter 2 posited that available potential energy can be created via an average up-gradient diapycnal buoyancy flux i.e. $\Phi_d = \langle \varphi_d \rangle < 0$ for some volume average $\langle \cdot \rangle$. This energetic framework provides a basis for defining double-diffusive convection, distinct from differential diffusion or 'double-diffusive effects'. For a fluid with two components of equal diffusivities i.e. $\kappa_T = \kappa_S$, the second term in Eq. 6.1 would equal zero, so the second term can be considered purely double-diffusive. If the second term in Eq. 6.1 makes a significant contribution to Φ_d, then 'double-diffusive effects' are clearly important, regardless of the sign of Φ_d. In 'double-diffusive convection', potential energy is being released into kinetic energy via a turbulent buoyancy flux $\langle w'b' \rangle$. This process requires the production of variations in density i.e. APE, created via diffusion to fuel the release of potential energy. The production of APE via diffusion is only possible if the second term in Eq. 6.1 is negative and dominates compared to the first term, giving $\Phi_d < 0$. In differential diffusion (Smyth et al., 2005, Jackson and Rehmann, 2003, Nash and Moum, 2002), the mixing rates of temperature and salinity are different, but no potential energy is being converted into kinetic energy. Double-diffusive effects must be important for differential diffusion, so the second term in Eq. 6.1 is significant, but APE is not being created, so $\Phi_d > 0$. Two regimes of differential diffusion are then possible: either the second term is positive, or it is negative and smaller than the first term. These two regimes could be further investigated using numerical simulations. For flows where double-diffusive effects are *not* important, for example in vigorous turbulence (Jackson and Rehmann, 2003), the spice and buoyancy gradients may be uncorrelated, leading the second term in Eq. 6.1 to be negligible and therefore $\Phi_d > 0$. Further simulations of common double-diffusive flows need to be conducted to diagnose the behaviour of Φ_d, however the terms in Φ_d are clearly useful for distinguishing between a variety of regimes in double-diffusive fluids.

The diapycnal buoyancy flux in Eq. 6.1 provides insight into how the magnitudes of the molecular diffusivities affect double-diffusive convection. In Chapter 1, we showed a plot of the diffusivity ratio κ_T/κ_S as it varies across the ocean. We made the claim that we do not expect this changing diffusivity ratio to have a large effect. Since $\kappa_S << \kappa_T$, the terms $\kappa_T + \kappa_S$ and $\kappa_T - \kappa_S$ are both $\approx \kappa_T$. This implies that a changing value of κ_S likely has a very small impact on the magnitude of the diapycnal buoyancy flux, and so will not have a strong affect on the dynamics. Changes in κ_T have a larger effect, for example, doubling κ_T doubles the diapycnal buoyancy flux Φ_d. However, κ_T only varies by a factor of 1.12 between temperatures of 0 and 35 °C and between salinities of 5 and 38 ppt (Sharqawy et al., 2010). Therefore, variations in κ_T across the ocean likely have a small effect on the magnitude of double-diffusive convection, with only a slight increase in diapycnal buoyancy flux at the warmest and saltiest locations. For a double-diffusive fluid other than salt-water, if κ_T and κ_S are of similar sizes, say $\kappa_T/\kappa_S = 2$, then the first term in Eq. 6.1 will have a larger weighting than the second term, in this case larger by a factor of 3. However, if the gradients in spice are large, the double-diffusive term can still dominate.

Future Directions

There are a variety of possible theoretical extensions to our work in Chapter 2 that we will discuss here, with some practical applications given in Chapters 3 and 4. Within APE theory, a convincing local budget for double-diffusive fluids needs to be developed, following on from the local budgets for a single component fluid suggested by Scotti and White (2014). In an initial analysis of this problem, it became clear that local APE in a double-diffusive fluid is not diffusive in the same way in as a single component fluid. To fully understand the dynamics of local APE it may be necessary to involve another variable that quantifies along-isopycnal variations in spice that are not captured by APE.

Theoretical connections between the ‘component potential energy’ framework of Smyth et al. (2005) and Ma and Peltier (2021) and our suggested framework in Chapter 2 would be valuable. Writing an explicit relationship between fields sorted by temperature or salinity and those sorted by buoyancy would help link the two possible notions of ‘available’ and ‘background’ potential energy. A general energetic model that incorporates irreversible mixing as well as representing a physical potential energy is desirable, however it is currently unclear if a definition of APE that achieves both these goals can be developed.

Layer formation is a topic of on-going research across fluid dynamics. In the literature concerning double-diffusive convection, there is debate over which of the many possible mechanism for layer formation is the dominant one (Radko, 2013). The equation we derive in Chapter 2 for the evolution of sorted buoyancy b^* may prove useful in investigating this question. Taylor and Zhou (2017) developed a general criterion for layer formation using the evolution equation for sorted buoyancy in a single-component fluid, and it is possible that a similar criterion could be developed for a double-diffusive fluid. Penney et al. (2020) developed an expression for the evolution of passive tracers in a sorted buoyancy coordinate which, if adapted, could provide an equation for the evolution of spice in a sorted buoyancy coordinate. This may help in analysing double-diffusive layer formation.

6.2 Melt-Driven Convection

Summary

In the experiment of Martin and Kauffman (1977), they showed the existence of melt-driven convection in salt water beneath a horizontal ice surface. Gade (1979) suggested that a low level of turbulence would be sufficient to damp this melt-driven convection, so it may not be important geophysically. However, in borehole data collected from beneath George VI Ice Shelf, thermohaline staircases were observed adjacent to the ice, and melt-driven convection was proposed as the driving process by Kimura et al. (2015). Further evidence of this was seen in the simulations of Rosevear et al. (2021) who found the formation of layers in LES of a sheared, stratified boundary layer beneath a melting ice base. In Chapter 3 we presented numerical simulations of forced turbulence underneath a melting ice shelf to investigate the effect of turbulence on melt-driven convection.

Our simulations showed two distinct regimes. In one, the turbulent buoyancy flux $\langle w'b' \rangle$ was positive, indicating that buoyancy was acting to add kinetic energy to the system via double-diffusive convection. In the other, $\langle w'b' \rangle$ was negative, indicating that stratification was acting to remove kinetic energy, damping turbulence. The simulations were initiated with a constant temperature and salinity, which caused all simulations to initially display melt-driven convection. However, in the colder simulations, and those with a stronger mechanical forcing, the simulations transitioned to the damped-turbulence regime after a few hours.

We showed that steady state, melt-driven convection would require a fresh boundary layer (with boundary salinity $S_b <\sim 4$ ppt), so all simulations should be expected to eventually transition. However, the warm simulations (0 °C), even with substantial mechanical forcing, did not transition within the 50 hours simulated. A cold, weakly turbulent simulation took ~ 200 hours to transition. This suggests that if triggered, melt-driven convection may be long lasting. Therefore, it is a viable possibility beneath ice shelves. A similar conclusion was reached in Rosevear et al. (2021).

We developed an explanation for the transition away from melt-driven convection. We found that convection was maintained by an up-gradient buoyancy flux, where APE was being released from BPE (Chapter 2), triggering convection. The region of up-gradient buoyancy flux exists when there are no turbulent motions altering the opposing angle between temperature and salinity gradients. When the region of up-gradient buoyancy flux becomes influenced by turbulence, double-diffusive convection is damped. Turbulence itself was found to be controlled by the stratification close to the ice. Therefore, we could develop a criterion for the damping of convection in terms of the width of the region of up-gradient buoyancy flux (parameterised using the density ratio R_ρ) and the width of the region where turbulence was damped by buoyancy (parameterised using the buoyancy Reynolds number Re_b). We applied our criterion to a simple diffusive model for evolving thermal and haline sublayers to map out parameter space in terms of far-field temperature and mechanically-forced dissipation rate.

Implications

Our simulations, along with those of Rosevear et al. (2021), showed that melt-driven convection is a viable possibility beneath ice shelves. The layering in the Rosevear et al. (2021) simulations also provided evidence that melt-driven convection may be responsible for the observed layers under George VI Ice Shelf, although as discussed in Chapter 5, understanding the exact cause of double-diffusive layering is not necessary for understanding of the large-scale drivers of ice shelf melt. If melt-driven convection is active beneath ice shelves, then a process for triggering it must exist. This could be in the form of intermittent bursts of turbulence, as seen in the data in Chapter 5. Bursts of turbulence could homogenise the temperature and salinity, as in the initial condition of our simulations, allowing melt-driven convection to form.

If melt-driven convection is prevalent more broadly than just beneath George VI Ice Shelf, then that would have significant ramifications for our modelling of ice shelf-ocean boundary layers. This is discussed further below in the implications of Chapter 5. In Chapter 3, we compared different under-ice shelf regimes by applying our criterion to a simple diffusive model for temperature and salinity (Martin and Kauffman, 1977). This comparison suggests that other ice shelves with warm temperatures and low turbulence levels may also be susceptible to double-diffusive convection. Applying our criterion to a 1D model that captures the evolution of temperature, salinity and turbulence within an ice shelf-ocean boundary layer would help determine when melt-driven convection is likely.

Future Directions

Adjacent to the ice, sublayers for temperature and salinity form. The thermal sublayer is thicker than the haline sublayer, creating a region of up-gradient buoyancy flux. These sublayers are comparable to the ones that occur in a thermohaline staircase in the interface region (Carpenter et al., 2012). The key difference is that in the ice case there is a solid boundary above the diffusive sublayers, rather than another convecting layer. In the ice case, the gradients in temperature and salinity are also much stronger than those typically found in a double-diffusive staircase. The controls on turbulence beneath ice may be different from the controls on turbulence in a thermohaline staircase, however the general principle of turbulence damping the layer of up-gradient buoyancy flux may hold. It would be interesting to apply the criterion from Chapter 3 to simulations of a thermohaline staircase.

As an extension of our simulations, melt-driven convection with changing far-field conditions could be considered. In Chapter 5 we suggested that lateral transport of temperature and salinity may be key to the evolution of a double-diffusive boundary layer, so lateral gradients could be included within simulations. To understand the possible triggers for melt-driven convection, simulations with a changing mechanical forcing would be useful. Sheared simulations as in Rosevear et al. (2021) with the addition of a tidal cycle, or intermittent bursts of turbulence, may trigger melt-driven convection and so would be worthwhile to simulate. These sorts of simulations could help develop a quasi-steady view of double-diffusive convection in the ice shelf-ocean boundary layer. Constraints on the occurrence of double-diffusive convection will help in developing a parameterisation that can distinguish between regions of melt-driven convection and stratification-damped turbulence.

6.3 Predicting Double-Diffusive Dissipation

Summary

In Chapter 4, we presented a method for predicting the dissipation rate due to double-diffusive convection using only a CTD (Conductivity, Temperature Depth) section. This method was based on the energetic balance for double-diffusive convection proposed in Chapter 2. Namely, the balance $\varepsilon = \langle w'b' \rangle = -\Phi_d$ where Φ_d is the average diapycnal buoyancy flux. As Φ_d is expressed purely in terms of temperature and salinity gradients, we can predict the dissipation rate by estimating the gradients in temperature and salinity at the scale where the energetic balance holds. To estimate small scale gradients in temperature and salinity, we projected measured gradients down to small scales. We found our method was effective at reproducing observed dissipation rates across data from an Arctic Eddy on the Chukchi slope, first presented in Fine et al. (2018).

Our method relies on the notion, discussed in Smith and Ferrari (2009), that spice is preferentially mixed along isopycnals. We assumed that buoyancy variations on sub-measurement scales are negligible. We then enhanced observed spice gradients, using a wavenumber scaling, down to the Ozmidov scale L_{Oz} which we took as our overturning scale. Our method assumed that the driver of double-diffusive convection is the lateral stirring of spice along isopycnals. The method captured much of the observed variation in dissipation rate, with 72% of predictions within a factor of 3 of the observations. The method did not perform well for large buoyancy Reynolds numbers $Re_b > 20$, which is in keeping with the notion that double-diffusive convection is not active in strongly turbulent regions. We applied the method to a coarse sub-sampling of the CTD data, and found that the method still performed well, despite the disagreement between the observed spice spectrum and the assumed spectrum. This lack of sensitivity suggests the method may have useful applications in coarser data sets.

Implications

In the Arctic eddy data, we followed Fine et al. (2018) in applying the Osborn (1980) method to approximate heat fluxes from dissipation rates. This method worked well, however the Osborn (1980) method relies on the assumption that the turbulent vertical diffusivity of buoyancy $K_b = \langle w'b' \rangle / N^2$ is equivalent to the turbulent vertical diffusivity of temperature $K_T = \langle w'T' \rangle / \frac{\partial T}{\partial z}$. This assumes that the turbulent diffusivity for salinity $K_S = \langle w'S' \rangle / \frac{\partial S}{\partial z}$ is equal to K_T. This assumption is not ideal, as we know that in a variety of forms of double-diffusive convection $K_T \neq K_S$. If we assume double-diffusive convection drives turbulence, then we can balance the turbulent buoyancy flux $\langle w'b' \rangle$ with the dissipation rate ε. However, the flux ratio $\gamma = \alpha \langle w'T' \rangle / \beta \langle w'S' \rangle$ varies for different forms of double-diffusive convection. Understanding the controls on γ is key to furthering our understanding of double-diffusive convection and turbulence in the ocean.

Double-diffusive convection is not usually assumed to occur in doubly stable regimes, as there is no unstably distributed component in the vertical. However, if we assume that spice is stirred along isopycnals, then even in a doubly stable background stratification, we could get double-diffusively unstable gradients on smaller scales than the measured ‘background’ stratification. Along-isopycnal stirring could also lead to horizontal gradients that are not captured in vertical profile measurements. A necessary ingredient for double-diffusive convection, as discussed in Chapter 4, is that buoyancy and spice gradients are anti-correlated. We may expect anti-correlation rather than correlation for background gradients where $|R_\rho| < 1$, however further observational work needs to be conducted to test this expectation. In Chapter 4, we found that our method performs well in doubly stable regions, suggesting that our assumption of double-diffusive convection could be accurate.

Our method has many potential applications, including estimating dissipation rates and heat fluxes in regions without microstructure measurements. In data with microstructure measurements, our method is useful for identifying how much of the magnitude and variability in dissipation rate can be explained by double-diffusive convection, where stirring of spice is active. One application of our method is considered in Chapter 5, and a further application to Arctic intrusions is briefly discussed in the Recent Developments section of Chapter 4. The method could be used to reevaluate previous estimates of the contribution of double-diffusive convection to Arctic mixing (e.g. Lenn et al., 2009, Schulz et al., 2021, Fer et al., 2020), extending the analysis beyond thermohaline staircase-based parameterisations.

Future Directions

There are still uncertainties in our method that need to be investigated further. These uncertainties can be investigated used numerical simulations and observations. Firstly, obtaining observations of $\mathcal{O}(1\ \mathrm{m}) - \mathcal{O}(100\ \mathrm{m})$ scales would be useful. Our method relies on an assumed spice spectrum at these scales, and so observational measurements of the wavenumber scaling for spice at small scales are desirable. Chapter 5 presents evidence for a $\tilde{k}^{-1}$ scaling in temperature at small scales, but coupled temperature and salinity observations would be preferable. In the application of our method to Arctic intrusions (see Recent Developments in Chapter 4), a spice spectrum with wavenumber dependence $\tilde{k}^{-2}$ provided a better dissipation rate prediction than the $\tilde{k}^{-1}$ model used in Chapter 4. Different dynamical regimes likely stir spice in different ways, so constraining the behaviour of spice in the $\mathcal{O}(1\ \mathrm{m}) - \mathcal{O}(100\ \mathrm{m})$ range is of key importance. Observational methods to evaluate the $\mathcal{O}(1\ \mathrm{m}) - \mathcal{O}(100\ \mathrm{m})$ length scales could involve towing temperature and salinity probes at slow speeds, similar to the work of MacKinnon et al. (2016).

A further assumption within our method is that the overturning length scale, where $-\Phi_d$ balances ε, is the Ozmidov length scale L_{Oz}. We gave a reasoning in Chapter 4 for why we applied this assumption, referencing the work of Zhou et al. (2016). However, considering the energy balance in spectral space within numerical simulations would be a sensible next step. Simulations of double-diffusive convection due to the stirring of spice would also provide insight into how shear effects may be incorporated into our method. Ideally, we would run simulations that could capture both the stirring of spice variance and the double-diffusive convection that it triggers. However, it may be difficult to achieve the necessary scale separation within simulations of a limited domain size.

6.4 Double-Diffusive Ice Shelf-Ocean Boundary Layers

Summary

In Chapter 5 we considered data from a mooring beneath George VI Ice Shelf, installed via two boreholes in 2012. Initial CTD measurements through the boreholes showed evidence of a double-diffusive staircase in the upper 20 m adjacent to the ice, which had not previously been observed (Kimura et al., 2015). We analysed the year-long mooring data, with a focus on measurements of turbulent dissipation rate and heat flux. The measured dissipation rate did not vary with mean flow speed, particularly in comparison to a similar mooring deployed beneath Larsen C Ice Shelf. This suggested that the boundary layer was not shear-driven. We applied the method from Chapter 4 to mooring measurements of temperature sampled over 15-20 minute periods, advected along with the mean flow using a frozen field assumption. The salinity necessary for calculations of spice and buoyancy was inferred based on the measured temperature and using the T/S relation from the initial CTD data. We found that the method from Chapter 4 reproduced the magnitude and variability of observed dissipation rates, including the differences between the upper and lower turbulence instruments. This suggested that double-diffusive convection was sufficient to explain the measured turbulence.

We also showed that the measured heat flux at the lower instrument, and inferred heat flux at the upper instrument, were insufficient to fuel the observed melting. This discrepancy, which increased with depth, is consistent with our model for double diffusive convection that intensifies with a stronger stratification and larger lateral spice variance. Our work suggested that the observations beneath George VI Ice Shelf were consistent with a predominantly double-diffusive ice-shelf ocean boundary layer.

Implications

A double-diffusive ice shelf-ocean boundary layer suggests a different driver of basal melt than the one commonly assumed in ocean models. In ocean models the basal melt rate is generally assumed to be proportional to the mean flow speed. However, based on our model of double diffusion beneath George VI Ice Shelf, the heat flux is sensitive to lateral variations in spice, and so the melt rate may be as well. Determining the spice variance in a watermass may be crucial for understanding its impact on the melting dynamics of warm-water ice shelves. Warm-water ice shelves are some of the most vulnerable regions to the effects of a changing climate.

A question that we did not answer in Chapter 5 is: what is the source of the lateral variations in spice and the lateral stirring of spice? This question is intimately related to the tidal forcing of the boundary layer and the mesoscale and submesoscale dynamics. In Chapter 4, the hypothesis was that the intrahalocline eddy was providing both the lateral variations in spice and also the stirring which we projected downscale to predict the dissipation rates. However, it is not immediately clear what the source of variability is in the temperature data collected beneath George VI Ice Shelf. Our spectral analysis suggested that there was a potential transition from a k^{-2} spice scaling to a k^{-1} scaling at similar scales to the data from MacKinnon et al. (2016), however we may be confusing temporal changes with spatial ones as we have only a point measurement of temperature. Our analysis also does not account for the potential tidal signals within the data, which may be a key source of variability. Understanding the sources of variation will be key to providing a workable parameterisation for the ice shelf-ocean boundary layer.

Future Directions

The results of Chapter 4 suggest that a very different ice shelf-ocean boundary layer regime is possible from the one previously observed. However, it is still unknown how prevalent this regime is. The results from Chapter 3 suggest that melt-driven convection could be prevalent within warm and weakly turbulent regimes. If melt-driven convection is present, then the driver of variations in melt rate may be lateral variations in spice, following our model for a double-diffusive boundary layer in Chapter 5. Further observations of ice shelf-ocean boundary layers in warm water and weak-shear regimes would help provide evidence about the prevalence of double-diffusive boundary layers.

Numerical simulations of double-diffusive convection underneath a melting boundary, resupplied by lateral gradients in temperature and salinity, would help provide clarity into the limits on double-diffusive boundary layers. Specifically, by forcing simulations, driven by lateral spice gradients, with shear we could determine the conditions under which the boundary layer transforms into a shear-driven boundary layer. These simulations could be similar to the simulations in Chapter 3 or in Rosevear et al. (2021), but they would need to reach a quasi-steady state in the presence of double-diffusive convection, rather than the time dependant models that have been investigated so far.

Developing a simple parameterisation of a double-diffusive boundary layer would be useful for representing double diffusion in ice shelf cavity models. To create a parameterisation, a model for the stratification and lateral spice variance in the boundary layer needs to be developed. Alternatively, a simple linear dependence of the friction velocity on far-field spice variance may capture most of the variability, as in the three equation formalism currently applied in ocean models (Dinniman et al., 2016), where the friction velocity is linearly related to the far field velocity. Further work investigating the accuracy of simple parameterisations and more complex stratification models should be conducted.

6.5 Outlook

Within this thesis we have considered the topics of double-diffusive convection and turbulence from a variety of angles: theoretical, observational and with numerical simulations. This thesis has focused on polar oceans, however the implications of our research also extend more broadly. For instance, the general double-diffusive processes in Chapters 2 and 4 are directly applicable to the non-polar oceans where double-diffusive convection occurs. Our studies of the ice shelf-ocean boundary layer, in Chapters 3 and 5, could also be applicable to double diffusive boundary layers occurring in the mixed layer. For example, a double-diffusive boundary layer was observed in Walesby et al. (2015) due to the influence of rain, and comparisons may be made here to the fresh water input from melting in an ice shelf-ocean boundary layer.

Many open questions about double-diffusive convection remain. Most importantly, we still do not understand the prevalence of double diffusion within the world's oceans. A recent study by van der Boog et al. (2021) identified layering within ARGO data (Argo, 2000) sampled at 1 m vertical resolution. In this study, they apply a 4/3 flux law (as in Shibley et al., 2017), to all identified staircases. They found that staircases made only a small contribution to global heat fluxes. However, layering is not a necessary feature of double-diffusive convection, and many layers will be smaller than 1 m, or transient, so not captured by the analysis of van der Boog et al. (2021). Further research into the prevalence of double diffusion is necessary. Our method from Chapter 4is useful in estimating the potential prevalence and impacts of double-diffusive convection, so could advance our understanding in this field.

Another key unknown regarding double-diffusive convection is its effect on ocean mixing. Currently we know that double-diffusive convection is particularly important for the flux of heat and salt in the Arctic Ocean (Shibley et al., 2017) as well as being important for fluxes in other locations, for example: the Southern Ocean (Bebieva and Speer, 2019), the Mediterranean (Ruddick, 1992), and the North Atlantic (St. Laurent and Schmitt, 1999). Double-diffusive convection may also influence the transport of biology, nutrients, and other chemical species (e.g. Glessmer et al., 2008, Nagai et al., 2021, Oschlies et al., 2003). Within this thesis we have shown that, in addition to these examples, double-diffusive convection may be important for the melting of Antarctic ice shelves. However, further study needs to be conducted to determine if the double-diffusive effect is significant on Antarctic-wide scales. Initial evidence suggests that in warm-water and weakly turbulent under-ice shelf regimes, double diffusion may be significant.

Within the energetic model in Chapter 2, we found that the condition for an up-gradient buoyancy flux depends only on the relative directions and magnitudes of temperature and salinity gradients in three dimensions. This condition is easily satisfied across a range of flows. Strong turbulence may be required to damp these double-diffusive effects (e.g. Jackson and Rehmann, 2003). Within our study of an Arctic Eddy, we found that double-diffusive convection could explain a significantly larger amount of the dissipation rate variability than would be assumed from a simple analysis of layering. Within the ice shelf ocean boundary layer, we found that double-diffusive convection could be prevalent and long-lasting within warm and weakly turbulent regimes. Within our observations beneath George VI Ice Shelf, double diffusion could explain most of the measured turbulence over an entire year. It is for these reasons that double-diffusive convection seems to me to be a relatively generic feature of ocean turbulence. The ocean is a double-diffusive fluid, and perhaps the question should be ‘when does double diffusivity not matter?’ rather than the other way around.

A powerful motivator for understanding the prevalence of double-diffusive convection in the ocean, is that it will help constrain the ocean response to climate change. In a changing ocean, we may expect the nature of mixing to change. Understanding the drivers of mixing and their potential response to changes in stratification, or spice variance, will help us constrain the feedbacks between a changing climate and ocean transport. It is my hope that a better understanding of the ocean transport of heat, salt, nutrients and biology, will help us make more accurate, and so more useful, predictions of how they will affect our earth system in coming decades. Our forecasts of changes in sea-level, ocean productivity, and ice-cover are vital for the adaptation of some of our most vulnerable communities in the climate crisis.

References

Argo, G. (2000). Argo float data and metadata from global data assembly centre (argo gdac). *SEANOE*.

Asbjørnsen, H., Årthun, M., Skagseth, Ø., and Eldevik, T. (2020). Mechanisms underlying recent arctic atlantification. *Geophysical Research Letters*, 47(15):e2020GL088036.

Bartello, P. and Tobias, S. (2013). Sensitivity of stratified turbulence to the buoyancy reynolds number. *Journal of Fluid Mechanics*, 725:1–22.

Barton, B. I., Lenn, Y.-D., and Lique, C. (2018). Observed atlantification of the barents sea causes the polar front to limit the expansion of winter sea ice. *Journal of Physical Oceanography*, 48(8):1849–1866.

Batchelor, G. K. (1953). *The theory of homogeneous turbulence*. Cambridge university press.

Batchelor, G. K. (1959). Small-scale variation of convected quantities like temperature in turbulent fluid part 1. general discussion and the case of small conductivity. *Journal of Fluid Mechanics*, 5(1):113–133.

Bebieva, Y. and Speer, K. (2019). The regulation of sea ice thickness by double-diffusive processes in the Ross Gyre. *Journal of Geophysical Research: Oceans*, 124(10):7068–7081.

Bebieva, Y. and Timmermans, M.-L. (2016). An examination of double-diffusive processes in a mesoscale eddy in the Arctic Ocean. *Journal of Geophysical Research: Oceans*, 121(1):457–475.

Bebieva, Y. and Timmermans, M.-L. (2019). Double-diffusive layering in the Canada Basin: An explanation of along-layer temperature and salinity gradients. *Journal of Geophysical Research: Oceans*, 124(1):723–735.

Begeman, C. B., Tulaczyk, S. M., Marsh, O. J., Mikucki, J. A., Stanton, T. P., Hodson, T. O., Siegfried, M. R., Powell, R. D., Christianson, K., and King, M. A. (2018). Ocean stratification and low melt rates at the Ross Ice Shelf grounding zone. *Journal of Geophysical Research: Oceans*, 123(10):7438–7452.

Bewley, T. (2012). *Numerical renaissance: simulation, optimization, & control*. Renaissance Press.

Bird, R. B. and Stewart, W. E. (1960). Lightfoot. *Transport phenomena*, 2:200.

Bishop, J. and Walton, J. (1981). Bottom melting under George VI Ice Shelf, Antarctica. *Journal of Glaciology*, 27(97):429–447.

Blunden, J. and Arndt, D. S. (2019). State of the climate in 2018. *Bulletin of the American Meteorological Society*, 100(9):Si–S306.

Bluteau, C. E., Jones, N. L., and Ivey, G. N. (2011). Estimating turbulent kinetic energy dissipation using the inertial subrange method in environmental flows. *Limnology and Oceanography: Methods*, 9(7):302–321.

Brown, J. M. and Radko, T. (2021). Diffusive staircases in shear: Dynamics and heat transport. *Journal of Physical Oceanography*, 51(6):1915–1928.

Cael, B. and Mashayek, A. (2021). Log-skew-normality of ocean turbulence. *Physical Review Letters*, 126(22):224502.

Callies, J. and Ferrari, R. (2013). Interpreting energy and tracer spectra of upper-ocean turbulence in the submesoscale range (1–200 km). *Journal of Physical Oceanography*, 43(11):2456–2474.

Carmack, E., Polyakov, I., Padman, L., Fer, I., Hunke, E., Hutchings, J., Jackson, J., Kelley, D., Kwok, R., Layton, C., et al. (2015). Toward quantifying the increasing role of oceanic heat in sea ice loss in the new Arctic. *Bulletin of the American Meteorological Society*, 96(12):2079–2105.

Carmack, E. C., Williams, W. J., Zimmermann, S. L., and McLaughlin, F. A. (2012). The Arctic Ocean warms from below. *Geophysical research letters*, 39(7).

Carpenter, J., Sommer, T., and Wüest, A. (2012). Simulations of a double-diffusive interface in the diffusive convection regime. *Journal of Fluid Mechanics*, 711:411–436.

Caulfield, C. (2021). Layering, instabilities, and mixing in turbulent stratified flows. *Annual Review of Fluid Mechanics*, 53:113–145.

Charney, J. G. (1971). Geostrophic turbulence. *Journal of the Atmospheric Sciences*, 28(6):1087–1095.

Corr, H. F., Jenkins, A., Nicholls, K. W., and Doake, C. (2002). Precise measurement of changes in ice-shelf thickness by phase-sensitive radar to determine basal melt rates. *Geophysical Research Letters*, 29(8):73–1.

Council—Alaska, I. C. (2015). Alaskan Inuit food security conceptual framework: How to assess the Arctic from an Inuit perspective: Summary and recommendations report.

Cox, G. F. and Weeks, W. F. (1974). Salinity variations in sea ice. *Journal of Glaciology*, 13(67):109–120.

Crapper, P. (1976). Fluxes of heat and salt across a diffusive interface in the presence of grid generated turbulence. *International Journal of Heat and Mass Transfer*, 19(12):1371–1378.

Dadonau, M., Partridge, J., and Linden, P. (2020). The effect of double diffusion on entrainment in turbulent plumes. *Journal of Fluid Mechanics*, 884:A6.

Davis, P. E. and Nicholls, K. W. (2019). Turbulence observations beneath Larsen C Ice Shelf, Antarctica. *Journal of Geophysical Research: Oceans*, 124(8):5529–5550.

Davis, R. E. (1994). Diapycnal mixing in the ocean: The Osborn–Cox model. *Journal of Physical Oceanography*, 24(12):2560–2576.

de Szoeke, R. (1998). The dissipation of fluctuating tracer variances. *Journal of physical oceanography*, 28(10):2064–2074.

Dewel, G., Borckmans, P., and Walgraef, D. (1983). Spatial patterns and double diffusion in chemical reactions. *Proceedings of the National Academy of Sciences*, 80(20):6429–6430.

Dillon, T. M. (1982). Vertical overturns: A comparison of Thorpe and Ozmidov length scales. *Journal of Geophysical Research: Oceans*, 87(C12):9601–9613.

Dinniman, M. S., Asay-Davis, X. S., Galton-Fenzi, B. K., Holland, P. R., Jenkins, A., and Timmermann, R. (2016). Modeling ice shelf/ocean interaction in Antarctica: A review. *Oceanography*, 29(4):144–153.

Dinniman, M. S., Klinck, J. M., and Hofmann, E. E. (2012). Sensitivity of circumpolar deep water transport and ice shelf basal melt along the west Antarctic peninsula to changes in the winds. *Journal of Climate*, 25(14):4799–4816.

Durkalec, A., Furgal, C., Skinner, M. W., and Sheldon, T. (2015). Climate change influences on environment as a determinant of indigenous health: Relationships to place, sea ice, and health in an Inuit community. *Social science & medicine*, 136:17–26.

Fer, I., Koenig, Z., Kozlov, I. E., Ostrowski, M., Rippeth, T. P., Padman, L., Bosse, A., and Kolås, E. (2020). Tidally forced lee waves drive turbulent mixing along the arctic ocean margins. *Geophysical Research Letters*, 47(16):e2020GL088083.

Fer, I. and Sundfjord, A. (2007). Observations of upper ocean boundary layer dynamics in the marginal ice zone. *Journal of Geophysical Research: Oceans*, 112(C4).

Fernando, H. J. (1989). Oceanographic implications of laboratory experiments on diffusive interfaces. *Journal of Physical Oceanography*, 19(11):1707–1715.

Fine, E. C., MacKinnon, J. A., Alford, M. H., and Mickett, J. B. (2018). Microstructure observations of turbulent heat fluxes in a warm-core Canada Basin eddy. *Journal of Physical Oceanography*, 48(10):2397–2418.

Flanagan, J. D., Radko, T., Shaw, W. J., and Stanton, T. P. (2014). Dynamic and double-diffusive instabilities in a weak pycnocline. part ii: Direct numerical simulations and flux laws. *Journal of physical oceanography*, 44(8):1992–2012.

Frank, F. C. (1950). Radially symmetric phase growth controlled by diffusion. *Proceedings of the Royal Society A: Mathematical, Physical and Engineering Sciences*, 201(1067):586–599.

Gade, H. G. (1979). Melting of ice in sea water: A primitive model with application to the Antarctic ice shelf and icebergs. *Journal of Physical Oceanography*, 9(1):189–198.

Garaud, P. (2018). Double-diffusive convection at low Prandtl number. *Annual Review of Fluid Mechanics*, 50:275–298.

Garrett, C. (1982). On the parameterization of diapycnal fluxes due to double-diffusive intrusions. *Journal of Physical Oceanography*, 12(9):952–959.

Gayen, B., Griffiths, R. W., and Kerr, R. C. (2016). Simulation of convection at a vertical ice face dissolving into saline water. *Journal of Fluid Mechanics*, 798:284–298.

Gearheard, S., Holm, L. K., Huntington, H., Leavit, J., Mahoney, A. R., Opie, M., Oshima, T., and Sanguya, J. (2013). The meaning of ice. *People and Sea Ice in Three Arctic Communities*.

Glessmer, M. S., Oschlies, A., and Yool, A. (2008). Simulated impact of double-diffusive mixing on physical and biogeochemical upper ocean properties. *Journal of Geophysical Research: Oceans*, 113(C8).

Gregg, M. (1989). Scaling turbulent dissipation in the thermocline. *Journal of Geophysical Research: Oceans*, 94(C7):9686–9698.

Gregg, M. (1999). Uncertainties and limitations in measuring ϵ and χ_t. *Journal of Atmospheric and Oceanic Technology*, 16(11):1483–1490.

Gregg, M., D'Asaro, E., Riley, J., and Kunze, E. (2018). Mixing efficiency in the ocean. *Annual review of marine science*, 10:443–473.

Griggs, J. A. and Bamber, J. (2011). Antarctic ice-shelf thickness from satellite radar altimetry. *Journal of Glaciology*, 57(203):485–498.

Gurvich, A. and Yaglom, A. (1967). Breakdown of eddies and probability distributions for small-scale turbulence. *The Physics of Fluids*, 10(9):S59–S65.

Guthrie, J. D., Morison, J. H., and Fer, I. (2013). Revisiting internal waves and mixing in the Arctic Ocean. *Journal of Geophysical Research: Oceans*, 118(8):3966–3977.

Haynes, P. and Anglade, J. (1997). The vertical-scale cascade in atmospheric tracers due to large-scale differential advection. *Journal of the atmospheric sciences*, 54(9):1121–1136.

Hellmer, H. H. and Olbers, D. J. (1989). A two-dimensional model for the thermohaline circulation under an ice shelf. *Antarctic Science*, 1(4):325–336.

Hickel, S., Adams, N., and Mansour, N. (2007). Implicit subgrid-scale modeling for large-eddy simulation of passive-scalar mixing. *Physics of Fluids*, 19(9):095102.

Holland, D. M. and Jenkins, A. (1999). Modeling thermodynamic ice/ocean interactions at the base of an ice shelf. *Journal of Physical Oceanography*, 29(8):1787–1800.

Holland, P. R., Bracegirdle, T. J., Dutrieux, P., Jenkins, A., and Steig, E. J. (2019). West antarctic ice loss influenced by internal climate variability and anthropogenic forcing. *Nature Geoscience*, 12(9):718–724.

Holland, P. R., Jenkins, A., and Holland, D. M. (2010). Ice and ocean processes in the Bellingshausen sea, Antarctica. *Journal of Geophysical Research: Oceans*, 115(5):1–16.

Holleman, R., Geyer, W., and Ralston, D. (2016). Stratified turbulence and mixing efficiency in a salt wedge estuary. *Journal of Physical Oceanography*, 46(6):1769–1783.

Holyer, J. Y. (1983). Double-diffusive interleaving due to horizontal gradients. *Journal of Fluid Mechanics*, 137:347–362.

Howland, C. J., Taylor, J. R., and Caulfield, C. (2020). Mixing in forced stratified turbulence and its dependence on large-scale forcing. *Journal of Fluid Mechanics*, 898.

Huntington, H. P., Quakenbush, L. T., and Nelson, M. (2017). Evaluating the effects of climate change on indigenous marine mammal hunting in northern and western Alaska using traditional knowledge. *Frontiers in Marine Science*, 4:319.

Huppert, H. E. and Linden, P. (1979). On heating a stable salinity gradient from below. *Journal of Fluid Mechanics*, 95(3):431–464.

Huppert, H. E. and Turner, J. S. (1980). Ice blocks melting into a salinity gradient. *Journal of Fluid Mechanics*, 100(2):367–384.

Inoue, R., Yamazaki, H., Wolk, F., Kono, T., and Yoshida, J. (2007). An estimation of buoyancy flux for a mixture of turbulence and double diffusion. *Journal of physical oceanography*, 37(3):611–624.

Jackett, D. R. and McDougall, T. J. (1985). An oceanographic variable for the characterization of intrusions and water masses. *Deep Sea Research Part A. Oceanographic Research Papers*, 32(10):1195–1207.

Jackson, P. R. and Rehmann, C. R. (2003). Laboratory measurements of differential diffusion in a diffusively stable, turbulent flow. *Journal of Physical Oceanography*, 33(8):1592–1603.

Jackson, R., Nash, J., Kienholz, C., Sutherland, D., Amundson, J., Motyka, R., Winters, D., Skyllingstad, E., and Pettit, E. (2020). Meltwater intrusions reveal mechanisms for rapid submarine melt at a tidewater glacier. *Geophysical Research Letters*, 47(2):e2019GL085335.

Jenkins, A. and Jacobs, S. (2008). Circulation and melting beneath George VI Ice Shelf, Antarctica. *Journal of Geophysical Research: Oceans*, 113(C4).

Jenkins, A., Nicholls, K. W., and Corr, H. F. (2010). Observation and parameterization of ablation at the base of Ronne Ice Shelf, Antarctica. *Journal of Physical Oceanography*, 40(10):2298–2312.

Kawaguchi, Y., Itoh, M., and Nishino, S. (2012). Detailed survey of a large baroclinic eddy with extremely high temperatures in the western Canada Basin. *Deep Sea Research Part I: Oceanographic Research Papers*, 66:90–102.

Keitzl, T., Mellado, J. P., and Notz, D. (2016). Reconciling estimates of the ratio of heat and salt fluxes at the ice–ocean interface. *Journal of Geophysical Research: Oceans*, 121(12):8419–8433.

Kimura, S., Jenkins, A., Dutrieux, P., Forryan, A., Naveira Garabato, A. C., and Firing, Y. (2016). Ocean mixing beneath Pine Island Glacier Ice Shelf, west Antarctica. *Journal of Geophysical Research: Oceans*, 121(12):8496–8510.

Kimura, S., Nicholls, K. W., and Venables, E. (2015). Estimation of ice shelf melt rate in the presence of a thermohaline staircase. *Journal of Physical Oceanography*, 45(1):133–148.

Kimura, S. and Smyth, W. (2007). Direct numerical simulation of salt sheets and turbulence in a double-diffusive shear layer. *Geophysical Research Letters*, 34(21).

Kimura, S. and Smyth, W. (2011). Secondary instability of salt sheets. *Journal of Marine Research*, 69(1):57–77.

Klymak, J. M., Crawford, W., Alford, M. H., MacKinnon, J. A., and Pinkel, R. (2015). Along-isopycnal variability of spice in the North Pacific. *Journal of Geophysical Research: Oceans*, 120(3):2287–2307.

Klymak, J. M. and Nash, J. D. (2009). Estimates of mixing. In *Encyclopedia of Ocean Sciences (second edition)*, pages 299–298. Oxford.

Knobloch, E., Moore, D. R., Toomre, J., and Weiss, N. O. (1986). Transitions to chaos in two-dimensional double-diffusive convection. *Journal of Fluid Mechanics*, 166:409–448.

Kolmogorov, A. N. (1941). The local structure of turbulence in incompressible viscous fluid for very large reynolds numbers. *Cr Acad. Sci. URSS*, 30:301–305.

Konopliv, N. and Meiburg, E. (2016). Double-diffusive lock-exchange gravity currents. *Journal of Fluid Mechanics*, 797:729–764.

Krishnamurti, R. (2003). Double-diffusive transport in laboratory thermohaline staircases. *Journal of Fluid Mechanics*, 483:287–314.

Kunze, E. (2003). A review of oceanic salt-fingering theory. *Progress in Oceanography*, 56:399–417.

Lenn, Y.-D., Wiles, P., Torres-Valdes, S., Abrahamsen, E., Rippeth, T. P., Simpson, J., Bacon, S., Laxon, S., Polyakov, I., Ivanov, V., et al. (2009). Vertical mixing at intermediate depths in the arctic boundary current. *Geophysical Research Letters*, 36(5).

Levine, M. D., Paulson, C. A., and Morison, J. H. (1985). Internal waves in the Arctic Ocean: Comparison with lower-latitude observations. *Journal of physical oceanography*, 15(6):800–809.

Lindborg, E. (2006). The energy cascade in a strongly stratified fluid. *Journal of Fluid Mechanics*, 550:207.

Linden, P. (1974). Salt fingers in a steady shear flow. *Geophysical and Astrophysical Fluid Dynamics*, 6(1):1–27.

Linden, P. and Shirtcliffe, T. (1978). The diffusive interface in double-diffusive convection. *Journal of Fluid Mechanics*, 87(3):417–432.

Locarnini, M., Mishonov, A., Baranova, O., Boyer, T., Zweng, M., Garcia, H., Seidov, D., Weathers, K., Paver, C., Smolyar, I., et al. (2018). World ocean atlas 2018, volume 1: Temperature.

Lorenz, E. N. (1955). Available potential energy and the maintenance of the general circulation. *Tellus*, 7(2):157–167.

Ludescher, J., Yuan, N., and Bunde, A. (2019). Detecting the statistical significance of the trends in the Antarctic sea ice extent: an indication for a turning point. *Climate dynamics*, 53(1):237–244.

Lueck, R. G., Wolk, F., and Yamazaki, H. (2002). Oceanic velocity microstructure measurements in the 20th century. *Journal of Oceanography*, 58(1):153–174.

Ma, Y. and Peltier, W. (2021). Parametrization of irreversible diapycnal diffusivity in salt-fingering turbulence using DNS. *Journal of Fluid Mechanics*, 911.

MacKinnon, J. A., Nash, J. D., Alford, M. H., Lucas, A. J., Mickett, J. B., Shroyer, E. L., Waterhouse, A. F., Tandon, A., Sengupta, D., Mahadevan, A., et al. (2016). A tale of two spicy seas. *Oceanography*, 29(2):50–61.

Malyarenko, A., Wells, A. J., Langhorne, P. J., Robinson, N. J., Williams, M. J., and Nicholls, K. W. (2020). A synthesis of thermodynamic ablation at ice-ocean interfaces from theory, observations and models. *Ocean Modelling*, page 101692.

Martin, S. and Kauffman, P. (1977). An experimental and theoretical study of the turbulent and laminar convection generated under a horizontal ice sheet floating on warm salty water. *Journal of Physical Oceanography*, 7(2):272–283.

Maykut, G. A. and Untersteiner, N. (1971). Some results from a time-dependent thermodynamic model of sea ice. *Journal of Geophysical Research*, 76(6):1550–1575.

McDougall, T. J. and Barker, P. M. (2011). Getting started with TEOS-10 and the gibbs seawater (gsw) oceanographic toolbox. *SCOR/IAPSO WG*, 127:1–28.

McDougall, T. J. and Turner, J. S. (1982). Influence of cross-diffusion on ‘finger’ double-diffusive convection. *Nature*, 299(5886):812.

McPhee, M. (2008). *Air-ice-ocean interaction: Turbulent ocean boundary layer exchange processes*. Springer Science & Business Media.

McPhee, M. G., Maykut, G. A., and Morison, J. H. (1987). Dynamics and thermodynamics of the ice/upper ocean system in the marginal ice zone of the Greenland Sea. *Journal of Geophysical Research: Oceans*, 92(C7):7017–7031.

Meredith, M., Sommerkorn, M., Cassotta, S., Derksen, C., Ekaykin, A., Hollowed, A., Kofinas, G., Mackintosh, A., Melbourne-Thomas, J., Muelbert, M., et al. (2019). Polar regions. chapter 3, IPCC special report on the ocean and cryosphere in a changing climate.

Merryfield, W. J. (2000). Origin of thermohaline staircases. *Journal of Physical Oceanography*, 30(5):1046–1068.

Moffat, C., Owens, B., and Beardsley, R. (2009). On the characteristics of Circumpolar Deep Water intrusions to the west Antarctic Peninsula continental shelf. *Journal of Geophysical Research: Oceans*, 114(C5).

Monin, A. S. and Obukhov, A. M. (1954). Basic laws of turbulent mixing in the surface layer of the atmosphere. *Contrib. Geophys. Inst. Acad. Sci. USSR*, 151(163):e187.

Morlighem, M., Rignot, E., Binder, T., Blankenship, D., Drews, R., Eagles, G., Eisen, O., Ferraccioli, F., Forsberg, R., Fretwell, P., et al. (2020). Deep glacial troughs and stabilizing ridges unveiled beneath the margins of the Antarctic ice sheet. *Nature Geoscience*, 13(2):132–137.

Moum, J. (1990). Profiler measurements of vertical velocity fluctuations in the ocean. *Journal of Atmospheric and Oceanic Technology*, 7(2).

Moum, J., Gregg, M., Lien, R., and Carr, M. (1995). Comparison of turbulence kinetic energy dissipation rate estimates from two ocean microstructure profilers. *Journal of Atmospheric and Oceanic Technology*, 12(2):346–366.

Nagai, T., Quintana, G. M. R., Gómez, G. S. D., Hashihama, F., and Komatsu, K. (2021). Elevated turbulent and double-diffusive nutrient flux in the Kuroshio over the Izu ridge and in the Kuroshio Extension. *Journal of Oceanography*, 77(1):55–74.

Nakamura, N. (1996). Two-dimensional mixing, edge formation, and permeability diagnosed in an area coordinate. *Journal of the Atmospheric Sciences*, 53(11):1524–1537.

Nakayama, Y., Menemenlis, D., Zhang, H., Schodlok, M., and Rignot, E. (2018). Origin of circumpolar deep water intruding onto the amundsen and bellingshausen sea continental shelves. *Nature communications*, 9(1):1–9.

Nash, J. D. and Moum, J. N. (1999). Estimating salinity variance dissipation rate from conductivity microstructure measurements. *Journal of Atmospheric and Oceanic Technology*, 16(2):263–274.

Nash, J. D. and Moum, J. N. (2002). Microstructure estimates of turbulent salinity flux and the dissipation spectrum of salinity. *Journal of Physical Oceanography*, 32(8):2312–2333.

Nayak, A. and Bhattacharyya, S. (2012). Double-diffusive convection in a cubical lid-driven cavity with opposing temperature and concentration gradients. *Theoretical and Computational Fluid Dynamics*, 26(6):565–581.

Oakey, N. (1982). Determination of the rate of dissipation of turbulent energy from simultaneous temperature and velocity shear microstructure measurements. *Journal of Physical Oceanography*, 12(3):256–271.

Orszag, S. A. (1971). On the elimination of aliasing in finite-difference schemes by filtering high-wavenumber components. *Journal of the Atmospheric sciences*, 28(6):1074–1074.

Osborn, T. R. (1980). Estimates of the local rate of vertical diffusion from dissipation measurements. *Journal of Physical Oceanography*, 10(1):83–89.

Osborn, T. R. and Cox, C. S. (1972). Oceanic fine structure. *Geophysical Fluid Dynamics*, 3(4):321–345.

Oschlies, A., Dietze, H., and Kähler, P. (2003). Salt-finger driven enhancement of upper ocean nutrient supply. *Geophysical research letters*, 30(23).

Padman, L. (1994). Momentum fluxes through sheared oceanic thermohaline steps. *Journal of Geophysical Research: Oceans*, 99(C11):22491–22499.

Paparella, F. and Von Hardenberg, J. (2012). Clustering of salt fingers in double-diffusive convection leads to staircaselike stratification. *Physical review letters*, 109(1):014502.

Parkinson, A. J. and Berner, J. (2009). Climate change and impacts on human health in the Arctic: an international workshop on emerging threats and the response of Arctic communities to climate change. *International Journal of Circumpolar Health*, 68(1):84–91.

Peltier, W. and Caulfield, C. (2003). Mixing efficiency in stratified shear flows. *Annual review of fluid mechanics*, 35(1):135–167.

Penney, J., Morel, Y., Haynes, P., Auclair, F., and Nguyen, C. (2020). Diapycnal mixing of passive tracers by Kelvin–Helmholtz instabilities. *Journal of Fluid Mechanics*, 900.

Petty, A. A., Kurtz, N. T., Kwok, R., Markus, T., and Neumann, T. A. (2020). Winter arctic sea ice thickness from icesat-2 freeboards. *Journal of Geophysical Research: Oceans*, 125(5):e2019JC015764.

Phillips, O. (1972). Turbulence in a strongly stratified fluid—is it unstable? In *Deep Sea Research and Oceanographic Abstracts*, volume 19, pages 79–81. Elsevier.

Polyakov, I. V., Rippeth, T. P., Fer, I., Alkire, M. B., Baumann, T. M., Carmack, E. C., Ingvaldsen, R., Ivanov, V. V., Janout, M., Lind, S., et al. (2020). Weakening of cold halocline layer exposes sea ice to oceanic heat in the eastern arctic ocean. *Journal of Climate*, 33(18):8107–8123.

Polzin, K. L., Garabato, A. C. N., Huussen, T. N., Sloyan, B. M., and Waterman, S. (2014). Finescale parameterizations of turbulent dissipation. *Journal of Geophysical Research: Oceans*, 119(2):1383–1419.

Pope, S. B. (2001). Turbulent flows.

Portwood, G. D., de Bruyn Kops, S., and Caulfield, C. (2019). Asymptotic dynamics of high dynamic range stratified turbulence. *Physical review letters*, 122(19):194504.

Potter, J., Paren, J., and Loynes, J. (1984). Glaciological and oceanographic calculations of the mass balance and oxygen isotope ratio of a melting ice shelf. *Journal of Glaciology*, 30(105):161–170.

Potter, J. R. and Paren, J. G. (1985). Interaction between ice shelf and ocean in George VI Sound, Antarctica. *Oceanology of the Antarctic continental shelf*, 43:35–58.

Radko, T. (2003). A mechanism for layer formation in a double-diffusive fluid. *Journal of Fluid Mechanics*, 497:365–380.

Radko, T. (2013). *Double-diffusive convection*. Cambridge University Press.

Radko, T. (2019). Thermohaline-shear instability. *Geophysical Research Letters*, 46(2):822–832.

Radko, T., Ball, J., Colosi, J., and Flanagan, J. (2015). Double-diffusive convection in a stochastic shear. *Journal of Physical Oceanography*, 45(12):3155–3167.

Radko, T., Flanagan, J., Stellmach, S., and Timmermans, M.-L. (2014). Double-diffusive recipes. part ii: Layer-merging events. *Journal of physical oceanography*, 44(5):1285–1305.

Rao, K. and de Bruyn Kops, S. (2011). A mathematical framework for forcing turbulence applied to horizontally homogeneous stratified flow. *Physics of Fluids*, 23(6):065110.

Rignot, E., Jacobs, S., Mouginot, J., and Scheuchl, B. (2013). Ice-shelf melting around Antarctica. *Science*, 341(6143):266–270.

Rignot, E., Mouginot, J., Scheuchl, B., Van Den Broeke, M., Van Wessem, M. J., and Morlighem, M. (2019). Four decades of Antarctic ice sheet mass balance from 1979–2017. *Proceedings of the National Academy of Sciences*, 116(4):1095–1103.

Riley, J. J. and Lindborg, E. (2008). Stratified turbulence: A possible interpretation of some geophysical turbulence measurements. *Journal of the Atmospheric Sciences*, 65(7):2416–2424.

Riley, J. P. and Chester, R. (2016). *Chemical oceanography*. Elsevier.

Roget, E., Lozovatsky, I., Sanchez, X., and Figueroa, M. (2006). Microstructure measurements in natural waters: Methodology and applications. *Progress in Oceanography*, 70(2-4):126–148.

Roquet, F., Madec, G., Brodeau, L., and Nycander, J. (2015). Defining a simplified yet "realistic" equation of state for seawater. *Journal of Physical Oceanography*, 45(10):2564–2579.

Rosevear, M. G., Gayen, B., and Galton-Fenzi, B. K. (2021). The role of double-diffusive convection in basal melting of Antarctic ice shelves. *Proceedings of the National Academy of Sciences*, 118(6).

Ruddick, B. (1992). Intrusive mixing in a mediterranean salt lens—intrusion slopes and dynamical mechanisms. *Journal of Physical Oceanography*, 22(11):1274–1285.

Ruddick, B. and Kerr, O. (2003). Oceanic thermohaline intrusions: theory. *Progress in oceanography*, 56(3-4):483–497.

Ruddick, B. and Richards, K. (2003). Oceanic thermohaline intrusions: observations. *Progress in Oceanography*, 56(3-4):499–527.

Ruddick, B. and Turner, J. (1979). The vertical length scale of double-diffusive intrusions. *Deep Sea Research Part A. Oceanographic Research Papers*, 26(8):903–913.

Rudnick, D. L. and Ferrari, R. (1999). Compensation of horizontal temperature and salinity gradients in the ocean mixed layer. *Science*, 283(5401):526–529.

Rudnick, D. L. and Martin, J. P. (2002). On the horizontal density ratio in the upper ocean. *Dynamics of atmospheres and oceans*, 36(1-3):3–21.

Salehipour, H., Peltier, W., Whalen, C., and MacKinnon, J. (2016). A new characterization of the turbulent diapycnal diffusivities of mass and momentum in the ocean. *Geophysical Research Letters*, 43(7):3370–3379.

Scalo, C., Piomelli, U., and Boegman, L. (2012). Large-eddy simulation of oxygen transfer to organic sediment beds. *Journal of Geophysical Research: Oceans*, 117(C6).

Schlichting, H. and Gersten, K. (2016). *Boundary-layer theory*. Springer.

Schmitt, R. W. (1994). Double diffusion in oceanography. *Annual Review of Fluid Mechanics*, 26(1):255–285.

Schulz, K., Janout, M., Lenn, Y.-D., Ruiz-Castillo, E., Polyakov, I., Mohrholz, V., Tippenhauer, S., Reeve, K. A., Hölemann, J., Rabe, B., et al. (2021). On the along-slope heat loss of the boundary current in the eastern arctic ocean. *Journal of Geophysical Research: Oceans*, 126(2):e2020JC016375.

Scotti, A. and White, B. (2014). Diagnosing mixing in stratified turbulent flows with a locally defined available potential energy. *Journal of Fluid Mechanics*, 740:114–135.

Sharqawy, M., Lienhard, J., and Zubair, S. (2010). Thermophysical properties of seawater: a review of existing correlations and data. *Desalination and water treatment*, 16(1-3):354–380.

Shibley, N. and Timmermans, M.-L. (2019). The formation of double-diffusive layers in a weakly turbulent environment. *Journal of Geophysical Research: Oceans*, 124(3):1445–1458.

Shibley, N. C., Timmermans, M.-L., Carpenter, J. R., and Toole, J. M. (2017). Spatial variability of the Arctic Ocean's double-diffusive staircase. *Journal of Geophysical Research: Oceans*, 122(2):980–994.

Shimada, K., Kamoshida, T., Itoh, M., Nishino, S., Carmack, E., McLaughlin, F., Zimmermann, S., and Proshutinsky, A. (2006). Pacific Ocean inflow: Influence on catastrophic reduction of sea ice cover in the Arctic Ocean. *Geophysical Research Letters*, 33(8).

Smith, D. A. and Klinck, J. M. (2002). Water properties on the west Antarctic peninsula continental shelf: a model study of effects of surface fluxes and sea ice. *Deep Sea Research Part II: Topical Studies in Oceanography*, 49(21):4863–4886.

Smith, K. S. and Ferrari, R. (2009). The production and dissipation of compensated thermohaline variance by mesoscale stirring. *Journal of Physical Oceanography*, 39(10):2477–2501.

Smyth, W., Nash, J., and Moum, J. (2005). Differential diffusion in breaking Kelvin–Helmholtz billows. *Journal of Physical Oceanography*, 35(6):1004–1022.

Smyth, W. D. and Moum, J. N. (2000). Length scales of turbulence in stably stratified mixing layers. *Physics of Fluids*, 12(6):1327–1342.

St. Laurent, L. and Schmitt, R. (1999). The contribution of salt fingers to vertical mixing in the North Atlantic Tracer Release Experiment. *Journal of Physical Oceanography*, 29(7):1404–1424.

Steele, M., Morison, J., Ermold, W., Rigor, I., Ortmeyer, M., and Shimada, K. (2004). Circulation of summer Pacific halocline water in the Arctic Ocean. *Journal of Geophysical Research: Oceans*, 109(C2).

Stephenson Jr, G. R., Sprintall, J., Gille, S. T., Vernet, M., Helly, J. J., and Kaufmann, R. S. (2011). Subsurface melting of a free-floating Antarctic iceberg. *Deep Sea Research Part II: Topical Studies in Oceanography*, 58(11-12):1336–1345.

Stevens, C., Hulbe, C., Brewer, M., Stewart, C., Robinson, N., Ohneiser, C., and Jendersie, S. (2020). Ocean mixing and heat transport processes observed under the Ross Ice Shelf control its basal melting. *Proceedings of the National Academy of Sciences*, 117(29):16799–16804.

Suter, L., Streletskiy, D., and Shiklomanov, N. (2019). Assessment of the cost of climate change impacts on critical infrastructure in the circumpolar Arctic. *Polar Geography*, 42(4):267–286.

Tailleux, R. (2013). Available potential energy density for a multicomponent boussinesq fluid with arbitrary nonlinear equation of state. *Journal of Fluid Mechanics*, 735:499–518.

Tailleux, R. (2018a). APE dissipation is a form of Joule heating. It is irreversible, not reversible. *arXiv preprint arXiv:1806.11303*.

Tailleux, R. (2018b). Local available energetics of multicomponent compressible stratified fluids. *Journal of Fluid Mechanics*, 842.

Talley, L. D., Lobanov, V., Ponomarev, V., Salyuk, A., Tishchenko, P., Zhabin, I., and Riser, S. (2003). Deep convection and brine rejection in the Japan Sea. *Geophysical Research Letters*, 30(4).

Taylor, J., de Bruyn Kops, S., Caulfield, C., and Linden, P. (2019). Testing the assumptions underlying ocean mixing methodologies using direct numerical simulations. *Journal of Physical Oceanography*, 49(11):2761–2779.

Taylor, J. and Zhou, Q. (2017). A multi-parameter criterion for layer formation in a stratified shear flow using sorted buoyancy coordinates. *Journal of Fluid Mechanics*, 823.

Taylor, J. R. (2008). *Numerical simulations of the stratified oceanic bottom boundary layer*. PhD thesis, UC San Diego.

Taylor, J. R. and Stocker, R. (2012). Trade-offs of chemotactic foraging in turbulent water. *Science*, 338(6107):675–679.

Tennekes, H. and Lumley, J. L. (2018). *A first course in turbulence*. MIT press.

Thwaites, F. and Williams, A. (1996). Development of a modular acoustic velocity sensor. In *OCEANS 96 MTS/IEEE Conference Proceedings. The Coastal Ocean-Prospects for the 21st Century*, volume 2, pages 607–612. IEEE.

Timmermans, M.-L. and Marshall, J. (2020). Understanding Arctic Ocean circulation: A review of ocean dynamics in a changing climate. *Journal of Geophysical Research: Oceans*, 125(4).

Timmermans, M.-L., Toole, J., and Krishfield, R. (2018). Warming of the interior Arctic Ocean linked to sea ice losses at the basin margins. *Science advances*, 4(8):eaat6773.

Timmermans, M.-L., Toole, J., Krishfield, R., and Winsor, P. (2008). Ice-Tethered Profiler observations of the double-diffusive staircase in the Canada Basin thermocline. *Journal of Geophysical Research*, 113:C00A02.

Toole, J. M., Timmermans, M.-L., Perovich, D. K., Krishfield, R. A., Proshutinsky, A., and Richter-Menge, J. A. (2010). Influences of the ocean surface mixed layer and thermohaline stratification on Arctic sea ice in the central Canada Basin. *Journal of Geophysical Research: Oceans*, 115(C10).

Tseng, Y.-h. and Ferziger, J. H. (2001). Mixing and available potential energy in stratified flows. *Physics of Fluids*, 13(5):1281–1293.

Turner, J. (1968). The behaviour of a stable salinity gradient heated from below. *Journal of Fluid Mechanics*, 33(1):183–200.

Turner, J. (1985). Multicomponent convection. *Annual review of fluid mechanics*, 17(1):11–44.

van der Boog, C. G., Dijkstra, H. A., Pietrzak, J. D., and Katsman, C. A. (2021). Double-diffusive mixing makes a small contribution to the global ocean circulation. *Communications Earth & Environment*, 2(1):1–9.

Venables, E., Nicholls, K., Wolk, F., Makinson, K., and Anker, P. (2014). Measuring turbulent dissipation rates beneath an Antarctic ice shelf. *Marine Technology Society Journal*, 48(5):18–24.

Veronis, G. (1965). On finite amplitude instability in thermohaline convection. *J. mar. Res*, 23(1):1–17.

Vitagliano, V. and Lyons, P. A. (1956). Diffusion coefficients for aqueous solutions of sodium chloride and barium chloride. *Journal of the American Chemical Society*, 78(8):1549–1552.

Vreugdenhil, C. A. and Taylor, J. R. (2018). Large-eddy simulations of stratified plane couette flow using the anisotropic minimum-dissipation model. *Physics of Fluids*, 30(8):085104.

Vreugdenhil, C. A. and Taylor, J. R. (2019). Stratification effects in the turbulent boundary layer beneath a melting ice shelf: Insights from resolved large-eddy simulations. *Journal of Physical Oceanography*, 49(7):1905–1925.

Walesby, K., Vialard, J., Minnett, P. J., Callaghan, A. H., and Ward, B. (2015). Observations indicative of rain-induced double diffusion in the ocean surface boundary layer. *Geophysical Research Letters*, 42(10):3963–3972.

Wang, L.-P., Chen, S., Brasseur, J. G., and Wyngaard, J. C. (1996). Examination of hypotheses in the Kolmogorov refined turbulence theory through high-resolution simulations. part 1. velocity field. *Journal of Fluid Mechanics*, 309:113–156.

Watanabe, E. (2011). Beaufort shelf break eddies and shelf-basin exchange of Pacific summer water in the western Arctic Ocean detected by satellite and modeling analyses. *Journal of Geophysical Research: Oceans*, 116(C8).

Welch, P. (1967). The use of fast fourier transform for the estimation of power spectra: a method based on time averaging over short, modified periodograms. *IEEE Transactions on audio and electroacoustics*, 15(2):70–73.

Whalen, C. B., MacKinnon, J. A., Talley, L. D., and Waterhouse, A. F. (2015). Estimating the mean diapycnal mixing using a finescale strain parameterization. *Journal of Physical Oceanography*, 45(4):1174–1188.

Williams 3rd, A. J. (1975). Images of ocean microstructure. In *Deep Sea Research and Oceanographic Abstracts*, volume 22, pages 811–829. Elsevier.

Winters, K. and D'Asaro, E. (1996). Diascalar flux and the rate of fluid mixing. *Journal of Fluid Mechanics*, 317:179–193.

Winters, K., Lombard, P., Riley, J., and D'Asaro, E. (1995). Available potential energy and mixing in density-stratified fluids. *Journal of Fluid Mechanics*, 289:115–128.

Woodgate, R. A., Weingartner, T., and Lindsay, R. (2010). The 2007 Bering Strait oceanic heat flux and anomalous Arctic sea ice retreat. *Geophysical Research Letters*, 37(1).

Zhou, S.-Q., Lu, Y.-Z., Song, X.-L., and Fer, I. (2016). New layer thickness parameterization of diffusive convection in the ocean. *Dynamics of Atmospheres and Oceans*, 73:87–97.

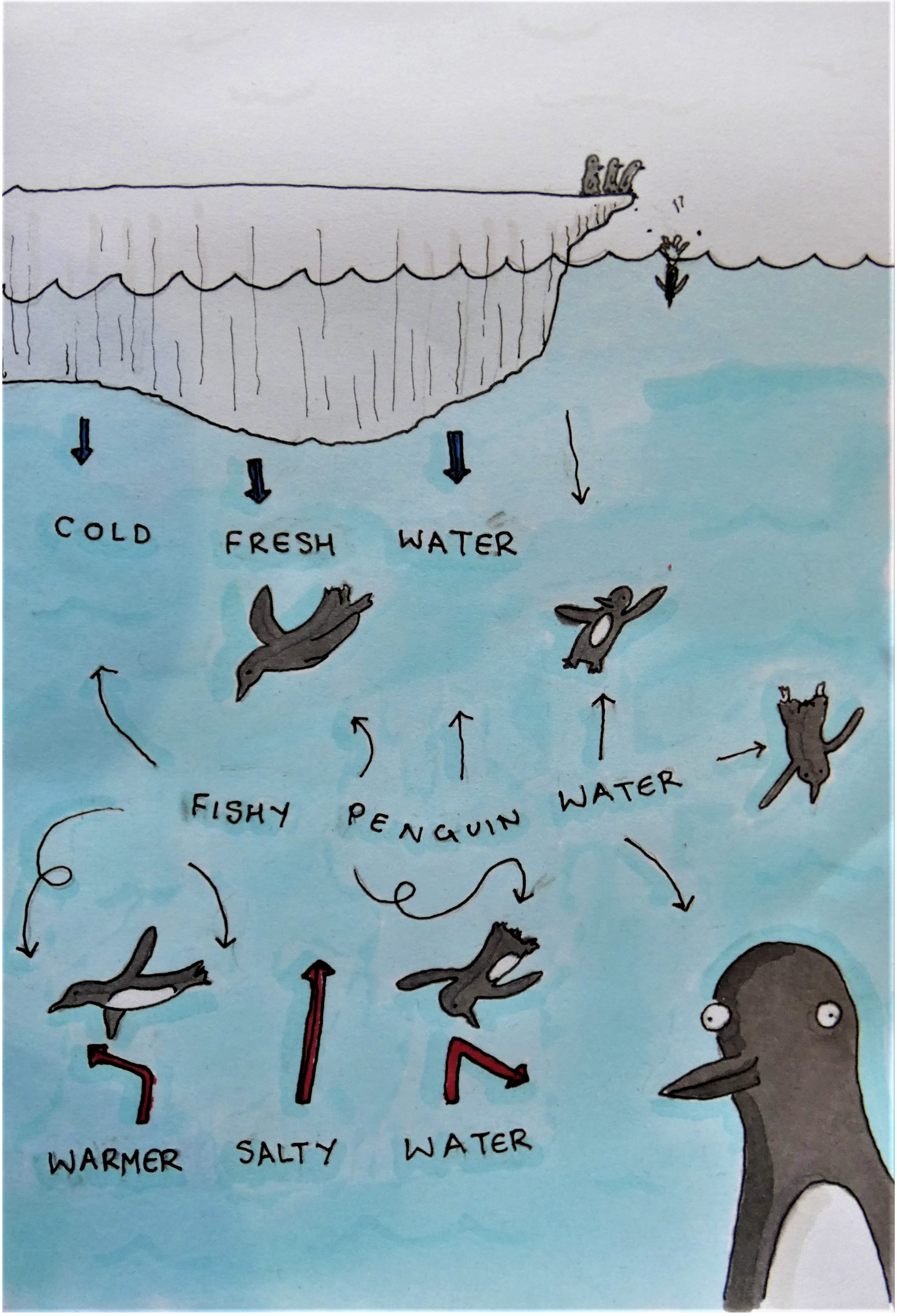
COLD
FRESH
WATER
FISHY
PENGUIN
WATER
WARMER
SALTY
WATER

Fig. 6.1 Preview of my next paper, courtesy of Reuben Ruxton.
The problem of penguins: The influence of millions of tiny flippers on double diffusion.